Experimental and numerical study of flow distribution in compact plate heat exchangers

Chiara Galati

THÈSE

En vue de l'obtention du

DOCTORAT DE L'UNIVERSITÉ DE TOULOUSE

Délivré par :

Institut National Polytechnique de Toulouse (INP Toulouse)

Discipline ou spécialité :

Energétique et Transferts

Présentée et soutenue par :

Mme CHIARA GALATI

le mercredi 13 décembre 2017

Titre :

Etude numérique et expérimentale de la distribution de fluide dans un échangeur de chaleur compact à plaques

---

Ecole doctorale :

Mécanique, Energétique, Génie civil, Procédés (MEGeP)

Unité de recherche :

Laboratoire de Génie Chimique (L.G.C.)

Directeur(s) de Thèse :

M. LAURENT PRAT

M. CHRISTOPHE GOURDON

Rapporteurs :

M. HASSAN PEERHOSSAINI, UNIVERSITE PARIS 7

M. LAURENT FALK, CNRS

Membre(s) du jury :

M. HASSAN PEERHOSSAINI, UNIVERSITE PARIS 7, Président

M. CHRISTOPHE GOURDON, INP TOULOUSE, Membre

M. LAURENT PRAT, INP TOULOUSE, Membre

M. LIONEL CACHON, CEA CADARACHE, Membre

Mme MARIA ADELA PUSCAS, CEA SACLAY, Membre

A mia madre e a mio padre

...e a Te,

che mi hai sempre protetto sotto il

tuo manto celeste senza lasciarmi mai sola.

Résumé

Ce travail de thèse s'inscrit dans le cadre du programme R&D du CEA en support au système de conversion d'énergie à gaz du prototype industriel de Réacteur à Neutrons Rapides refroidi au Sodium (RNR-Na). Cette technologie représente une alternative aux cycles Rankine conventionnels à eau/vapeur, ayant pour avantage principal l'élimination du scenario accidentel de réaction sodium-eau. Cependant, la faible capacité de transfert de chaleur du gaz nécessite une technologie d'échangeurs compacts à plaques avec un nombre élevé de canaux à alimenter. Coté sodium, une section minimale de passage est nécessaire pour éviter le risque de bouchage par impureté. Cela induit de très faibles pertes de pression dans le faisceau qui, couplées à une condition de vitesse élevée à l'entrée, génèrent un risque réel de mauvaise distribution du débit. Les performances d'échange thermique et la tenue mécanique du composant sont alors dégradées.

L'objectif principal de ce travail de thèse a été de résoudre ce problème de mauvaise distribution, en s'appuyant sur une conception innovante (BREVET FR16 57543), sur une stratégie de calcul numérique et l'établissement d'une base de données expérimentale pour la validation des travaux théoriques.

Le nouveau système de distribution sodium se compose d'un collecteur d'entrée dont le design permet de guider la trajectoire du jet et d'un système de bifurcation de canaux qui augmente les pertes de pression dans le faisceau. De plus, des communications latérales entre les canaux sodium aident à homogénéiser davantage le flux.

Deux installations expérimentales ont été conçues pour caractériser l'écoulement dans les canaux de bifurcation et dans le collecteur d'entrée. La conception des maquettes a permis de quantifier leur effet sur la distribution du flux entre les canaux. La base de données aérodynamiques PIV acquises a permis de valider les modèles numériques et de prouver l'efficacité du système de distribution proposé.

Après avoir validé les modèles de turbulence CFD et la stratégie d'étude de la distribution dans le module SGHE, une optimisation de chaque composant du système de distribution de sodium a été réalisée.

Le travail de cette thèse s'achève par la description de la conception optimale retenue pour la phase actuelle du projet ASTRID.

Mots Clés : Echangeur compact à plaques, Mauvaise distribution, Mécanique des fluides numérique (CFD), Vélocimétrie par image des particules (PIV), Jet tridimensionnel, Jets parallèles.

Abstract

This PhD work was motivated by the CEA R&D program to provide solid technological basis for the use of Brayton power conversion system in Sodium-cooled Fast nuclear Reactors (SFRs). Multi-channel compact heat exchangers are necessary for the present application because of the low heat transfer capacity of the gas foreseen. In ASTRID project, a minimum size of Na channels section is required to avoid the plugging risk. However, this induces very low pressure losses in the bundle. Considering an additional inlet flow condition, a real risk of bad flow distribution remains. As a result, the thermal performance and thermal loading of the heat exchanger degrades due to it.

The main goal of this work was to overcome the flow maldistribution problem by means of an innovative design of sodium distribution system (PATENT FR1657543), the development of a numerical strategy and the construction of an experimental database to validate all theoretical studies.

The innovative sodium distribution system consists on an inlet header which tries to guide the evolution of the impinging jet flow while a system of bifurcating pre-distribution channels increases pressure drops in the bundle. Lateral communications between pre-distribution channels are introduced to further homogenize the flow.

Two experimental facilities have been conceived to study the flow behavior in bifurcating channels and in the inlet header, respectively. At the same time, their effect on the flow distribution between channels is evaluated. The acquired PIV aerodynamic database allows to validate the numerical models and to prove the design basis for the proposed distribution system.

Once having validated the CFD turbulence models and the strategy to study the flow maldistribution in the SGHE module, a decisive and trustworthy optimization of each component of the sodium distribution system has been performed.

Finally, an optimal configuration has been proposed for the actual phase of ASTRID project.

Keywords: Compact Heat Exchanger, Flow maldistribution, Computational Fluid Dynamics (CFD), Particle Image Velocimetry (PIV), Three-dimensional jet flow, Parallel jets.

Remerciements

A l'issue de ce travail de recherche, je suis convaincue que la thèse n'est pas seulement une expérience professionnelle mais une expérience de vie. On se retrouve souvent seule face à des problèmes qu'on ne sait pas forcement résoudre et qui nous donnent le temps de découvrir nos faiblesses mais aussi nos points forts. Durant cette phase délicate, le soutien d'un grand nombre de personnes m'a été indispensable. Leur générosité, leur bonne humeur et leur intérêt manifesté à l'égard de ma thèse m'ont permis d'évoluer et de progresser.

En première lieu, je tiens à remercier Monsieur Lionel Cachon pour la confiance qu'il m'a accordée en me confiant une mission très intéressante. Je le remercie pour m'avoir accompagné pendant ces trois dernières années, pour m'avoir apporté son savoir-faire et son savoir-être et pour être tout simplement une image professionnelle par laquelle on apprend beaucoup.

Je souhaiterais exprimer ma gratitude à mon directeur de thèse, monsieur Laurent Prat, qui malgré la distance et son emploi du temps très chargé a toujours été présent dans les moments difficiles. Il m'a appris qu'on peut avoir de grandes responsabilités tout en restant disponible pour les autres. Je dois aussi le remercier pour toutes les conférences et les formations auxquelles j'ai pu participer, cela m'a donné la possibilité de présenter mes travaux à l'international et d'améliorer mes compétences sur des thématiques spécifiques.

Merci à Christophe Gourdon pour avoir été l'encadrant le plus optimiste de ma thèse, merci pour sa participation scientifique ainsi que le temps qu'il a consacré à ma recherche

Merci à Monsieur Sylvain Madelaine, pour m'avoir accueilli dans son laboratoire depuis mon stage de fin d'étude. J'ai été extrêmement sensible à ses qualités humaines d'écoute et de compréhension tout au long de ce travail doctoral.

Quand, en Février 2014, je suis arrivée au CEA depuis l'Italie, je n'étais qu'une jeune étudiante pas très douée en français et assez timide. Mais j'ai eu la chance de travailler dans un laboratoire avec des personnes uniques qui m'ont tout de suite fait sentir comme chez moi.

Merci à Corinne et Stéphane, chaque matin vous étiez présentes pour discuter et rire ensemble avant de commencer la journée de travail. Merci à Xavier et Christophe, les piliers de la salle de calcul, les discussions avec vous m'ont toujours permis d'approfondir mes compétences scientifiques et mon savoir-vivre.

Je n’oublierai jamais l’oiseau siffleur, Pierre Charvet, qui a eu la patience de supporter toutes mes demandes d’aide, que cela soit pour des problèmes informatique ou les circuits électrique de mes plaques. Des giga octets de merci !

Je ne pourrais jamais assez remercier Thomas Marchiollo, qui restait tous les après-midis après 17h, pour écouter mes plaintes et pour me soutenir quand tout paraissait difficile. Tu ne m’as pas seulement aidé à concevoir des veines fluides et des maquettes mais mon projet de thèse dans sa globalité. Tu as partagé avec moi DANAH, nous y avons cru ensemble et nous avons réussi à la réaliser. Merci pour ton amitié.

Merci à Isabelle Tkatschenko et David Guenadou pour m’avoir accueilli dans leur laboratoire et pour m'avoir laissé tout le temps nécessaire pour pouvoir compléter de façon adéquate mes mesures. Valérie et Fabienne, merci pour votre patience et pour m’avoir dédié beaucoup de temps afin d’obtenir des résultats expérimentaux exploitables. Un grand merci à Jean Philippe et Philippe, les co-équipiers plus atypiques qui se sont toujours débrouillés pour réparer DANAH et qui m’ont appris avec leur style de vie à apprécier le travail et relativiser dans les moments difficiles.

Merci aussi à Giulio Mancini et Giovanni Baldi, qui se sont chargés de plusieurs parties importantes de ce travail et qui m’ont permis d’avancer dans des axes de recherche que je n’aurais jamais pu investiguer autrement.

Merci à Elena d'être ma binôme de bureau cool et pleine d’énergie qui m’a accompagné dans cette expérience. Merci pour ton amitié et pour les longues discussions sincères.

Merci à tous mes amis italiens expatriés comme moi, merci pour tous les bons moments passés ensemble.

Un merci particulier à mon mentor, Francesco Vitillo. Même après la fin de sa mission de tuteur de stage, il était là pour me montrer les différentes étapes à franchir et me permettre d’avancer. Il m’a fait profiter de son expérience pour éviter des erreurs et je le remercie d’avoir cru en moi. Il est surement la personne qui a enrichi le plus ma connaissance scientifique.

Merci également à l’atelier et à toutes l’équipe du LGC qui ont su m’accueillir à Toulouse et me supporter pendant tous les problèmes de la maquette EASY-B. Sans leur engagement il n’aurait pas été possible de mener à bien ces mesures.

Merci à Alain et Alec les gardiens de l’INP ENSIACET, qui ont mis à ma disposition l’école à des horaires improbables et qui m’ont tenu compagnie pendant les longs post-traitements de mesures.

Je ne pourrais finir ces remerciements sans penser à ma famille qui encore une fois m'a permis de réaliser un grand projet dans ma vie, même si cela a engendré un éloignement familial. Merci à Mamma et Papà, pour avoir été toujours présents pendant les choix importants de ma vie. Merci pour votre patience et votre aide quotidienne. pour faire toujours tout le possible pour m'aider. Merci Roberta pour ton soutien et tes conseils précieux qui deviennent de plus en plus indispensables dans ma vie. Merci Francesco, pour être un frère si spécial qui fait mon bonheur et ma joie de vivre. Enfin merci à Nonno et Nonna pour votre affection infinie et pour être mon plus grand exemple de Famille.

Merci à Titti et Stefania, les amies de toujours qui continuent à me supporter depuis 25 ans ! Et merci à tous mes amis du sud, qui m'ont permis de me ressourcer pendant mes vacances.

Enfin, le plus grand merci revient à Pierre-Yves, qui est entré dans ma vie seulement à la moitié parcours de thèse et il a accepté sans aucune hésitation de rester à mes côtés pour construire la plus belle histoire d'amour. Merci pour ta patience et ta bienveillance, mais également merci de m'avoir transmis ta sérénité et ta joie qui ont été nécessaires pour surmonter mes plus grandes difficultés.

Contents

Liste of Figures

Liste of Tables

List of most cited acronyms:

- CEA : Commissariat à l'énergie atomique et aux énergies alternatives
- GIF: Generation IV International Forum
- FR: Fast Reactor
- SFR: Sodium-cooled Fast Reactor
- ASTRID: Advanced Sodium Technological Reactor for Industrial Demonstration
- SGHE: Sodium-Gas Heat Exchanger
- SWR: Sodium-Water Reaction
- ECS: Energy Conversion System
- SGHE: Sodium-Gas Heat Exchanger
- PIV : Particle Image Velocimetry
- Re: Reynolds number
- RANS: Reynolds-Averaged Navier Stokes
- RSM: Reynolds Stress transport Model
- SST: Shear Stress Transport model
- ASST: Anisotropic Shear Stress Transport model

Chapter 1

Context and scope of the work

1.1. Context

As of August 2017, there are over 440 commercial nuclear power reactors operable in 31 countries, with over 390,000 MW_e of total capacity. About 60 more reactors are under construction. They provide over 11% of the world's electricity as continuous, reliable power to meet base-load demand, without carbon dioxide emissions [1].
Fig.1.1 shows the nuclear energy production worldwide during the last 50 years.

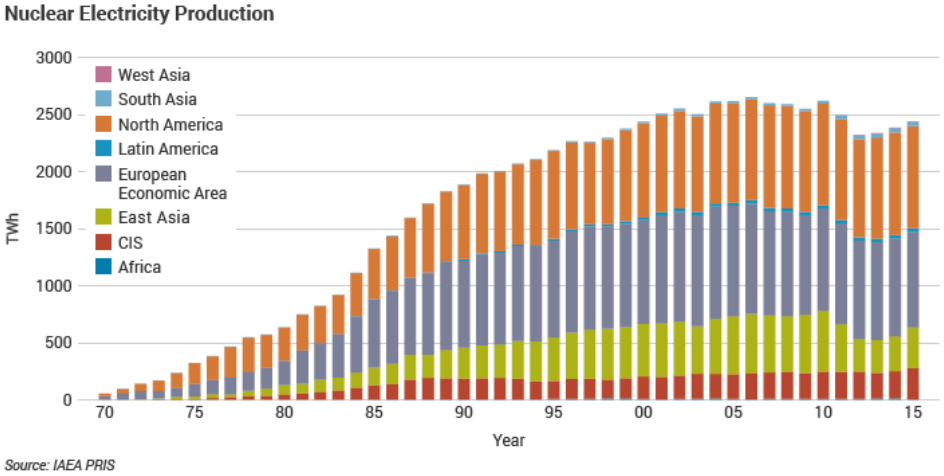

Fig.1. 1 – Nuclear electricity production during last 50 years [1]

France derives about 75% of its electricity from nuclear energy as a consequence of a long-standing policy based on energy security [1]. Following the 1970's first oil crisis, Paris, which was highly dependent on energy imports, developed a strategy involving a massive of domestic nuclear power [2].

This has made France one of the world's largest net exporters of electricity due to its very low cost of generation. Today, it gains over €3 billion per year from this.

Nevertheless, one of the major issues related to the actual generation of French reactors is the radioactive waste storage, i.e. the production of medium and long-life fission products which are supposed to take some million years to reach natural radioactivity levels.

In this sense, an international cooperation project named "Generation IV International Forum (GIF)" has been created, aiming to develop a new generation of nuclear fission reactors capable to meet the challenge of major energy production with minor nuclear waste. In France, thanks to their fast spectrum and the reprocessing of spent fuel, new generation reactors should produce energy and more fuel while destroying the Plutonium and long-lived elements created by current reactors. In addition, the huge stores of uranium-238 rejected by previous generations[1] can be finally employed as refilling fuel. This means that there is no need for mining uranium for the fourth-generation reactors for thousands of years [3]. Fig.1.2 illustrates the nuclear energy production cycle that would occur with the introduction of the new reactor generation [3].

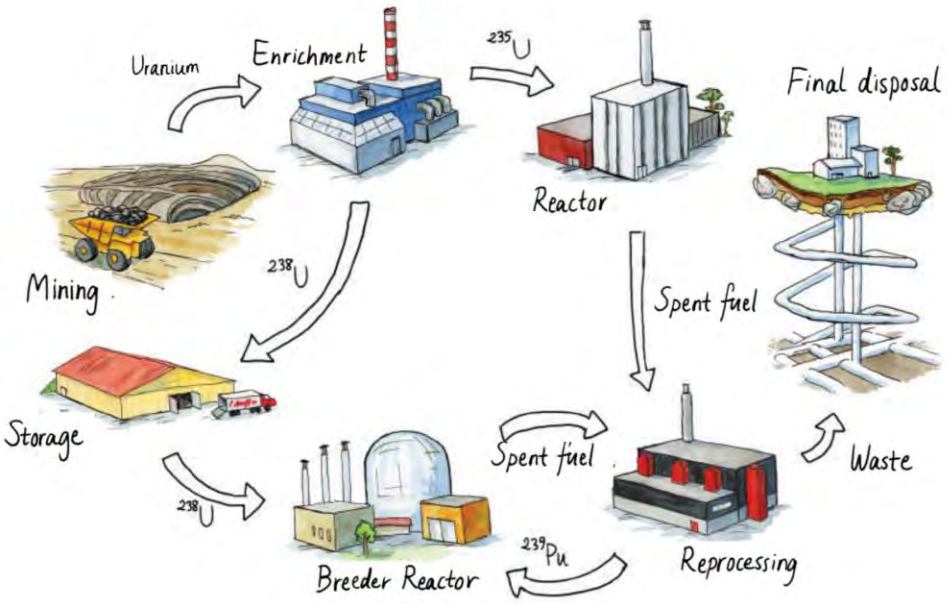

Fig.1. 2 - Introduction of IV Generation Nuclear Power [3]

In conclusion, Generation IV reactor should improve safety, sustainability (treatment and disposal of radioactive wastes), economic competitiveness and proliferation resistance.
Six different concepts of reactors have been identified by GIF as candidates for further development (Table 1.1).

[1] The isotope uranium-238 has been put aside over the years as a by-product of the process where uranium-235 was enriched to the concentration required for the current reactors.

Abbreviation	Full Designation	Neutron energy Spectrum
GFR	Gas-cooled Fast Reactor	Fast
LFR	Lead-Cooled Fast Reactor	Fast
SCWR	Supercritical Water-cooled Reactor	Fast/Thermal
SFR	Sodium-cooled Fast Reactor	Fast
MSR	Molten Salt Reactor	Fast (thermal in the past)
VHTR	Very High Temperature Reactor	Thermal

Table 1. 1 - IV Generation reactor technologies

It is worth noting that almost all proposed technologies are based on a fast neutron energy spectrum.

Among the possible FR technologies, SFR is the one with higher accumulated experience, since several prototypes and commercial SFRs operated and operate worldwide [4]. Fig.1.3 summarizes the French experience on SFR reactors.

Fig.1. 3 - French experience on SFR reactors [5]

In France, which is one of the nine original members of the GIF, the first prototype of SFR "*Rapsodie*" achieved criticality in 1967 in CEA Cadarache Center with a nominal capacity of 20 MW_{th}. The reactor, whose power was increased to 40 MW_{th} for 10 years, operated until April 1983 when it was shut down permanently [5].

After this prototype, two commercial SFRs, *Phenix* and *Super-Phenix*, operated and were connected to the electrical grid in 1973 and 1986, respectively. *Phenix* reactor of 250 MW_e was built in Marcoule and had a remarkable operational record (final shutdown in 2010). The CEA has acquired an important experience and know-how on sodium fast reactor through *Phenix* reactor [5].

Differently for *Super-Phenix*, a 1,242 MW_e fast breeder reactor which suffered from a series of cost overruns delays and enormous public protests. Only 15 years after the construction, the reactor reached its design operational goals (1985). The plant was powered down in December 1996 for maintenance, and while it was closed it was subject to court challenges that prevented its restart. In June 1998, *Super-Phénix* was closed permanently [5].

Fig.1.4 shows the conceptual scheme of sodium pool-type reactors.

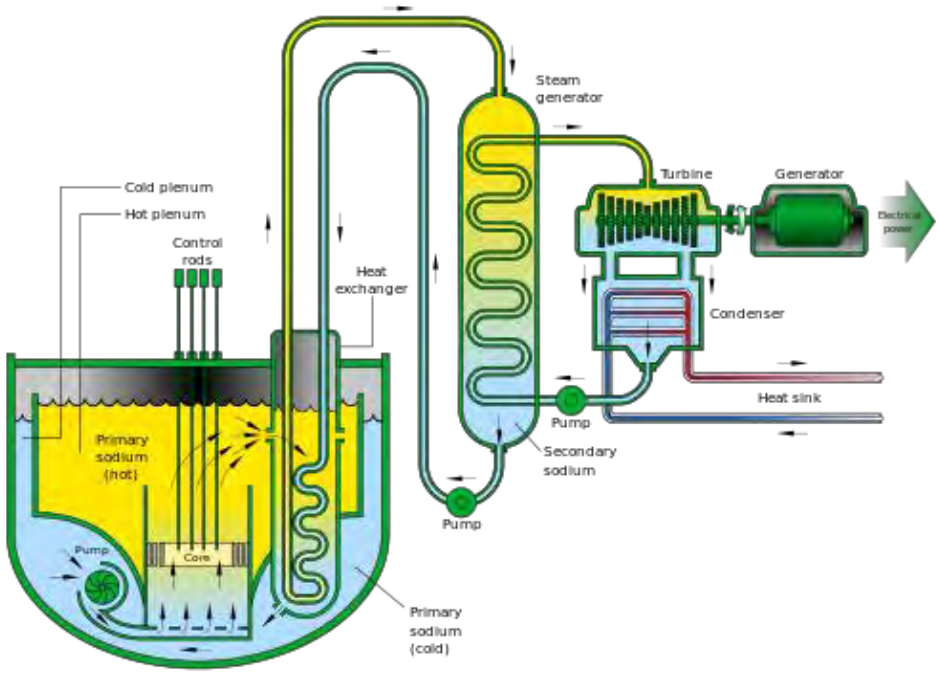

Fig.1. 4 - Pool-type Sodium-cooled Fast Reactor [4]

The primary vessel, containing the core, is circulated by liquid sodium, which behaves as coolant. Intermediate heat exchangers (IHX) are also placed in the primary vessel, allowing the primary sodium to exchange thermal power with the secondary loop, also circulated by liquid sodium. The aim of the secondary loop is to avoid any radioactive material outlet from the primary vessel.

The secondary loop transfers thermal power from the primary loop to the third one, which is the power conversion cycle. Sodium circulating the first loop is practically at atmospheric pressure, being pressurized at not more than 5 bars. Its core inlet and outlet temperatures are 395°C and 545°C, respectively. The secondary loop is slightly more pressurized than the primary one, in order to avoid primary sodium transfer to the secondary loop in case of leakage.

Concerning the energy conversion cycle, the conventional water Rankine cycle was employed for the French *Phenix* and *Super-Phenix* power plants, and for all the others commercial SFRs worldwide. Steam generator design employs water in the tube side (which can be straight or helicoidal) and sodium in the shell side. However, this layout involves a safety issue related to the Sodium-water reaction (SWR) in case of leakage inside the steam generator. Even if the accidental SWR scenario is well managed by the mitigation systems, without safety impact on the reactor, it constituted a weak point considering public acceptance.

1.2. The ASTRID Project

In June 2006, the French government passed a law focused on the disposition of long life high activity waste. An industrial demonstrator, capable of transmutation and separation of long life isotopes, was scheduled for the end of 2020. It was named ASTRID, which stands for "Advanced Sodium Technological Reactor for Industrial Demonstration". ASTRID project began in 2010 and CEA is in charge of the responsibility for the operational management, core design and R&D work. CEA, along with its industrial partners (French ones: EDF, AREVA etc. and international ones: JAEA, GE, etc.), followed the timetable (Fig.1.5).

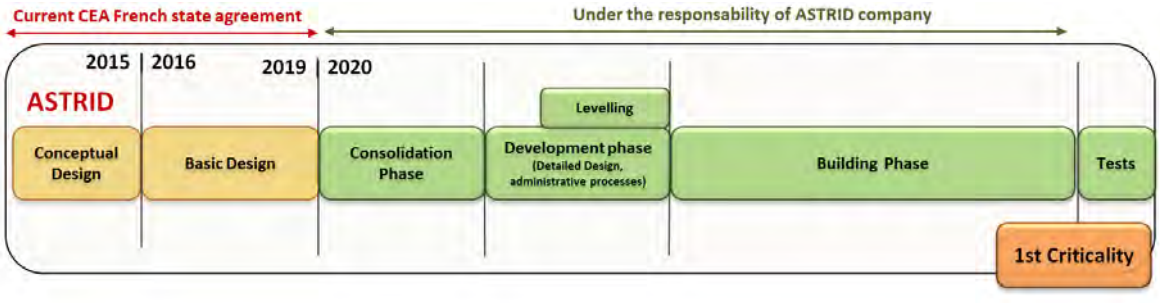

Fig.1. 5 - Overall schedule of the ASTRID project [6]

As already said, ASTRID is the prototype of a GENIV reactor and, as a consequence, it must achieve the requirements established by the GIF.
The major objective, of course, is to build a prototype which can exploit better the natural resources (uranium-238, transuranic) and which can allow to close the fuel cycle (Fig.1.2). In addition, being a prototype, ASTRID has to demonstrate the technological feasibility of sodium fast reactor to electrical energy production, as well as, the sustainable and profitable features from an economic point of view. The choice of the power ($600MW_e$) is reasonable to extrapolate a business plan for future analogous reactors [6].

All these goals must be reached in a structure of improved safety, i.e. [7]:

- Improved core design to lower the probability of core meltdown and/or the energy release following during an accident scenario;
- Better in-service and out-of-service inspection methods and instrumentation;
- Civil structures have to account for mechanical integrity in case of internal or external hazards;
- Three independent shutdown systems;
- Innovative gas power conversion system.

One of the most important improvements along with the new core design is the innovative *Energy Conversion System* (ECS), which gives a simple and final response to the chemical reactivity between sodium and water.

It consists in a classical Brayton cycle placed at the tertiary loop of ASTRID reactor layout ending in the turbine generator group producing electrical power, as shown in Fig.1.6.

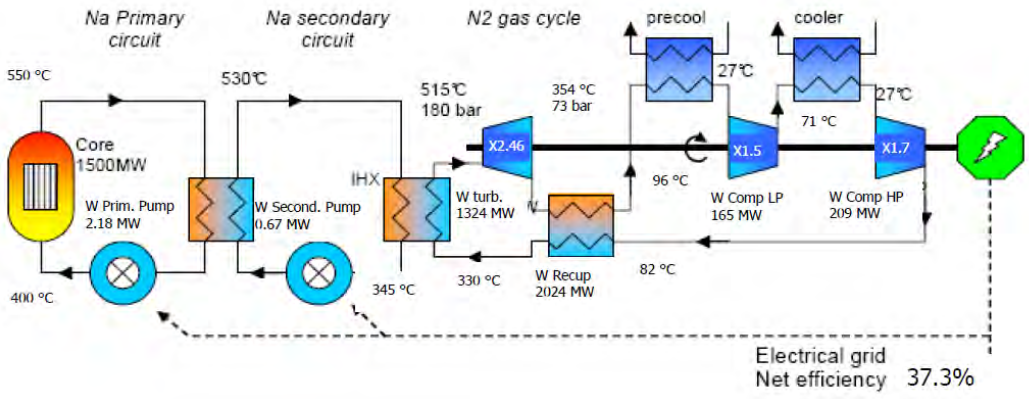

Fig.1. 6 - Gas Power Conversion System (PCS) Layout [7]

In this framework the most crucial component to be designed is the sodium-gas heat exchanger (SGHE). In fact, it is responsible for the effective heat transfer from the secondary sodium to the gas that will eventually go through the turbines. Saez et al. [8] highlight that pumping power has a first order impact on the Brayton cycle efficiency. So, gas circuit total pressure drops have to be minimized: the best estimated compromised between efficiency of the cycle and technological constrains is a sodium/gas heat exchanger pressure drop of 1 bar at maximum on the gas side. This is one of the most important design constraints to be respected.
On the other hand, an electro-magnetic pump (EMP) is used for the circulation of Na in the secondary loop. The power and the sizing of this component (and consequently its impact on the efficiency) are also very sensitive to pressure drops. A design value of 1,5 bar is chosen for the pressure drops of the SGHE Na side.
Being a good compromise between the high thermodynamically efficiency (37.3%) and the R&D effort for the development of gas turbines, the nitrogen gas (N_2) is actually the reference option for ASTRID Energy Conversion System (ECS).

1.2.1. The compact Sodium Gas Heat Exchanger (SGHE)

Due to lower heat transfer capacity of nitrogen gas compared to that of boiling water (lower thermal diffusivity α), a significant increase of the heat transfer area is needed. This technical solution would not be admissible in term of fabrication cost, size, and weight if applied to shell and tube heat exchangers. Therefore, compact heat exchanger technology has been chosen for ASTRID Energy Conversion System.

Fig.1.7 shows an overview of the SGHE 2014' design [9].

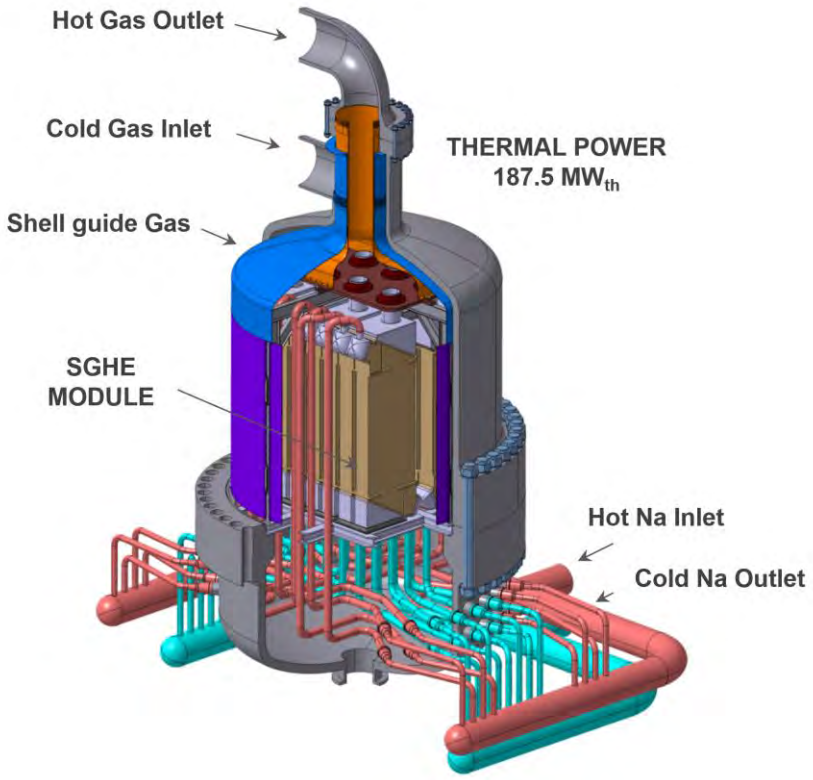

Fig.1. 7 – Sodium Gas Heat Exchanger 2014' design

The sodium/gas heat exchanger is a compact plate counter-flow heat exchanger composed by 8 compact plates modules which are placed in a pressurized vessel at 180 bars (Fig.1.7). Coaxially with the pressure vessel, there is the so-called "shell guide gas". The cold gas flows down from a nozzle to the region between pressure vessel and shell guide gas, then it crosses upward the SGHE modules where the heat exchange takes part. The hot gas flows out from a nozzle at the upper part of the SGHE.

On the other hand, hot sodium enters in the exchanger from the bottom part, but it flows across SGHE module downward. In fact, the Na pipes inside the pressure vessel bring the Na at the top of the module. This configuration allows the counter-flow exchange. The cold sodium is then collected in pipes at the bottom part of the structures.

Fig.1.8 displays an overview of the SGHE module.

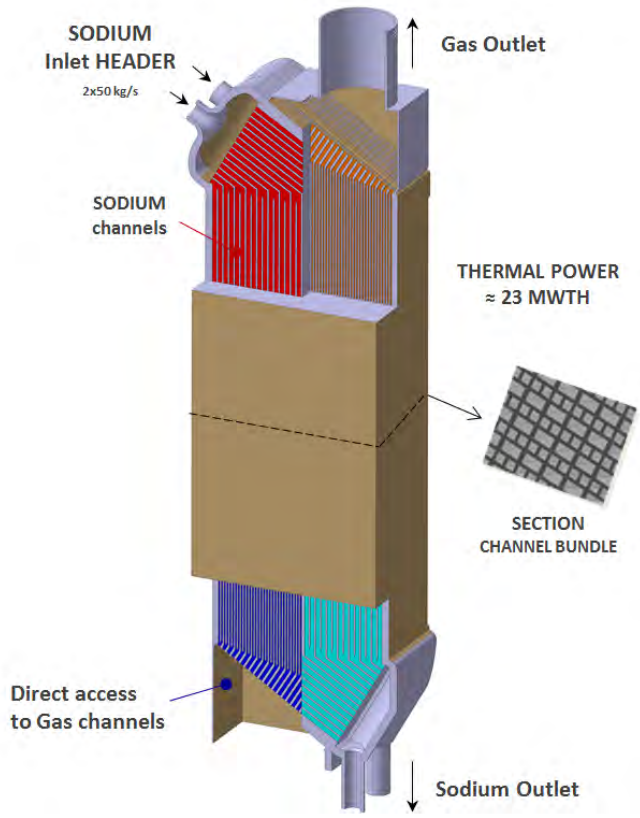

Fig.1. 8 - SGHE Module

The SGHE half module consists of a stack of 72 Na channels layers intercalated with 72 gas channel layers. Each Na layer is constituted by 125 sodium channels which means that a total of 9000 rectangular sodium channels, with a 3 x 6 mm^2 cross section and a length around 2.2 m, have to be fed. This configuration is required to achieve the thermal-mechanical performance of the heat exchanger module (23.4 MW_{th}).

On sodium side, 100kg/s mass flow rate supplies the vast number of parallel channels through two admission pipes which are also placed into the pressure vessel, subjected to 180 bars of external pressure at a temperature of 530 ° C (Fig.1.6). Their diameter of 90mm is the compromise between the mechanical resistance of the admission pipe and hydraulic requirements concerning the cavitation risk and pressure drops (inlet sodium velocity < 10m/s).

Table 1.2 summarizes the main features of the flows in SGHE module.

	Power exchanged [MW_{th}]	Na mass flow [kg/s]	N_2 mass flow [kg/s]	Na Inlet T [°C]	Na Outlet T [°C]	N_2 Inlet T [°C]	N_2 Outlet T [°C]
SGHE module	23.4375	100	100	530	345	310	515

Table 1. 2 – SGHE module thermos-hydraulic features

Note that, the design of the module and the arrangement of the pipes in Fig.1.7 are currently under further investigation, but even if some details can be changed the conceptual design is now consolidated.

1.3. Scope of the work

The SGHE design proposed by the CEA involves important benefits for the project. For instance, the minor pressure drops in gas-side comparing other design solutions tested, the optimization of thermomechanical stresses and the minimization of the Na inventory (8 m^3) are surely some of the most important [9].

However, one critical problem occurs in the sodium side, i.e. the flow "maldistribution". As the prefix *mal* suggests, flow maldistribution denotes a defective distribution of mass flow rate between parallel channels of the HE.
The description of SGHE module in Section 1.2.1 makes already evident some geometrical features and flow conditions which inevitably lead to a serious problem of flow maldistribution, i.e. the high dynamic pressure at the inlet ($v_{inlet} = 10\ m/s$) and the low pressure drop of the large bundle (minimal required channel cross-section). All maldistribution causes are discussed in detail in Section 2.4.1.
The maldistribution factor[2] σ associated to the present SGHE design is estimated to 25 %.
The deriving temperature variation between sodium channels generates internal thermal stress and thus deformation of structure. As conclusion, the current design of the SGHE

[2] In the present work, the flow maldistribution will be evaluated using the following factor, based on standard deviation:

$$\sigma = \frac{\sqrt{\frac{\sum_i^N (\dot{m}_i - \bar{\dot{m}})^2}{N}}}{\bar{\dot{m}}} x100 \quad (1)$$

where $\dot{m}_i$ is the mass flowrate in a channel; $\bar{\dot{m}}$ the average mass flowrate of the whole channels and N is the number of channels.

module is not attainable since thermo-mechanical stresses are not allowable (higher than 200 MPa).
Therefore, the scope of the present work consists in studying the 'maldistribution' in compact heat exchangers, in order to identify possible design solutions and to understand the physical phenomena providing flow maldistribution conditions. The physical understanding will be used to determine the research patterns that will be followed in this PhD work to increase the SGHE performance and to provide validated tools to correctly study the 'maldistribution' issue.

1.4. Thesis Outline

After this brief introduction to the issue of flow 'maldistribution' in ASTRID Sodium-Gas heat exchanger, the entire PhD work will give out as in the following:

- A bibliographic overview on different types of flow distributor commonly used in industrial applications will be exhibited in Chapter 2. The study offers the possibility to explore flow performance under various geometries suggesting the configuration best suited to meet ASTRID Sodium-Gas heat exchanger requirements. An innovative homogenization system will be presented.

- Chapter 3 will describe the two experimental facilities used in the present work; one is dedicated to the investigation of sodium flow in pre-distribution channels and the other to the study of flow behavior in the integral geometry of the SGHE module. The experimental database will be useful to actually validate the numerical models.

- The numerical approach and turbulence model selected to study the flow in pre-distribution bifurcating channels will be presented in Chapter 4. Numerical and experimental results will be shown together. Once the model is validated, a design optimization will be provided, showing the optimal solution for sodium pre-distribution channels in ASTRID SGHE module.

- Chapter 5 deals with the study of the global flow 'maldistribution' between sodium channels in the SGHE module. Numerical results will be compared with the experimental data collected during the second experimental campaign. The validated numerical model will be used to propose a final SGHE design of sodium header and pre-distribution channels allowing a uniform flow distribution.

- Conclusions and perspectives of the present work will be presented in Chapter 6.

Chapter 2

Bibliographic Study

Maldistribution of flow is a key topic for efficiency and operability of heat exchangers.
A great number of theoretical models and experimental studies can be found in the context of flow distribution in heat exchangers. Three different types of flow headers commonly used in industrial applications are considered in this work, i.e. consecutive manifold, normal-flow header and bifurcation manifold. Their analysis offers the possibility to explore flow distribution performance under various geometries suggesting the configuration best suited to ASTRID Sodium-Gas heat exchanger requirements.

In Section 2.1, the interest in studying flow distribution in the simple geometry of consecutive manifolds stems from the fact that generalized equations of analytical models allow to easily identify key factors influencing flow maldistribution. However, most of existing works based their formulations on assumptions ignoring some complex and important physical aspects for ASTRID project.

Other authors developed computational models and experimental investigations to predict flow distribution in bifurcation manifolds and normal-flow headers (Section 2.2 and Section 2.3). Generalized recommendations for preventing the negative consequences of flow maldistribution and some improved configurations are presented giving some suggestions for SGHE design. However, due to many geometrical variations and lack of any available theory, previous studies are not sufficient to asses an optimized design for ASTRID heat exchanger.

Most problems must be solved by intelligent design and diagnosis on an individual basis. In this sense, the last section will expose how the main findings and conclusions of the bibliographic study delineate the strategy to improve flow maldistribution in ASTRID heat exchanger (Section 2.4).

Before describing all various types of flow distributors and the associated experimental and modeling studies, let us focus the attention on the general maldistribution problem in compact heat exchanger technologies.

Flow Maldistribution in Compact Heat Exchanger

Compact heat exchangers are characterized by a large heat transfer surface area to volume ratio. This permits a great deal of heat transfer to take place between streams in a very small volume and with very small driving temperature differences. However, a large heat transfer surface embodied in a small volume will require a vast number of small channels for making effective use of the available primary and secondary surface.

Starting from the conceptual design of compact HE illustrated in Fig.2.1, the inherent difficulties in providing the uniform flow distribution are clear to understand.

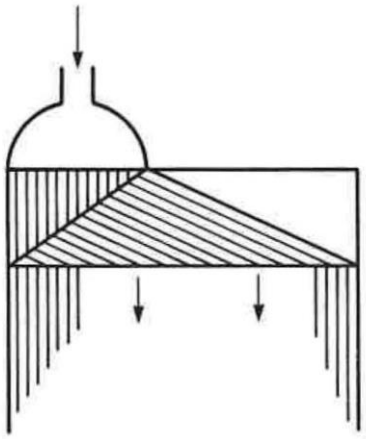

Fig.2. 1 – Compact heat exchanger – Inlet Header [12]

First of all, the flow passages of small size are certainly susceptible to imperfect manufacturing processes. Therefore, fabrication and manufacturing tolerances may result in unacceptably poor performances of the heat exchanger[3] [11].

The second problem is mainly related to the inlet flow conditions. The inlet stream flow is admitted thorough a small port compared to the large surface of the heat exchanger core (bundle channel). As a consequence, a stream jet occurs in the inlet flow distributor resulting in a non-uniform distribution between channels of the core. In addition, the shape of inlet flow distributor could produce high-velocity regions leading to localized erosions at the core face as well as unallowable thermo-mechanical loads [11].

[3] The proper distribution of uniform flow distribution is essential to achieve the required thermal performance. In fact, the flow non-uniformity may result in performance deterioration and may affect the mechanical integrity of the compact heat exchanger.

The magnitude of these effects strongly depends on the design of the fluid distribution elements connecting the heat exchanger core and the inlet and outlet fluid flow lines. Their modeling is actually very important to predict the impact on heat exchanger performance.

2.1. Consecutive Manifold

A consecutive manifold is one of the most commonly structures used for the distribution of fluid stream in compact heat exchangers. It consists in a flow channel for which fluid enters or leaves through a multiple sidewall outlet. Basic types of flow manifold are illustrated in Fig.2.2. In dividing-flow manifolds (a), fluid enters laterally and exits the manifold axially. Inversely, in combining-flow manifolds (b). When interconnected by lateral branches, these manifolds result in parallel (c) and reverse-flow systems (d), or U- and Z-flow arrangements.

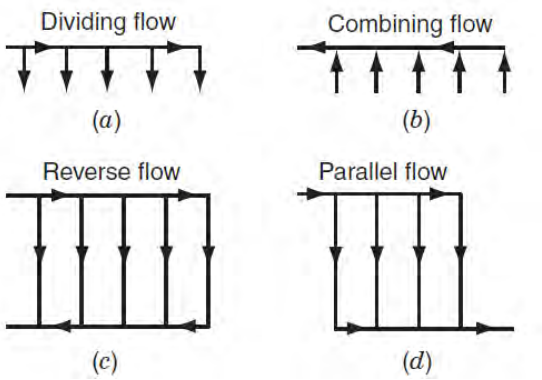

Fig.2. 2 - Major types of manifolds [12]

This type of distributor [12] is widely used in many industrial applications due to their clear advantages of simplicity. This means low development cost and time-efficient design for the manufacturing cycle. Furthermore, available explicit analytical solutions based on differential equations enable the development of generalized methods correlating flow distribution performance and manifold structure, i.e. an easy-to-use guidance for manifold designers.

The object of a consecutive manifold is to provide an equal distribution of flow through the multiple side openings. This is essentially prevented from the variation of pressure field along the main channel. In fact, in a dividing flow header, the main fluid stream is decelerated due to the loss of fluid through side openings and flow pressure rises in the direction of flow (*fluid-momentum effect*) (Fig.2.3c-d) [12]. However, in the main channel, also named header, the effect of fluid friction against the internal surface of main channel can make pressure falls in the direction of flow (*friction effect*). This means that a uniform

pressure along the dividing flow header can be obtained by a suitable adjustment of the flow parameters; the pressure regaining due to flow branching balances the pressure losses due to friction.

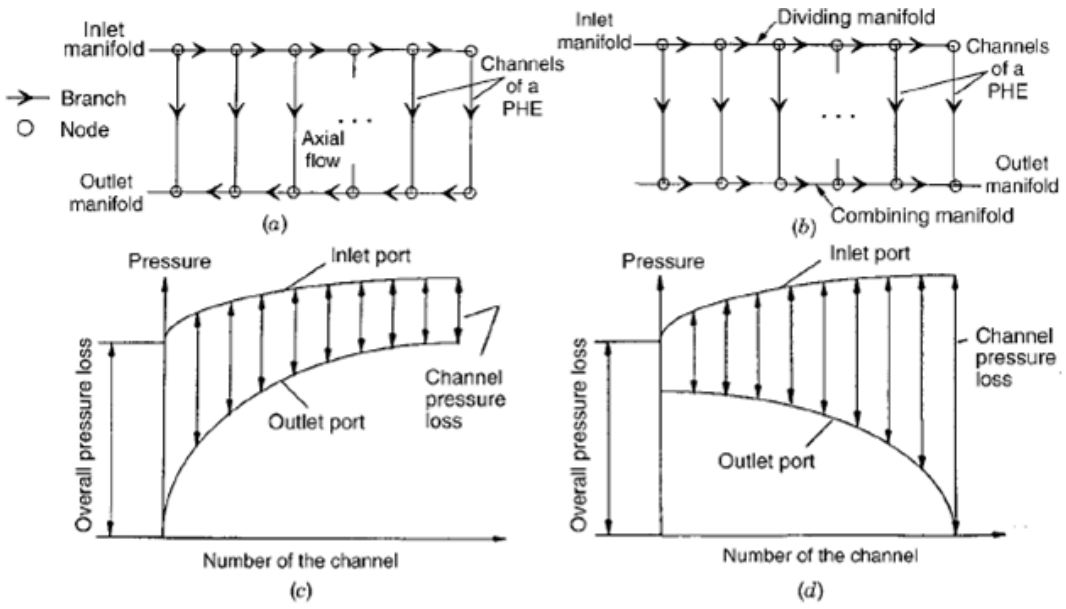

Fig.2. 3 - Manifold configurations: (a) U-flow or parallel flow configuration; (b) Z-flow or reverse-flow configuration. Pressure profile in (c) U-flow configuration, (d) Z-flow configuration [12]

It is worth noting that as shown in Fig.2.3c, for parallel manifold the friction and momentum effect work in opposite direction, the first tending to produce a pressure drop and the second a pressure rise. For reverse manifold, both friction and moment effect tend to create a lower pressure at the open and the closed end of manifold (Fig.2.3d).

To identify geometrical and physical parameters providing the suitable adjustment of fluid-momentum and friction effect in consecutive manifolds, various theoretical, experimental and numerical studies have been proposed in the past and they are presented below.

2.1.1. Theoretical studies of flow manifold

The simplicity of the analytical approach used to study consecutive manifolds allows to easily identify some relevant parameters influencing flow distribution such as cross-sectional area of all lateral channels A_c, header cross-sectional area A (A_i for the intake header and A_e for the exhaust header), header length L, and the resistance of lateral channels ξ(Fig. 2.4).

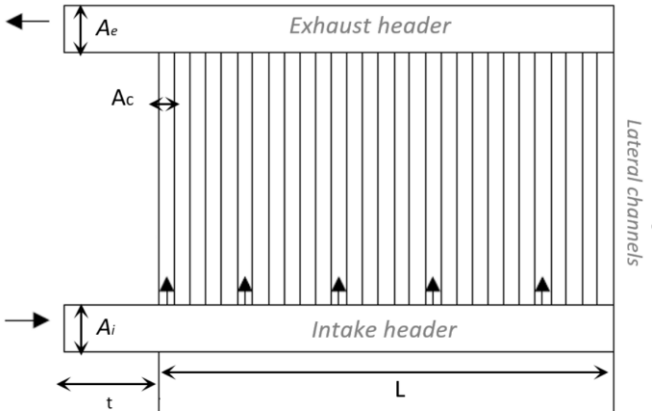

Fig.2. 4 – Geometrical parameters influencing flow distribution [20]

However, the weakness of theoretical models of flow manifold is related to the generalization of analytical solutions. In fact, despite their good description of the physics, analytical solutions are usually valid only for specific manifolds and flow conditions.
For sake of clarity, in the following section we will examine the development of some significant analytical solutions of continuous models [12-20]. Special attention will be paid to the theoretical approach chosen to represent the branching process.

In presenting flow modeling of different authors, a U-type arrangement of flow manifold constructed from a main channel of constant cross-sectional area (A) and equally spaced channels of uniform size is selected as general computational domain (Fig.2.5).

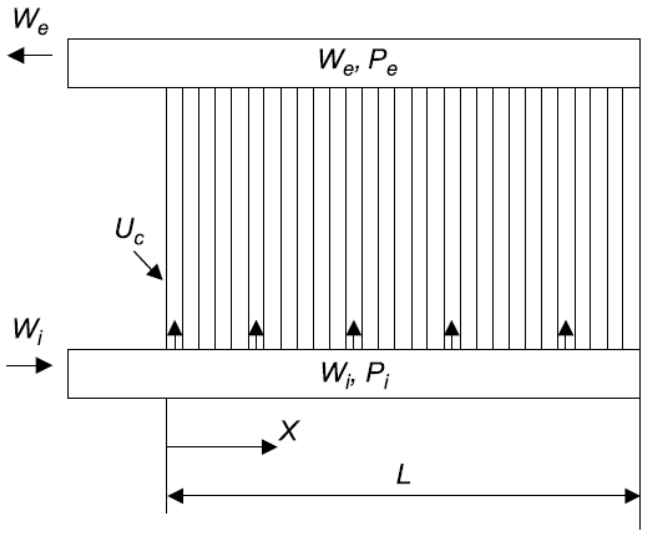

Fig.2. 5 - Schematic diagram of U-Type manifold [20]

Control volumes describing the flow streams near a dividing and combining flow branch point are illustrated in Fig.2.6.

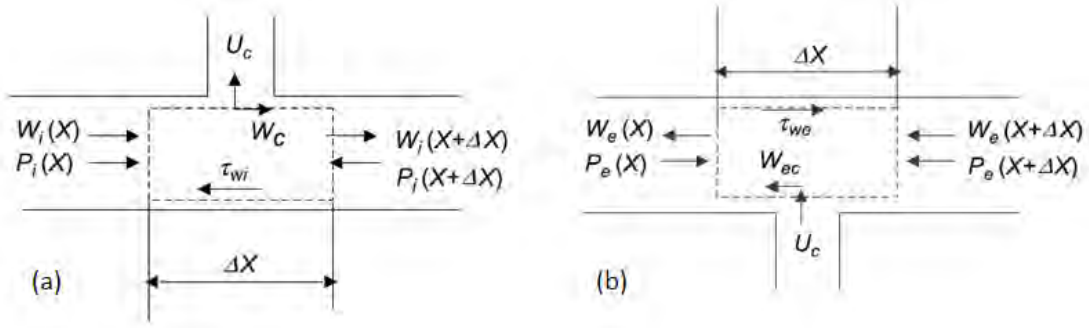

Fig.2. 6 - Control volume for intake (a) and exhaust (b) header [20-21]

Acrivos et al. [13] analyzed the performance of a simple dividing manifold (Fig.2.6a) by applying a momentum equation along the main channel. To represent the pressure recovery phenomena, they modified Bernoulli equation by introducing a correction term of momentum. The correction term was determined experimentally from observed pressure changes in near a single outlet port [13].

In their model, they essentially related the pressure variation to the momentum changes in the main flow stream (*momentum effect*) and the fractional losses based on the local flow spread (*friction effect*).

The resulting nonlinear, second-order, ordinary differential equation is written as:

$$\frac{dP}{dX} + \bar{W}\frac{d\bar{W}}{dx} + F_0\bar{W}^{\frac{7}{4}} = 0 \qquad (2)$$

where P, W and X are the axial pressure, the velocity and the coordinate of manifold. F_0 represents the combination of the friction and the pressure recovery effects.

Nevertheless, Acrivos' model could not be considered as a general analytical solution for flow in manifold. First of all, for the straight-tube section of manifold they assume that the friction factor varies with fluid flow velocity of the power of -1/4 which limits the applicability of the model for Blasius' flows. Secondly, the combination of the friction and the pressure recovery factors complicates the understanding of mutual interaction between the two effects. In addition, the model had been applied only to the case of simple dividing manifolds.

It's worth noting that in the above theoretical model, the effects of axial momentum transport by the lateral fluid stream (U_c in Fig.2.6a) are not considered.

To overcome this problem, Bajura and Jones [14-15] integrated, for the first time, a discharge equation for lateral flow in super-heated power plant boilers. The overall mass and momentum balance can be resolved for the whole control volume (Fig.2.6a-b) and the

effects of the branching process are directly included in the analysis. Bassiouny and Martin extended the model for plate fin-heat exchangers [16-17].
The resulting differential equation for the velocity in the intake header is written as:

$$\frac{1}{\rho}\frac{d(P_i - P_e)}{dX} + \frac{1}{2}\left[\frac{f_i}{D_i} + \frac{f_e}{D_e}\left(\frac{A_i}{A_e}\right)^2\right] {W_i}^2 - \left[(2-\beta_e)\left(\frac{A_i}{A_e}\right)^2 - (2-\beta_i)\right] W_i \frac{dW_i}{dX} = 0 \qquad (3)$$

where A, D and P are the cross-sectional area, the diameter and the axial pressure of manifold. The term β represents the fraction of axial velocity W_i that will be branched off through the main channel ($W_c = \beta W_i$). Subscripts i and e refer to intake and exhaust headers.
In equation (3), the second term in the left hand of the equation represents the friction contribution to the pressure drop in lateral channels and the third term the momentum contribution due to the flow branching in the channels.
However, both Bassionuy and Martin [16-17] and Bajura and Jones [14-15] provided an analytical solution of equation after neglecting the frictional term. For plate fin-heat exchangers, the friction loss in the main channel can be effectively neglected compared to the pressure drop in lateral channels and the momentum change due to the branching process. The analytical solution is then valid only for short manifolds where friction effects are negligible small compared to momentum effects.
On the other hand, Maharuadraya et al. [18] retained the frictional term but neglected the inertial term. The solution of equation (3) is valid only for long manifolds, where the frictional effects dominate. In addition, the first limitation of Acrivos' model remains in both models.
As conclusion, despite a good description of the physics, the above presented models present limits for designing manifold system with uniform flow distribution. In fact, an isolated adjustment of pressure-recovery effect or friction effect could result in the failure of uniform design.

Only in 2010, the first general analytical solution of governing equation (3) for flow distribution in U-type arrangement manifold has been provided by Wang et al. [19-20]. Both the frictional and momentum term are finally taken into account in their solution. The explicit expression of the analytical solution allows manifold designers to easily identify key factors influencing flow maldistribution [21].

Significant geometrical and physical parameters are reported below.

Flow area ratio, M

Flow area ratio M is defined as the ratio of the total cross-sectional area of all lateral channels (NA_c) to the header cross-sectional area (A). Wang et al. [19] show in Fig.2.7 that a uniform flow distribution can be obtained when M is smaller. For a larger M, the momentum cannot balance friction effect. Bajura and Jones [6] suggest M< 1 for the manifold system design.

V_c, in Fig.2.7, corresponds to the dimensionless volume flow rate flowing in each port of the consecutive manifold.

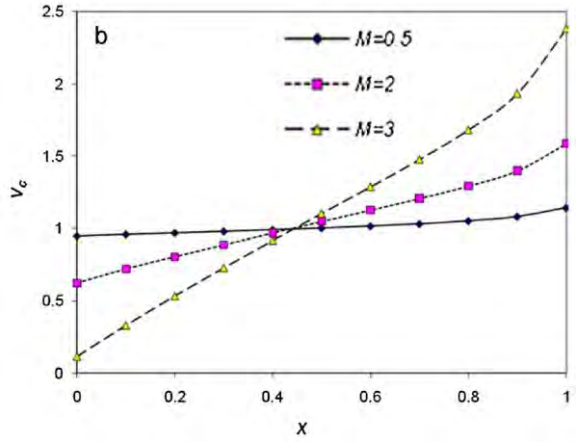

Fig.2. 7 –Effect of flow area ration M on flow distribution [19]

Ratio of header length to diameter, E

E is defined as the ratio of the total length of header (L) to the diameter (D). For a larger E, a less uniform distribution occurs (Fig.2.8). In fact, friction resistance increases along the manifold and more momentum is needed. Varying only this parameter it would be difficult to improve flow distribution. Wang et al. [19] also demonstrated that a ratio E < 5 has not a significant impact on flow distribution.

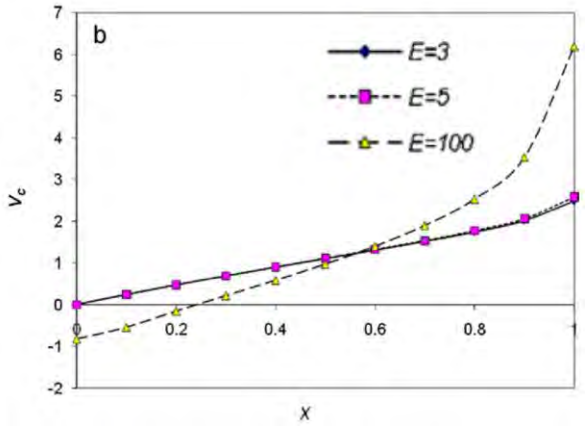

Fig.2. 8 - Effect of Ratio of header length to diameter *E* on flow distribution [19]

Flow resistance in lateral channels, ξ

The total pressure loss coefficient of lateral channels ξ has a decisive impact on flow distribution. A more uniform distribution may be reached for a higher resistance of lateral channels (Fig.2.9). For an infinite value of ξ, the manifold will act as a closed system and an absolute uniform distribution can be reached. However, for $\xi > 5$, there is not a remarkably improvement of flow distribution [19].

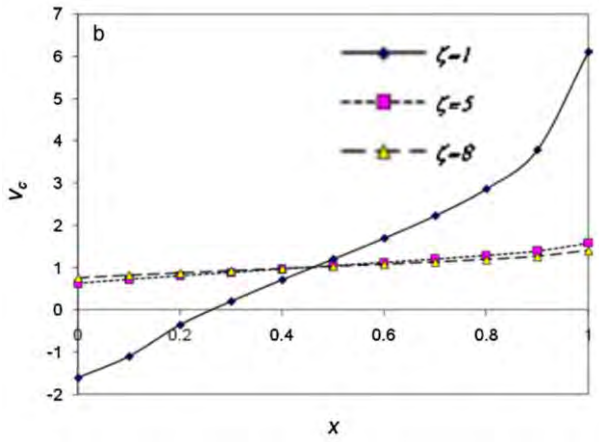

Fig.2. 9 - Effect of flow resistance in lateral channels ξ on flow distribution [19]

Inlet Reynold Number or entrance effect

A high inlet Reynolds number implies an increase of pressure drop along the manifold (friction effect) leading a less uniform distribution.
However, when E is smaller, the influence of inlet Reynolds Number can be neglected. In fact, as demonstrated by Bassiouny et al. [16-17], in short manifolds the momentum effect is predominant and the friction term can be neglected.

Flow direction

Datta and Majumdar [18] studied the influence of flow direction in intake or exhaust headers on flow distribution. They demonstrate that, for the same flow area ratio, U-type arrangement manifold provides a more uniform distribution than Z-type. This could be explained by the more uniform distribution of pressure difference between two headers for U-type manifold systems (Fig.2.3 c).

As conclusion, the present section demonstrated how one-dimensional analytical numerical model can represent a suitable tool for the optimization of manifold geometry and the preliminary design.

However, the simplicity of one-dimensional analytical numerical models excludes a proper characterization of strongly three-dimensional flow structures occurring in flow distributors. Flow separation and recirculation downstream the branching channel and the header are not captured. Furthermore, flow distribution in more complex geometries of flow manifold, such as improved configurations with perforated grid or double header, cannot be analyzed analytically. Experimental analysis and numerical CFD computation have been then used to study fluid flow in manifolds.

2.1.2. Experimental studies of flow manifold

Wang et al. [22-23] investigated experimentally flow distribution in compact parallel heat exchanger through typical rectangular headers having square cross-section area and 9 circular lateral tubes. Water was heated by a thermostat and maintained at 25°C.
To calculate the flow rate in each lateral tube, pressure drop measurements are performed using pressure taps drilled vertically on parallel channels[4].
Different geometrical and physical parameters have been tested in Wang et al.'s experimental apparatus [22], i.e.:

- Flow direction (U-Type and Z-Type)
- Diameter of parallel channels d_i
- Flow rate Q
- Entrance manifold length, t (see Fig.2.4 for explanation)
- Gravity

Experimental flow distribution data confirmed all above conclusions about the influence of geometrical parameters and flow rate on distribution (Section 2.1.1). Moreover, Wang et al. demonstrated the irrelevant effect of gravity and the better flow uniformity in manifold with a larger entrance length t [22].

Based on the above considerations about flow and pressure distribution in a typical rectangular manifold, Wang et al. also proposed improved configurations of the inlet header [23], i.e.:

---

[4] The measurement of pressure drop in each tube is used to calculate the flow rates among the tubes. The total pressure drop includes gravitational drop $\Delta P_g = \rho g h$ and frictional drop ΔP_f , i.e.:

$$\Delta P_T = \Delta P_f + \Delta P_g \qquad \Delta P_g = 4f \frac{\Delta L}{D} \frac{\dot{m}^2}{2\rho} \tag{4}$$

where D: inner tube diameter, ΔL: tube length for ΔP measurement, f: Fanning friction factor,ρ: density and $\dot{m}$: mass flux. With the measured ΔP for each tube, the mass flux ($\dot{m}_i$) and volume flow rate ($Q_i = \dot{m}_i A/\rho$) could be calculated.

- Trapezoidal manifold
- Multi-step manifold
- Two inclined perforated grids
- Perforated inlet tube

Fig.2.10-13 show a schematic representation of each one of the above listed improved configurations.

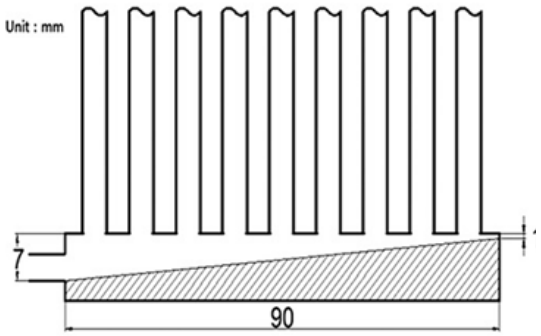

Fig.2. 10 - Trapezoidal header [23]

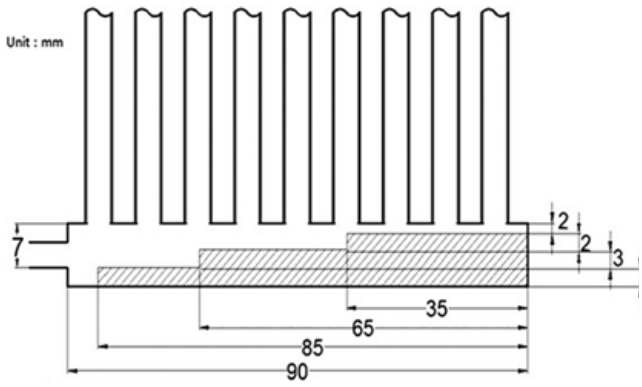

Fig.2. 11 - Multi-step header [23]

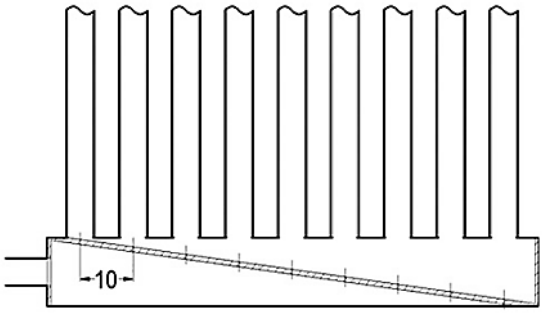

Fig.2. 12 - Inclined grid installed in the header [23]

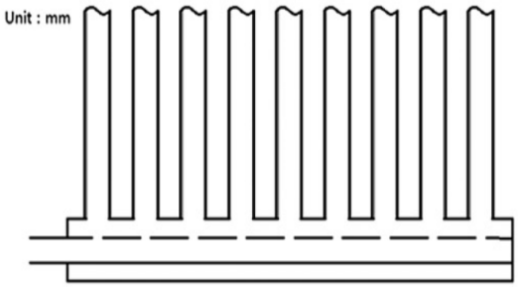

Fig.2. 13 - Modified header with tube baffle [23]

To compare flow distribution performance of different tested headers (rectangular and modified inlet headers), the maldistribution parameter (ϕ) are given in Fig.2.14 for U-type arrangement at different flow rates [5].

[5] The "maldistribution" parameter ϕ is defined as:

$$\phi = \sqrt{\frac{\sum_i^N (Q_i - \bar{Q})^2}{N}} \quad (5)$$

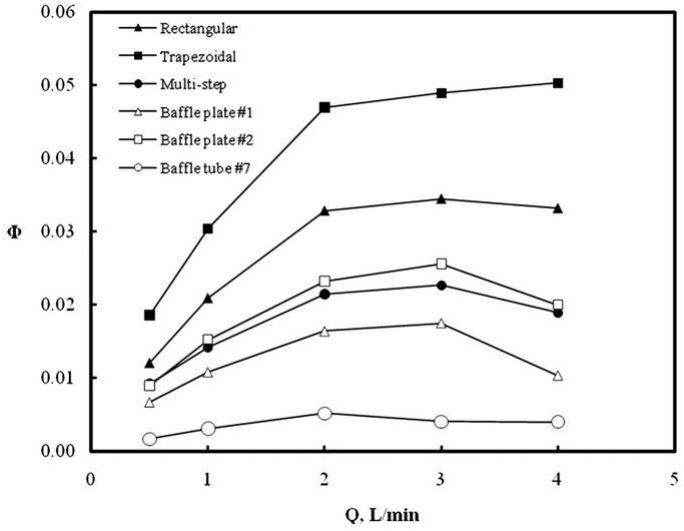

Fig.2. 14– Flow maldistribution vs Volume flow rate for U-type flows with the tested headers [23]

The first design solution of a trapezoidal header showed a less uniform flow distribution than a typical header [23]. In fact, the violent interaction of the jet flow with the trapezoidal header surface causes an intensified vortex at the entrance, thus a negative flow rate in first lateral channels (Fig.2.10). Multi-step header leads to a more uniform distribution thanks to the first and second step which force some flow towards lateral channels near the entrance (Fig.2.11).

The introduction of an inclined perforated grid in the header could be an effective solution to flow distribution problem (Fig.2.12). Multiple halls of grid increase flow resistance and break down vortex generated by the jet flow. Two different perforated grids have been tested. As shown in Fig.2.14, the first grid with constant diameter holes (Baffle plate #1) provides a better distribution than grid (Baffle plate #2) with largest holes near the inlet (lower flow resistance). However, the flow rate of two first lateral channels is still lower than the others.

It is worth to note that the insertion of a perforated grid in the manifold might be a non-suitable solution for compact heat exchanger due to the high manufacturing cost for installing, assembling and immobilization during operating condition.

To overcome the problem related to the introduction of an external homogenization device, the concept of the header with a tube baffle was suggested (Fig.2.13). Tube baffle holes are numerically designed to provide a comparatively small resistance which guides

---

where Q_i is the mass flow rate in a channel; $\bar{Q}$ the average mass flow rate of the whole channels; N is the number of total parallel channels.

more flow rate in lateral channel near the entrance [23]. Fig.2.14 shows the best uniform distribution of tube baffle solution design.

2.1.3. Computational studies of flow manifold

Huang et al. [24] performed numerical simulations to study the effect of header entrance t on flow maldistribution in a Z-Type arrangement manifold. Computational domains reproduced the experimental test sections of Wang et al. (see Section 2.1.2). This enabled an experimental validation of the selected numerical model.

The computer program CFD-ACE+ used for the present simulation was based on three-dimensional Reynolds Navier-Stokes equations. The grid number in the system was 479.590. The flow is expected to be fully turbulent, thus a turbulent model standard k-ε was adopted, coupled with standard wall functions to account for the laminar sub layer near the walls.

The comparison of flow ratio[6] β between numerical simulations and experimental data is shown in Fig.2.15a-b for manifolds with different entrance length t. Their geometries are illustrated in Fig.2.16a-b.

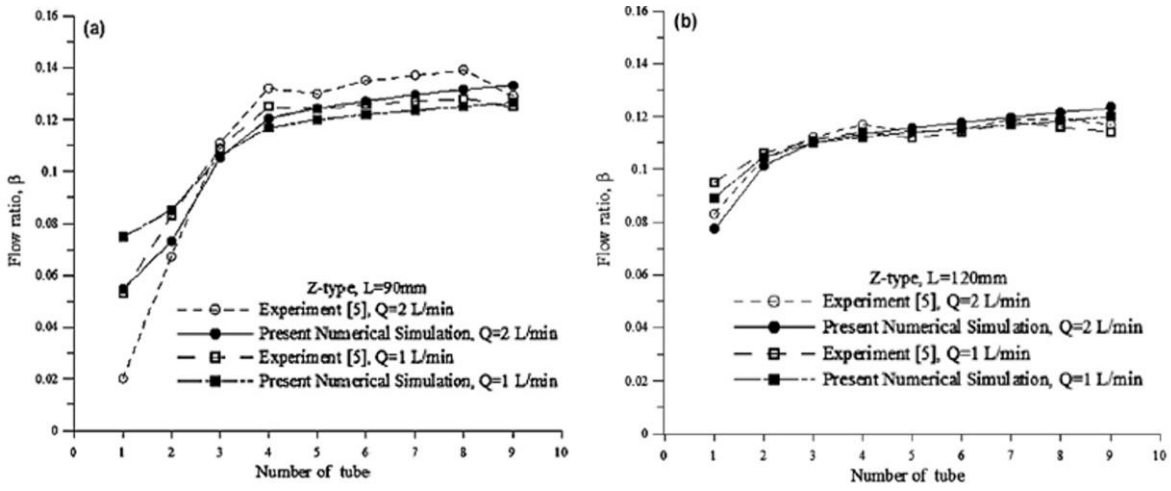

Fig.2. 15 - Comparison between experimental and numerical flow ratio β for two different inlet mass flows Q ($t = 3.5\ mm$ (a) or $t = 18.5\ mm$ (b)) [24]

[6] The velocity ratio β, maximum difference of velocities between channels is another factor that can indicate the uniformity of flow distribution, i.e.:

$$\beta = \frac{v_{max}}{v_{min}}$$

Important discrepancies of flow ratio (β) can be noticed in the first tubes of a shorter entrance length manifold t where a severe flow recirculation occurs (Fig.2.15a). The numerical model could be not appropriate to describe these phenomena.

For a better understanding of flow pattern near the entrance of manifold, CFD velocity streamlines are illustrated in (Fig.2.16a-b).

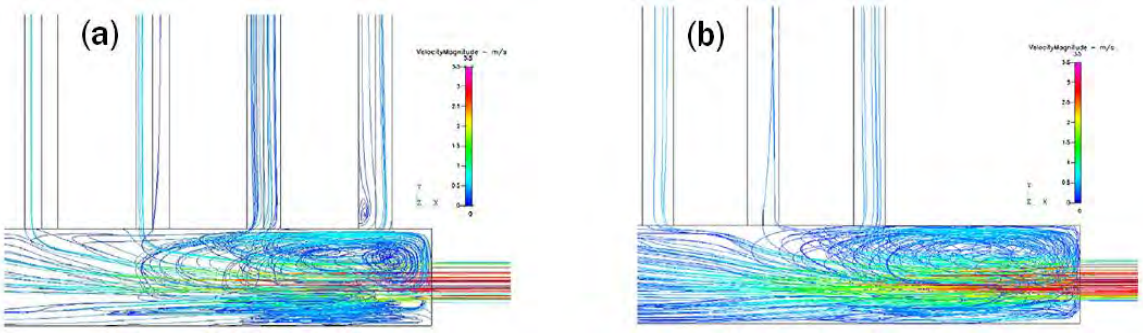

Fig.2. 16 - CFD velocity streamlines for consecutive manifold with t = 3.5mm (a) and t=18mm (b) [24]

In both cases, a jet flow grows at the entrance of the inlet header creating a vortex that circulates at the upper side close to the first four branching tubes. This vortex will reduce the flow rate in the first tubes (Fig.2.16a). As already demonstrated experimentally [22], header with a larger entrance length presents a more uniform distribution because of the vanishing of the small eddy occurring near the inlet of the first tube.

A more detailed analysis of three-dimensional turbulent flow generated in square cross-section manifold and at the entrance of each branching tube has been reported by Fu et al. [25]. The authors presented a three-dimensional simulation of turbulent water flow through two-branch manifold. Turbulence model adopted for this analysis was an isotropic k-ε model by Launder and Spalding [26] with standard wall functions near wall. To verify the ability of the isotropic model to catch the flow separation and recirculation at the entrance of branching tubes, measurements of mean velocity and secondary flow were obtained using Laser Doppler Anemometry (LDA).

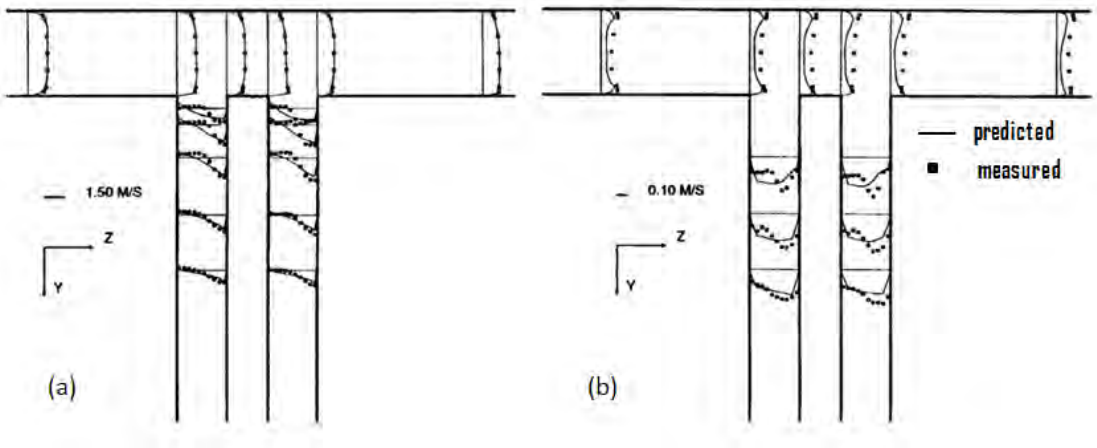

Fig.2. 17- Comparison of predicted and measured axial velocity profiles (a) and axial RMS velocity profiles in plane of symmetry (b). Inlet flow rate 3.3 x m^3/s [25]

As shown in Fig.2.17a, the agreement of measured and calculated streamline velocities on symmetry plane is good in the header, whereas in the admission zone of lateral branches the asymmetry of velocity profile is under predicted by k-ε model. Fu et al. also demonstrated that a more important deviation results in the comparison of measured and calculated RMS axial velocity fluctuations (Fig.2.17b). The author attributed this discrepancies to numerical diffusion and the shortcomings of k-ε model in dealing with recirculating flows. Although a reasonable agreement between prediction and measurement was obtained, this study manifests the need of a validated numerical model to characterize the flow in distributors. Note that, any authors provided an experimental validation of the numerical prediction in the complex recirculating zone at the entrance of manifold (Fig.2.16).

2.2. Normal -Header

A different design, like a tank or a box, characterizes the normal-flow header [3] (Fig.2.18). Its function is to join the inlet face of the heat exchanger bundle channel to the inlet pipe. A serious problem of flow distribution occurs in this configuration due to the jet which grows from the inlet pipe and then increases into the header volume before impinging into bundle channel. Modeling inlet header requires the analysis of the three-dimensional confined jet and its recirculation into the large volume. Therefore, analytical solutions are hardly possible. An accurate modeling of flow header can be done only numerically and experimentally.

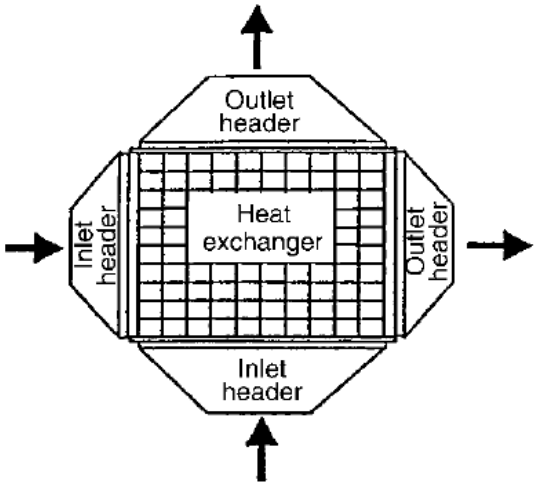

Fig.2. 18 - Typical Compact Heat Exchanger - Normal-Header [3]

Experimental studies and numerical simulations of flow distribution in plate-fin heat exchanger will be discussed in the following.

2.2.1. Experimental studies of flow in Normal -Header

Lalot et al. [27] investigated gross flow maldistribution in electric heaters. Their test sections (Fig. 2.19) did not include the outlet header in order to facilitate the measurement of the air turbulent flow rate in parallel channels (*Re 10 000÷40 000*). Velocity at the outlet of the 128 channels was measured using hot-wire probe and for less intrusive measurements, using two static pressure probes per channel.

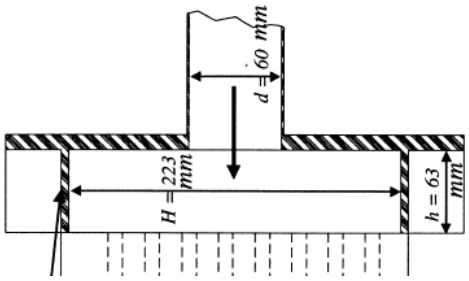

Fig.2. 19 – Geometrical features of tested header [27]

They analyzed flow pattern in inlet headers with different ratios of $G_1 = \frac{H}{h}$ and $G_2 = \frac{h}{d}$ (Fig.2.19) to identify in which conditions the reverse flow occurs (negative velocity ratio). As shown in Fig. 2.20, inlet headers with small depth h and small inlet pipe diameter d deteriorate the flow distribution.

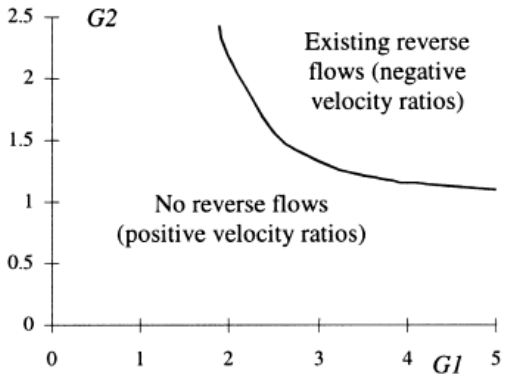

Fig.2. 20 – Reverse flow in inlet header [27]

They identified that the kinetic energy of the fluid at the admission pipe $\left(\frac{1}{2}\rho v_0^2\right)$ causes local pressure variations at the entrance to the channels, which could result in a reverse flow. Based on their experimental observations, the flow maldistribution was estimated using the following expression:

$$\eta = \frac{\left(\frac{1}{2}\rho v_0^2 + \overline{\Delta P}\right)}{\overline{\Delta P}} \tag{6}$$

where $\overline{\Delta P}$ is the average pressure drop across the heat exchanger and $\frac{1}{2}\rho v_0^2$ is the dynamic pressure at the inlet pipe. This shows that an increase in the pressure drop leads to a more uniform distribution (Fig.2.21).

For the purpose of increasing the pressure drop, they installed a uniform perforated grid in the midway between the inlet tube and the core of the heater. Different grids characterized by different pressure loss coefficients, depending on the distance between

the 4mm diameter holes, have been tested. They concluded that any further improvement is not possible due to the generation of reverse flow in the section downstream the grid (Fig.2.21).

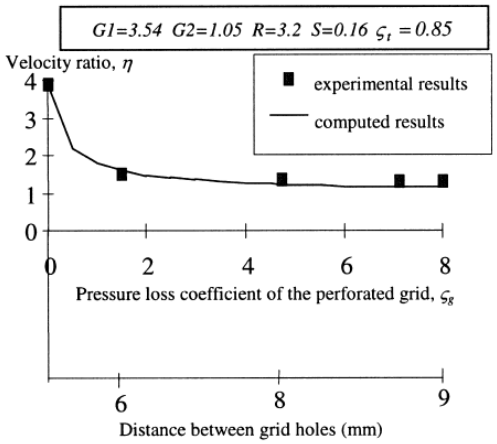

Fig.2. 21 - η versus pressure loss coefficient of the perforated grid [27]

They also demonstrated that the outlet header has not influence on flow distribution [27]. Note that, Lalot's study is limited to the header with square cross section.

Jao et al. [28] experimentally investigated flow distribution in plate fine heat exchanger testing a new concept of inlet header. It consists in a classical distributor presenting a second header directly integrated into the inlet fluid cavity (Fig.2.22). Two second headers with different number of holes and a 38 mm inlet pipe diameter were investigated (Fig.2.23).

To evaluate flow distribution in the numerous and too small micro-passages (1100 port of fin dimension of 9x2x0.3mm^2), they divided the cross-section in thirty zones grouping the small channels and simplifying the measurement of mass flow. Two standard containers and a stopwatch were used to measure the passage flow volume and time [28].

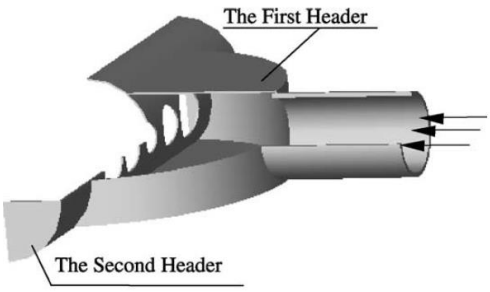

Fig.2. 22 - Double header [28]

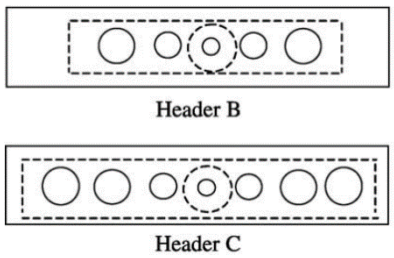

Fig.2. 23 - Second Header B and C [28]

Flow distribution of typical header (Header A without second header) was compared with the new concept. Fig.2.24 shows the velocity difference between the single passage flow and the whole passage flow at $Re \approx 1000$ and $Re \approx 3000$ respectively.

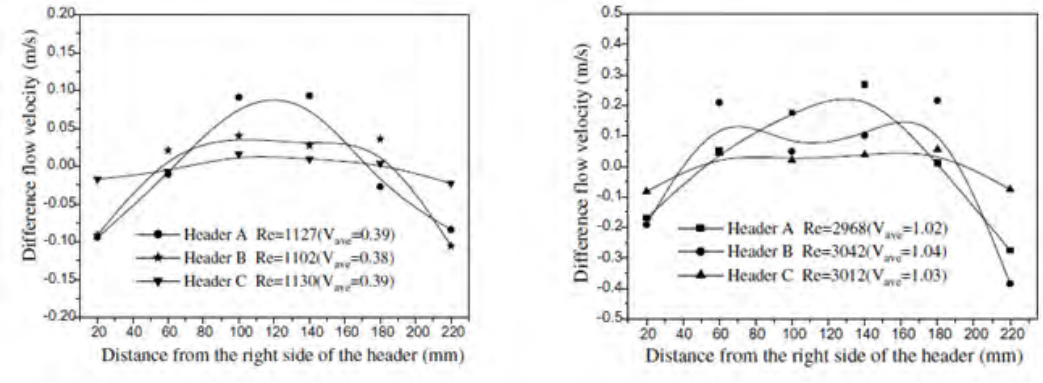

Fig.2. 24 - Distribution of the difference flow velocity at Re 1000 and Re 3000 [28]

For typical header Configuration A, the flow velocity peak appears in the center of the header. Configuration B and C showed a more uniform distribution of flow uniformity in both regimes of flow. The new concept, which is a sort of perforated grid directly integrated in the inlet header, is a very interesting solution to flow maldistribution because it reduces all mechanical resistance and maintenance issues related to an external homogenization device.

The two research works presented in this first part of Section 2.2.1 studied the effect of the inlet header configuration on flow distribution. However, the evolution of the impinging jet into the inlet header is still unknown.

Wen et al. [29], [30], [31] employed PIV laser velocimetry technique to study the characteristics of fluid distribution in inlet headers. Author performed velocity measurement with a two-dimensional PIV equipment including a light source supplied by a Nd-YAG twin laser system (wavelength λ = 532mm, pulse energy = 50MJ) and a camera PIVCAM 30 of type 630046 (resolution factor 1018x1018 pixel) capturing two images with time separation 1μs. The software controlling PIV system and data analysis is Insight NT. It captured 1000 frames pictures in succession. To generate tracer particles (average diameter of 1÷2 μm) and fuming liquid for air, Rosco 1600 generator, was used.

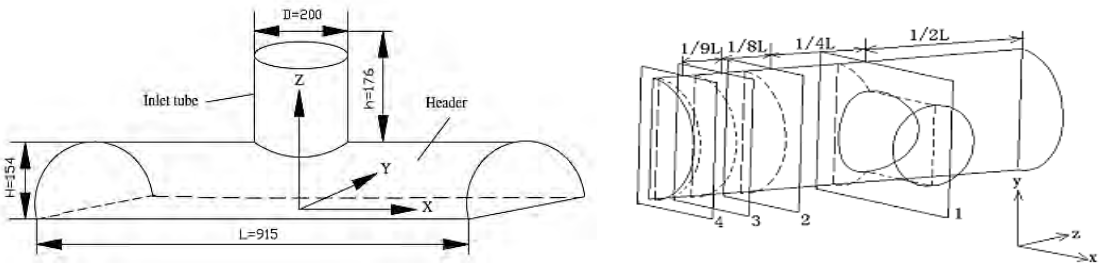

Fig.2. 25 - Test header configuration and v [29]

Inlet header geometry and some of eleven cross-sections investigated by PIV are illustrated in Fig.2.25. Considering the structural symmetry, half of the header length was measured.

PIV velocity vectors and streamlines graphs on cross sections 1 and 2 in Fig.2.26 confirm that flow distribution in a typical header (Configuration A) is strongly influenced by fluid vortex and transverse pressure gradient.

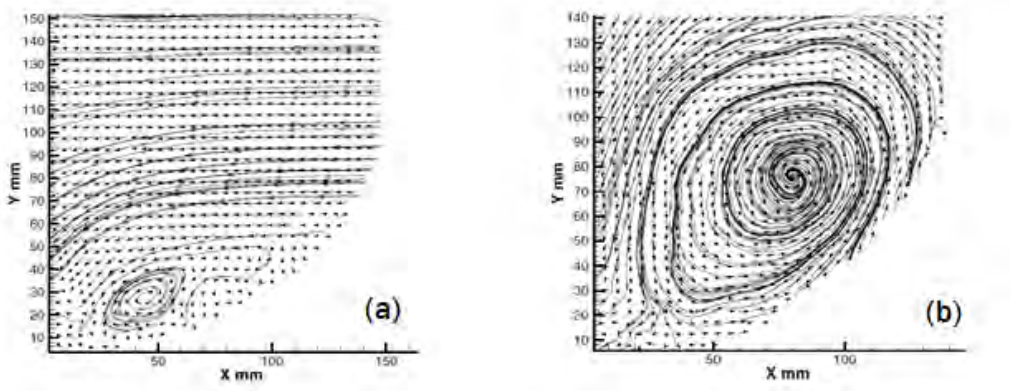

Fig.2. 26 - PIV velocity vectors and streamlines of cross-section 1 (a) and 2 (b) [29]

After the sudden enlargement of header geometry, the main flow separates from the surface to form a vortex. As the distance from the inlet tube increases (Cross-section 2), small vortex enlarges gradually into large scale vortex (Fig.2.26b). Its dissipation allows a more uniform distribution also in y–direction.

Wen et al. investigated also the effect of the introduction of the perforated grid in Fig.2.27 at the ½ height of the header (Configuration F).

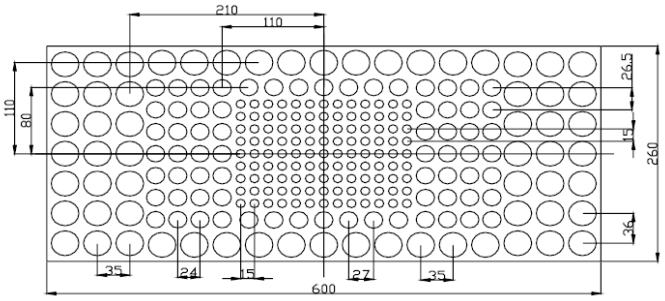

Fig.2. 27 - Example of a perforated grid (Configuration F) [29]

They demonstrated that, in the improved header (Configuration F), the velocity facing the inlet tube decreases significantly, while increases in peripherical zones of the header (Fig.2.28). In fact, the smallest diameter holes placed in the center of the grid create much resistance to the fluid and transverse pressure gradient is formed to oblige the fluid flow all around. Note that, the flow distribution profile was deduced from the eleven PIV investigated cross-sections in the half of header length.

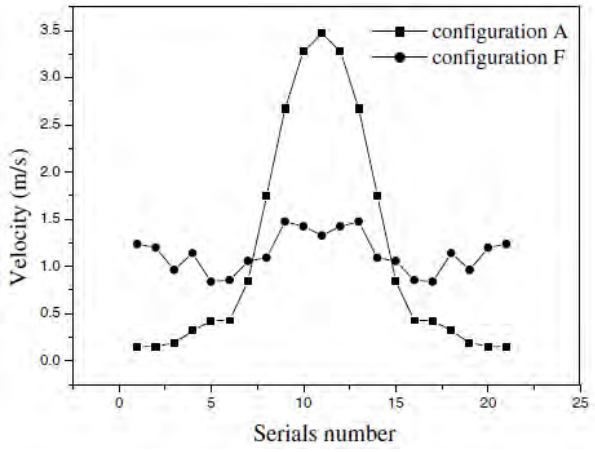

Fig.2. 28 - Velocity distribution of different headers at Re 6x10⁴ [29]

The installation of a perforated grid in header provides a more uniform distribution not only in z-direction but also in the y-direction. In fact, as shown in Fig.2.29a, while the smaller holes create much resistance to decrease inlet tube velocity, the larger diameter of the holes at the edge of the grid enables fluid flow to pass through with no trouble. In addition, due to viscous shear with around low-speed fluid, some vortices rise behind the perforated grid, after going through the small holes.

In cross-section 2, a big vortex appears in front of the grid but the fluid is distributed uniformly after going through this (Fig.2.29b).

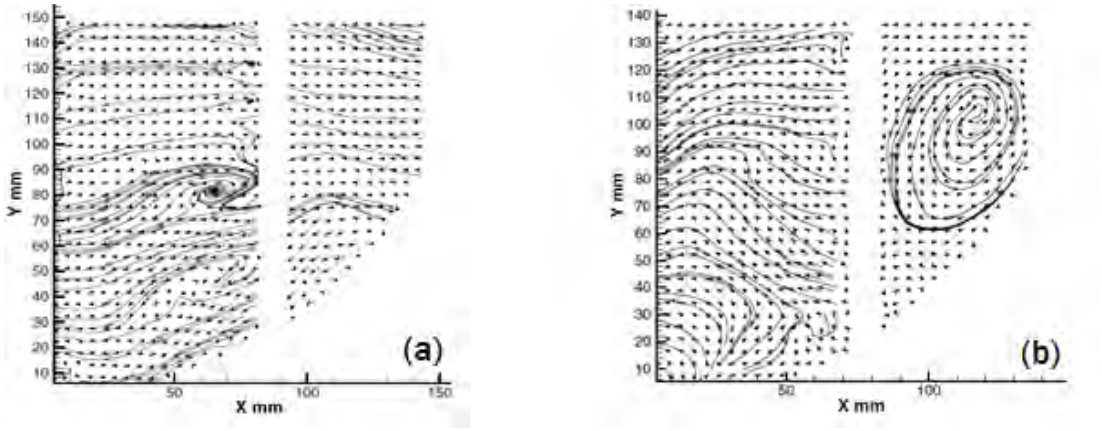

Fig.2. 29 - PIV velocity vectors and streamlines of cross-section 1 (a) and 2 (b) after the installation of the perforated grid [29]

Unfortunately, as repeatedly stated, the increase of pressure drop due to the perforated grid could not be acceptable for plate-fin heat exchanger. An optimization of grid design is required.

Wen et al. [32] optimized the grid design evaluating the impact on flow distribution and pressure drop of the following geometric parameters:

- Grid length
- Holes size
- Holes distribution in in-line or staggered arrangement
- Punched ratio

They concluded that the uniform flow distribution is approached when the grid length increases, the holes are distributed in staggered arrangement and the punched ratio gradually increases from axes along with the dam board length.

2.2.2. Computational studies of Normal-Header

Zhang et al. [33] simulated flow distribution in plate fin-heat exchanger using CFD Software FLUENT. Jao et al.'s header Configuration A was selected as computational domain. To predict turbulent flow in the header, the finest mesh (150.000 cells) was implemented using Fluent and the standard k-ε model was chosen to. As shown in Fig.2.30, the distribution of the average velocity is in good agreement with the experimental data of Jao et al. at Re 2100 [28].

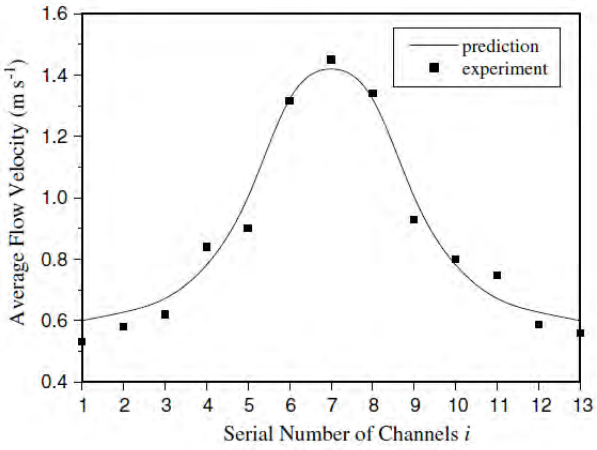

Fig.2. 30 - Comparison between experimental and numerical data of average velocity at Re 2100 [33]

Zhang et al. [33] performed numerical simulations at different Reynolds numbers (range 500-3000) showing that flow non-uniformity first increases with Re, then after reaching its maximal value at Re 2500 decreases. The authors explained this trend by the transition from laminar into turbulent flow which leads to a new distribution of the local resistance between the central zone and the others parts, so a flow redistribution in header.
In addition, they confirmed the improved flow distribution of two modified headers B and C (Fig.2.23).

Wen et al. [29] and Raul et al. [34] took a step forwards in the validation of numerical model demonstrating their ability to correct predict the complex turbulent flow structures in the entrance header. The same CFD Software Fluent, solver and numerical model were used to predict turbulent flow in the inlet header of plate-fin heat exchangers. The computational domain corresponds to the test section of Wen et al. experiment (Fig.2.25).
Wen et al. finest mesh involved 245.817 cells while Raul et al. ones, 320.000 cells.
For a qualitative numerical validation, velocity streamlines and vectors are compared with experimental data at Re 60000.
Both authors demonstrated that CFD numerical model is capable of capturing all major features of the complex flow pattern in inlet header.

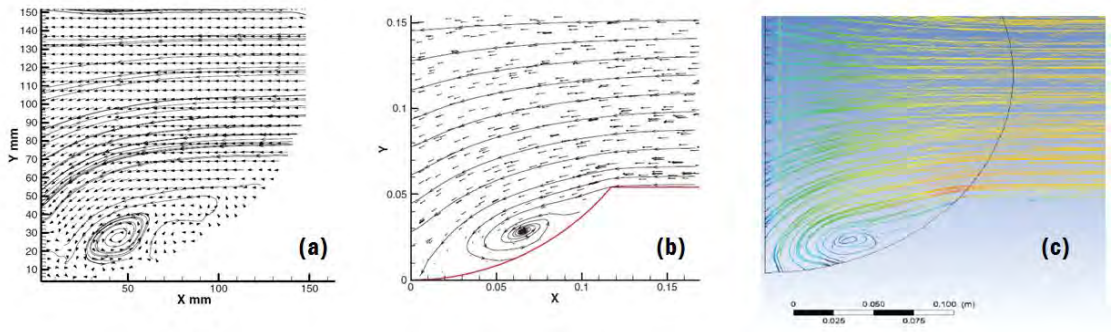

Fig.2. 31 - Velocity vector and streamlines of cross section 1: (a) PIV [29] (b) CFD Wen [29] (c) CFD Raul [34]

In cross section 1, the dead zone formed for a reverse flow at the spot deviated from inlet tube is well predicted by the k-ε turbulent model (Fig.2.31).

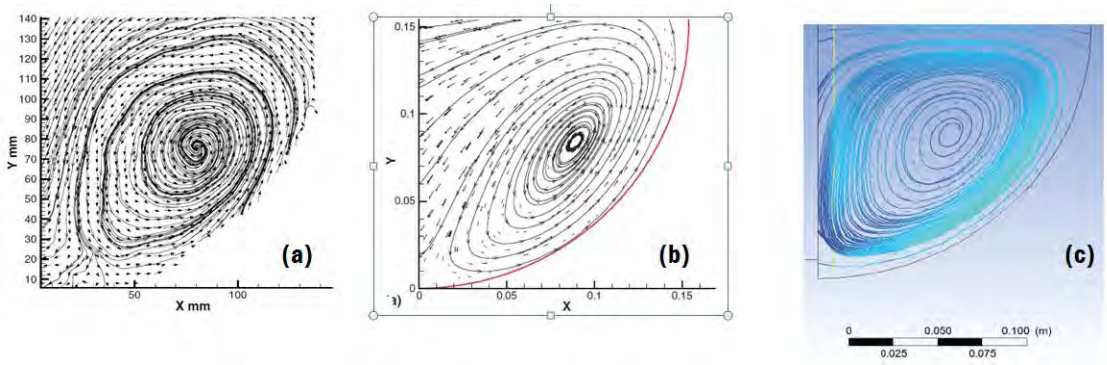

Fig.2. 32 - Velocity vector and streamlines of cross section 2: (a) PIV [29] (b) CFD Wen [29] (c) CFD Raul [34]

The dissipation of vortex in cross section 2 of PIV measurements seems to be more rapid than in CFD data (Fig.2.32).

Wen et al. also [29] demonstrated the ability of the numerical model to predict flow distribution in improved header configuration with perforated grid. Obviously, vortices rising behind the grid cannot be discerned because of the utilization of the wall functions and the zero velocity at solid wall [29].

A quantitative comparison of measured and predicted value of flow maldistribution parameter at Re 60000 for header Configuration A is reported in Table 2.1.

Maldistribution	PIV results Wen et al.	CFD results Wen et al.	CFD results Raul et al.
$\boldsymbol{\theta}$	1.210	1.124	1.176

Table 2. 1 - Flow maldistribution: PIV results [29], CFD Wen [29] et al. and CFD Raul et al [34]

Raul et al. [34] also analyzed flow maldistribution for header with a double baffle plate having staggered arrangement. It was demonstrated the new concept offers the most uniform distribution.

It is important to mention that all numerical and experimental studies of Wen et al. evaluated and compared flow maldistribution in plate fin-heat exchanger starting from the analysis of flow pattern in the inlet header. However, the tendency of flow distribution along the header may not correspond to the real repartition of flow between channels of heat core.

Wen and Li [35] simulated the nitrogen passage through the 43 micro-channels. Their arrangement is illustrated in Fig.2.33.

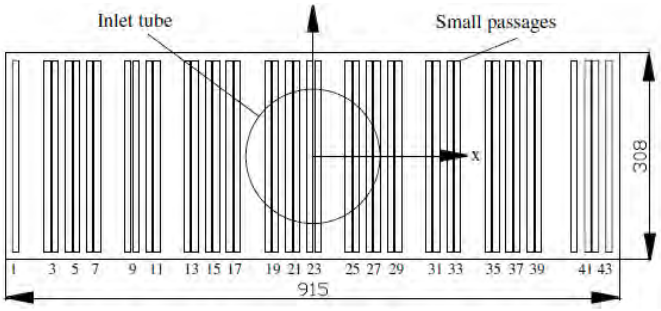

Fig.2. 33 - Definition of the channels at the outlet of header [35]

Composite constructive mesh grids are used in the analog computation and the finest implemented grid involved about 245,817 cells. A further refinement was considered in some local place where parametric variation is severe. Authors always employed the same setting of CFD Software Fluent [29].

The distribution of normalized velocity in each channel of heat core is shown in Fig.2.34.

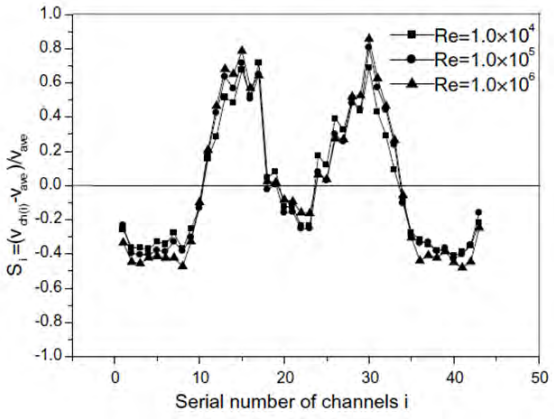

Fig.2. 34 - Maldistribution parameters along with x direction at different Re [35]

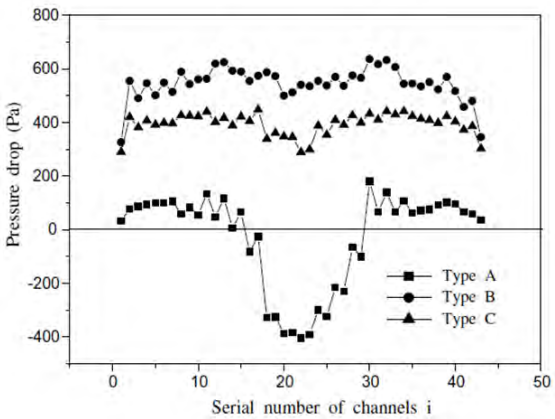

Fig.2. 35 - Pressure drop versus different type of headers at Re 1x10⁵ [35]

As expected from the flow distribution in inlet header, the fluid tends to go preferentially into channels at the center. However, the velocities of central passages straightly facing the inlet tube result now lower (Fig.2.34). This could be explained if one looks at the pressure drop distribution for the examined header (Type A). In Fig.2.35, a negative pressure drops happens in the center part of header outlet due to the flow stagnation in this zone. The flow dynamic head compensates for the hydrostatic head and the flow is rejected on the two sides.
This means that if we are interested to study the flow distribution between parallel channels of the header bundle, a PIV analysis of flow pattern at the inlet header could be not sufficient.

The other two types of header, Type B and C in Fig.2.36 and Fig.2.37, include the perforated grid with smaller holes at the center in-line and in staggered arrangement respectively. The increase of flow resistance and the breakdown of the impinging jet recover the negative pressure in the isolation zone improving the uniformity of flow distribution [35].

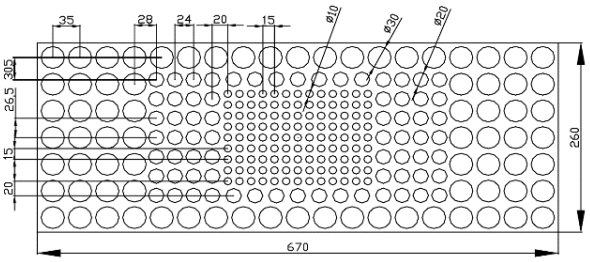

Fig.2. 36 - Type B – Perforated grid with holes in-line arrangement [35]

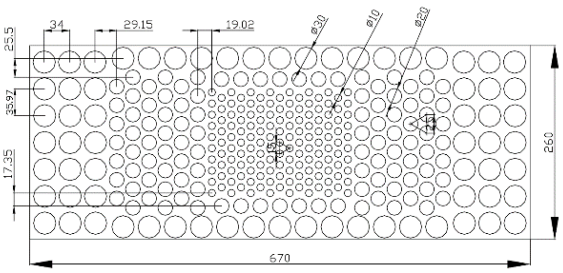

Fig.2. 37 - Type C - Perforated grid with holes staggered arrangement [35]

2.3. Bifurcation Manifold

Another commune structure of manifolds used for flow distribution includes channel bifurcation structures. As shown in Fig.2.38, the consecutive manifold tube is substituted by an arborescent system in which successive channel bifurcations are duplicated in a cascade manner to construct the large number of active channels.

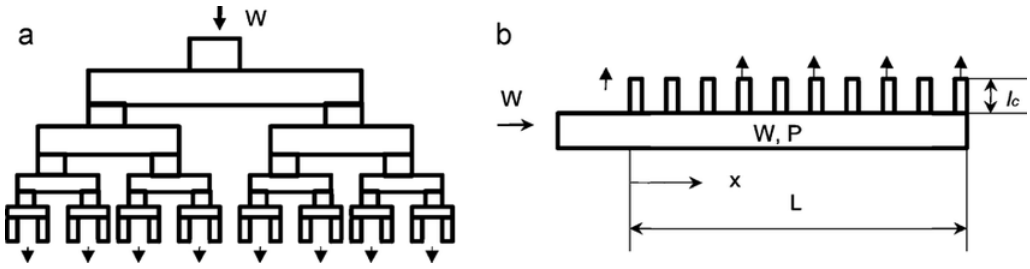

Fig.2. 38 - Bifurcation and Consecutive Manifold [19]

The channel-bifurcation structure is mirrored in the outlet zone of parallel heat exchangers and serves as manifold to the active channels at the last level.

Alvarado et al. [36] demonstrated the advantages of this type of fluid distributor for liquid-cooled heat sink. They compared numerically flow distribution in three different distribution systems in Fig.2.39, i.e. Consecutive manifold (a), Normal-Header manifold (b) and Bifurcation manifold (c).

Fig.2. 39 - Consecutive Manifold (a) - Normal-Header (b) - Bifurcation Manifold (c) [36]

For each header configuration, they also studied the effect of the presence of lateral communications between channels (Fig.2.40).

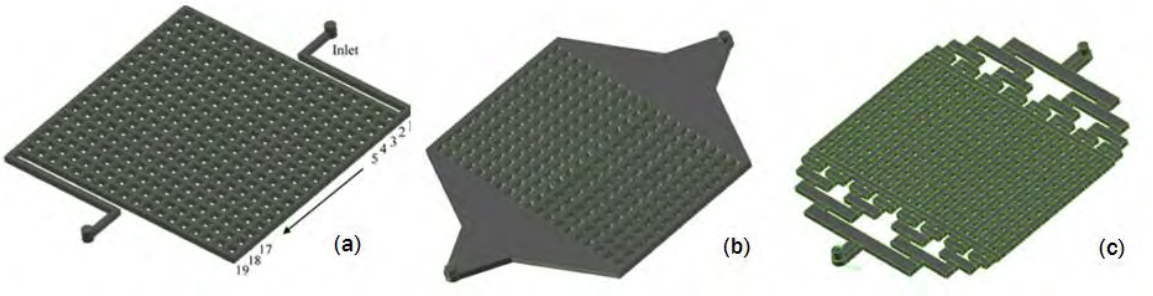

Fig.2. 40 - Different types of manifold with lateral channel communications [36]

The flow regime was limited to laminar and CFD Software ANSYS FLUENT was used for the analysis. After a mesh sensitivity study on total pressure drop, a finer size was selected for any different hear sinks (≈ 4000.000 elements). The computation employed a second order upwind scheme for convective terms and a SIMPLE method to handle the coupling of pressure with velocity fields [36].

The comparison between all flow distributors revealed that consecutive manifold provides the worst flow distribution whereas a significant improvement occurs in normal-header manifold. However, higher flow rate still exists in channels facing to the inlet port of normal-header. With the introduction of a bifurcations system a uniform distribution is finally approached.

They also concluded that flow distribution uniformity is improved when parallel channels have lateral connections. In fact, whenever flow maldistribution exists, these connections help to homogenize velocity and pressure fields allowing for a redistribution of flow. Almeida et al. [37] achieved the same result investigating fluid flow through two-dimensional ramified structures by direct simulation of the Navier-Stokes equations.

Another interesting conclusion of Alvarado et al. analysis concerns the different trend of flow distribution with Reynolds number for the three types of distributor. In typical manifold system, the flow distribution uniformity increases with the increase of Reynolds number, whereas in a normal-header heat sink does not change very much. In bifurcation manifold, at higher Reynolds number an important flow separation in bifurcation zones occurs avoiding the redevelopment of a symmetric velocity profiles in generated channels. A very bad distribution characterized bifurcation manifold at high Reynolds number.

After this brief comparative analysis, a more detailed description of flow distribution bifurcation manifold is provided in the following.

It is important mentioning that lot of physicists modeling biological systems provided an interesting general *Constructal Theory* for designing a perfect distribution in vascular or respiratory system of living beings [38-39-40]. However, due to the PhD scheduled deadlines, it has not been thoroughly examined. One of their main conclusions is that the geometrical structures of bifurcations can affect the flow uniformity dramatically. In the following experimental and numerical studies deal with this problem.

2.3.1. Experimental studies of bifurcation manifold

Liu et al. [41] investigated experimentally and numerically the issue of flow distribution in fuel cell stacks. Different versions of a basic bifurcation design in Fig.2.41a were investigated to identify key physical and geometrical parameters influencing flow distribution.

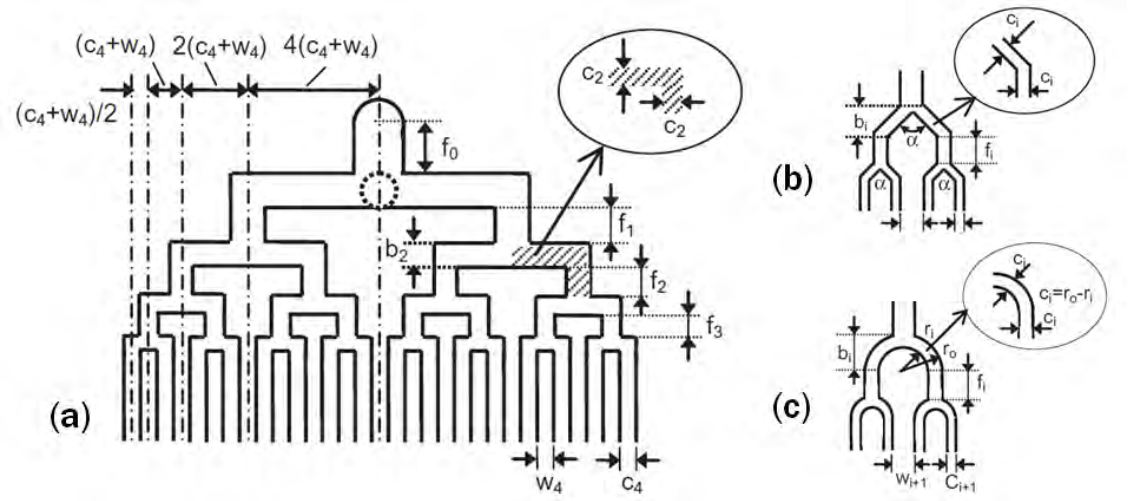

Fig.2. 41 - Flow distributor constructed by T-shape bifurcation of channels (a) Tree-shaped structure (b) – Circular-shaped structure (c) [41]

For sake of clarity, studied structures are categorized in two typical designs, tree-shape and circular-shape flow bifurcations in Fig.2.41b and c respectively. Tree-shape structures may vary due to the angle, α. Tree-shape with α equal to 180° will be named Tee-shape.

In the experimental test, flow distribution uniformity was evaluated for 3 Tee-shape and 3 Circular-shape structures varying only in parameter f_i/c_i which is the normalized length of straight channels.

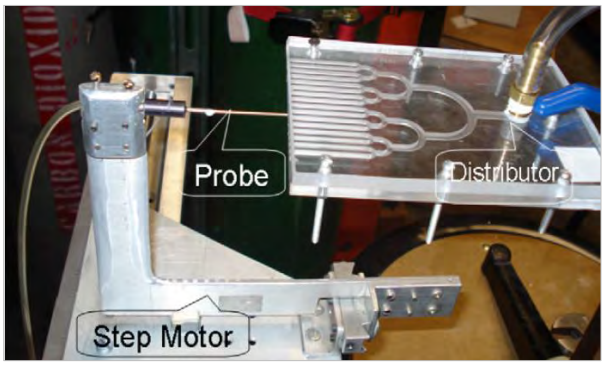

Fig.2. 42 - A close-up view of the flow distributor and Pitot tube set-up [41]

All mockups were fabricated in Plexiglas plates using CNC[7] machines to ensure high accuracy. Velocities of the airflow at the exit of flow channels of each distributor were measured using specially developed Pitot tube. Its tip was placed facing the discharging flow at the exit of a flow channel (Fig.2.42).

An example of the experimental velocity profile on the centerline of the height of channel for a circular shape distributor at the flow rate of 2.83 m³/h is illustrated in Fig.2.43. Here, u is the individual local velocity and U_{mean} is the average of velocities on the centerline of the heights of 16 channels. Geometrical characteristics of flow distributor are shown in Table 2.2.

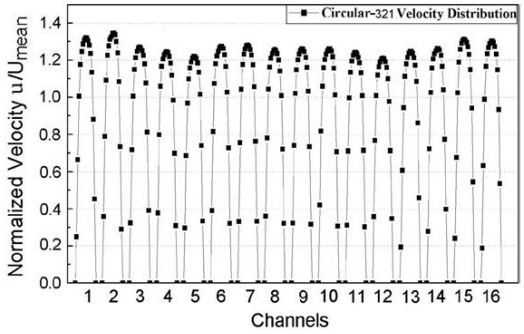

Fig.2. 43 - Measured velocity profiles at the centerline of height of channel [41]

Entrance	c_0 (mm)	f_0 (mm)	f_0/c_0 (mm)				
	4.52	20.00	4.42				
Bifurcation	c_i (mm)	f_i (mm)	f_i/c_i	c_i/c_{i-1}	w_i (mm)	r_i (mm)	r_i (mm)
1	3.48	10.45	3	0.77	–	14.14	17.62
2	2.68	5.36	2	0.77	–	6.60	9.28
3	2.06	2.06	1	0.77	–	2.94	5.00
4	1.59	30.00	18.87	0.77	2.38	1.19	2.78

Height of all channels: h = 1.59 mm.

Table 2. 2 - Characteristics of flow distributor Circular-321 [41]

The large experimental database achieved by the authors provides some important conclusions about the impact of bifurcation structure on flow distribution. All of them are listed below.

[7] CNC: Computer Numerical Control

Length of straight channels, f_i/c_i

As expected, for both types of bifurcation structure, the higher value of f_i/c_i improves flow uniformity.

Circular-type and Thee-type flow distributor

For the same combination of channel lengths f_i/c_i , Circular-shape structure provides a better distribution compared to Three-shape. This can be explained if one considers the larger length of $(f_i + b_i)$ in circular bifurcation zone which allows the development of a more symmetric velocity profile upon reaching the next level of bifurcation. Circular shape also reduces the flow separation after bifurcation.

Effect of Re number

The sensitivity of flow distribution to Reynolds number depends on the length of channels in the bifurcation levels. At higher flow rate, flow separation in bifurcation zone is severe, thus the flow needs a larger length to develop a symmetric velocity profile.

Pressure losses

Circular-shape distributors have lower pressure losses than tee-type distributors. In fact, the circular structure alleviates flow separation and recirculation at the inner walls of bifurcations reducing total pressure drop of distributor.

However, Liu et al. demonstrated that some flow channel fabrication defects may be responsible for the poor symmetry of velocity profile, particularly at high flow rate. For this reason, in industrial applications, tee type distributors are preferred to the circular ones. A more precision control is guaranteed for tee-type flow channels which are easy to fabricate without using CNC machines.

2.3.2. Computational studies of bifurcation manifold

Li et al. [42] [43] also performed numerical studies on flow distribution in basic designs of bifurcation structure. Their analysis was conducted using commercial software ANSYS Fluent.

In order to validate their numerical model, Circular channel structure (see Section 2.3.1) was studied. The CFD domain was built using SolidWorks CAO software and meshed in GAMBIT (Cell number 3.8×10^6) to serve the computation package Fluent.

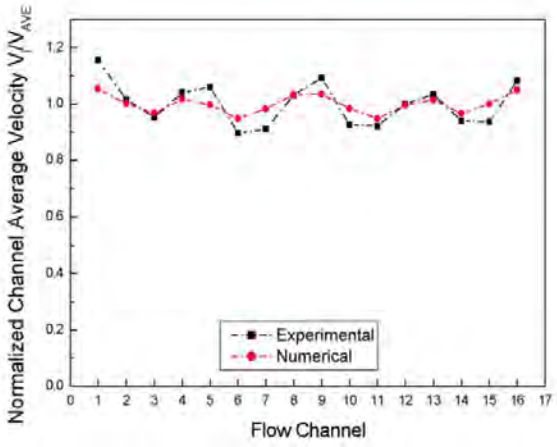

Fig.2. 44 - Experimental and numerical results of non-dimensional velocity distribution - Circular321 [42]

The comparison between numerical and experimental data is illustrated in Fig.2.44. The predicted normalized profile of velocity distribution at the exit of flow channel results in good agreement with the calculated one.

After the successful validation, numerical methods and procedures have been used by the authors to identify some relevant geometric and physical parameters influencing flow distribution in channel bifurcations, i.e.:

Circular-type and Tree-type flow distributor

As already mentioned, Circular-type provides a better distribution than Tee-type. However, in the case of assumption of constant length between two successive bifurcations, the Tee-type structure could result more efficient in term of distribution than the equivalent Circular one. The longer length f_i significantly benefits the flow distribution uniformity (see Fig.2.41 for explanation).

Bifurcation Angle for Tree-type flow distributor

To correctly compare the uniformity of flow distribution for tree-type structures having different bifurcation angle α (90°,120°,150°,180°), the value total length ($f_i + b_i$) was fixed. Flow distributors with higher bifurcation angle show a better distribution [42] [43]. This is due to the smaller bifurcation zone b_i in larger bifurcation angle cases ($f_i + b_i$ fixed). The consequent larger downstream length f_i allows developing a more uniform velocity profile. On the other hand, in channel bifurcation with a high angle α, pressure drops increase because of the more direct blockage of flow at the bifurcation zone.

Length of straight channels

The length of straight channel f_i determines the symmetry of flow velocity profile before it reaches the next bifurcation. For all types of distributors, the longer the allowed development length, the better the symmetric velocity profile will be.

It is well known that the fully developed length is proportional to the Reynolds number of flow.

Effect of Re number

Liu et al. [43] demonstrated that the flow uniformity in a bifurcation structure decreases with the increase of Reynolds number. For laminar flow, the Tee-type seems to work better than the equivalent Circular-type which has a shorter straight section to redevelop the uniform profile [43].

However, at high Reynolds numbers, flow separation phenomena at bifurcation zone for Tee-type structures, seriously degrade the uniformity of flow distribution.

Despite the better distribution performance of Circular-type bifurcation manifolds, Tee-shape manifolds are still preferred for their convenient manufacturing process. Another study of Liu et al. [43] demonstrates how slight variations of fillet structure in Tee-type distributors could effectively reduce flow separation and the consequent maldistribution.

Two Tee-type distributors having different fillet structures (Fig.2.45) were analyzed at Re 988 and Re 13000.

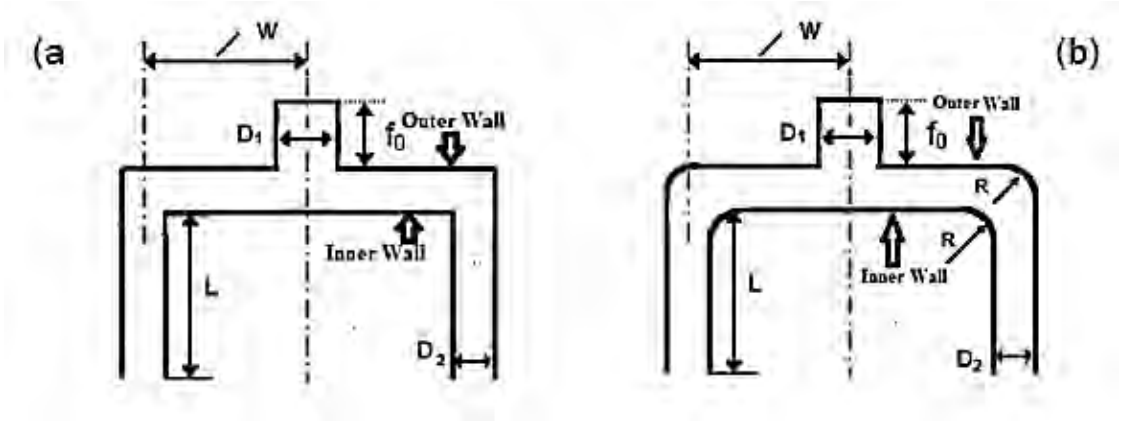

Fig.2. 45 - Sharp fillet (SF) (a) and Curvature fillet (EF) (b) [43]

Tee-type distributor: Effect of Fillet structure

For turbulent flow, Curvature Fillet distributors (Fig.2.45b) show an improved flow distribution compared to Tee-Types with Sharp Fillet (Fig.2.45a).

Tee-type distributor: Effect of Lateral distance w/c_i

Liu et al. observed that the increase of lateral distance w_i/c_i helps to increase the symmetry of velocity profile downstream bifurcation zone. However, a value of normalized distance greater than 4.56 has not a significant impact on flow distribution.

Finally, Zhang et al. [45] focused their attention on the secondary flow and recirculation flow motions in bifurcations and bends of channel network for micro-electronic chip. They described numerically the evolution of vortices at different Reynolds numbers by using the commercial code CFD-ACE+20166 based on the finite volume methods (FVM).
The computational domain was reduced to a single channel of network having two branches at the exit level, and the branching angle is set to 180°. The velocity distribution over half the cross section in the diffluent flow at T joint is shown in Fig.2.46.

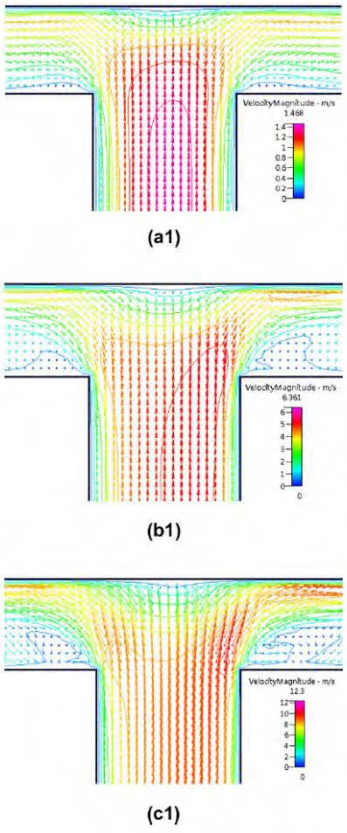

Fig.2. 46 - Velocity of the diffluent flows at a T joint (a1) Re 187, (b1) Re 810, (c1) at Re 1560 – Transverse vortices [45]

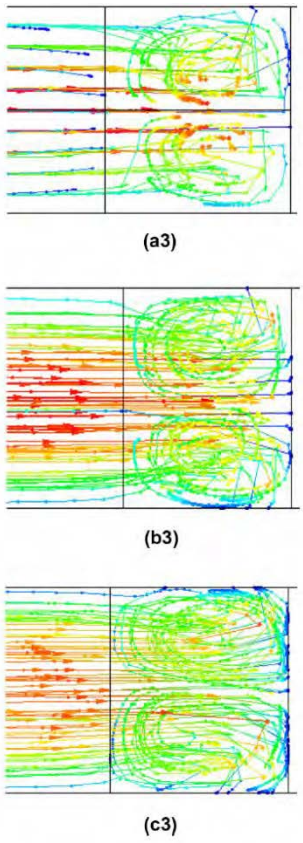

Fig.2. 47 - Streamlines of the diffluent flows at a T joint (a3) Re 187, (b3) Re 810, (c3) at Re 1560 – Longitudinal vortices [45]

It was demonstrated that for lower Reynolds number the flow is slightly disturbed (Fig.2.46a1), then flow separation and recirculation appear near the two inner corners of

bifurcation but no transverse vortices are generated. Transverse vortices induced by the viscous forces and the higher negative pressure gradient occur for Reynolds 1560 (Fig.2.45c1). Fig.2.47 shows longitudinal vortices that spiral the flow around their axes in the stream-wise direction and always imply three-dimensional flow. A pair of vortices is created with the opposite rotation and as Reynolds number increases, their intensities increase and their center moves forwards the outer walls.

The same separation phenomena occur in L bend (Fig.2.48-49), where the fluid moves outward because of the radial pressure gradient. At each corner of the bend, the transverse vortices have been generated and a pair of longitudinal vortices swirls the flow downstream (Fig.2.49).

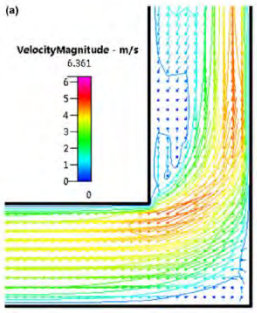

Fig.2. 48 - Velocity of the diffluent flows at a T joint Re 810– Transverse vortices [45]

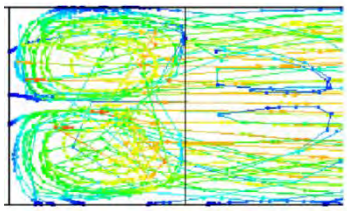

Fig.2. 49 – Streamlines of the diffluent flows at a T joint at Re 810– Transverse vortices [45]

The correct prediction of transverse and longitudinal vortices has an important role in the selection of most efficient flow distributor systems. In previous works, channel recovery length and fillet structures were designed using RANS isotropic turbulence models. Nevertheless, literature demonstrated that they are unable to correctly describe the flow separation and recirculation at the bifurcation zone. A more sophisticate formulation of numerical models including anisotropic effects needs to be tested and validated experimentally.

2.4. Adopted strategy

2.4.1. Flow maldistribution conditions in ASTRID Compact Heat Exchanger

The extensive bibliographic study provided a better understanding of the flow maldistribution issue in all reviewed configurations of compact heat exchangers suggesting some general recommendations to reduce the unequal repartition of flow. It also came out clearly that flow maldistribution conditions are related to the specific HE layout and its operating conditions.

For this reason, a detailed description of ASTRID Sodium-Gas heat exchanger module and its interfaces with the whole tertiary circuit are discussed in the following.

As explained in Section 1.2.1, the flow maldistribution will be analyzed only in the sodium side of one of the eight modules that compose the SGHE.

The SGHE half module consists of a stack of 72 Na channels layers intercalated with 72 gas channel layers (Fig.2.50). Each Na layer is constituted by 125 sodium channels which means that 9000 rectangular sodium channels, with a 3 x 6 mm² cross section and a length around 2.2 m, have to be fed. This configuration is required to achieve the thermal-mechanical performance of the heat exchanger module (23.4 MW_{th}). Note that, the relatively large cross section of sodium channels is also necessary to avoid the sodium plugging risk.

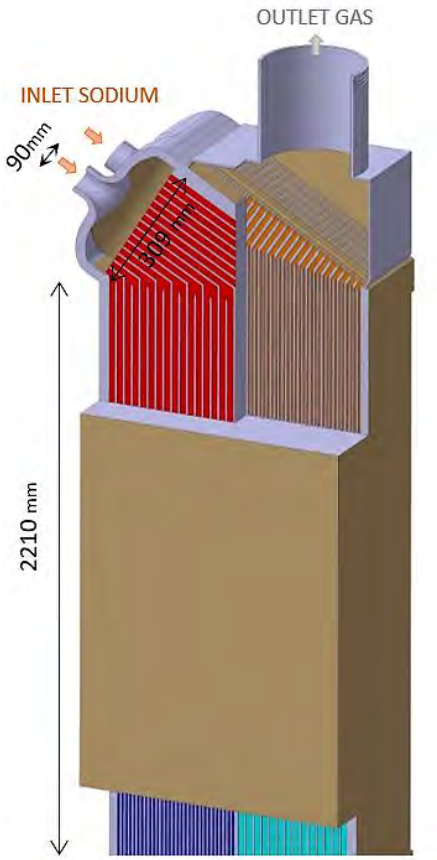

Fig.2. 50 – Overview of the 2014' design layout of SGHE module

On the inlet side, 100kg/s mass flow rate is required to achieve heat exchange performance. The inlet admission implies two pipes which are placed into the pressure vessel, subjected to 180 bars of external pressure at a temperature of 530 ° C. Their diameter of 90mm is the results of mechanical analysis aiming to reduce the mechanical loads. In addition, in order to reduce the cavitation risk and the pressure drop, the inlet pipe cross-section is chosen such that the

rate of flow of the sodium is limited to 10 m/s.

The above description of SGHE module and the overall bibliographic study finally permit to draw a clear representation of flow maldistribution conditions occurring in our geometry. Firstly, the large channel bundle facing to the small admission pipe is characterized by a flow area ratio M of 13.5. The best suited value suggested by Wang et al. [19], for a uniform flow maldistribution, is M< 1.
Secondly, the maldistribution conditions are worsened by the low resistance of parallel channels, where sodium flows at Reynolds 9000 [19]. This means that the sodium jet flow from the inlet pipe (v_0=10m/s) does not face any resistance ($\overline{\Delta P}$~60 mbar) and goes through channels after the impingement on the bundle. According to the Lalot criterion [27], the resulting imbalance between the dynamic pressure at the sodium inlet header and the average pressure drop across the channel bundle acts as the primary responsible of the flow maldistribution in the SGHE module ($\eta = 2.77$).

The sodium mass flow rate distribution between channels is illustrated in the 3D graph in Fig.2.51. As expected, due to the low resistance of channel bundle, a significant overfeeding of channels facing the admission occurs.
The maldistribution factor σ, corresponding to the standard deviation of channel mass flow, is 25 %.

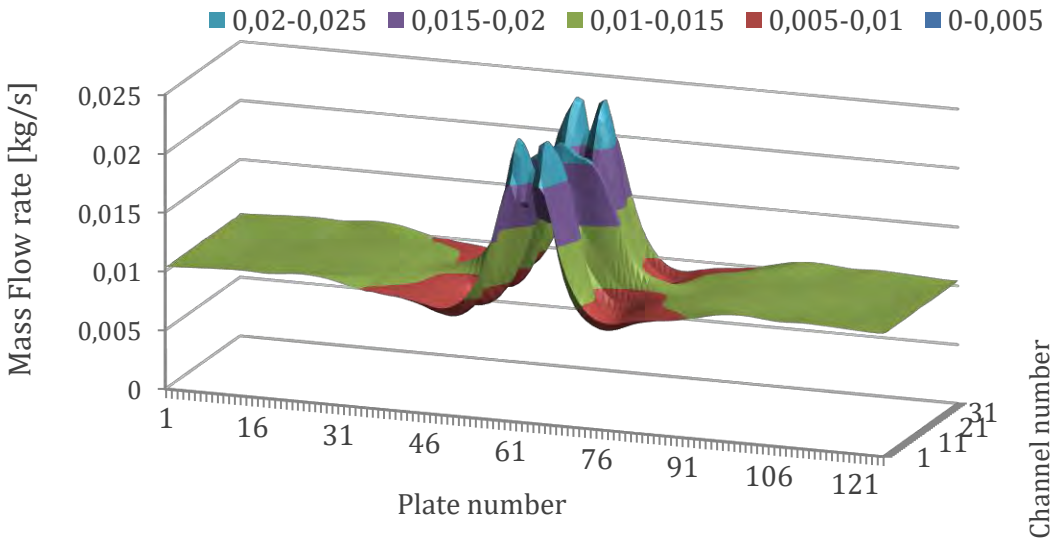

Fig.2. 51 - Mass Flow distribution in 14' Design SGHE

The maldistribution factor provides a first important information about the quality of flow distribution. However, it is not possible to conclude about the impact of the distribution on the mechanical resistance and thermal exchange performance of the component. Being primarily concerned by sodium temperature gradients in the channel bundle, the results of a preliminary thermo-hydraulic calculation have been shown in Table 2.3 [46].

SGHE 14	Velocity inlet	Pressure Drop	Lalot criterion	Maldistribution factor	Mass Flow Rate		Temperature		
	m/s	Pa	-	%	kg/s		°C		
	10	6000	2.77	25	min	max	min	max	mean
					0.008	0.024	314	437	348

Table 2. 3 – Distribution performance of 2014 design of SGHE module

The high temperature variation between sodium channels in Table 2.3 generates internal thermal stress and thus deformation of structure. A previous thermo-mechanical study [47] stated that the current design of the SGHE module is not attainable since thermo-mechanical stresses degrade the mechanical integrity of the module (higher than 200 MPa).

To overcome this problem, the bibliographic study suggests several design solutions which could homogenize flow distribution in similar flow conditions. However, before proposing any solutions, it is important to perform a *functional analysis* of the SGHE design which will be integrated in the pressure vessel of ASTRID Power Conversion System. All requirements are listed and discussed in the following.

2.4.2. ASTRID Compact Heat Exchanger requirements

In the design process, the first step is to identify primary and secondary functions of ASTRID flow distributor system.

Primary functions are referred to component requirements for any type of compact heat exchanger regardless of the specific project, i.e.:

I.1 *No direct contact between thermally interacting fluids*

The selected design of sodium distributor must ensure the physical separation of the two working fluids. Na header designs, allowing most compact arrangement of Na/N_2 plates and N_2 header, will be preferred for the present work.

I.2 *Uniformity of flow distribution*

The fluid distributor has to provide a uniform distribution between channels of the heat core. As already explained, in the present work the uniformity will be estimated starting from considerations about the repartition of mass flow rate between channels.
The flow *maldistribution factor* is defined as follow:

$$\sigma = \frac{\sqrt{\frac{\sum_i^N (\dot{m}_\iota - \bar{\dot{m}})^2}{N}}}{\bar{\dot{m}}} x100 \qquad (1)$$

where $\dot{m}_\iota$ is the mass flowrate in a channel; $\bar{\dot{m}}$ the average mass flowrate of the whole channels and N is the number of channels.

It is important to note that, from a mechanical stand point, a uniform flow distribution is the one that provides allowable mechanical loads. However, in this phase of the study, we will only take care of the reduction of the hydraulic flow maldistribution. Then, an appropriate thermomechanical analysis of component will be done to investigate the effect of the resulting temperature field. The entire design process is detailed in PhD perspectives in Section 6.2.1.

I.3 *Pressure losses in heat exchangers*

The flow distribution system must be able to adapt pressure drops in order to favor the uniform distribution and a proper integration with the whole hydraulic circuit. The total pressure loss due to the inlet pipe, headers and heat core is limited to 1,5 bars.

Differently, secondary functions are directly related to the project and take into account external operating conditions (temperature and pressure) in which the heat exchanger is going to be operated. At the same manner, the manufacturing process, safety, environmental protection, maintenance and cost are included in secondary functions. Note that in the present thesis, all of them will be considered as guidelines in the design process however they are not further investigated.

II.1 *Mechanical integrity: Steady-state operating pressure and temperature*

The structure of flow distributor has to maintain its integrity under the external pressure of 180 bars.

A proper thickness of wall has to be provided using RCC-MRx code criteria[8]. Creep-fatigue and buckling damages are considered in the analysis due to the Sodium Inlet Temperature ($T_{inlet}^{Na} = 530°C$) and the high external pressure [47].

II.2 *Mechanical integrity: Temperature gradients*

The structural integrity of flow distributor has to be ensured for each temperature variation which inevitably generate internal stress and thus deformation of structure. Temperature differences between inner and outer wall of the header and between channels of heat core will be considered.

II.3 *Sodium requirements*

In term of safety, maintenance and control, flow distributor design has to include a passive gravity system to move sodium out of the heat core while heat exchanger remains fixed into the pressure vessel. In this sense, for the ASTRID SGHE, a minimum sodium channel section of 3x6mm^2 and a sodium inlet velocity minor than 10m/s are imposed.

As conclusion, if any of primary and secondary function is not satisfied by the proposed design solution, then the solution is rejected.

2.4.3. Header solutions

Once detailed all SGHE requirements and the imposed flow conditions, the three types of fluid distributors studied in the bibliographic review have been considered as possible solutions for the SGHE design. Major attention is given to the achievement of primary functions of SGHE module.

This basic exercise allowed us to select a single concept of fluid distributor on which the entire PhD strategy has been developed.

- Consecutive Manifold

This design is very attractive because of its simplicity and the great knowledge achieved on fluid flow behavior. However, any of design solution proposed by authors in Section

[8] The RCC-MRx code was developed for sodium-cooled fast reactors (SFR), research reactors (RR) and fusion reactors (FR-ITER). It describes the rules for designing and building mechanical components involved in areas subject to significant creep and/or significant irradiation. In particular, it incorporates an extensive range of materials (aluminum and zirconium alloys in response to the need for transparency to neutrons), sizing rules for thin shells and box structures, and new modern welding processes: electron beam, laser beam, diffusion and brazing.

2.1 is suitable to reduce the imbalance between the high inlet velocity and the very low pressure drop of lateral channels. In fact, the cross-sectional area of lateral channels is fixed and lateral resistance cannot be increased [19]. The small diameter of the admission tube ($E = 11$) and the high inlet velocity result in a jet flow recirculating in the inlet header [19]. In addition, the introduction of perforated grids or baffle tubes does not fulfil secondary functions. Therefore, they are not considered as possible solution to flow maldistribution (i.e. mechanical integrity, manufacturing cost for installing, assembling and immobilization during operating condition) [48]. It can be concluded that the consecutive manifolds such that studied in literature cannot be used to distribute sodium flow in ASTRID heat exchanger.

However, a new design of flow distributor which gets close to the basic principles of the U-type consecutive manifold has been tested at the CEA [46] by using the commercial software ANSYS Fluent.

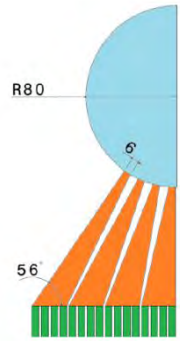

Fig.2. 52 - Modified U-type manifold

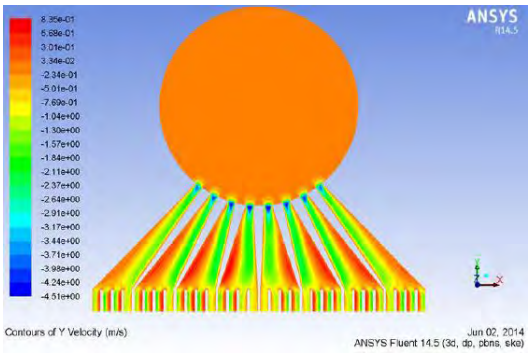

Fig.2. 53 - Velocity field in "*pre-faisceau*" zone

To increase lateral resistance of heat exchanger core and to reduce the area ratio, an intermediate distribution zone called "*pre-faisceau*" has been introduced between the main manifold tube and the heat core (Fig.2.52). By varying the cross-sectional area of distributors in "*pre-faisceau*" zone, a proper value of pressure drop could have been selected.

After several attempts, the study demonstrated that the uniformity of flow distribution surprisingly decreases with the increase of pressure drop [46]. This unexpected result may be due to the complex flow in "*pre-faisceau*" zone (Fig.2.53).

As shown repeatedly in Section 2.1.3, despite the increased pressure drop in the bundle, a jet flow rises at the entrance of the consecutive manifold leading to a reduction of flow rate in parallel channels nears the entrance(Fig.2.54).

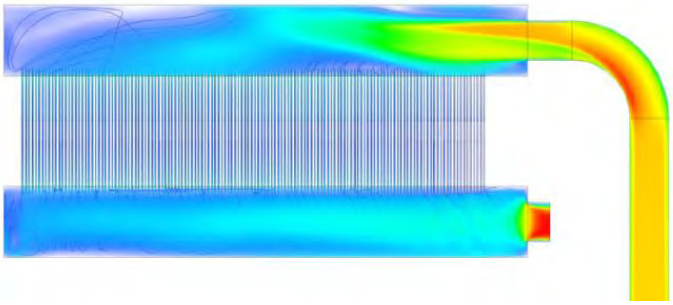

Fig.2. 54 - Velocity field in modified U-type manifold with inlet admission

In addition, the resulting layout of the heat exchanger would be difficult to be integrated in ASTRID tertiary circuit [90].

As conclusion, considering previous results and the few degrees of freedom to improve the flow maldistribution, the investigation of consecutive manifold concept has been excluded, at least temporarily, from possible solutions.

- Normal-Header

The normal-type header was the historical design solution for ASTRID project since it allows for an easy integration in the circuit.

Fig.2.55 shows a possible design of inlet header which is the result of a preliminary mechanical study [47]. Therefore, it fulfils secondary functions of the functional analysis and it will be considered as the reference solution for this type of distributor. The admission angle (27° in the Fig.2.55) may vary from 15° to 90° in accordance with ASTRID project progress conditions.

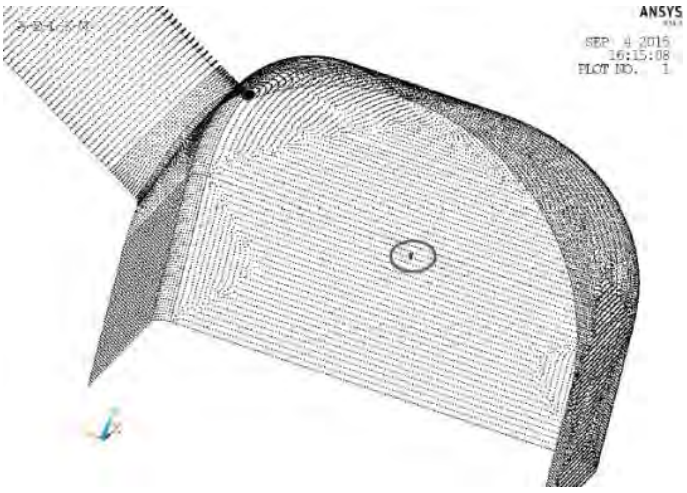

Fig.2. 55 - Selected geometry of Normal-Header *(II.1 function)*

This concept (A) also provides the most compact arrangement of Na/N_2 plates (Fig.2.56).

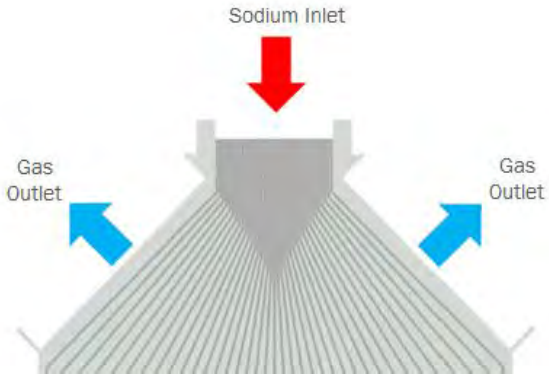

Fig.2. 56 - Na/N_2 plates arrangement *(I.1 function)*

However, as shown in Section 2.4.1, the uniformity of flow distribution is not as good as required ($\sigma = 25\%$). From the bibliographic study, the increase of header volume (parameter h) could help in the dissipation of the three-dimensional jet flow. However, a larger header volume requires more wall thickness thus non-allowable thermal stresses.

The introduction of a perforated grid could lead to a valuable improvement in flow distribution.
A previous study investigated the solution of a double uniform perforated grid placed in the midway between the inlet tube and the core of heat exchanger (Header B in Fig.2.57). As shown in Fig.2.57, multiple halls of double grid increase flow resistance and break down vortex generated by jet flow.

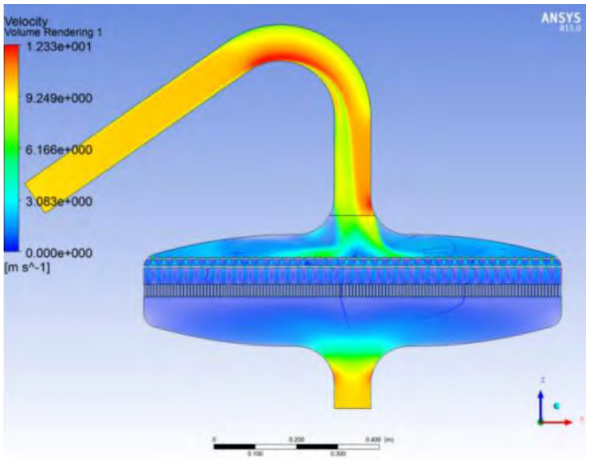

Fig.2. 57 - Velocity field in double grid Normal –Header with inlet admission

Table 4.2 shows a comparative analysis between headers with (B) and without (A) the perforated grid.

	Velocity inlet	Pressure Drop	Lalot criterion	Maldistribution factor	Mass Flow Rate		Temperature		
	m/s	Pa	-	%	kg/s		°C		
A	10	6000	2.77	25	*min*	*max*	*min*	*max*	*mean*
					0.008	0.239	314	437	348
B	10	13 400	1.35	3	*min*	*max*	*min*	*max*	*mean*
					0.010	0.012	334	355	345

Table 2. 4 - Flow maldistribution conditions in Normal-Header without (A) and with double grid (B)

A significant reduction of flow maldistribution can be noticed. The introduction of the grid allows increasing pressure drop without varying the channel sections in the active bundle. Furthermore, the value of pressure drop admits the integration in tertiary loop. Nevertheless, the maintenance and the mechanical loads related to the new external distribution element directly exclude this solution.

Anyway, this study demonstrated that, finding a different way to increase pressure drop in the bundle and to optimize the flow jet impingement, it is possible to reach a uniform distribution. The normal-header could be a possible solution for the SGHE.

- Bifurcation Manifold

This concept of manifold is not analyzed any further because of the large pressure drop of turning loss in symmetric bifurcations. However, such an analysis suggested a key design solution for ASTRID sodium plates which consists in the introduction of bifurcating channels in the pre-distribution zone. This allows to increase pressure drop in bundle channels without the introduction of external homogenization devices and without varying the dimension of active channels. The features of the bifurcation system are illustrated in the following section.

2.4.4. Adopted Solution for SGHE

All previous studies allow proposing a new design of sodium flow distribution system which best fulfill thermo-hydraulic and mechanical requirements of ASTRID heat exchanger and which will be extensively investigated during the PhD work.

System of bifurcating channels

First of all, to increase pressure drop in the heat core, a system of bifurcating channels (pre-distribution channels) is proposed to be directly integrated in the zone called "*pre-distribution zone*". As shown in Fig.2.58, the inlet sodium flow of each pre-distribution channel is conveyed into four active channels through three levels of channel bifurcations. The 4-fold mass flow in the main channel before bifurcation is primarily responsible of the increase of pressure. Note that, the sodium channel sections remain fixed in each bifurcation level.

In addition, the bifurcation system allows to reduce the volume of normal-header facing the "*pre-header*" zone (sodium channel number is reduced by a factor of 4). The small header better fulfills ASTRID mechanical requirements.

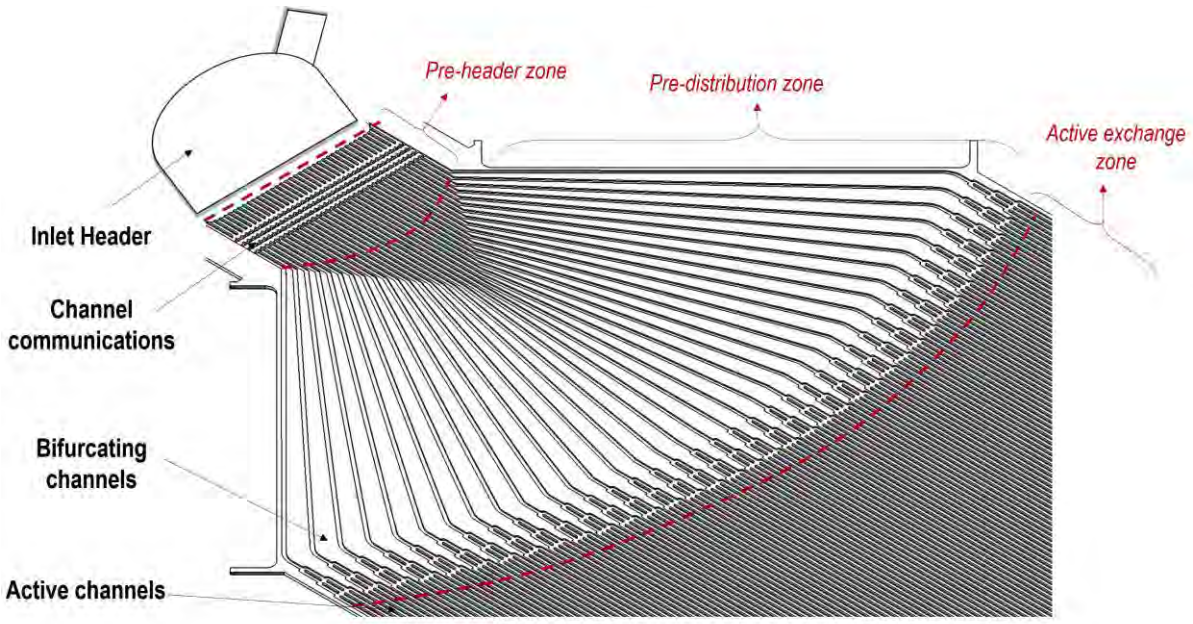

Fig.2. 58 - Sodium plate: Channel communications and Bifurcation system

However, an improper design of channel bifurcation could amplify flow maldistribution in the last level of generated channel ($\sigma_{bifurcation}$ or σ_b). This means that an additional term of flow maldistribution induced by bifurcations could be added to the maldistribution due to the inlet header. In fact, as already shown in Section 2.3, the

symmetry of the flow velocity profile in straight channels before the next bifurcation directly influences the uniformity of the flow distribution between generated channels.
An optimization of pre-distribution channels design is required to minimize σ_b . Chapter 3 and Chapter 4 of the present thesis deal with this problem.
A bifurcation system whose distribution performances are completely independent from the header-induced flow distribution is proposed in this work.

Channel communications

The bibliographic study in Section 2.3 also demonstrated that the presence of lateral communications between parallel channels in heat exchanger helps to homogenize velocity and pressure field allowing for a redistribution of flow [37]. The same concept is proposed for ASTRID SGHE module where a system of channel communications is introduced in the zone called "*Pre-Header*" (Fig.2.58). Note that, the mutual arrangement between sodium and gas plates admits channel connections in both normal directions to the streamwise flow (X-Z connections). This distribution system is actually protected by patent FR165743 [89]. The optimization of channel connections in the "Pre-Header" zone is discussed in APPENDIX II.

For sake of clarity, an overview of the operating principle of the connections system[9] is briefly summarized in Fig.2.59 which illustrates the flattering of the mass flow inlet profile (Gaussian profile) through each level of channel communications. The "maldistribution" factor is progressively reduced by passing through the connection system.

[9] Being a good compromise between CFD computational effort and the analogy with the real 32x35 SGHE bundle, a "10x10" model has been chosen as reference geometry for the optimization of channel connections.

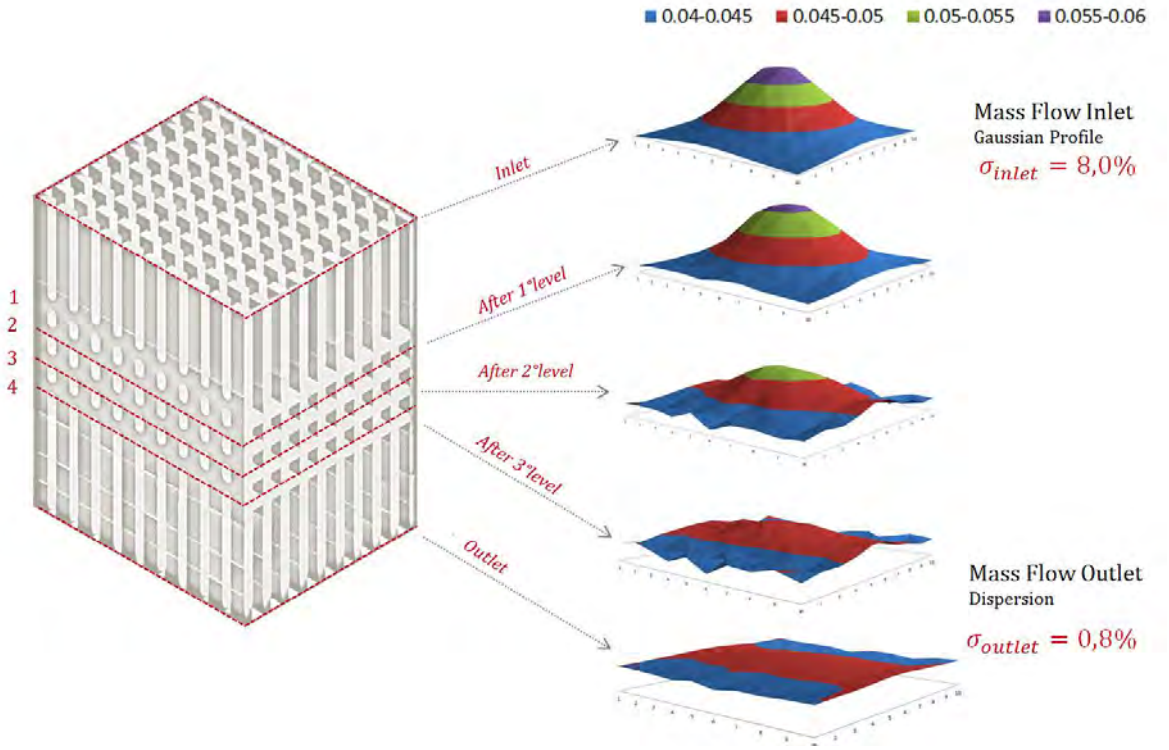

Fig.2. 59 - Operating principle of channel connections in a 10x10 bundle channel

Inlet Header

Finally, a normal-header manifold, like the one described in the previous section (Fig.2.55), is used to convey the inlet sodium flow into the pre-distribution channels. The admission angle and the header volume are optimized to obtain the suited jet flow impingement and recirculation allowing for a uniform flow distribution.

Experimental Approach

To validate the numerical model and to prove the design basis of the proposed sodium distribution system, an experimental database is of primary importance. Literature does not really provide test-cases similar to the innovative distribution system. In fact, some validations of flow distribution in specific geometry of bifurcating channels or normal-header have been identified, but all of them lack in some important features of the proposed distribution solution. An experimental database on the actual geometries is then necessary.

It is important to point out immediately that, in the present work, the layout of the innovative distribution system and the specific function of each distribution unit allow a

separated investigation of bifurcating channels from the rest of the module (inlet header and channel connections).
Therefore, thesis strategy required the conception of two experimental facilities. Both of them will be discussed in detail in Chapter 3 together with the experimental techniques employed to characterize the flow in pre-distribution channels and the global flow "maldistribution" in the integral module. In this latter, the attention will be focused on the influence of the jet flow evolution in the header on flow repartition between channels.

PIV measurements of velocities and Reynolds stresses will provide the information needed to a full investigation of the fluid flow phenomena and validation of the adopted numerical model.

Numerical Approach

To complete the long and expensive time schedule of an experimental investigation, numerical analysis is used to provide more accurate information. In this sense, it is of primary importance to determine which model and which numerical approach can give the most accurate results in terms of physical description of fluid flow, based on experimental comparison.

Following the thesis strategy, a separated investigation of bifurcating pre-distribution channels will be performed in Chapter 4. The validated numerical model will be used to design the bifurcating channel able to increase pressure drop without introducing any additional maldistribution in the bundle.

Then, the global flow maldistribution between channels of the integral SGH module will be studied numerically in Chapter 5.
As regard to the computed domain, the whole geometry including inlet/outlet header and the long heat core composed by 9000 bifurcating channels has to be discarded in a CFD numerical approach. In fact, no precise physical flow description can be achieved, due to the very large domain requiring a coarse mesh to run calculations not too long in time. Chapter 5 will describe the computational strategy adopted in this study; porous media model and some physical assumptions will be discussed and validated.
The ability of numerical models to correctly describe the jet flow recirculation in the inlet header and the resulting flow distribution between channels will be verified.

As regards the turbulence model, LES approach is discarded because the needed computational resources would be very costly. In fact, the final goal of our numerical

analysis is to have an industrial model able to provide fast and accurate information enough. Hence, Reynolds-Averaged Navier-Stokes (RANS) approach is selected.

Conclusions from the bibliographic study show, that a RANS high-Reynolds number approach globally provides correct information about the three-dimensional flow jet behavior in normal inlet header. A turbulence k-ε model is then used for the analysis of flow distribution in the SGHE module (Chapter 5).
For the system of channel bifurcations, differently from the research works in literature, computations of the fluid flow all the way down to the wall is preferred in the present thesis. In fact, the smaller geometry of a single pre-distribution channel enables the use of a RANS low-Reynolds model based on ω equation. In particular, an anisotropic formulation of k- ω SST model will be used to provide better description of flow separation and recirculation in bifurcation zones (Chapter 4).

Chapter 3

Experimental Facilities

This chapter presents all the experimental activities carried out in this thesis work with the aim to validate the numerical models and to prove the design basis for the ASTRID SGHE module.
As shown in Section 2.4.4, the complexity of the proposed distribution system and the consequent fluid flow phenomena at different scales require a separated investigation of the pre-distribution channel system and the integral design of the module. Two water experimental facilities have been then conceived and studied experimentally, i.e. EASY-B and DANAH facility.

In the following and for each experimental facility, the pilot installation and measurement equipment used for the analysis are described. After a brief description of the measurement system technique, the entire experimental program is provided through definition of goals and interests. Finally, in order to demonstrate the consistency of the collected experimental database, a preliminary analysis of some key measurements is presented.

Water as simulant fluid

It is common practice in the SFR community to carry out hydraulic studies on reactor components or vessels by means of water experimental facilities. In fact, due to the similarity between sodium and water fluid property (especially density and viscosity), it is possible to carry out coherent thermal-hydraulics experimental studies with water instead of sodium. This is particularly true when dealing with validation of fluid-dynamics numerical codes or qualification of design options [49]. Certainly, sodium will be used when the aim is to further explore the mechanical behavior of structures undergoing thermal-hydraulic instabilities liable to lead to thermal fatigue and thermal striping damage phenomena.

Table 3.1 shows some physical properties of sodium and water at different temperatures.

Fluid Property	Temperature $T\ [°C]$	Density $\rho\ [kg/m^3]$	Dynamic Viscosity $\mu\ [kg/m \cdot s]$
Water	25	997.05	$8.9x10^{-4}$
Water	99	959.07	$2.85x10^{-4}$
Sodium	437	847.21	$2.61x10^{-4}$

Table 3. 1 - Water and Sodium properties

Benefits in using water are various. First of all, the conception and the manufacturing of the experimental device become less complicated because of lower mechanical stresses. Using water as simulant fluid, the security of employees is preserved. In addition, water is obviously cheaper and easy to be provisioned. Nevertheless, the main advantage resides in the no opacity of water which allows the use of the optical revelation system during experiments (Laser Velocimetry).

In this way, the GISEH platform was developed and built at the CEA Cadarache research center in 2014. It gathers all the hydraulic loops used for the qualification of the ASTRID components [50]. The PLATEAU facility (*PLATeforme en EAU/water platform* in French), belonging to the GISEH platform, accommodated one of the experiment presented in this PhD work, i.e. DANAH.

Fig.3.1 shows an overview of PLATEAU facility.

Fig.3. 1 - Overview of PLATEAU facility

What is important to mention immediately is that to carry out experiments in Reynolds analogy with Sodium at ASTRID operating condition, water at 100°C should be used [49]. However, both experimental mockups employed in this thesis are made in Plexiglas and they cannot resist to high temperature while maintaining their structural integrity (Plexiglas max service temperature = 70 °C). Experiments are then performed at lower Reynolds numbers, taking care to have a turbulent flow regime.

Preliminary CFD studies have been performed to evaluate the deviation in term of flow distribution and velocity field using sodium at ASTRID operating conditions and ambient water. In Table 3.2, the case study of flow distribution in the SGHE module is presented.

WATER at 25°C - $Re = 803\,636$	SODIUM at 437°C - $Re = 2\,740\,624$
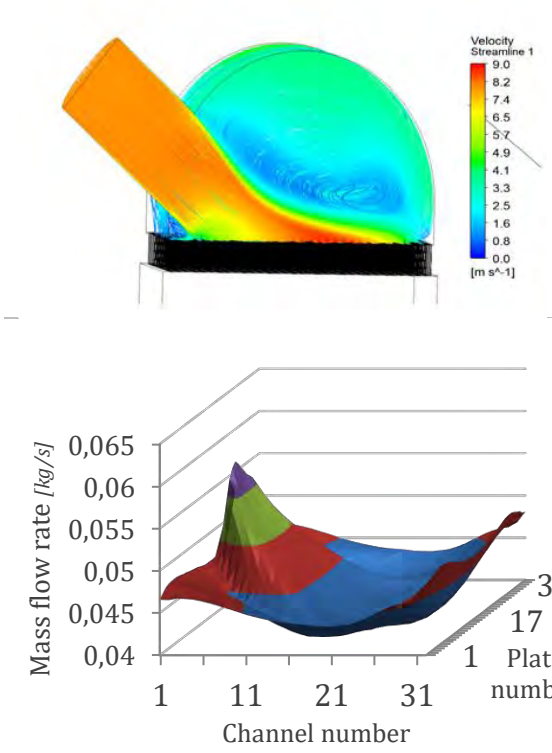	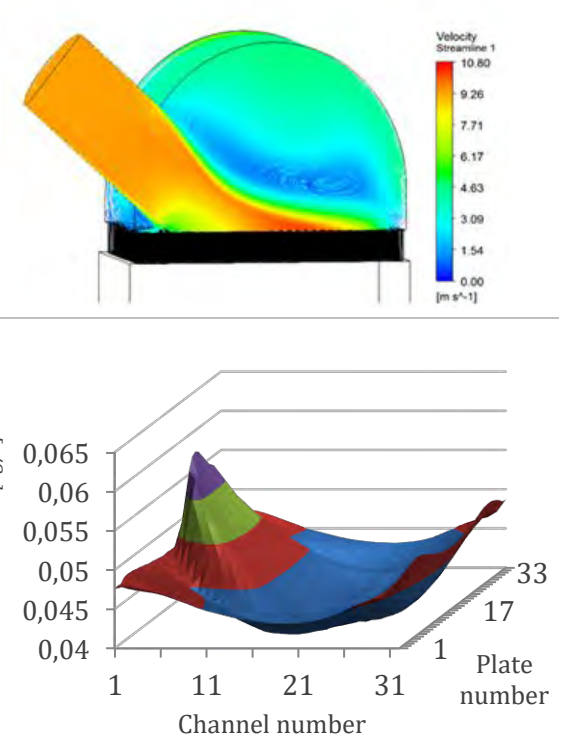

Maldistribution factor	Mass Flow Rate		Maldistribution factor	Mass Flow Rate	
%	kg/s min	kg/s max	%	kg/s min	kg/s max
7.04	0.040	0.058	8.02	0.039	0.059

Table 3. 2 – Water/Sodium comparison

As expected, the complex flow pattern of the inlet jet flow is exactly the same for the two different turbulent Reynolds numbers. At the same manner, the resulting 3D profiles of mass flow rate per channel show the same distribution trend.

Some discrepancies can be noticed in the maldistribution factor and the min and max values of mass flow rate. However, the uncertainties of CFD simulations and the slight difference between two calculated values extensively validate the use of water at temperature lower than 100°C for the experimental validation of numerical codes and the qualification of design options.

3.1. EASY-B: Experimental Analysis of SYmmetric Bifurcating channels

To study the flow distribution in ASTRID SGHE pre-distribution channels in Fig.2.58, a specific pilot installation has been designed and assembled in the Laboratoire de Génie Chimique (UMR INP-UPS-CNRS 5503) of Toulouse. An overview of EASY-B facility, whose name stands for "*Experimental Analysis of SYmmetric Bifurcating channels*" is shown in Fig.3.2.

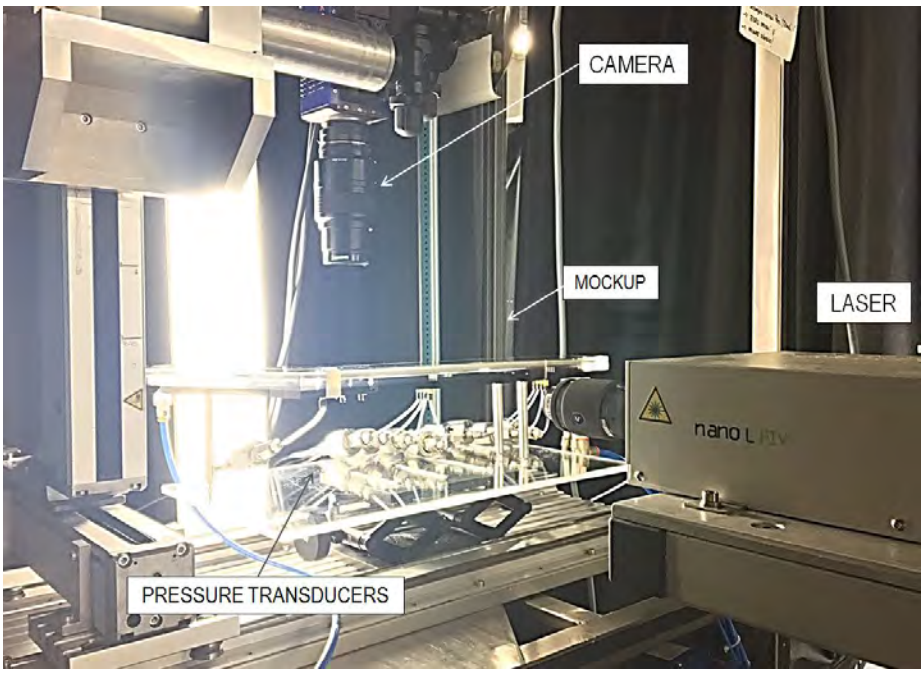

Fig.3. 2 - Overview of EASY-B Pilot Installation

A detailed schematic diagram of the EASY-B experimental set-up is illustrated in Fig.3.3. The experimental test bench is equipped with three different measurement systems, i.e. a

Particle Image Velocimetry (PIV) system, a differential pressure system and an electronic mass balance system. Each measurement system is highlighted with different colors in the schematic diagram.

During EASY-B experiments, the experimental mockups are installed in a hydraulic principal circuit shown in green in Fig.3.3. Water at ambient temperature and pressure is pumped from the storage tank in the mockup via a centrifugal pump *P01* (0-200 kg/s) associated with a frequency meter. A mass flow meter *MQ01* and a pressure sensor MP01 are placed downstream to check mass flow inlet and pressure pump. The mass flow inlet flowing in channel mockups during all PIV measurements is 160kg/s which corresponds to an inlet Reynolds number of around 9000.

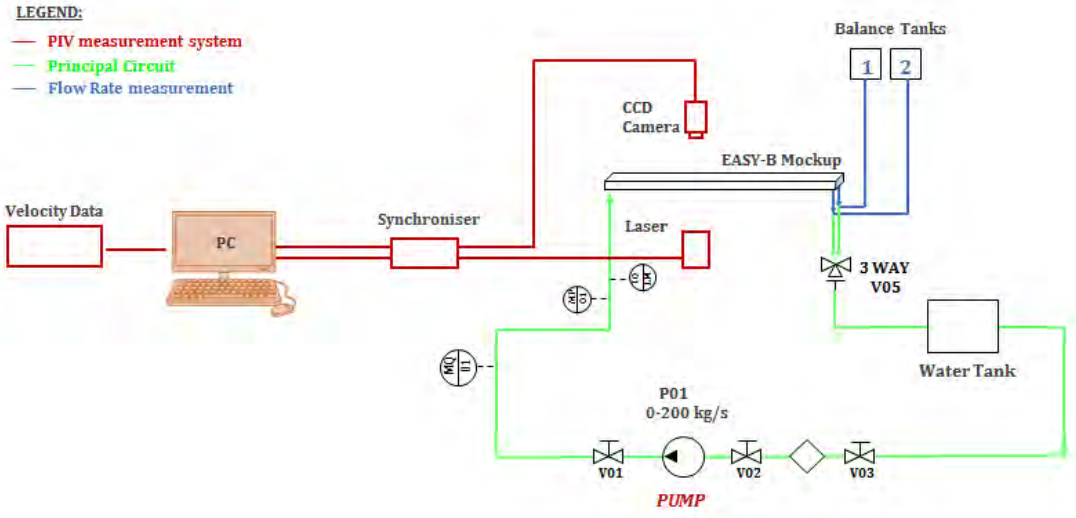

Fig.3. 3 - Experimental schematic circuit EASY-B

Before describing the measurement systems, an overview of experimental channel mockups tested during EASY-B campaign is provided below.

3.1.1. Experimental Mockups

To characterize the flow pattern in SGHE bifurcation system, three different mockups have been considered. Mockup 1, 2 and 3 are shown in Fig.3.4 with their geometrical features (Table 3.3). The engineering drawings of the three EASY-B mockups are reported in APPENDIX III.

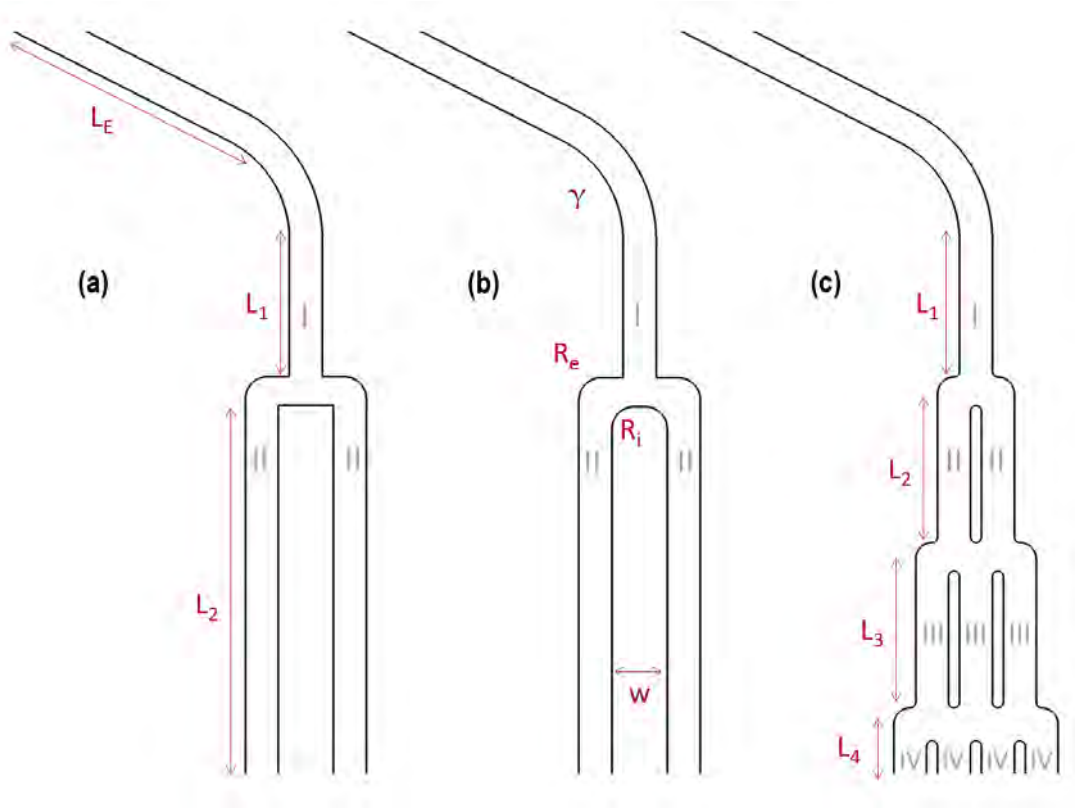

Fig.3. 4 - Mockup geometry: Test sections 1 (a), 2 (b) and 3 (c)

Mockup	Channel Section	L_E	L_1	L_2	L_3	L_4	R_e	R_i	w	γ
	[mm²]	*[mm]*	*[mm]*	*[mm]*	*[mm]*	*[mm]*	*[mm]*	*[mm]*	*[mm]*	*[°]*
1	3x6	160	25	280	-	-	4	0	10	117
2	3x6	200	25	320	-	-	4	4	10	117
3	3x6	200	25	25	25	386	3	1	2	117

Table 3. 3 – Geometrical features of three EASY-B mockups

Mockup 1 and 2 reproduce a basic geometry of one-level bifurcated channel (Fig.3.4a-b). A different structure of the inner fillet characterizes the bifurcation zone, i.e. a sharp fillet for Test Section 1 ($R_{in} = 0mm$) and a circular fillet for the Test Section 2 ($R_{in} = 4mm$).
These two first mockups take part in the first phase of the EASY-B experimental campaign whose aim was to set up a solid experimental database for numerical validation. The characterization of flow separation and recirculation at bifurcation zone and the identification of separation (SP) and reattachment points (RP) in generated channels are the main goals of these experiments.

Test Section 3 corresponds to a three-level bifurcated channel whose geometry represents the final design of sodium channels proposed for ASTRID bifurcation system (Fig.2.58). The objective of this second phase of EASY-B campaign becomes the experimental demonstration of flow distribution performance in ASTRID sodium plate.

Fig.3.5 shows the PMMA experimental mockup of Test section 2. Since PIV system needs two optical accesses to the test section for laser emission and for particle image acquisition, top and lateral sides of the mockup have been polished to achieve an optical quality. As shown in Fig.3.5, the test section is composed by two PMMA demountable plates. The black one at the bottom is required to prevent laser reflections. Inlet/outlet connection pipes are also visible in Fig.3.5.

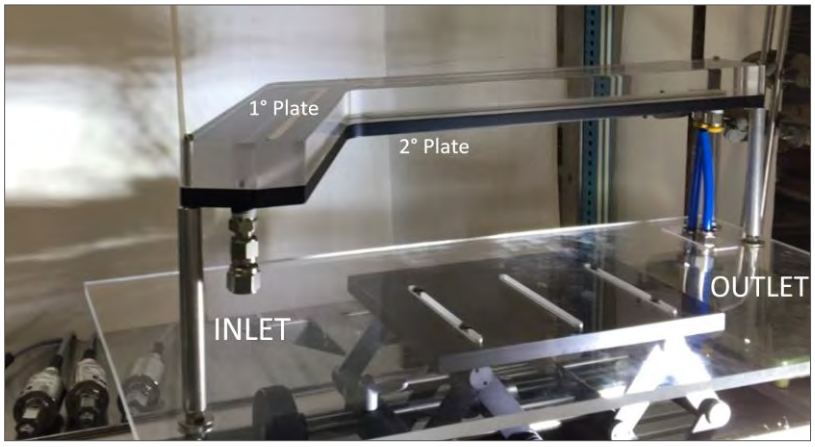

Fig.3. 5 - PMMA Test Section 2

It is worth mentioning that to increase pressure drop downstream the bifurcating channel of Mockup 1 and 2, a 3-way ball valve is installed at the outlet of the two blue pipes in Fig.3.5[10]. The use of a 3-way ball valve type ensures the same variation of pressure drop without introducing any unbalancing between the two generated channels. In the Mockup 3, pressure drops downstream bifurcations are provided by channel section constrictions (Fig.3.20).

[10] The 3-way ball valve induces pressure losses equivalent to the ASTRID SGHE pre-distribution channel downstream the first bifurcation.

3.1.2. PIV measurement system

3.1.2.1. PIV Experimental Measurement Technique Description

The major asset of the PIV technique is its ability to deliver a quantitative and instantaneous measurement of the velocity not only at one point, like conventional measuring technology, but over a whole plane simultaneously. Both visualization and quantification of the 2D flow structure become available [51].

Based upon the definition of velocity, i.e. the first derivative of position with respect to time, the technique consists in measuring the displacement of fluid (Δx) over a given time interval (Δt).
The position of the fluid is imaged through the light scattered by liquid or solid particles illuminated by a laser light sheet. In most applications, such particles are not naturally present in the flow which, therefore, has to be seeded with tracer particles, assumed to be sufficiently small and light to follow local flow velocity.

Fig.3.6 shows a typical standard two-component PIV (2C-PIV) setup.

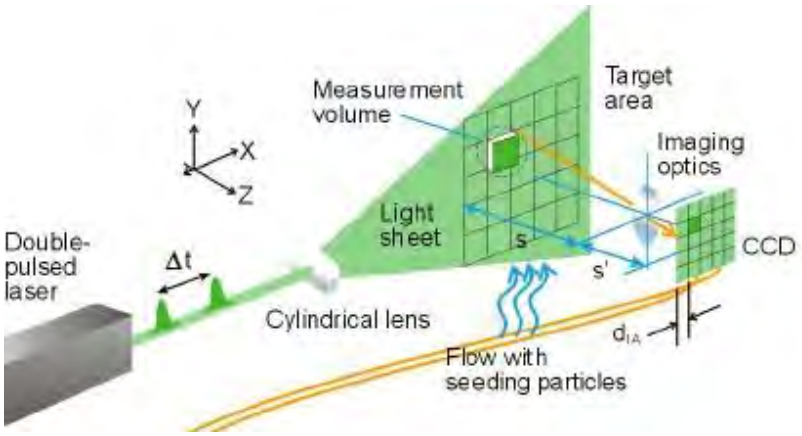

Fig.3. 6 - System components for PIV [51]

A plane within the flow is illuminated twice by means of two superimposed laser light sheets. The light scattered by the particles is recorded on two separate frames on a special CCD camera sensor, placed at 90° with respect to the laser sheet.
For evaluation, the digital PIV recording is divided in small areas called "interrogation windows" where a given number of particles can be detected (Fig.3.6). With the hypothesis that these particles (typically 5 to 20) in a sub-window move with the same

velocity at time t, we can look for the same sub-window at time t+Δt in all directions around the original one. Normally a 16 to 32 pixels zone is used as interrogation domain.

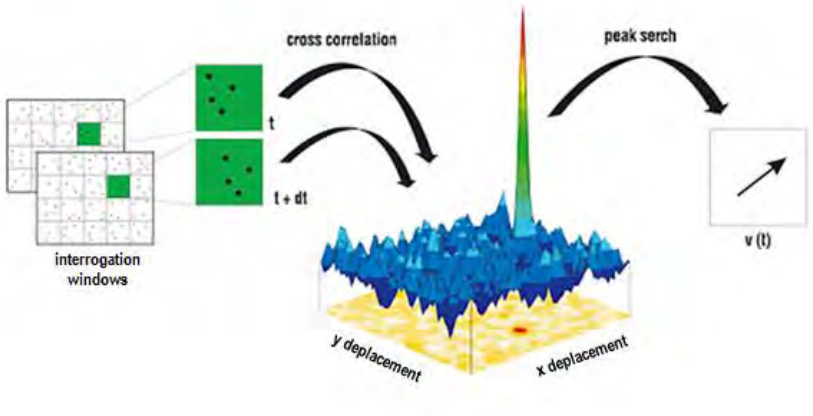

Fig.3. 7 - PIV Image evolution [51]

Using the cross-correlation method, the most likely displacement a time t+Δt is determined. The displacement in pixel unit, multiplied by the calibration factor (pixel unit to metric unit) and divided by time delay (Δt between two frames) will give the actual velocity value. Fig.3.7 shows an example of the cross-correlation procedure, where the maximum value of the cross-correlation (i.e. the most likely velocity) is given by the principal peak in figure, easily detected from the noise. The position of the maximum value related to the center of the sub-window will give the norm, the direction of the velocity vector.

3.1.2.2. PIV equipment in EASY-B experimental campaign

The PIV measurement system, red highlighted in Fig.3.3, is composed by a laser emission system and a particle image acquisition system which are typically on perpendicular plane.

Laser

Double Pulsed laser used was a Litron Nano L PIV Pulsed Nd: YAG Lasers (Neodymium doped Yttrium Aluminum Garnet). This laser emits green light with a wavelength of 532 nm and can produce pulses with a luminous energy of up to a 2x65 millijoules. It is a double cavity Nd-YAG that emits each light pulse from a separate laser. Its pulse frequency is between 0 and 15 Hz. The Litron Laser is shown in Fig.3.8 with its manual 3D displacement system.

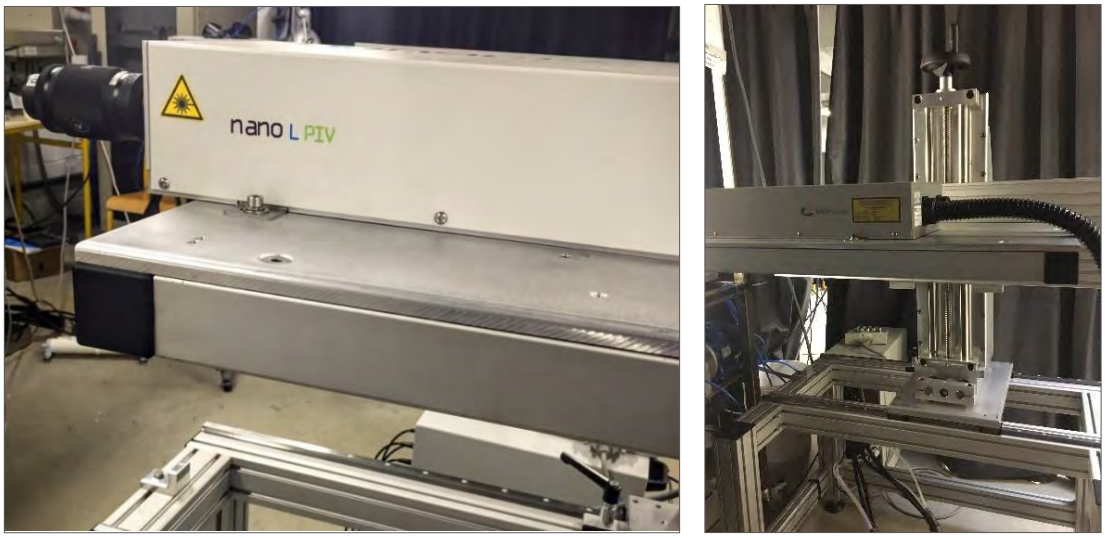

Fig.3. 8 - Nano L PIV Laser (left side) and its displacement system (right side)

The light-sheet optics include cylindrical and spherical lenses, which limit the light-sheet thickness to 0.5 mm. After controlling that the laser sheet was perfectly horizontal and normal to the lateral wall of the channel, the laser sheet alignment at exact position at half-height of the channel has been done using a printed millimeter paper.

Seeding particles

The light of the laser sheet must be scattered in order to be captured by the photo-sensitive device. To do this, the studied fluid must be seeded with tracer particles of small size susceptible to follow the flow faithfully. In addition, it is important remembering that seeding concentration is one of the most important operational parameters and is one of the most common factors responsible for erroneous vectors [52]. If the seeding concentration is too low, there are not a sufficient number of particles to statistically represent the flow which results in a poor correlation between the two successive images. In contrast, increasing the seeding to too high concentration does not always have a beneficial effect. When the number of seeding particles in the flow is increased, the optical transparency of the fluid is reduced [53].

In the first tested mockup (Test Section 1), Rhodamine-B particles provided by Microparticles GmbH (excitation/emission wavelengths: 575 nm/584 nm, 1 μm < diameter < 20 μm) have been selected for PIV measurements. An example of water seeded with Rhodamine B particles is shown on the left side of Fig.3.9.

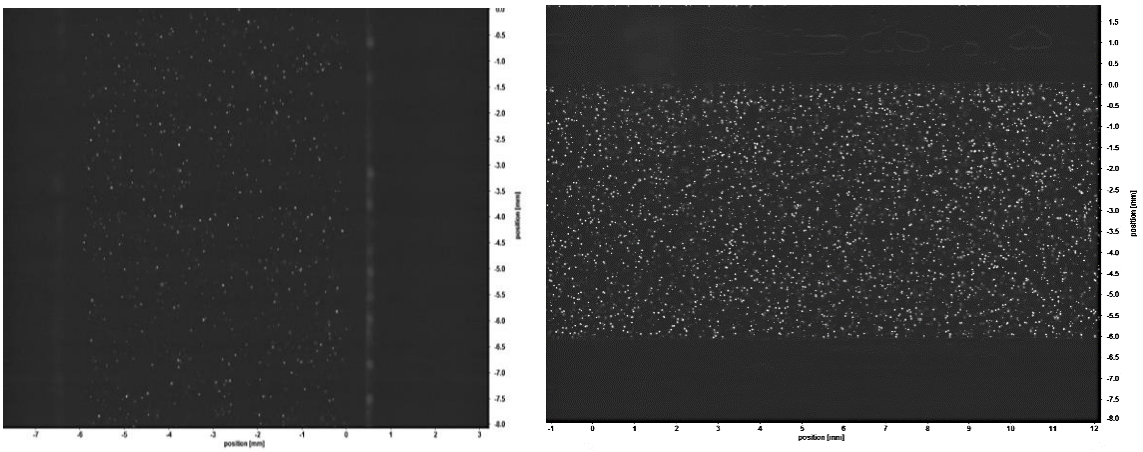

Fig.3. 9 - Rhodamine B: Test section1 (left) and PS FluoRed: Teste Section 2 (right) exposed by the Nd-YAG light sheet

See that, despite the constant addition of seeding particle during PIV experiments, their concentration results too low to have the best suited setting of PIV parameters. This is probably due to the high Rhodamine B particle sedimentation proceed in all the circuit components. As a consequence, high PIV uncertainties have to be expected for PIV measurements of Mockup 1.

For the investigation of remaining test sections (Mockup 2 and 3), Fluo Red particles (excitation/emission wavelengths: 530 nm/607 nm, diameter =10.22 μm), which are characterized by a lower density (1.09 $\frac{g}{cm3}$), have been provided. The exposed PIV plane (Test Section 3) on the right side of Fig.3.9 shows the higher concentration seeding which allows to have between 8 and 12 particles in each 32×32 pixels² interrogation window.

Camera

The image signal acquisition is recorded by a CCD camera (Charged Coupled Device) LaVision Imager pro X with a resolution of 1600 x1200 pixels.

The camera is fitted with a Nikon 105 mm Macro f/8 lens and extended with a series of extension tubes with a total length of 68 mm (Fig.3.10). A 540 nm OD 6 high-pass filter is placed in front of the camera in order to reject laser light and only collect fluorescence light from seeding particles.

The camera displacements are controlled by a three-axis sliding table with manual adjustment in xyz axis (Fig.3.10 right).

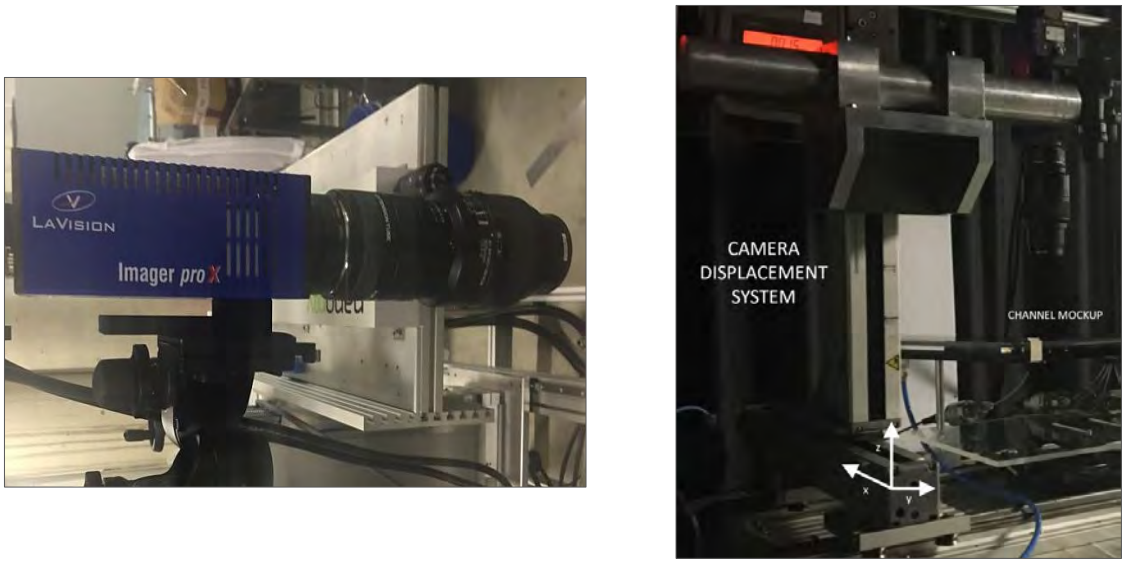

Fig.3. 10 - Imager Pro X Camera (left) and its displacement system (right)

The distance from the CCD Camera to the test section was adjusted according to the location of each test cross-section. As an example, for Test section 3 the dimensional resolution factor is 8.28μm/pixel and an effective 32x32 square pixel interrogation window was used for image processing. According to the fluid velocity in EASY-B test section and the rule that particle displacement between two pulse intervals should be less than 1/4 the effective interrogation area, the pulse interval was set between 15-30 μm.
A synchronizer is used to control the output of the laser pulses and the sequence of image acquisition, which guarantees all parts are coordinated according to the regular order. The software controlling the PIV system and data analysis used was LaVision8.0.

3.1.2.3. Experimental program definition

The EASY-B experimental campaign has been defined taking into account the main objective of PIV experiments, i.e. the validation of CFD numerical models.
Hence, critical zones where complex flow occurs and some inlet sections to study the experimental boundary conditions have been investigated by PIV.

It is important mentioning immediately that all PIV measurements in x-y direction are referred to the velocity field at the half-height of the channel in z-direction (Fig.3.11).

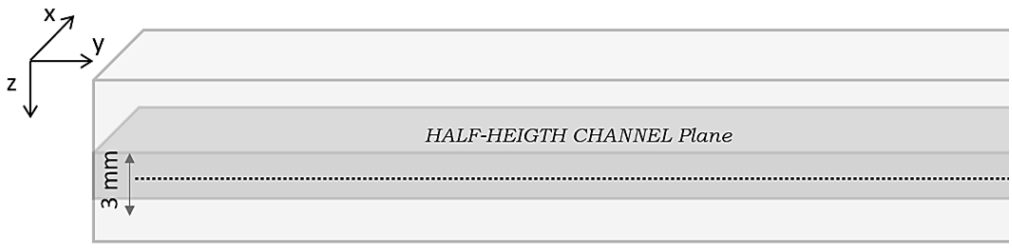

Fig.3. 11 – PIV measurement plane in z-direction

Fig.3.12 shows an overview of all x-y PIV fields analyzed during experiments except the studied inlet sections at 100 mm after the admission. To name each field in Fig.3.12, the following nomenclature has been used:

1. X, Y Z to denote first second and third bifurcation zone;
2. Cardinal numbers to denote each field downstream the bifurcation;
3. L, M and R for left, middle and right channel;
4. L' and R' for the inner left and right channel in the last bifurcation level of Test Section 3.

It can be noticed that only a partial length of channels generated downstream bifurcations are considered in the PIV analysis (about 70 mm downstream bifurcation).

Note that the interrogation windows have different dimensions for each Test Section according to the distance between the CCD camera and the channel mockup.

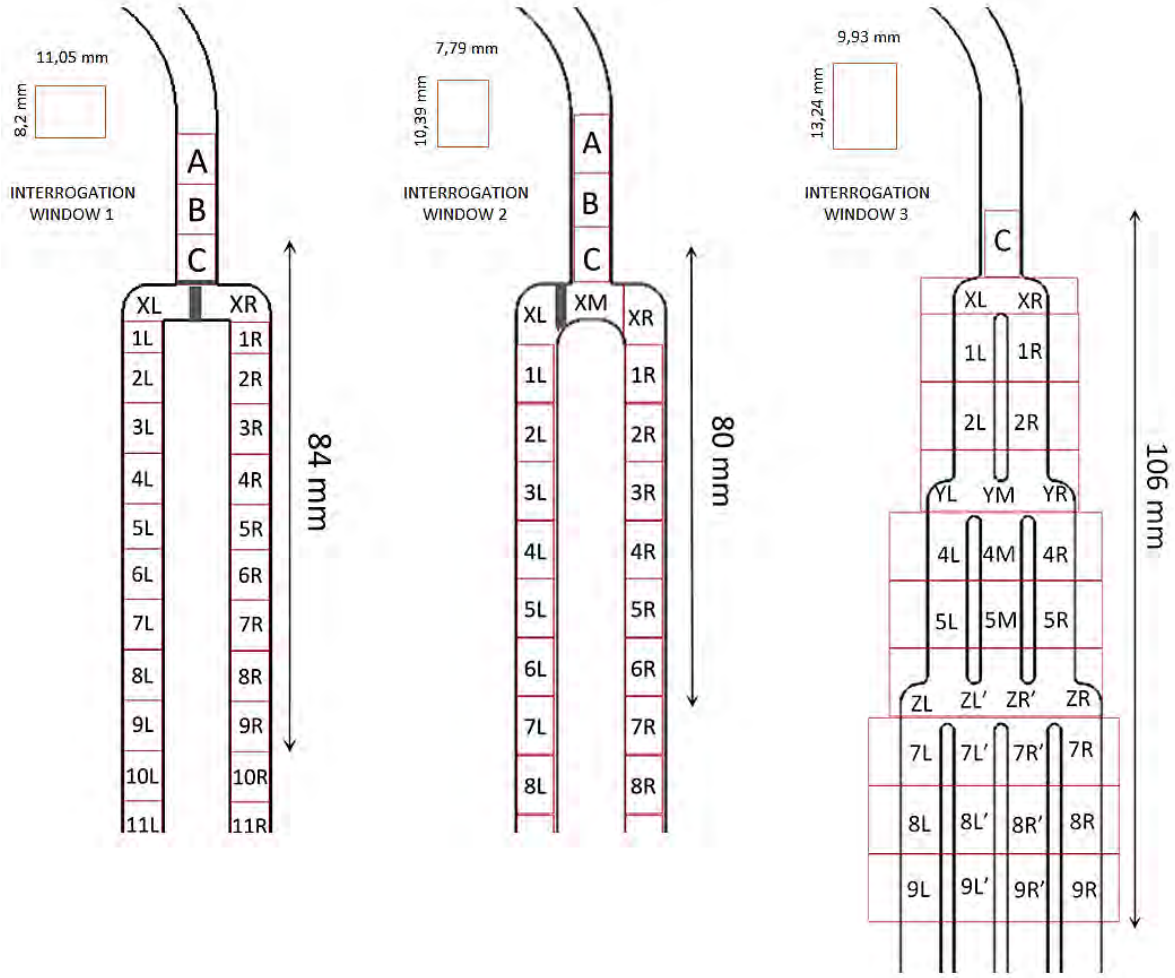

Fig.3. 12 - PIV measurements fields in x-y direction

3.1.2.4. Calibration and testing

An accurate PIV calibration is necessary in order to transform pixel unit in metric unit. Two different methods have been used in the first EASY-B experiment (Test Section 1) to double-check the calibration. The first one is to define, in a captured picture, a line corresponding to the known channel width. As shown in Fig.3.13, LaVision software allows to select two lines overlapping vertical channel walls in a captured picture and to specify their known distance. The resulting camera scale factor for the PIV velocity field (4L-Teset section 1) is 0.006772 mm/pixel.

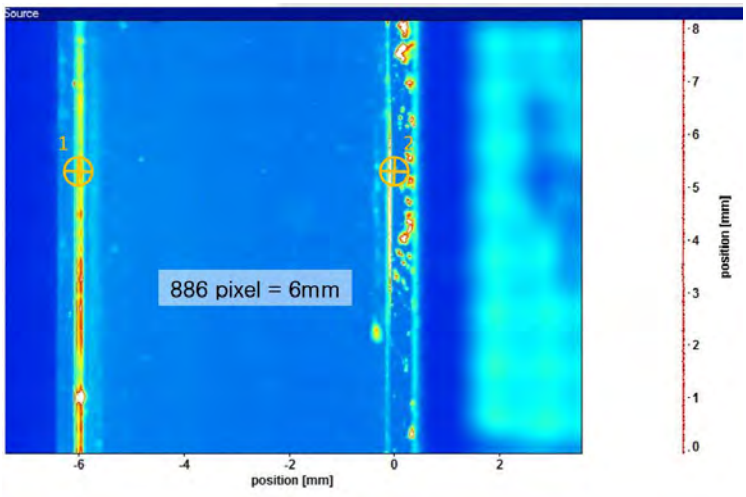

Fig.3. 13 - Camera calibration using channel boundaries

In the second method, the calibration is always done on the boundary geometry of the channel. However, the calibration picture considered in this case is issued from a LaVision post processing (Time series/Sliding Max Over Time) which consists on the overlapping of a captured particle image series [55]. As shown in Fig.3.14, channel walls are now clearly defined by tracer particles cumulated in the final PIV image. The camera scale factor issued by this alternative calibration process for the PIV velocity field (4L-Test Section 1) is 0,006881 mm/pixel.

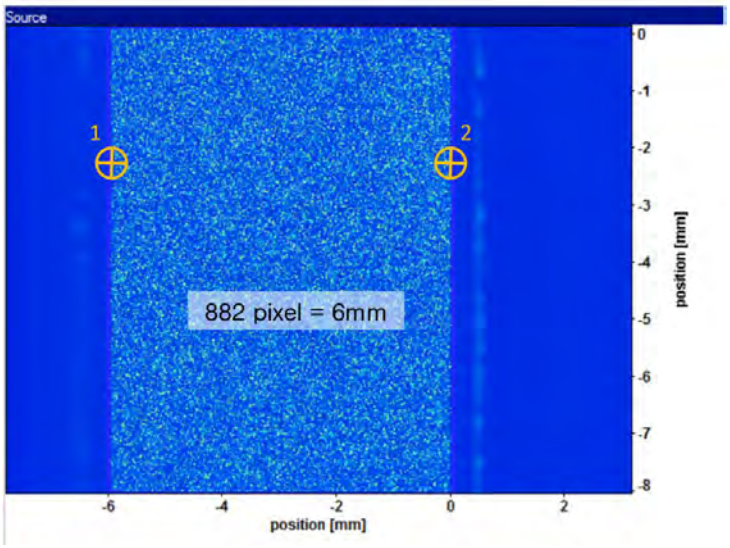

Fig.3. 14 – Camera Calibration using SlidOverTime LaVision Post Processing

The comparison between two calibration methods reveals a very slight difference in the scale camera factor value. The two methods could be considered equivalent. Nevertheless,

in the first method, the light scattered by channel walls and residual pollutant particles could distort the calibration process (Fig.3.13). For this reason, the second calibration method has been considered for all PIV measurements.

3.1.2.5. Measurements statistical convergence

The preliminary analysis of the statistical convergence of PIV measurement in a test plane is extremely necessary. What is ought to be verified is that the number of captured images is sufficiently large to obtain fully converged value of the measured variable.

In the EASY-B experimental campaign, the PIV convergence evaluation study has been checked on some of the investigated planes presenting a more complex flow. Fig.3.15 shows the velocity magnitude contour of Plane 1R in Test Section 2 which is placed immediately after the bifurcation (see Fig.3.12). Here, three different monitoring points have been defined to provide a local convergence analysis using up to 500 images (SONDE 1, 2, and 3 in Fig.3.15).

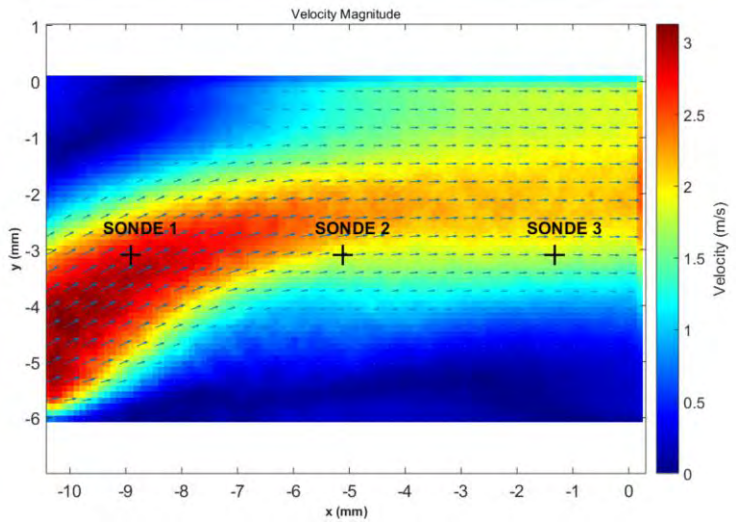

Fig.3. 15 - 1R_Test Section 2 -Velocity field and monitoring points position

For velocity components, u and v, as well as the velocity fluctuations u' and v', the cumulative average has been computed and plotted versus number of images. Fig.3.16 shows an example of their trend at SONDE 2 position.

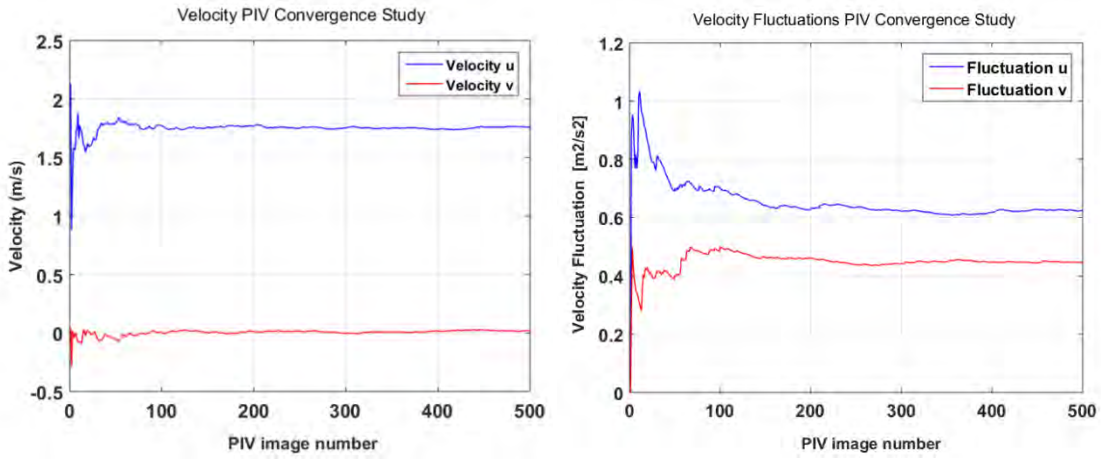

Fig.3. 16 - SONDE 2: u, v velocity (left) and u', v' Velocity Fluctuations (right)

As expected, the oscillation of measured values decreases as the number of images increases. However, while the statistical convergence of u and v velocity is reached after 100 images (Fig.3.16 left), the velocity fluctuations u' and v' need a larger number of images. To ensure the convergence in all other planes for which the convergence evaluation study has not been performed, at least 300 images per measurement have been acquired.

3.1.2.6. Experimental uncertainty evaluation

Three types of uncertainties have been identified during the experimental campaign, specifically the uncertainty due to the PIV data system, the uncertainty due to environmental conditions and the uncertainty due to the measurement plane position.

PIV uncertainty

Regarding PIV uncertainty, although the sources of PIV measurement error are well known, quantifying their corresponding uncertainty continues to be a challenge [56]. There are two different main sources of uncertainty in the experimental results of turbulent quantities. One arises from the statistical sampling of the data and the other from the PIV random error (instantaneous velocity uncertainty). This latter can be caused by hardware/experimental setup (calibration error, background noise, out-of-plane particle motion, particle response, peak locking, non-uniform particle reflection etc.) and algorithm selection (interrogation window size, strong velocity gradients within windows, peak detection scheme, etc.). The available LaVision software does not provide any algorithm able to account for the instantaneous velocity uncertainty of the PIV system.

Nevertheless, it was demonstrated that, when dealing with turbulent flow, the velocity fluctuations are larger than the systematic instantaneous uncertainty due to the PIV acquisition system (single PIV image). This means that the uncertainty quantification of statistical quantities, like time-averaged velocity, is mainly dominated by the finite image number and does not require the knowledge of the uncertainty of the instantaneous velocity fields [57].

In the present analysis, the uncertainties have been then calculated by applying the PIV uncertainty methodology of Sciacchitano and Wieneke [57].
The PIV uncertainty of velocity is defined as:

$$\delta V_{PIV} = \frac{\delta V}{\sqrt{N_{eff}}} \tag{7}$$

where N_{eff} is the effective number of independent PIV images and δV is the standard deviation of mean velocity.
Note that, in EASY-B experiment the low acquisition frequency ($f = 9Hz$) provides measurements of the instantaneous velocity field from which time-independent flow statistics can be derived ($N_{eff} = N$).

For each test cross-section, 300 sample of transient velocity field have been captured in the experiment. The time averaged velocity field of each test cross-section is then obtained through batch processing. The standard deviation value of velocity components is defined as:

$$\Delta u_{i,j} = \sqrt{\frac{\sum_{k=1}^{300}(u_{i,j,k} - \overline{u_{i,j}})^2}{299}} \text{ and } \Delta v_{i,j} = \sqrt{\frac{\sum_{k=1}^{300}(v_{i,j,k} - \overline{v_{i,j}})^2}{299}} \tag{8}$$

where $u_{i,j,k}$, $v_{i,j,k}$ are denoted as the x-direction and y-direction velocity component of measuring point *(i, j)* in frame *k* and $\overline{u_{i,j}}$, $\overline{v_{i,j}}$ are denoted as time average value of velocity components.
The standard deviation of velocity δV is defined as:

$$\delta V = \sqrt{{\Delta u_{i,j}}^2 + {\Delta v_{i,j}}^2} \tag{9}$$

The highest relative measurement error of average velocity which has been measured all over the EASY-B experiments is around 1,12 %.

Environmental condition uncertainty

To quantify the influence of experimental conditions which may vary over time during the measurements, such as a degraded optical quality of the test section, in-day temperature variation and so on, a repeatability test has been performed. Four identical measurements at the same plane position at various times of the day and various days have been acquired.

The uncertainty has been evaluated based on the mean difference between the four measurements. The standard deviation has been then calculated as the mean difference was distributed on uniform probability density function, i.e.:

$$\delta V_{Exp.Conditions} = \Delta v_{mean}/\sqrt{3} \quad (10)$$

Note that, the max difference between four measurements should be considered as reference value for the PIV field. However, to neglect some local peak differences due to local defects of the mockup or PIV parameters, a mean value is preferred for the estimation of environmental condition uncertainty.

Measurement plane uncertainty

Finally, to evaluate the uncertainty due to the plane position, identical PIV measurements have been performed on adjacent planes shifted up and down by 0.5 mm from the reference one. The position of the plane enlightened by the laser sheet (0.5 mm thickness) has been manually monitored by moving the mockup in z-direction (Fig.3.11). The displacement device in Fig3.17, on which the mockup was installed, has been used for this purpose.

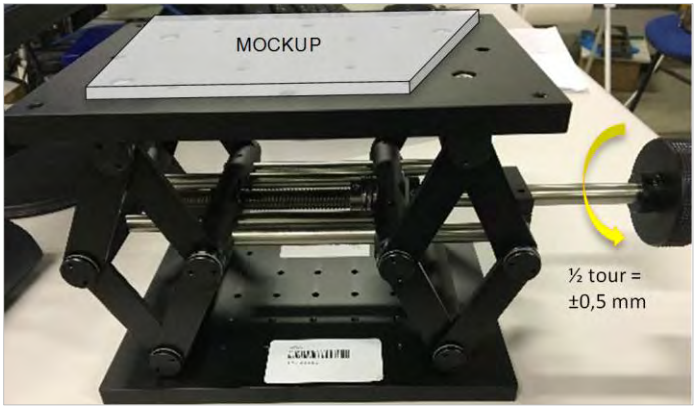

Fig.3. 17 – Mockup displacement device

Again, the uncertainty has been evaluated based on the mean difference between the three measurements. The standard deviation has been then calculated as the mean difference was distributed on uniform probability density function.

$$\delta V_{Position} = \Delta v_{mean}/\sqrt{3} \quad (11)$$

Table 3.4 shows the results of the overall uncertainty analysis for one of the most challenging measurement plane of the bifurcating channel, i.e. *Plane 1R- Test Section 2* in Fig.3.12. Here, a more complex flow characterized by strong velocity gradients occurs.
The total uncertainty δ is calculated as the combined standard deviation determined by adding the variance of each source of uncertainty.

Test Section 2	Mean Value	PIV Uncertainty	Environmental Condition Uncertainty	Plane Position Uncertainty	Total Uncertainty δ
1R	1.12 m/s	0.028 m/s	0.074 m/s	0.065 m/s	$\pm$0.124 m/s

Table 3. 4 – PIV experimental uncertainty evaluation

3.1.2.7. Flow Inlet Conditions

According to the final goal of validating the numerical model used in CFD simulations, it is important to study experimentally the flow inlet conditions. The same boundary conditions have to be ensured in numerical simulations to perform a proper comparison.

The experimental mockup has been designed with an inlet channel length of $50d_h$ (entrance length = $50d_h$) and an inlet Reynolds of 9000. A fully developed turbulent flow is therefore expected before flow reaches the bifurcation [44]. Fig.3.18 shows an example of the measured velocity profile at 18 mm from the inlet of Test Section 2. A typical velocity profile for fully developed turbulent flows with a sharp drop near the channel wall can be easily recognized in the figure.

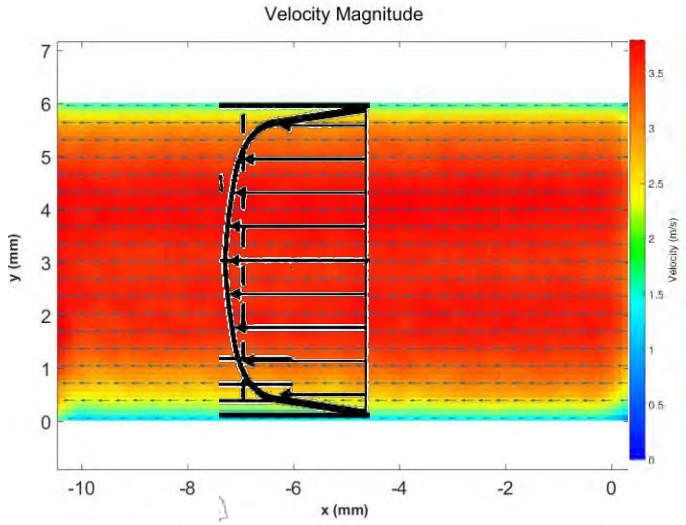

Fig.3. 18 – Velocity field at 18mm from the inlet admission – Test Section 2

3.1.3. Pressure measurement system

To get information about mass flow distribution between bifurcation generated channels, a differential pressure measurement system has been conceived and installed on EASY-B mockups. It consists on evaluating the mass flow rate per channel with the measurements of pressure losses (ΔP) for a fluid element (ΔL) of the channel.

KELLER Series 41-X capacitive pressure transmitters are then installed along generated channels at the last stage of each Test Section (see Fig.3.19 for explanation). The position of pressure sensors is detailed in the schematic drawing in Fig.3.20. Note that, the pressure transmitters (P_1-P_2 and P_3-P_4) in Test Section 2 have been shifted downstream the bifurcation with respect to Test Section 1. In this way, the first two sensors are moved away from the fluid region at high recirculation after bifurcation where the static pressure measurements could be affected by the complex flow (integration of dynamic pressure). During the first campaign (Mockup 1), pressure transducers at the position P1 and P2 revealed more important fluctuations than the others.

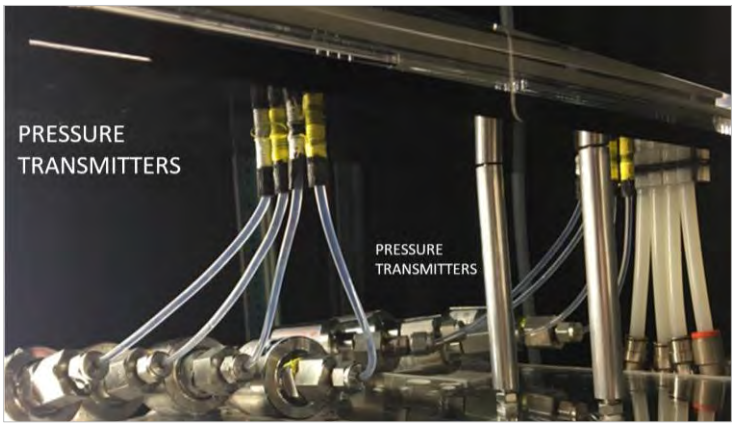

Fig.3. 19 - KELLER Pressure transmitters

Mockup 1	Mockup 2	Mockup 3
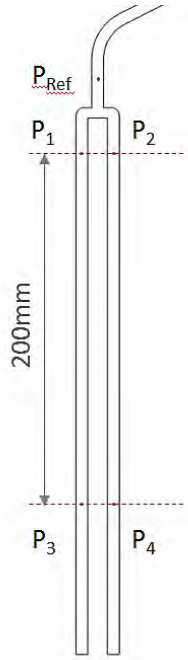	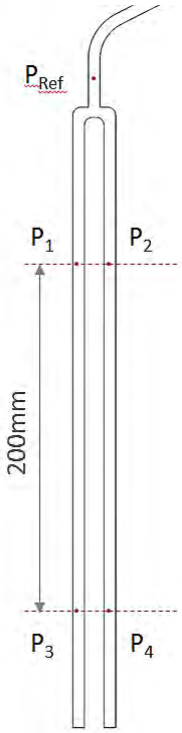	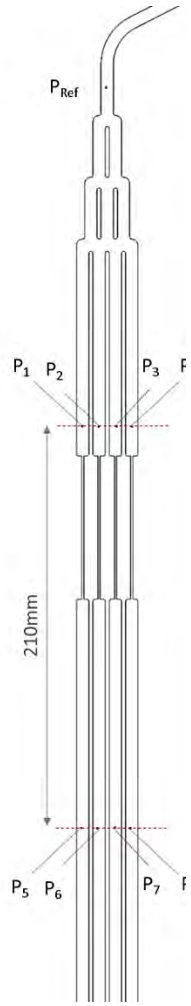

Fig.3. 20 - Pressure transmitter position: Mockup 1, Mockup 2 and Mockup 3

3.1.3.1. Capacitive Pressure Transmitter Description

The working principle of a KELLER capacitive pressure transducer is illustrated in Fig.3.21. As shown in the figure, the capacitive transducer has a static plate and a deflected flexible ceramic diaphragm that are separated to each other by a dielectric. When a force is exerted to the outer side of the diaphragm, the distance between the diaphragm and the static plate changes. The applied pressure produces a change in capacitance.
The high frequency capacitance detector circuit uses a high-frequency AC excitation signal to measure the difference in capacitance between the two plates, translating that into a 4-20mA DC signal. This current becomes the output signal of the pressure transmitter.

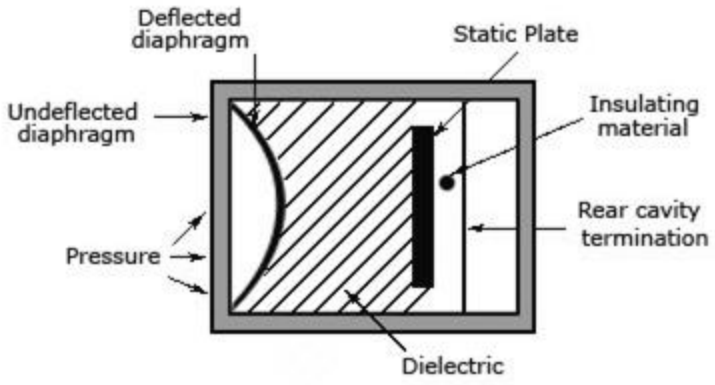

Fig.3. 21 - Working principle of a capacitive pressure transducer

Table 3.5 summarizes the performance and other technical characteristics of KELLER Series 41-X capacitive pressure transmitters used in the EASY-B experiment.

Specifications

	Standard FS Pressure Ranges			
PR-41 X (relative) PD-41 X (diff.)	30	100	300	mbar
Overpressure	300	1000	1500	mbar
Neg. Overpressure	30	100	300	mbar

	2-Wire	3-Wire
Supply (U_B) 41 X	8…28 VDC	13…28 VDC
Supply (U_B) 41 X Ei	10…30 VDC	15…30 VDC
Analog Output (scaleable)	4…20 mA	0…10 V
Load (kΩ)	<(U_B-$U_{B\,min.}$) / 20 mA	≥ 100
Error Band typ.*	± 0,1 %FS	± 0,2 %FS
Error Band max.*	± 0,2 %FS	± 0,3 %FS

* Within the compensated temperature range

Stability	FS ≥ 100 mbar: ± 0,1 %FS	FS ≤ 100 mbar: ± 0,1 mbar
Operating Temperature	-20…80 °C	
Compensated Range	10…50 °C	

Table 3. 5 - Technical characteristics of KELLER Series 41-X capacitive pressure transmitters

To allow pressure measurements in EASY-B experiments, Keller Capacitive pressure sensors have been calibrated on its maximum Standard FS Pressure range of 0-300 mbar.

3.1.3.2. Experimental uncertainty evaluation

To assign the uncertainty values to the measured pressure data, the error cumulated in the entire pressure measurement process need to be considered.

Fig.3.22 illustrated the pressure measurement chain in EASY-B experiments.

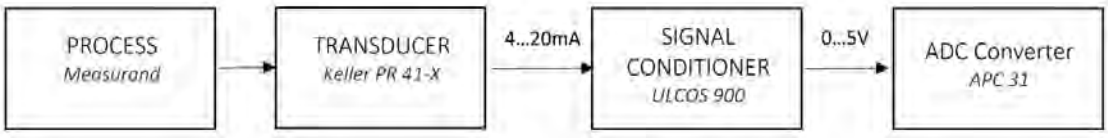

Fig.3. 22 - Pressure measurement chain

The first principle of measurement uncertainty is that the measurand[11] must be correctly and unambiguously defined. In EASY-B, the pressures transducers are expected to measure the static pressure in the bifurcating channel. At the beginning of this section, it

[11] Measurand: A quantity intended to be measured.

was already mentioned the problem of measurement perturbation due to the presence of complex flow, i.e. the integration of dynamic pressure in the measurand. However, the uncertainty of the "process measurand" remains difficult to estimate.

The measurement process in Fig.3.22 continues with the KELLER capacitive transducer which transforms the mechanical energy of the ceramic diaphragm into electrical signals (Output signal: 0-20mA). This transmitter, scaled for pressure measuring range 0-300 mbar, is characterized by an overall error band of ±0.1 % for the temperature compensation range of 10-50 °C. This means an error of $\delta p = \pm 0.03\ mbar$.

The generated current signal is then amplified and converted into a voltage signal (0-5 V) by the ULCOS 900 D1 device which, at the same time, filters and cleans the signal (Fig.3.22). Since the amplifier relationship between input and output is linear, the associated error can be neglected.

Finally, the voltage analog (continuous) signal is transformed into a digital signal that can be processed by the APCI-311 Data acquisition card (Fig.3.22). The ADC for the DasyLAB digitizer has a 12-bit analog-to-digital quantizer that quantifies an analog data sample into 1 of 4096 possible digital values. The resulting error (ADC resolution) is δ_{ADC} ±1.22 mV (0.0122%).

The uncertainty of the combined measurement system has been calculated using a RSS method, i.e.:

$$\delta_{Pressure\ Chain} = \sqrt{\delta p^2 + \delta_{ADC}{}^2} \cong 0.1001\ \% \qquad (12)$$

It can be concluded that the measurement chain provides a very small contribution to the total pressure error.

To complete the estimation of pressure data acquisition uncertainties, experimental errors due to the environmental conditions and sensor installation effects (Zero signal) need to be taken into account.
In this sense, three identical measurements, at the same inlet Reynolds at various times of the day, have been acquired for all test sections. The uncertainty has been evaluated based on the maximum difference between the three measurements. The standard deviation has been then calculated as the maximum difference was distributed on uniform probability density function. As an example, the value of the estimated standard deviation at the position P_{Ref} of Test Section 2 (Fig.3.20) is $\delta p_{Env.Condition} \approx 1.33\ mbar$ (0.605%). This high

value is essentially due to the variation of the zero signal up to ±0.55 %FS during daily measurements. The final pressure uncertainty is calculated as the combined standard deviation determined by adding the variances of each source of uncertainty (Table 3.6).

Test section 2	Mean Value	Data Acquisition Uncertainty	Environmental Condition Uncertainty	Total Uncertainty δ
P_{ref}	219 mbar	0.22 mbar	1.33 mbar	± 1.34 mbar

Table 3. 6 - Pressure uncertainty evaluation

3.1.4. Mass flow measurement system

3.1.4.1. Precision Balance Description

The electronic weighing system is composed by two electronic balances which measure the fluid mass flowing in each tank placed at the outlet of the channel, i.e. m_1 and m_2 (Fig.3.23).

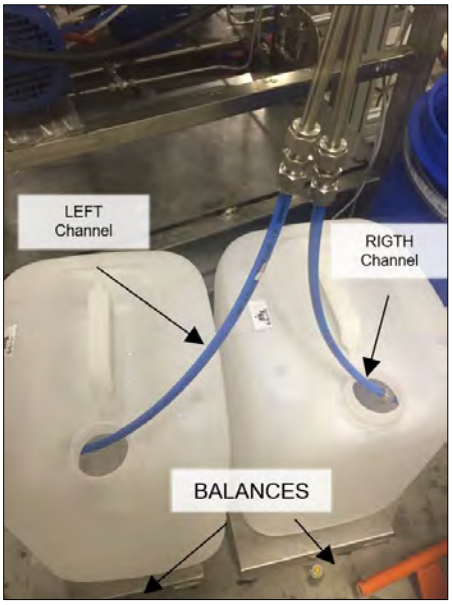

Fig.3. 23 - EASY-B electronic weighing system

Sartorius Combics 1 CAW1P*L precision balances with a weighing capacity of 15 kg and a readability of 1 g have been used in EASY-B experiments (Fig.3.24).

Fig.3. 24 - Sartorius Combics 1 CAW1P*L precision balances

The time of filling tank, t, is measured by a digital chronometer automatically triggered by the operator.

3.1.4.2. Experimental uncertainty evaluation

Two types of uncertainties can be identified in the measurements of mass flow rate for each channel, i.e. the uncertainty due to the data acquisition system and the uncertainty due to the environmental conditions and the human operator.
The uncertainty value related to the data acquisition system has been obtained from the following equation:

$$\delta\dot{m}_{Data\ Acquis.} = \delta\left(\frac{m}{t}\right) = \left[\left(\frac{\delta\dot{m}}{\delta m}\delta m\right)^2 + \left(\frac{\delta\dot{m}}{\delta t}\delta t\right)^2\right]^{\frac{1}{2}} = \left[\left(\frac{1}{t}\delta m\right)^2 + \left(-\frac{m}{t^2}\delta t\right)^2\right]^{\frac{1}{2}} \quad (13)$$

For instance, the measured accuracies of the primary measurements (mass and time) to the derived parameter $\dot{m}_1$, which corresponds to left channel of Mockup 2, its associate uncertainty can be estimated as $\delta\dot{m}_{1_{Data\ Acquis.}} \approx 3.31 \times 10^{-6}\ \frac{kg}{s}$.
To take into account the uncertainties due to the experimental conditions and the human operator, a repeatability test has been performed. Five identical measurements of mass flow rate at the same inlet Reynolds at various times of the day have been acquired. Again, the uncertainty has been evaluated based on the maximum difference between the five measurements. The standard deviation is estimated to be $\delta\dot{m}_{\ Env.cond.} \approx 2.24 \times 10^{-6}\ \frac{kg}{s}$.

Note that during the experimental procedure, a filling time of around 5 minutes is considered to reduce the weight of operator error in starting and stopping the chronometer (human reaction time) with respect to the final value of mass flow rate.

The final mass flow uncertainty is calculated as the combined standard deviation determined by adding the variances of each source of uncertainty (Table 3.7).

Test section 2	Mean Value	Data Acquisition Uncertainty	Environmental Condition Uncertainty	Total Uncertainty δ
$\dot{m}_1$	22,19233 g/s	0,00331 g/s	0,00224 g/s	$\pm$ 0,00399 g/s

Table 3. 7 – Mass flow uncertainty evaluation

3.1.5. Mass flow data from pressure measurements

Once collected pressure data from pressure transducers (ΔP) and mass flow data from the electronic weighing system ($\dot{m}$), a mathematical correlation between two variables can be estimated ($\dot{M} = f(\Delta P)$). This empirical correlation based on EASY-B experimental data allows evaluating the mass flow rate per channel by means of pressure losses (ΔP) measurements for a fluid element of the channel during PIV flow characterization.
Note that, other general correlations between pressure drop and the mass flow rate exists in literature, such as the Darcy-Weisbach's formula which can be expressed in Pascal as follow [58]:

$$\Delta P = P_1 - P_2 = 4 f \frac{\Delta L}{D} \frac{\dot{m}^2}{2\rho} \quad (14)$$

where D is the inner tube diameter, ΔL the tube length for ΔP measurement, f the Fanning friction factor, ρ the density and $\dot{m}$ the mass flow rate. Nevertheless, the equation Eq.14 cannot be applied to the specific case of EASY-B experiment. In fact, if geometrical values like diameter D or channel length L in Eq.14 can be easily obtained, the friction factor value, which depends on the roughness of the manufactured channel, remains difficult to estimate. The need of a new correlation is clear.

Linear or a second degree of polynomial methods are used to fit a series of 5 experimental data points for each generated channel branch in EASY-B experiment.
The uncertainties of data fitting methods δf, are provided and combined to data uncertainties. Note that, mass flow data are supposed to be not subject to uncertainty ($\delta \dot{m} \cong 0$). This assumption is suitable in view of the negligible value of balance system uncertainty estimated in Section.3.1.4.2.

The empirical correlation is here computed for Test Section 2 of EASY-B experiment. Fig.3.25 shows pressure experimental data plotted against mass flow rate data for both generated channels ($\dot{m}_1$ and $\dot{m}_2$).

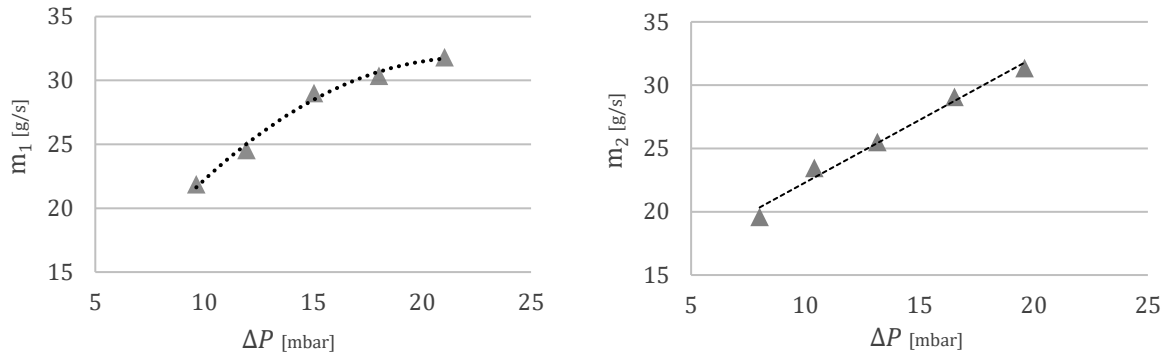

$$\dot{M}_1 = -0.0647\,\Delta P^2 + 2.8683\,\Delta P \qquad R^2 = 0.9907$$

$$\dot{M}_2 = -0.9861\,\Delta P + 12.453 \qquad R^2 = 0.9832$$

Fig.3. 25 – Empirical correlation between pressure drop and mass flow – Test Section 2

The resulting R-squared values of around 0.99 demonstrate how well the two models fit the experimental data which are very close to the fitted regression line.

The error which has to be accounted into the final result of mass flow rate $\dot{M}$ can be expressed as follow:

$$\delta\dot{M} = \sqrt{\delta f^2 + \delta\Delta P_f{}^2} \tag{15}$$

where δf is the uncertainty of correlation and $\delta\Delta P_f$ is the propagation of the pressure drop uncertainty.

The δf uncertainty is quantified by assuming the distance between data and fitted line normally distributed, i.e.:

$$\delta f = \sqrt{\frac{\sum_{i=1}^{N}(\dot{m} - f(\Delta P))^2}{N - p}} \tag{16}$$

Note that the difference at the denominator of Eq.16 corresponds to the number of data point measurements N minus the number of parameters calculated from these measurements, i.e. $p = 2$ for the quadratic regression $\dot{M}_1$ and $p = 1$ for the linear regression $\dot{M}_2$ (Fig.3.25).

The $\delta\Delta P_f$ uncertainty is given by:

$$\delta\Delta P_f = \dot{M}' \cdot \delta\Delta P \quad (17)$$

For the specific correlation in Fig.3.25, the total uncertainty, are respectively $\delta\dot{M}_1 = \pm 1{,}34\ g/s$ and $\delta\dot{M}_2 = \pm 1{,}37\ g/s$.

3.1.6. Conclusion

An experimental test bench has been implemented to test flow in bifurcating channels. It allows measuring pressure drop, mass flow rates and acquiring PIV measurements. The uncertainty analysis shows the accuracy level of each measurement. A trustful experimental database is provided for the numerical model validation.

Particularly, PIV experimental data on the Test Section 1 and 2 will allow checking the best numerical model which correctly describes the development of the velocity profile in generated channels downstream bifurcation. In addition, the pressure system and the EASY-B empirical correlation will provide an additional validation in term of flow distribution performance of tested mockups.

PIV experimental data of Test Section 3 will allow verifying the ability of the CFD model to predict the flow field in the best suited design option for ASTRID sodium channels.

3.2. DANAH: Distribution Analysis of Na in Headers

DANAH experimental facility, whose name stands for "*Distribution Analysis of Na in Headers*", has been developed at the CEA Cadarache for the study of sodium flow distribution in the global geometry of ASTRID SGHE module.
The main goal of the experimental campaign is to analyze the evolution of the sodium jet in different configurations of the inlet header evaluating their effect on the flow distribution between channels.
For this purpose, DANAH mockup has been conceived to enable flow measurements at the inlet header for the characterization of the three-dimensional jet flow and, at the same time, flow measurements at the outlet of the channel bundle for the estimation of the resulting flow distribution.

The mockup is composed by three demountable units entirely made in PMMA, i.e. the inlet header, the bundle channel and the outlet header (Fig.3.26). It represents half of the SGHE module, at scale 1:1 for the inlet header.

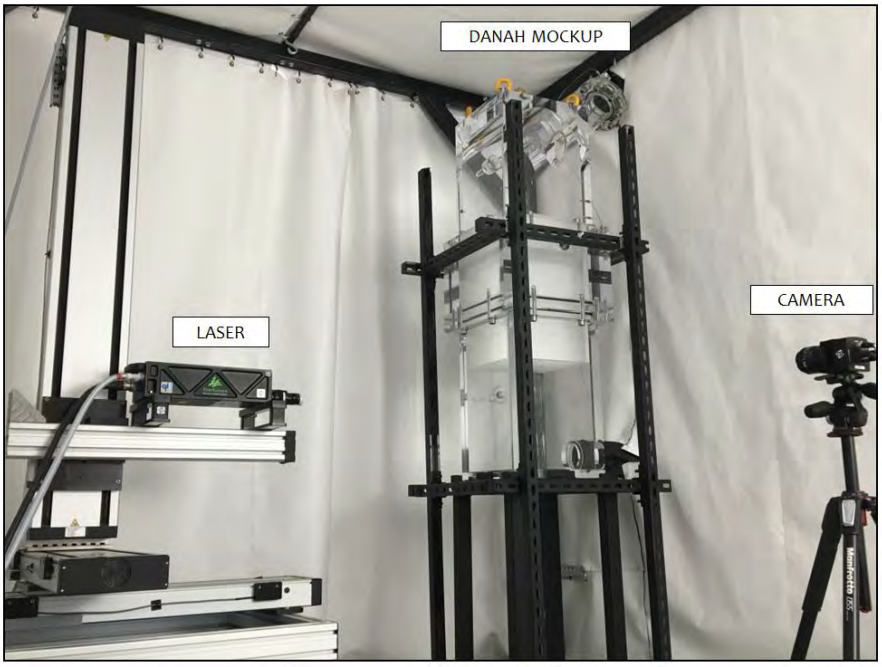

Fig.3.26 - DANAH Experimental Facility

Before detailing each unit of DANAH mockup, an overview of the entire experimental circuit which includes the thermal-hydraulic loop water loop and a PIV system is presented below.

Fig.3.27 shows a schematic drawing of DANAH experimental facility.

DANAH mockup is directly connected to the PLATEAU [50], the CEA thermal-hydraulic loop which gathers all the hydraulic loops used for the qualification of the ASTRID components (Green circuit in Fig.3.27).

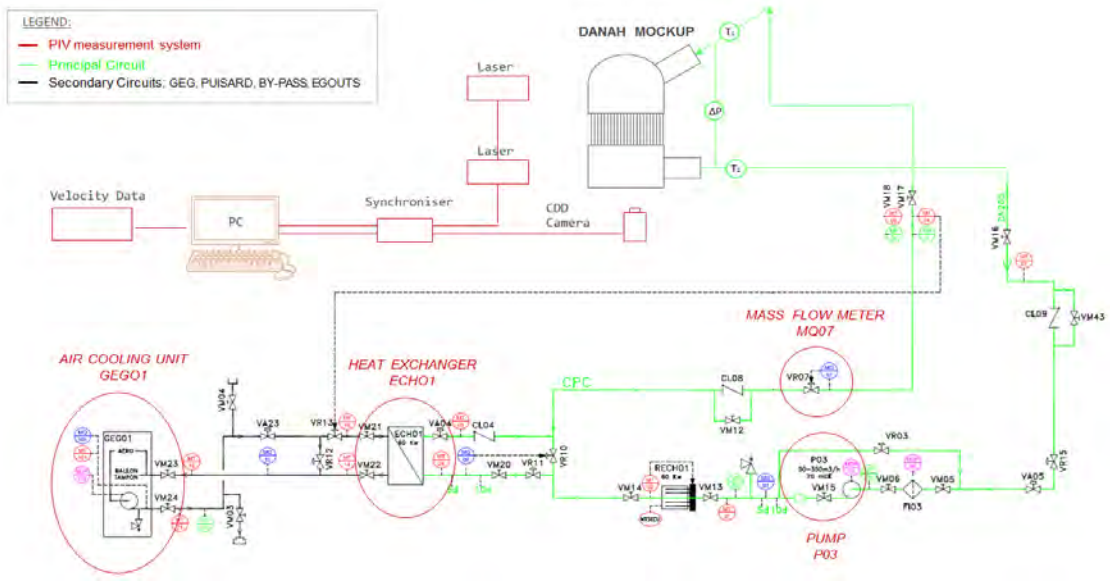

Fig.3. 27 - Experimental schematic diagram and PIV Measurements System

In the closed-loop, demineralized water at ambient temperature and atmospheric pressure is supplied by a centrifugal pump to the inlet header of DANAH mockup. The pump *P03* in the loop is a horizontal centrifugal pump with a capacity range of 0-350 m3/h. The *MQ07* Coriolis mass flow meter (capacity range 0-1000 m3/h) was calibrated to work in the range of 0-350m3/h. A piezometric differential pressure transducer measures pressure drop between inlet and outlet tubes of DANAH mockup. Temperature sensors (PT100 sensor - range A 0-100°C) monitored fluid temperature at the inlet and outlet of DANAH mockup.

Fluid temperature control during experiments is assured by the cooling unit *GEOG1* and the plate heat exchanger *ECHO1* (40 kW) in Fig.3.27.

3.2.1. Experimental Mockup

A typical configuration of the DANAH mockup, totally assembled and installed on a specific support, is shown in Fig.3.26. The three principal units of the mockup can be easily

distinguished in the figure. Their geometrical features and technical detail are reported on engineering drawings in APPENDIX III.

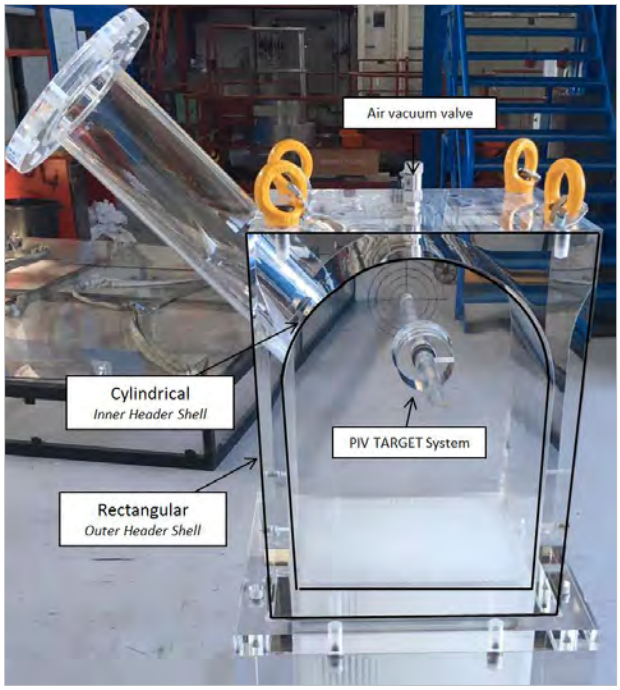

Fig.3. 28 – Inlet Header (1)

The inlet header (1) in Fig.3.28 has a cylindrical shape and it has been obtained from a solid rectangular block of PMMA by removing material. An external structure of square-section incorporates the cylindrical surface of the inlet header minimizing shell curvature and refraction problems during PIV measurements.
To be rigorous and to totally ensure the absence of light refractions, the layer between the square external section and the inlet header should be filled by a fluid with the same refractive index of the PMMA material (n ~ 1.5). This modification was considered not necessary for the experimental apparatus used in this study as the curvature radius of the inlet header is large enough to avoid high refraction effects.

The same design concept has been considered for the second inlet header which has been tested in DANAH experiments (Section 3.2.3). Its geometry characterized by a double cross-cylinder dome represents the real design header which will be installed on the SGHE module because of its better resistance to the external pressure.

Fig.3. 29 - Outlet Header

With the same objective to avoid light reflections, the outlet header has been conceived and designed as a rectangular box which is not representative of the real design of Na outlet header in ASTRID SGHE module (Fig.3.29). Here, with respect to the inlet header, the complexity of PIV analysis at zones very close to the channel outlets requires optimal light conditions to achieve PIV measurement goals. In this sense, the dimensions of the outlet header are the results of a preliminary CFD calculations ensuring an unperturbed flow at the outlet of the bundle.

Both inlet and outlet header are then polished above all the surface to obtain optical quality PMMA test sections.

Fig.3.29 also shows the calibration system in DANAH experiment which is composed by a 2D target fixed on a Plexiglas sliding stick. The sliding stick is mechanically coupled through a leakage-free system with the lateral wall of the header. This system allows to place the target in the laser light sheet plane during calibration and to retire it during measurements.
The target, shown in Fig.3.30 has a circular Plexiglas surface with a radius of 10 cm. A black cross and concentric circular lines (1 cm) with known (X, Z) locations are graved on it. Rectangular targets made of stainless steel are also used in DANAH campaign (Fig.3.37).

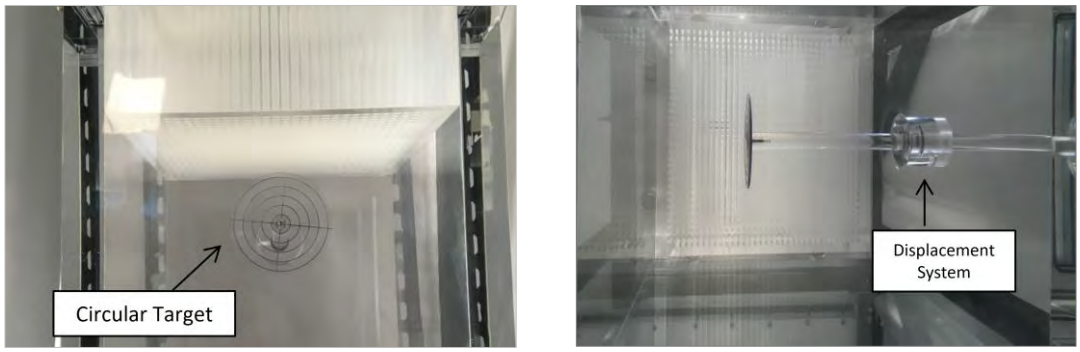

Fig.3. 30 – PIV target (left) and its displacement system (right)

Fig.3.28 also shows the automatic air vacuum valve which is installed on the top of the inlet header to discharge the volume of air from the pipeline system when the mockup is initially water filled.

DANAH bundle channel is shown in Fig.3.31-32. The solid unit, entirely made in PMMA, is composed by 35 plates, each containing 32 channels of 3x6 mm² cross section. Its manufacturing process has been a real challenge in the view of the small size of channels and the leakage-free bonding of plates necessary to avoid channel clogging. Fig.3.31 also shows a single plate before the assembly of the entire bundle via a polymeric fusion process.

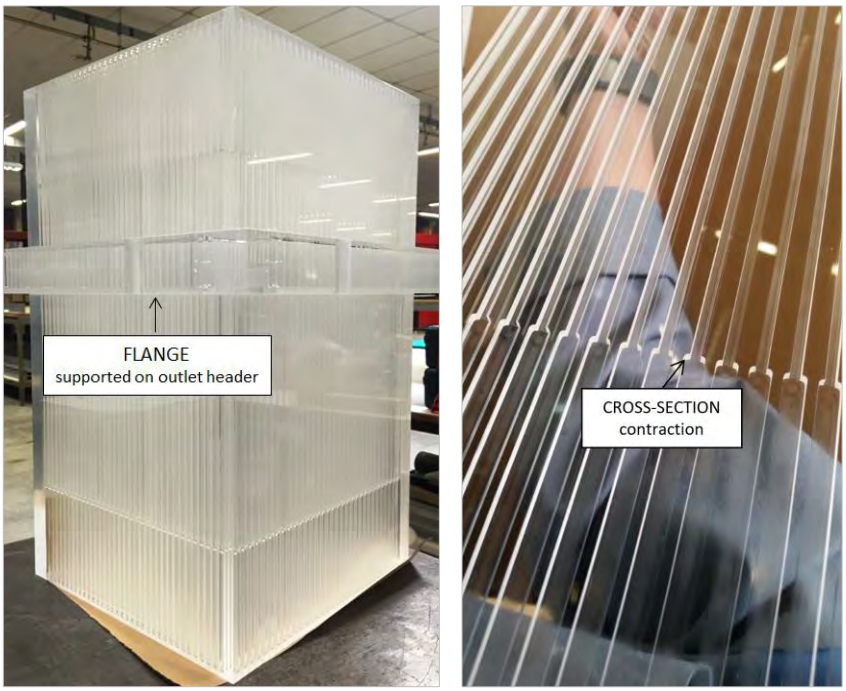

Fig.3. 31 – DANAH bundle channel (left) and detail on a single plate (right)

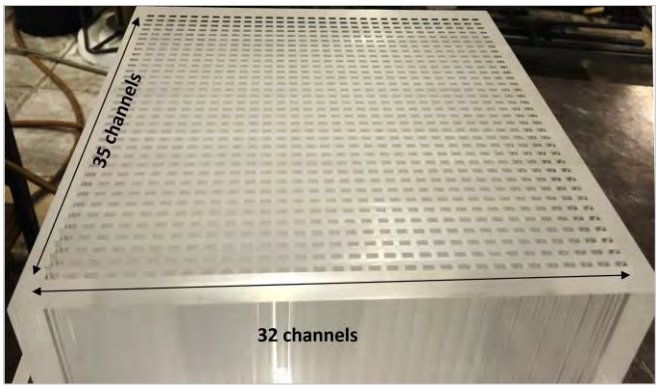

Fig.3. 32 - Section of DANAH bundle channel

See that at the half of the plate's length (Fig.3.31), the cross-section area of the channel is reduced by 50%. Saving in space and material, this geometry provides the appropriate equivalent pressure drop to study the flow maldistribution in ASTRID SGHE operating conditions.

Fig.3.33 shows an additional component of DANAH mockup, i.e. the "*Pre-header*". It has the same basic structure of the bundle (Fig.3.31-32) with the only difference in channel pattern. Here, the 1200 parallel channels communicate between them in x and z-direction thanks to the presence of additional engraved veins linking channels. The "*Pre-header*" has been conceived to be coupled with the main bundle as shown in Fig.3.33 (right) and its performance has been tested during DANAH experiments.

Fig.3. 33 - Pre-Header component (left) and Pre-Header in DANAH mockup (right)

After its assembly, DANAH mockup is installed on a specific structural support with the main role of ensuring mechanical strength and stability of the mockup during PIV

measurements. In fact, the mechanical vibrations due to the high inlet flow velocity ($v_{in} = 6.8\,m/s$) could induce serious noises in PIV analysis or even a brittle failure of the admission tube across steel-Plexiglas junctions.

The support system is composed by two main standing structures of aluminum frames which are fixed on the floor. Structure A in Fig.3.34 ensures the mechanical stability of the inlet pipeline and the fluid box installed at the highest point of the circuit. In addition, to avoid an extremely rigid coupling between the pipeline and the mockup and to absorb vibrations, two expansion joints have been installed upstream the fluid box and downstream the mockup outlet pipe.

Structure B, black painted to capture laser light, stiffens the mockup (Fig.3.35).

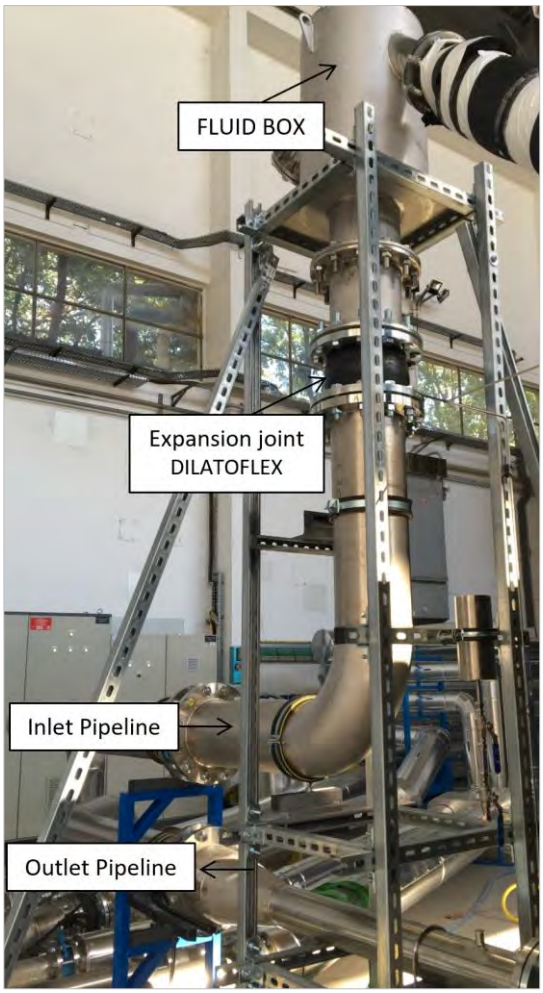

Fig.3. 34 - DANAH Support - Structure A

Fig.3. 35 –DANAH Support – Structure B

3.2.2. PIV equipment in DANAH experimental campaign

The PIV measurement system in DANAH experiments is highlighted in red in Fig.3.27.

Laser

The used laser is a double cavity 2x200 mJ pulsed QUANTEL EverGreen 200 YAG Laser (Yttrium Aluminum Garnet). It provides light sheet with a wavelength of 532 nm and its pulse frequency is between 0 and 15 Hz. The QUANTEL EverGreen Laser is shown in Fig.3.36 with its automatic displacement system. The laser displacements are controlled by the three-axis sliding table with micrometric fine adjustment in xyz axis.

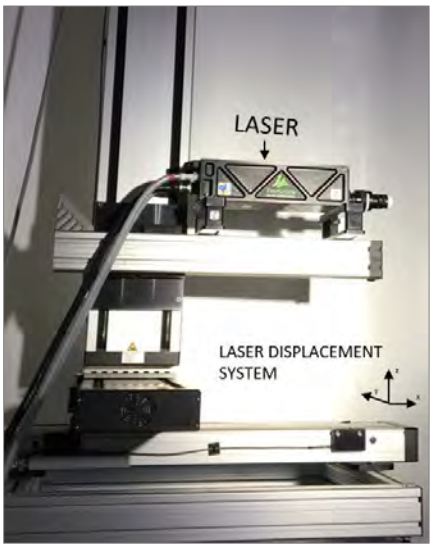

Fig.3. 36 - Nano L PIV Laser (left side) and its displacement system (right side)

The light-sheet optics includes cylindrical and spherical lenses, which limit the light-sheet thickness to 1 mm. The alignment of the laser sheet of 1mm thickened at the exact position of the inlet and outlet header has been done using the target system and geometric boundaries of the header (Fig.3.37).

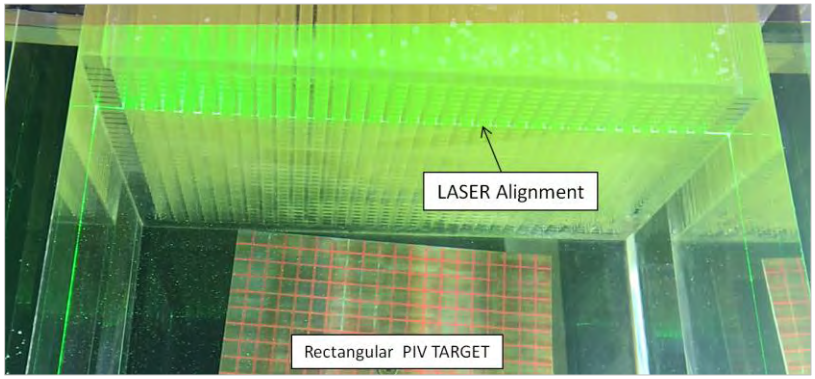

Fig.3. 37 - Laser alignment at the outlet header

Seeding particles

To scatter the light of the laser, water has been seeded with nylon sphere-like particles with diameter 4μm. They were chosen for tracing the flow because of their density similar to that of the water. A seeding density of 10 particles per interrogation window is considered in PIV measurements.

However, during the first phase of DANAH experiments, it was noticed that some of the nylon particles remained attached to the wall (electrostatic effect). The dirty surfaces prevented a correct capture of the light scattered by moving particles. Glass hollow spheres have been then preferred for flow visualization in the rest of the experimental campaign. The glass hollow spheres are borosilicate glass particles with a spherical shape and smooth surface. The particle size of 10 microns leads to a strong scatter of the laser light and a very good stability against water (1.05 g/cm^3).

An example of water seeded with glass hollow spheres captured photographically in the inlet header is shown in Fig.3.38.

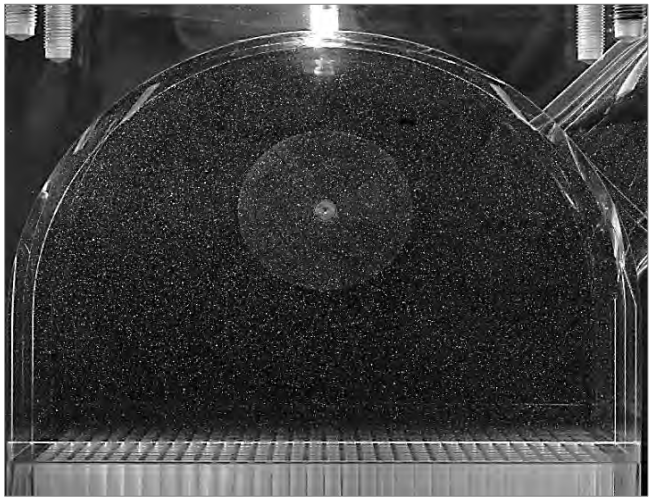

Fig.3. 38 – Capture of seeding particles at the inlet header

Camera

The image signal acquisition is recorded by a CCD camera (Charged Coupled Device) PowerViewTM Plus 4MP, with a resolution of 2048x2048 pixels and a frame-straddling time up to 200 ns. The camera, shown in Fig.3.39, was equipped with the telephoto lens Nikon – AF MICRO 35 mm/2.8 that was used to focus on the laser sheet. A high pass filter was placed in front of the camera which enabled capture of light with a wavelength greater than 550 nm, protecting the CCD sensor from unwanted light reflections from gas bubbles and improving contrast.

It is worth noting that, during DANAH measurements, the camera remained attached to the tripod in front of the inlet or outlet header and there was not displacement in any direction (Fig.3.26). The investigated x-y planes have been designated by the laser sheet moving in z-direction. The camera focus required some adjustments after a laser sheet movement of 2 cm.

A synchronizer has been used to control the output of the laser pulse and the sequence of image acquisition, which guarantees all parts are coordinated according to the regular order. The software controlling the PIV system and data analysis used was Insight 4G.

Fig.3. 39 - Camera

3.2.3. Experimental program definition

The following section presents the overall experimental program initially scheduled for DANAH project. It was defined taking into account the main objectives of the experimental validation as well as the modular design of the experimental mockup.

The experimental program included the PIV analysis of six different DANAH configurations which have been classified in two experimental campaigns, i.e. the Green and Blue DANAH campaign.

For sake of clarity, each configuration is named following the notation:

```
ColorCampaignD_HeaderType_Volume_PreHeader
```

The first campaign, also named *Green DANAH (GD)*, was conceived with the principal aim to validate CFD simulations. For this purpose, an inlet header with a regular shape has been chosen for the analysis (Fig.3.40). In fact, even if the header geometry (1) doesn't fill the mechanical resistance criteria of the ASTRID project, it performs very well as test section for PIV measurements. In fact, the reduced scatter lights and background noises provide more accurate PIV measurements.

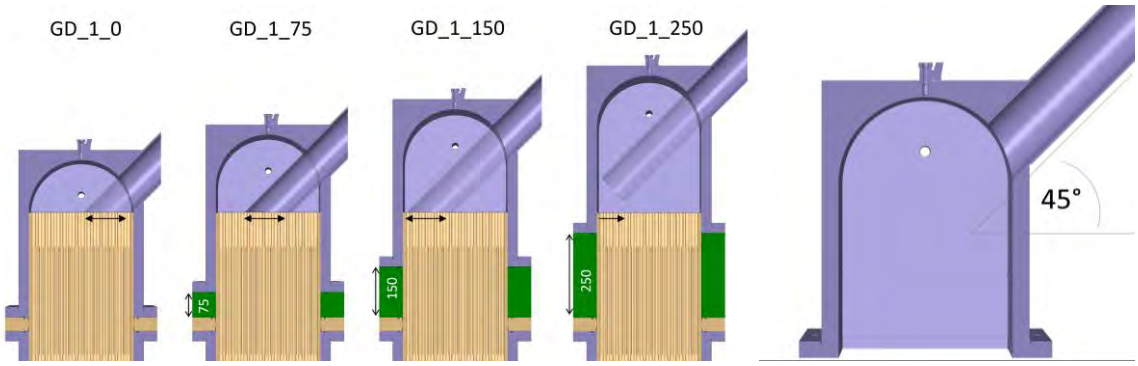

Fig.3. 40 - Green DANAH experimental campaign and inlet header (1)

In order to build a solid experimental database and to study the influence of the distributor volume on flow distribution, the header (1) was tested in four different DANAH configurations, i.e. `GD_1_0, GD_1_75, GD_1_150` and `GD_1_250`. As shown in Fig3.40, interposing different size wedges between the bundle channel unit and the inlet header, it is possible to vary the header volume. Note that, the vertical translation of the header causes the variation of jet impingement position on flow distribution (black arrows in Fig3.40).

The second campaign, named as *Blue DANAH (BD)*, consists on the experimental demonstration of the efficiency of a specific header design which is the most plausible to be integrated in the ASTRID SGHE module.
Fig.3.41 shows the inlet header (2) with the double cross-cylinder dome. The particular shape, more resistant to the external pressure of SGHE vessel, has been investigated in DANAH experiments (`BD_2_75_NC`).

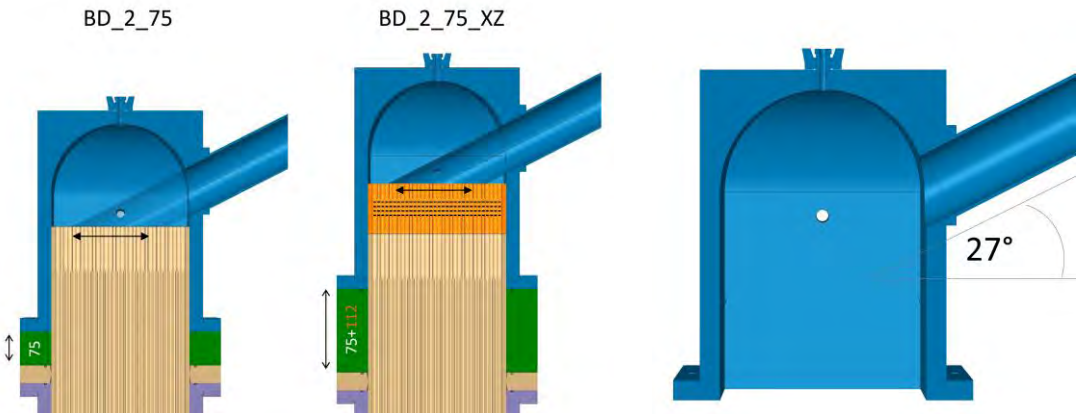

Fig.3. 41 - Blue DANAH experimental campaign and inlet header (2)

The flow distribution in the presence of channel communications (C) has been also tested (`BD_2_75_C`). During PIV measurements, the "Pre-Header" component (Orange in Fig.3.41) is perfectly aligned and placed on the bundle channel.

PIV measurement program

Each configuration described above has been experimentally studied by PIV measurement technique. The PIV measurement program adopted for both inlet and outlet header is detailed below.

At the inlet header, the primary objective was the characterization of the jet recirculating in the large volume. Five x-y measurement planes along the direction of header length (z) are then considered in DANAH experiment (Fig.3.42 left).
I-Plane 3 is located at the symmetry plane of the header. *I-Plane 2-4* are deviated from the symmetry plane of 50 mm along the direction of header length. *I-Plane 1-5* are placed at 100 mm from the symmetry plane. A letter I is added to the nomenclature of PIV inlet planes to distinguish them from measurements at the outlet (O).

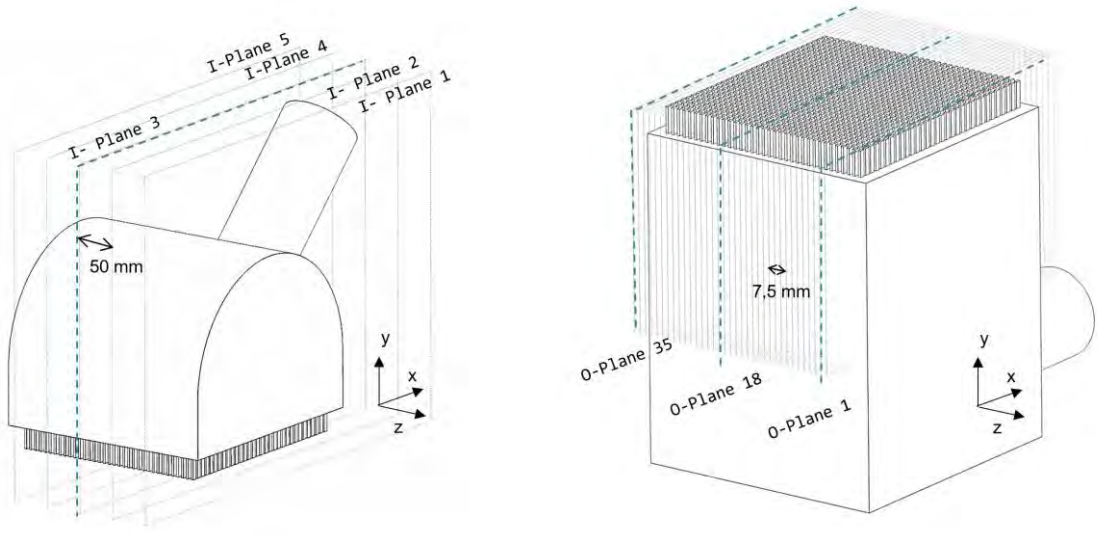

Fig.3. 42 - PIV measurement planes at the inlet (left) and outlet (right) header

PIV measurements at the outlet header have the ambitious objective to determine the flow repartition between channels of the bundle starting from the characterization of confluent parallel jets in the outlet header.

35 x-y planes, corresponding to the 35 plates are measured along the z-direction (Fig.3.42 right). Each PIV plane is aligned with the central section of the 32 channels in a single plate.

3.2.4. PIV measurements calibration and testing

An accurate PIV calibration is necessary in order to correlate the number of pixels in the line with its actual geometrical length.

For this purpose, in DANAH experimental mockup, 2 mm thick targets are installed on a Plexiglas rod moving along the inlet and the outlet header (Fig.3.30). This calibration system allows the operator to move the target forward to the measured plane during the calibration process and to draw it back to the outer header wall during PIV measurements.

Fig.3.43 shows the calibration process using the circles and rectangular targets for measurements in inlet and outlet header respectively. The camera focus has been done on targets. As shown in Fig.3.43, Insight 4G software allows to define a line on targets and to specify its known distance. For instance, in Fig.3.43 (left), the know target length of 80mm corresponds to 258.79 pixels which means a calibration in x and y of 309.14 $\mu m/pixel$.

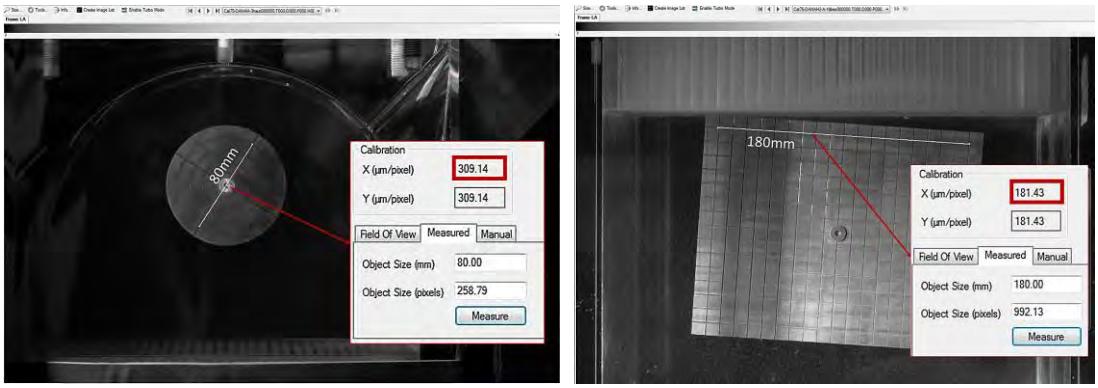

Fig.3. 43 - Camera Calibration on PIV target at the inlet (left) and outlet (right) header

To double-check the camera calibration, another calibration method has been used in DANAH experiment. It consists on defining, in a captured picture, a line between the outer walls of header corresponding to the known header width (309 mm in Fig.3.44). For instance, in Fig.3.44 (left), the know header length of 309mm corresponds to 997.01pixels which means a calibration in x and y of 309.93 µm/pixel.

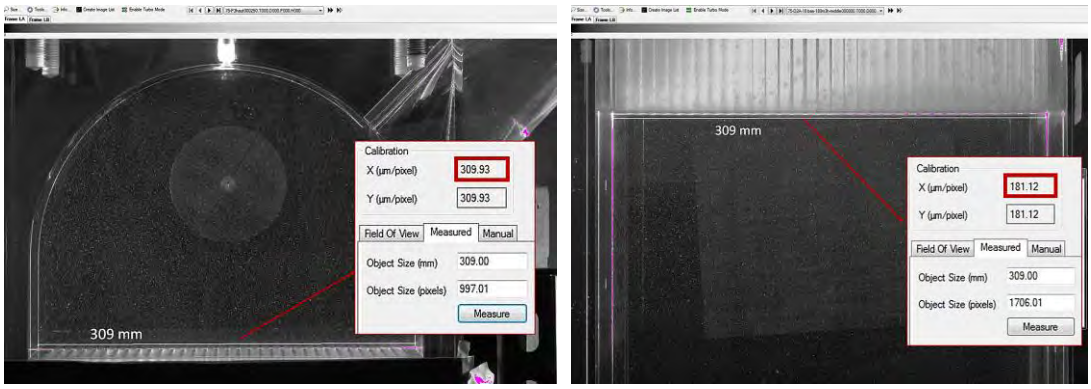

Fig.3. 44 - Camera calibration on mockup dimensions

As it can be seen from the comparison between calibration values issued from two methods, in both inlet and outlet header there is only slightly differences in pixel length (Δ_{inlet}= 0.25% and Δ_{outlet}= 0.17%).
For DANAH measurements, the calibration done by defining the known header width has been preferred when the camera focus is not necessary (deep depth of field). In addition, it is worth noting that using this calibration method a larger checked geometry is considered, which means a potentially lower uncertainty in defining the number of sub-windows in a known length.

3.2.5. Measurements statistical convergence

A preliminary analysis of the statistical convergence of the single measurement is necessary. What is ought to be verified is that the number of captured images is sufficiently large to obtain fully converged value of the measured variable.

In the DANAH experimental campaign, the PIV convergence evaluation study has been done on the symmetry plane for both inlet (*I -Plane 3*) and outlet header (*O -Plane 18*).

As regard to the inlet header, tests with 50, 100, 150, 200 and 250 images each had been run to determine the final number of image for each measurements of the experimental campaign. To easily check the measurements statistical convergence, the average velocity field differences have been plotted for the four cases in Fig.3.45, i.e. $V_{50} - V_{100}$, $V_{100} - V_{150}$, $V_{150} - V_{200}$ and $V_{200} - V_{250}$.

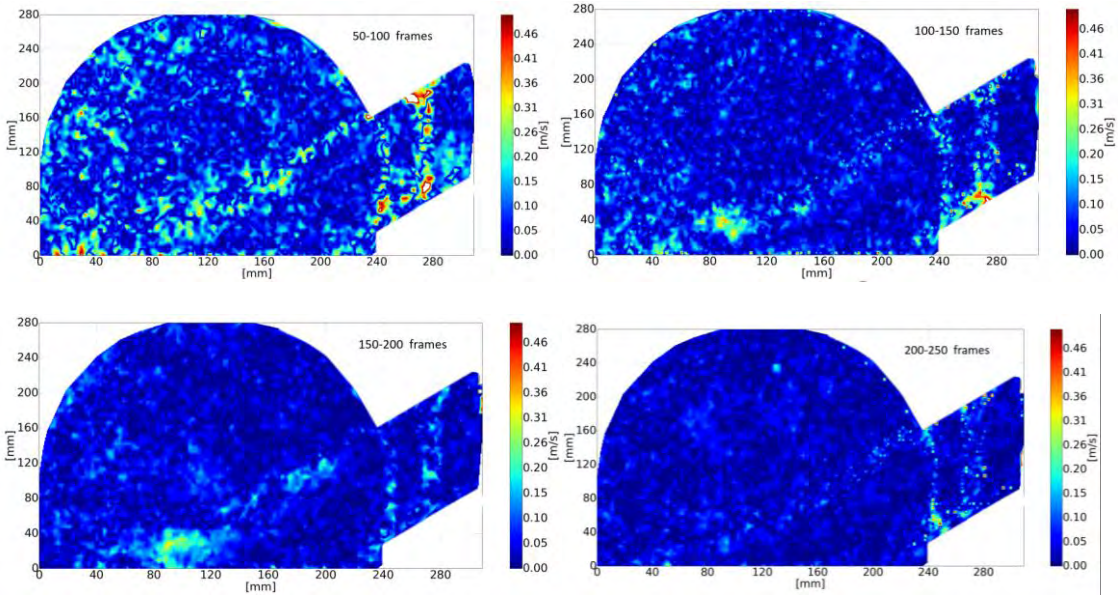

Fig.3. 45 - PIV measurements statistical convergence at the inlet header

As expected, the differences decrease as the number of picture increases. In particular, referring to Fig.3.45, the maximum difference is about 0.3 m/s for the 0-50 frames case, whereas only 0.1 m/s for the 200-250 frames case. It can be noticed that some high concentrated differences persist at the inlet tube region for all cases. They are essentially due to the mockup laser reflections (Fig.3.48) and they cannot be eliminated with the increase of pictures numbers. Moreover, they are not located in the studied area, hence they are not considered in measurement convergence estimation. As conclusion, 250 pictures have been captured for each PIV plane at the inlet header. This choice results a good compromise between a good measurement statistical convergence and a reasonable volume of data to be processed and stored during the large experimental campaign.

The same procedure has been used to study the statistical convergence of the single measurement at the outlet header. However, only three tests 50, 100 and 150 images each had been run. It is important to remember that the main objective of outlet PIV measurements is to quantify a flow distribution and not to validate a CFD model. In addition, the physical behavior of flow outcoming from channels appears less complex than the evolution on the jet flow in the inlet header. Therefore, 150 frames were considered numerous enough for the convergence study.
The average velocity field differences have been plotted in Fig.3.46, i.e. $V_{50} - V_{100}$ and $V_{100} - V_{150}$..

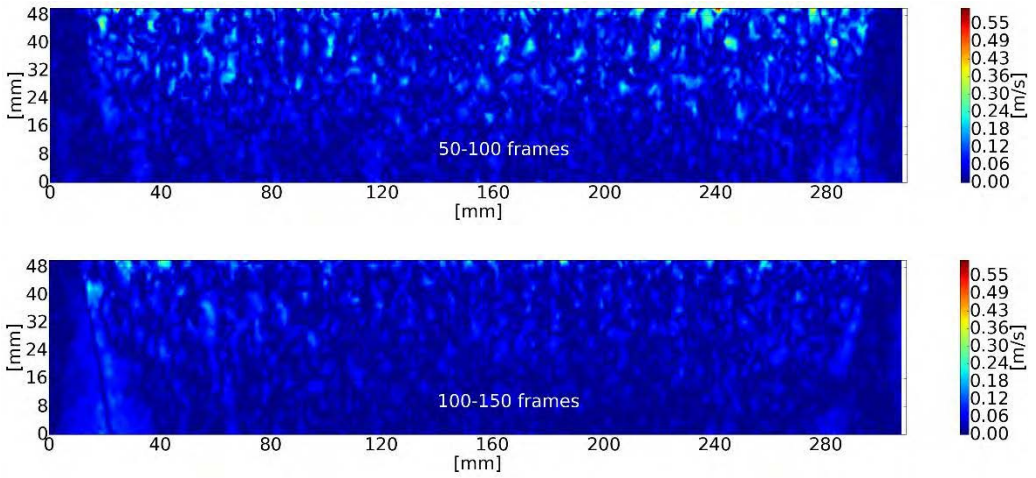

Fig.3. 46 - PIV measurements statistical convergence at the outlet header (BD_2_75)

Again, the differences decrease as the number of picture increases. In the 100-150 frames case, the maximum difference is about 0.12 m/s which could be a still too high value to have fully converged measurement. Nonetheless, because of PIV grid resolution at the outlet, a larger number of images would involve an excessive post-processing time for each investigated plane (35 planes at the outlet).

3.2.6. Experimental uncertainty evaluation

To evaluate the experimental uncertainty in DANAH experiment, the same approach of Section 3.1.2.6 has been used. Three types of uncertainty are identified: the uncertainty due to the data acquisition, the uncertainty due to environmental conditions and the uncertainty due to the measurement plane position.

Data acquisition uncertainty

Regarding the data acquisition, it was already mentioned the difficulty in quantifying PIV measurement uncertainties of the instantaneous velocity. However, four different methods for PIV uncertainty quantification have been proposed in literature in the last three years [56]. Any of them was implemented in "La Vision" PIV Software used in EASY-B experiments, so they are neglected in the uncertainty evaluation. This assumption is licit since, for statistical quantities, the uncertainty is mainly related to the number of images [57].

Differently in DANAH experiments, "Insight 4G" PIV Software was equipped by a specific algorithm able to take into account PIV uncertainties of the instantaneous velocity field, i.e. the 'peak ratio' method of Charonko and Vlachos [60] [61].
This method is based on the assumption that, the correlation peak contains information about uncertainty. According to the authors, PIV uncertainty is correlated with image quality which contains many possible sources of error in an experiment including the PIV algorithm (interrogation window size, pixel displacement, image pre-processing, etc.). A more accurate estimation of PIV uncertainty is then provided for DANAH experimental database.

Fig.3.47 shows the Standard Uncertainty of the velocity magnitude in the symmetry plane of the inlet header (*I -Plane 3*).

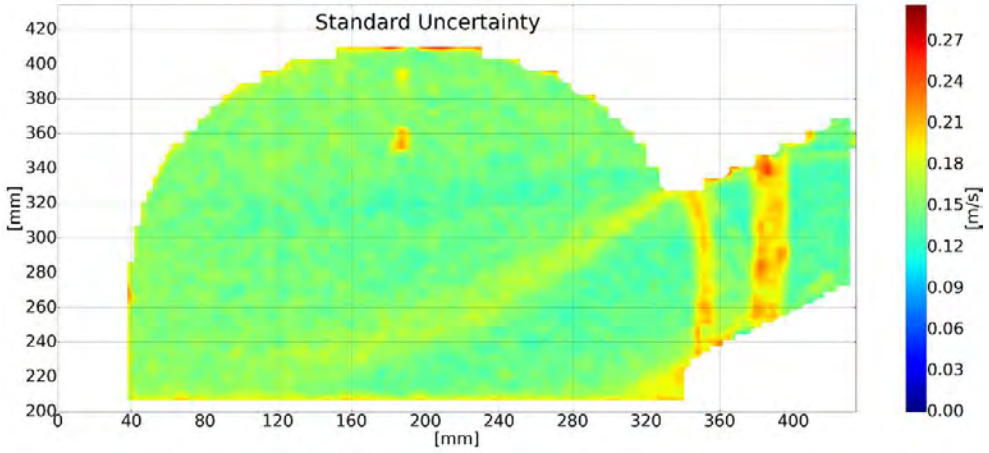

Fig.3. 47 - PIV standard uncertainty at the inlet header (BD_2_75)

The average value of standard uncertainty all over the field is about 0.15 m/s. However, few higher values can be noticed in specific areas of the inlet header, i.e. the inlet tube, the channel bundle or the jet flow adjacent zones (Fig.3.47).
If it is clear that the strong velocity gradients within interrogation windows are responsible of greater velocity errors in jet flow adjacent zones, the same cannot be said for the other spots. As shown in Fig.3.48, these latter are essentially due the laser reflections of the interface between the header and the inlet tube, the bundle channel at the bottom of the header and the automatic air-vent valve located at the top.

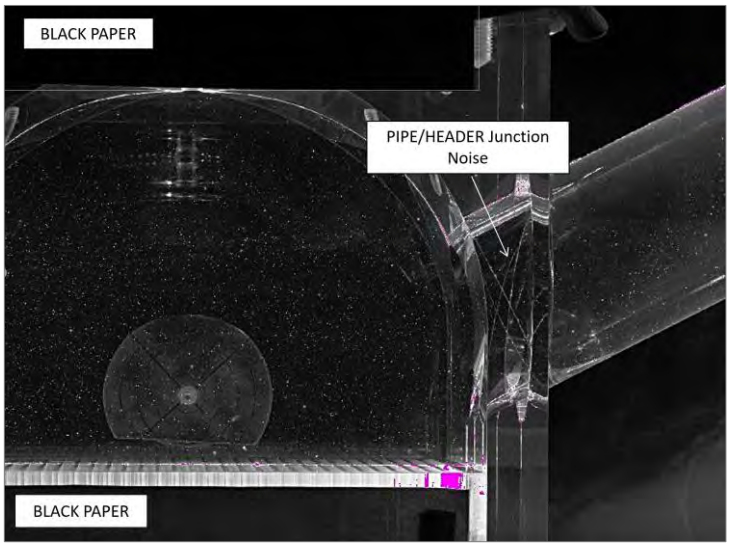

Fig.3. 48 - Scatter light and background noise at the inlet header (BD_2_75)

The same method of Charonko and Vlachos [60] has been used to estimate PIV uncertainties at the outlet header. Fig.3.49 shows the Standard Uncertainty on the outlet header plane, i.e. *O -Plane 18*.

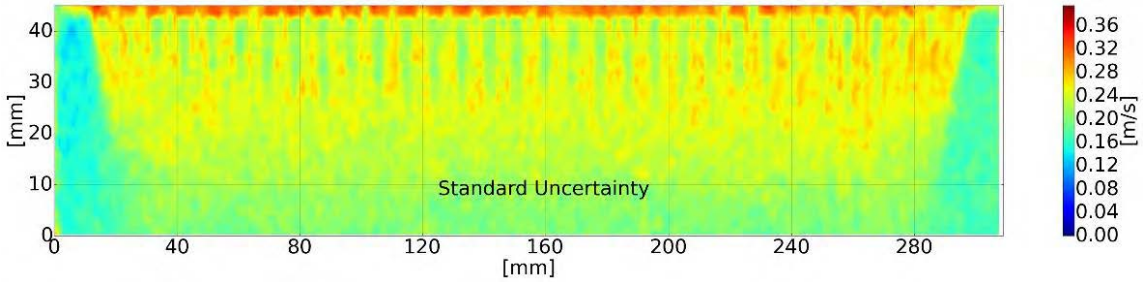

Fig.3. 49 - PIV standard uncertainty at the outlet header (BD_2_75_NC)

High uncertainties can be noticed at the top of Fig.3.49. This reflects the extreme difficulty in having a proper setting of PIV parameters to characterize a zone very close to the outlet of the channel bundle. To better understand the main cause of the low accuracy, a zoom on a raw PIV image at the channel outlets is shown in Fig.3.50.

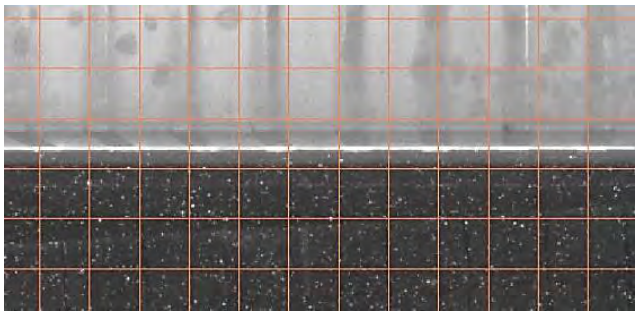

Fig.3. 50 – Raw Data- PIV Image zoom on the outlet header

First of all, an important background noise due to the light refractions of the bundle can be detected (grey shaded area in Fig.3.50). In fact, to illuminate the small diameter seeding particle, high laser powers and large apertures of camera shutter are needed.
Secondly, as illustrated in Fig.3.50, the random incorrect positioning of the PIV grid allows important errors on PIV processing for the cut interrogation windows at the outlet. Each window at the boundary of the bundle contains part of Plexiglas structure. To overcome this problem, smaller interrogation windows should have been used in PIV processing. In turn, this would have meant a more important feeding of tracer particles. This solution was not possible due to their unexpected tendency to settle on Plexiglas surfaces when present in large amounts (additional noise).

To improve the raw image quality before processing, a background image subtraction technique [62], available in Insight 4G software, is always run and illustrated in Fig.3.51. It consists in removing some fixed parts of the image like targets, walls and scattered lights making more apparent the variable part.

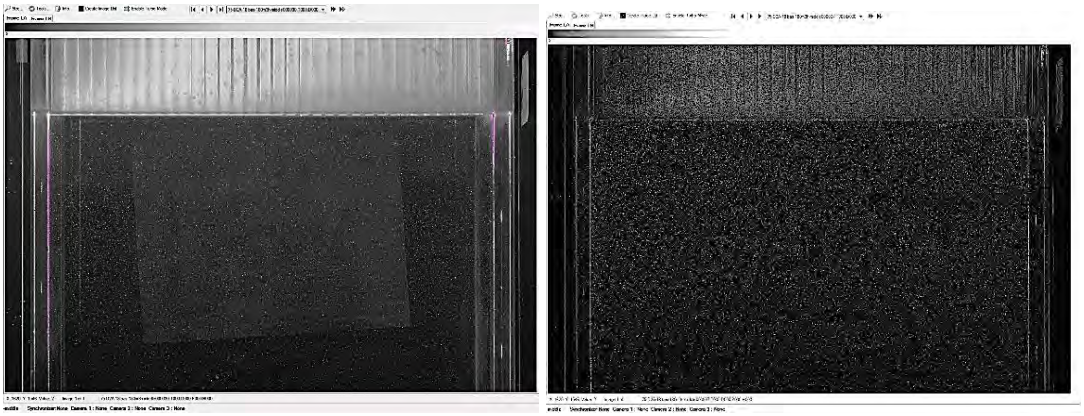

Fig.3. 51 - PIV image before (right) and after (left) the INSIGHT 4G Pre-processing

However, the pre-processing of the image is not sufficient to reduce the high standard uncertainties at the outlet boundary of the channel bundle (Fig.3.49).

Environmental condition uncertainty

To quantify the influence of experimental conditions, two identical measurements at the same plane position at various times of the day and various days have been acquired.
The uncertainty has been evaluated based on the mean difference between the two measurements. The standard deviation has been then calculated as the mean difference was distributed on uniform probability density function, i.e.:

$$\delta V_{Exp.Conditions} = \Delta v_{mean}/\sqrt{3} \quad (18)$$

Table 3.8 shows the estimated value of environmental conditions uncertainties for Plane 3I and Plane 18O. Note that, for both inlet and outlet headers the uncertainty tests have been done only in the symmetry plane of the module. The approximation is therefore to apply this uncertainty in other investigated planes. The approximation could be more important for the inlet header where a 3D development of the jet flow occurs.

Plane Position uncertainty

Finally, to evaluate the uncertainty due to the plane position, three measurements have been performed on adjacent planes shifted left and right by 1 mm from the reference one (I-Plane 3). Again, the uncertainty has been evaluated based on the mean difference between the four measurements. The standard deviation is defined as:

$$\delta V_{Position} = \Delta v_{mean}/\sqrt{3} \quad (19)$$

The laser displacements by 1mm to the left and right side of the reference plane are then controlled by a three-axis sliding table with micrometric fine adjustment in xyz. The operator aligned the laser sheet, whose thickness has been estimated around 1 mm, on the reference plane helped by header geometric boundaries and highlighter marks traced on the lateral boundaries of Plexiglas header. This marks strongly lighted by the laser sheet allows monitoring not only the measured plane position but also the correct alignment of the laser sheet across the header width. See the two marks on both left and right lateral boundary of the header in Fig.3.51 (left).

Table 3.8 shows the estimated value of plane position uncertainties for Plane 3I and Plane 18O.

	Data Acquisition Uncertainty	Environmental Condition Uncertainty	Plane Position Uncertainty	Total Uncertainty
I-Plane 3	0.15 m/s	0.21 m/s	0.18 m/s	±0,49 m/s
O-Plane 18	0.18 m/s	0.13 m/s	0.31 m/s	±0,38 m/s

Table 3. 8 – Uncertainty analysis of PIV measurements

Table 3.8 shows the results of the standard deviation for each source of uncertainty identified in the experimental campaign. The total uncertainty δ is calculated as the combined standard deviation determined by adding the variance of each source of uncertainty.

3.2.7. Flow Inlet Conditions

As for EASY-B experiment, it is important to study experimental flow inlet conditions to perform a proper CFD numerical validation.

DANAH experimental mockup and its water loop have been designed to achieve fully developed flow at the inlet header admission. A fluid box has been installed at the highest point of the hydraulic circuit for the purpose of attenuating the pipe-line circuit effects on the flow inlet conditions (Fig.3.34). The exhaust pipe from the box, designed with a length of $50d_h$ and an inlet Reynolds of 60 000, is there supposed to ensure a uniform flow at the inlet header admission. CFD numerical calculations (Realizable k-ε model [63]) helped to design the pipeline inlet system identifying the right length ensuring a fully developed flow.
PIV measurements have been done to verify the flow uniformity at the inlet header admission. Fig.3.52 shows the measured velocity field on the last 150 mm of the inlet pipe before the admission in the header volume.

Important measurements errors can be easily noticed from x=340 mm to x=430 mm, where the inlet tube intercepts the header rectangular box (Fig.3.48). They prevent any conclusions about the uniformity of velocity profile. On the other hand, starting from x=430 mm, a uniform velocity profile can be recognized (Fig.3.52).

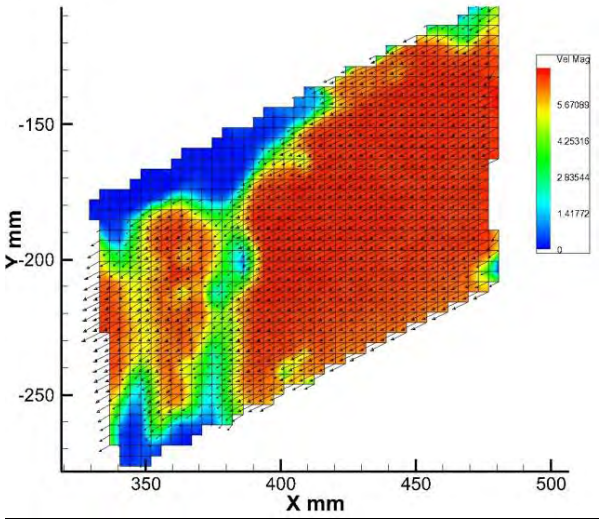

Fig.3. 52 – PIV velocity profile on the admission pipe

3.2.8. Flow Symmetry

DANAH mockup model was designed in perfect symmetry with respect to the x-y plane passing through the center of the inlet pipe (*I-Plane 3*). This means that based on the assumption of a good manufacturing process and a proper installation on the structural support system, a symmetric flow is expected in DANAH mockup.

To verify the flow symmetry, PIV measurements have been done on symmetrical x-y planes at the inlet header of each DANAH configuration. For sake of simplicity and due to the limited space, the flow symmetry is here demonstrated for only BD_2_75_NC configuration.

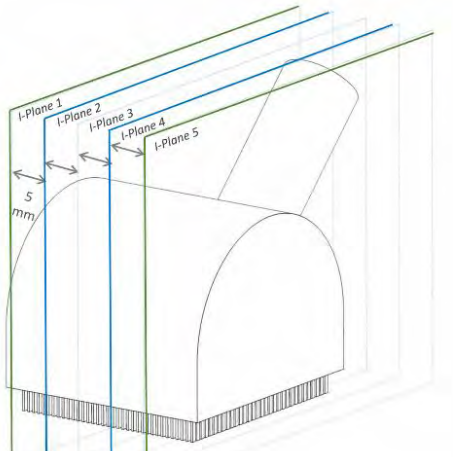

Fig.3. 53 – Symmetric planes

Fig.3.54 and Fig.3.55 shows the comparison of the velocity fields between *I-Plane 2* and *I-Plane 4* and *I-Plane* 1 and *I-Plane* 5 respectively (see Fig.3.53).

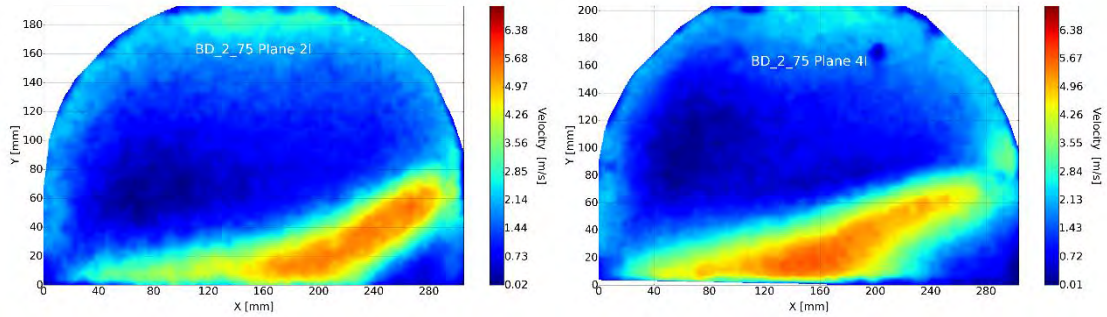

Fig.3. 54 - PIV velocity field at I-Plane2 (left) and I-Plane 4 (right)

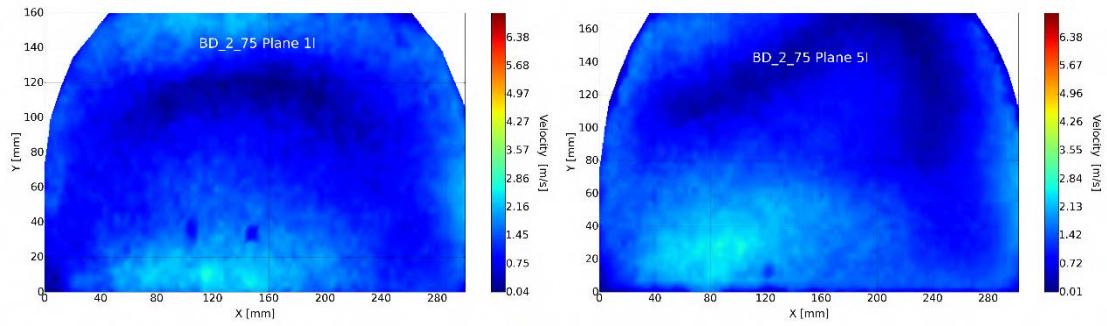

Fig.3. 55 - PIV velocity field at I-Plane1 (left) and I-Plane 5 (right)

Some differences can be noticed in Fig.3.54. After the jet impingement on the bundle channel, a different evolution of the fluid flow seems to occur within the two symmetrical volumes of the inlet header.
As the z-distance from the inlet tube increases (I-Plane 1 and I-Plane 5 in Fig.3.55), the jet dissipation makes differences less apparent. Therefore, we can conclude that the fluid flow is not perfectly symmetric in DANAH mockup.

The measured flow asymmetry could be related to a non-perfect alignment of laser sheet during PIV measurements or the asymmetry of the Plexiglas mockup (manufacturing tolerances). The inlet flow analysis at Section 3.2.2.5 excludes a non-uniform inlet flow condition as possible cause of flow asymmetry in the header volume. Similarly, for the unsteady nature of the flow.
As conclusion, since it has been demonstrated that the flow pattern is not symmetric in DANAH experimental mockup, the entire volume of outlet header should be investigated by PIV to correct characterize the flow in the mockup. However, due to the time constraints of DANAH campaign and the long post-processing, the PIV analysis at the outlet header has been limited, in any case, to half of the bundle (35/2 plates).

3.2.9. PIV Measurements at the outlet header

3.2.9.1. Influence of the outlet header geometry

The main goal of PIV measurements at the outlet header of DANAH mockup is to study the flow distribution between channels. Achieving this aim requires a correct characterization of the closely spaced jets developing at the outlet of the bundle channel.

For this purpose, the outlet header has been designed to ensure a regular and unperturbed fluid at the outlet of the bundle. A large rectangular volume with an outlet tube fitted to the bottom of the box was employed in experiments. The header geometry complies with PIV requirements of a regular Plexiglas interfaces to avoid laser sheet deflections. The dimensions of the outlet header are the result of a preliminary CFD calculation and some well-known engineering formulations.
In addition, to prove the negligible influence of the outlet header on the flow distribution, a comparative CFD analysis has been carried out with and without the header. The maldistribution factor σ varies less than 0,6%.

Fig.3.56 shows the measured velocity field on the symmetry *O-Plane 18*.

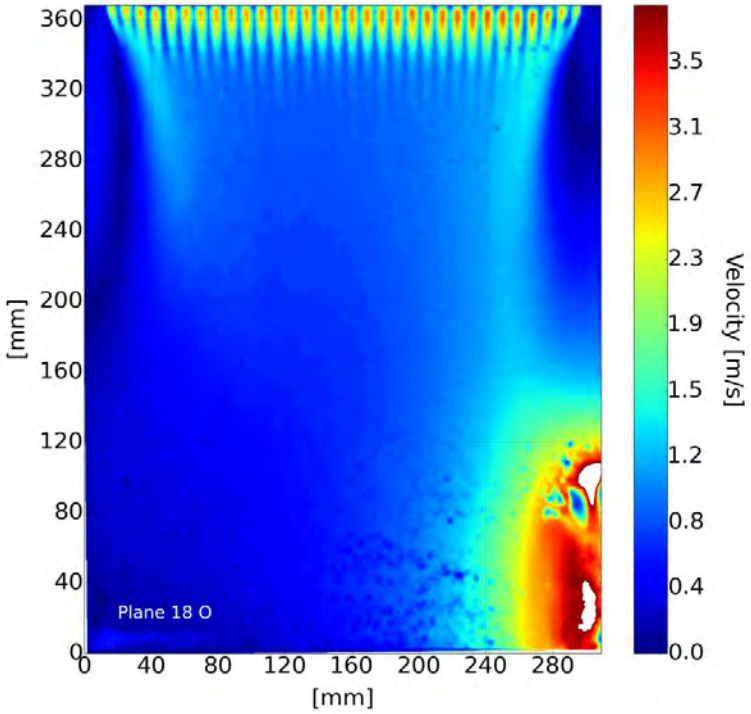

Fig.3. 56 - PIV velocity profile at the outlet header (O-Plane 18)

Referring to Fig.3.56, it can be noticed that the water plenum is large enough to provide a quiescent flow at the outlet of the bundle. The local suction effect of the outlet tube does not influence the evolution of parallel jets.

Fig.3.56 shows that the jets close to the lateral walls tends to deflect toward the center of the plate. This is due the different entrainment of fluid particles on the two layers of a peripheral jets. In fact, the mutual entrainment between parallel jet generates a sub atmospheric region attracting the peripheral jet whereas no entrainment occurs between the far confining wall and the jet [67] (see Section 3.2.9.2 for explication).

However, it was demonstrated that, if wall is closer to the jet, a low-pressure region happens near wall can cause the jet to stick to the wall. This known as Coanda effect. Fig.3.57 illustrates the Coanda effect for a single jet near a wall [64].

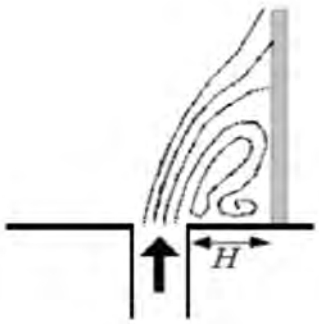

Fig.3. 57 - Coanda Effect [64]

3.2.9.2. Theoretical analysis of parallel jet flow evolution

Before proposing any strategies to study the flow distribution starting from velocity measurements at the outlet of bundle channel, it is important to understand the physical interaction process between parallel jets.

For this purpose, let us begin from the simplest case of one free jet[12] [65]. We can see in Fig.3.58 the two main regions characterizing a jet: the core, or potential core, and the shear layer. Into the core, the velocity remains unchanged with a value of U_0. Moving away from the orifice, the turbulent shear layer shrinks the core.

As a jet flows away from a slot it draws in fluid from the surrounding mass, causing the mass of fluid carried along by the jet to increase, a phenomenon called entrainment [66]. Viscous effects are the source of this phenomenon, and the result is that since the

[12] A jet of fluid is defined as free if it both issues into a reservoir of the same fluid without any wall influence and has a cross-sectional area one-fifth of the confinement, otherwise it is a confined jet.

centerline velocity passed the core region decreases, and the mass of the jet increases, there is a conservation of axial momentum, hence pressure remains constant.

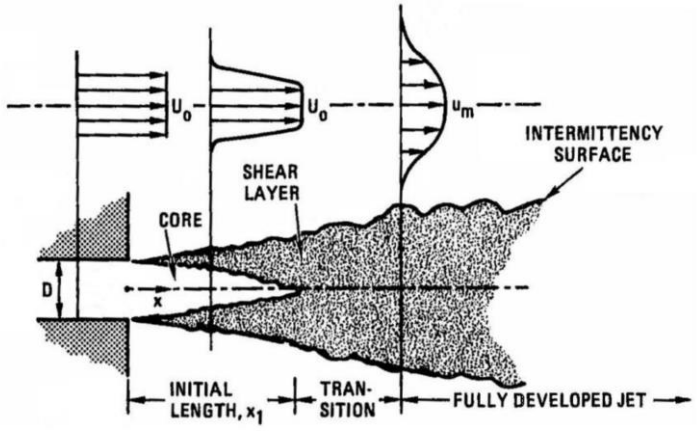

Fig.3. 58 - Schematics of a free turbulent jet

In the case of two parallel jets, when the jets expand, they are both trying to carry along particles from the area between them, and by doing so they create a subatmospheric pressure region that sucks the jets in and makes them combine after a certain length from the origin [66]. The result of this is the creation of two counter rotating vortexes in the "recirculation zone" (Fig.3.59). The interaction between jets was experimentally proved to act as a booster of instabilities which were found to be a function of jet spacing *s* and momentum [66].

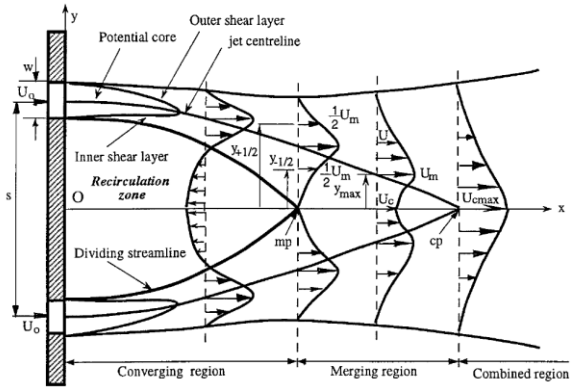

Fig.3. 59 - Schematics of two-parallel turbulent jets [67]

As for the case of a single free jet, the development of two parallel free jets can be distinguished in three regions (Fig.3.59) with different characteristics as we move along the x axis [67] [68]. First, the converging region experiences a subatmospheric pressure (recirculation zone), negative streamwise velocities and low turbulence. Once the merging region is reached, the interaction of the inner shear layers causes a pressure increase to

superatmospheric values, streamwise velocities becomes positive and turbulence peaks. Finally, after the mixing has occurred in the merging region, the jets start to resemble the behavior of a single jet, with wider but lower velocity profiles at the beginning of the combined region.
Fig.3.60 displays forces acting on a confined two-jet configuration (black jets) [71].

However, if one more jet, with the same flow properties as the others, is introduced in the recirculation region, its influence prevents the instabilities from happening (blue jet in Fig.3.60) [69] [70]. The deflection of jets is reduced but jets still tend to join together due to the asymmetrical forces of attraction applied on each of them (different entrainment of peripheral jets).
As already mentioned in the previous section, it is still possible to balance the forces acting on the jets by confining them (Coanda effect). Green jets in Fig.3.60 shows the three-jet behavior in presence of confined walls at the proper distance from peripheral jets.

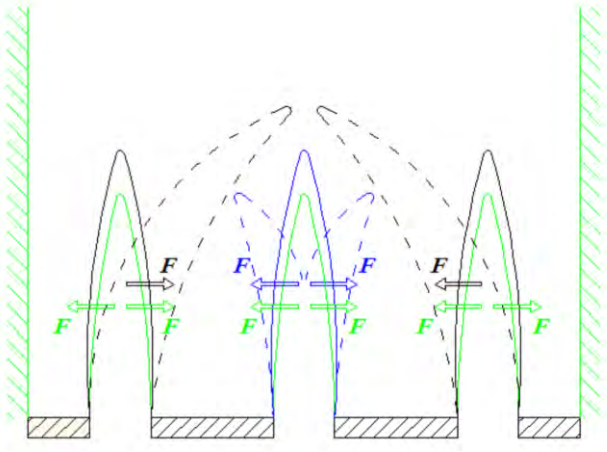

Fig.3. 60 - Typical flow pattern of plane jets [70]

3.2.9.3. DANAH parallel jet flow evolution

In the present section, the evolution of the confined parallel jets at the outlet of DANAH bundle channel is investigated.
Before starting with the analysis of confluent jet velocity profiles, it is important to verify the resolution of PIV measurements in DANAH experiment. In other words, it is important to understand how many experimental velocity data points are available to characterize each one of the 1120 closely spaced jets. Fig.3.61 illustrates the final post-processed velocity field with the overlaid PIV grid (O-*Plane 18*). Using the Recursive Grid

algorithm [62], it is possible to get a velocity vector per millimeter which means 4 experimental points to characterize a single spreading jet (see Fig.3.61 for explanation).

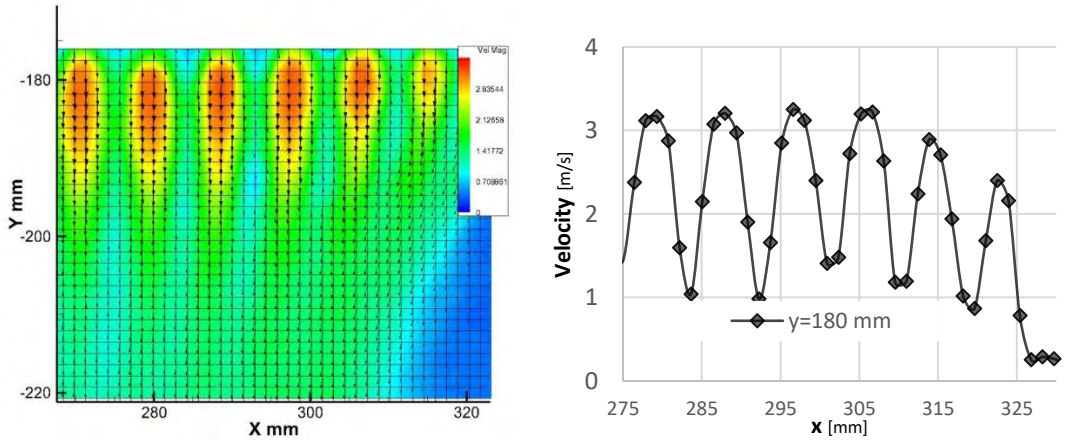

Fig.3. 61 – Post-processed velocity field in a part of the outlet header

As shown in Fig.3.61, trustful velocity measurements at the region very close to the channel outlet are prevented by the bundle scattered lights and the dimensions of the PIV interrogation windows (see Section 3.2.4). Nevertheless, PIV resolution globally allows the correct estimation of the jet flow velocity to study the flow 'maldistribution'.

In the following, a first analysis of jet flow pattern over a length far from the outlet is performed to characterize the evolution of confluent jets and the interaction phenomena. Then, a region very close to the outlet is investigated to determine the potential core velocity of each confluent jet. An estimation of the flow distribution on the half-bundle channel is provided.

Evolution of multiple jets

Fig.3.62 shows the evolution of multiple jets coming out from DANAH channels. The y-velocity profile is plotted at different positions along the y-direction up to $\frac{y}{d_h} = 10$ from the outlet. Note that, for a better visualization, only the half of the channel array of O-*Plane 18* (15-32 channels) is represented in Fig.3.62.

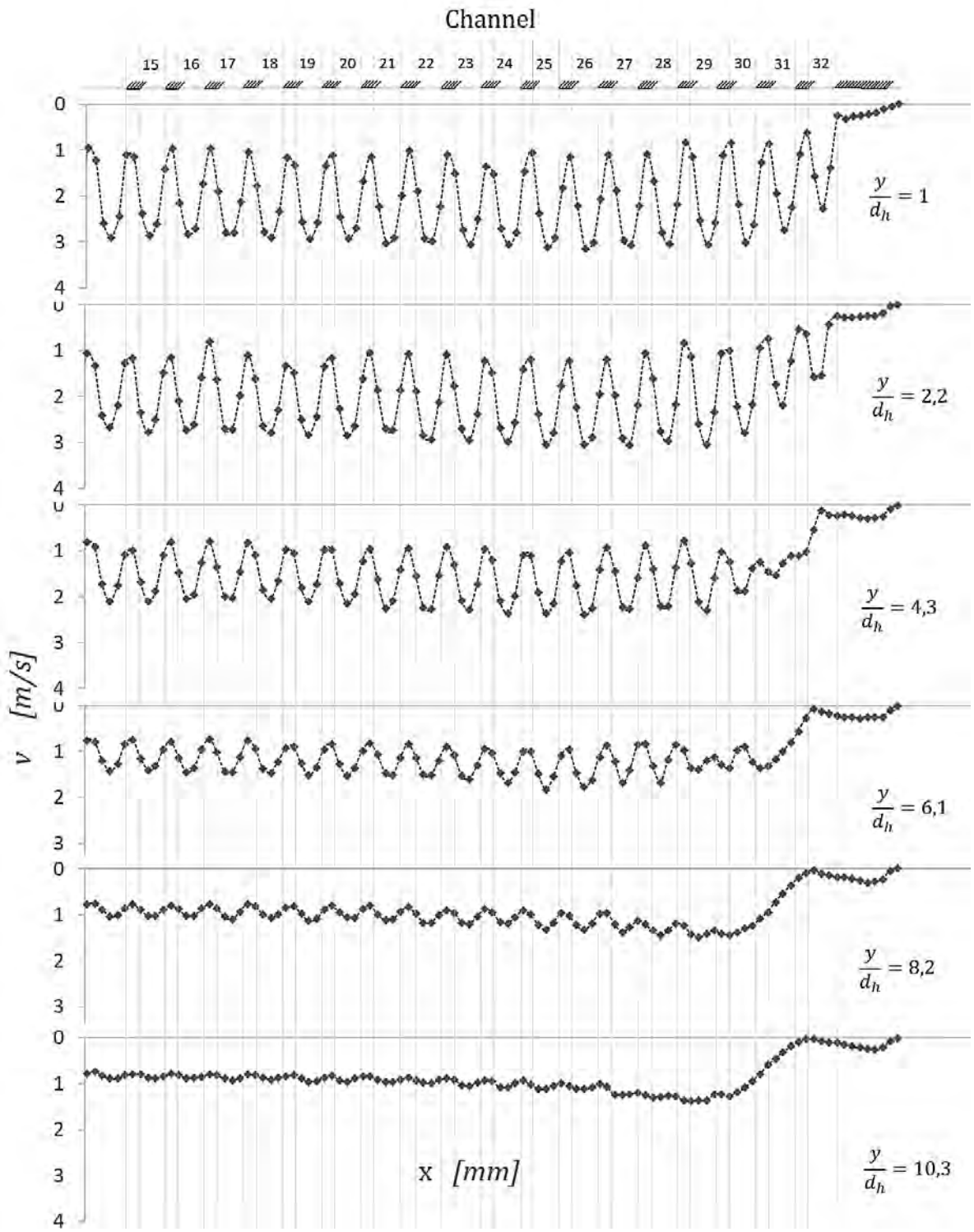

Fig.3. 62 – Y Evolution of multiple jets at DANAH outlet header

Two of the three typical regions characterizing the general flow field of parallel jets can be identified in Fig.3.62, i.e. the merging zone and the combined zone [67].
After leaving channels, the multiple jets seem to merge directly with each other, as demonstrated by velocity value greater than zero in the shear layer between two jets. The absence of the converging zone is probably due to the very small jet spacing ($\frac{s}{d_h} = 0.5$) which inevitably lead to a sudden entrainment of low velocity fluid in the shear layers of the jet.

As the distance from the bundle outlet increases, the jet velocity peak decreases. It is worth noting that, due to the equivalent entrainment of the surrounding fluid of each one of the equally spaced jets, the central axis remains vertical for jets at the center of the linear array. Differently, at the boundaries, the presence of the header walls causes a pressure difference between each side of peripheral jets resulting in jet deflection.
Further downstream from $\frac{y}{d_h} = 10$ onward (*combined zone*) the flow is homogenized and individual jets cannot be longer distinguished.

3.2.9.4. Flow distribution analysis: Adopted strategy

The theoretical analysis of parallel jets in Section 3.2.9.3 suggests that to get explicit information about the velocity distribution between channels, velocity profiles at zones very close to the bundle outlet should be considered (potential core region). In fact, in this region the confluent jet velocity remains unchanged and corresponds to the channel flow velocity.
Therefore, the selection of the velocity profile used for the estimation of flow distribution in a single plate is a matter of extremely importance.

Fig.3.63 display the measured velocity magnitude contour downstream the channels outlet.

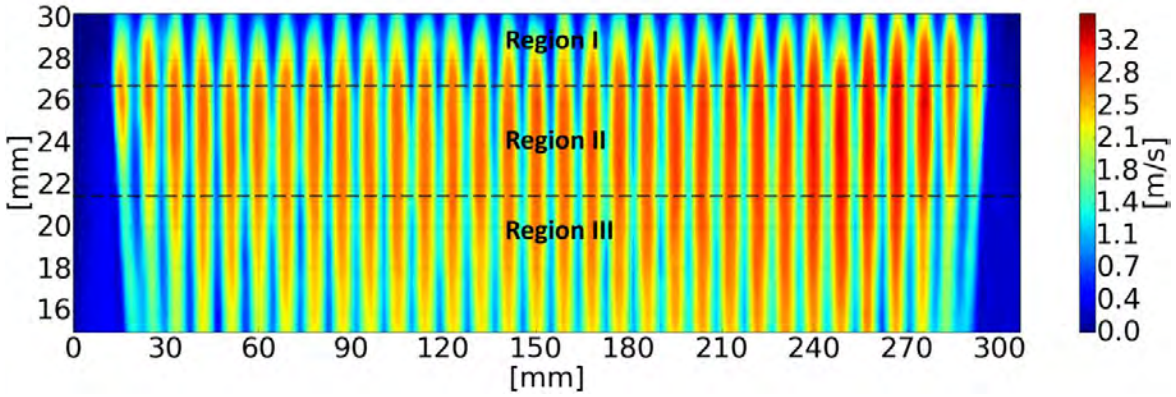

Fig.3. 63 - PIV velocity field on 15mm downstream the channel outlet

As shown in Fig.3.63, the velocity field has been divided in three different regions. For each of them, some vertical velocity profiles are plotted in Fig.3.64. Their analysis allows a better understanding of the reasons of this procedure.

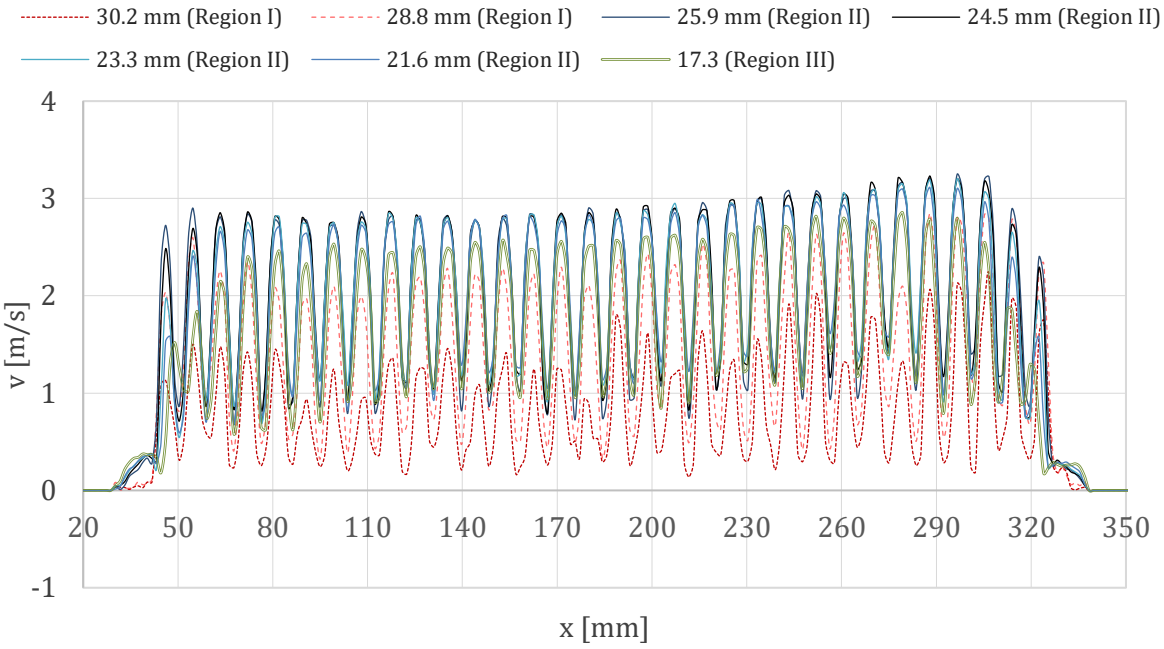

Fig.3. 64 - Y velocity profile at different y positions downstream the channel outlet

The two first red-colored velocity profiles at the position 30.2 and 28.8 mm are clearly affected by PIV measurement errors (background noise and interrogation window positions). Therefore, this first region, termed as *Region I*, will not very useful for the flow distribution analysis.

Note that the size of this zone could vary depending on the investigated plate and the relative position of the camera device and PIV interrogation windows.

In *Region II* (26.5mm <y<22 mm), typical velocity profiles of equally spaced stream jets can be observed. Note that, the four blue-based velocity profiles are almost overlaid. This means that the jet velocity remains constant for about 4 mm downstream except for the peripheral jets which begin to deflect (Fig.3.64).
Region II has been considered as the proper location to select the velocity profile characterizing the flow distribution in the plate. Obviously, peripheral channels (two for each plate side) will be not included in the analysis.

Finally, starting from y=10mm, in *Region III* the jets merge with each other and jet velocity peaks gradually decrease and coalesce into a single jet (Fig.3.64).

The velocity distribution
Starting from the selected velocity profile in *Region II*, a measurement representative of the different feeding of channels needs to be derived.

For this purpose and in the view of the PIV measurement resolution, the measured jet velocity peaks are considered as the most pertinent data values. Deriving the velocity y-velocity profile with respect to x and setting the condition for a maximum, the 32 velocity peaks values can be easily obtained.

Fig.3.65 shows the post processed velocity profile with the square markers highlighting the calculated velocity peaks.

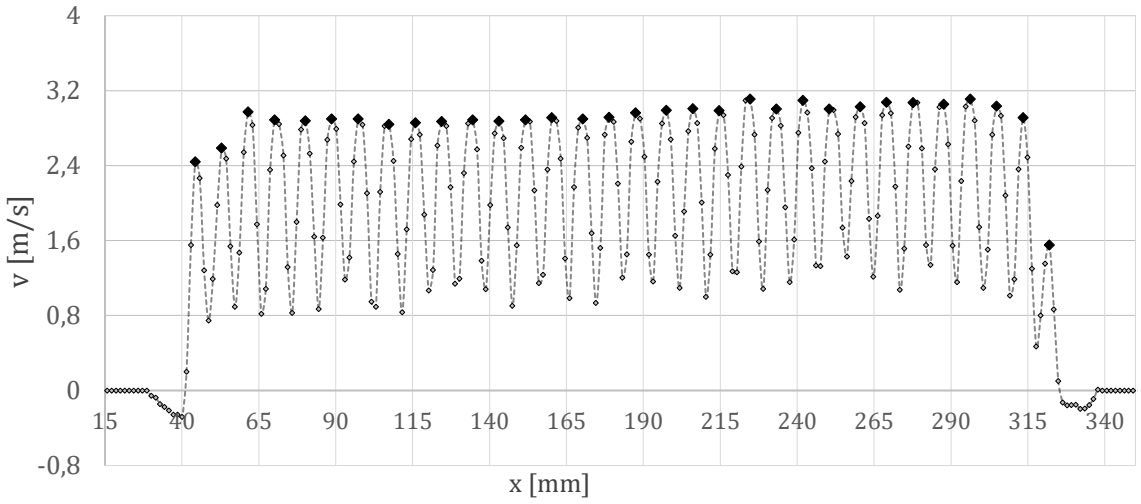

Fig.3. 65 – Y Velocity peaks of at the outlet of the 32 channels of plate 20 – (BD_2_75_NC)

Applying the same processing to the 18 PIV measurement planes, it is now possible to assign to each channel of the DANAH bundle a velocity value.
Nevertheless, based on all above considerations about the accuracy of PIV measurements and post processing strategy, some velocity values will be inevitably rejected from the final analysis of flow distribution. For instance, all peripheral channels of DANAH bundle which are affected by the jet deflection phenomena are excluded from the distribution analysis. Due to the different hydraulic conditions at the confining wall, the more rapid dissipation of peripheral jet avoids the designation of a true velocity value in the area of interest (*Region II*). The measured value of the deflected jet does not correspond to the channel velocity.

Fig.3.66 shows the schematic map of channel velocity values will be included in the experimental evaluation of velocity distribution in DANAH mockup.

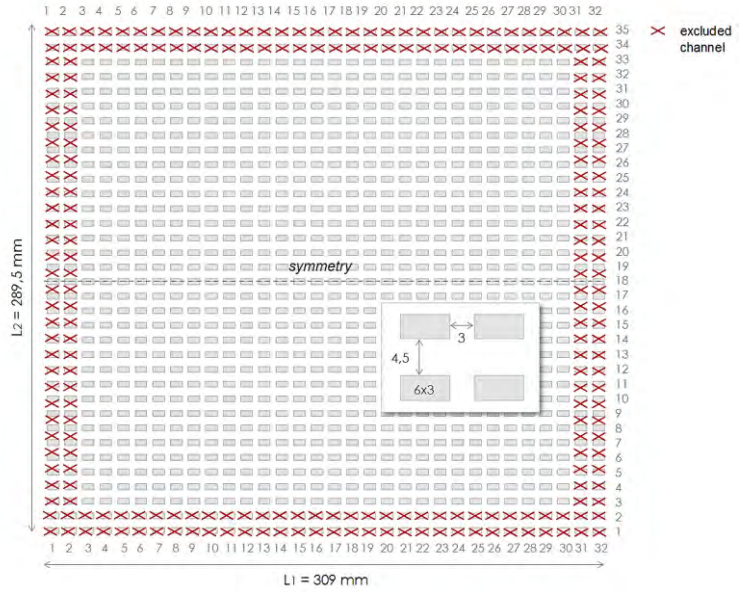

Fig.3. 66 - Schematic map of selected channels for flow analysis

The 3D velocity profile resulting by applying the velocity peak strategy is presented in Fig.3.67.

Once known the flow velocity per channel, it is possible to calculated the flow distribution parameter σ based on standard deviation. The maldistribution factor of the DANAH mockup studied in this chapter is σ = 4.44 %.

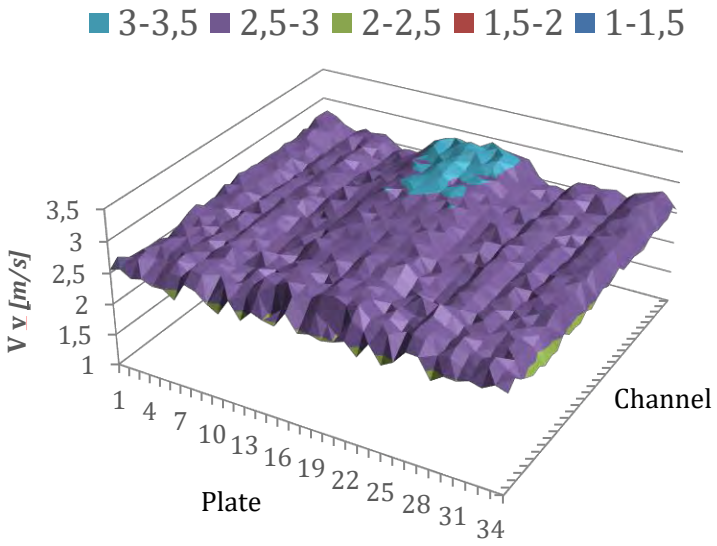

Fig.3. 67 - 3D y velocity profile

3.2.9.5. Influence of a plugged channel

In order to quantify the influence of channel manufacturing defects on the jet flow field, a single channel of DANAH bundle has been entirely plugged during the last phase of PIV campaign. This exercise was considered of great importance in the aim of discerning non-physical velocity measurements related to low accuracy PIV measurements from those related to geometry defects.

As shown in Fig.3.68, a thin Plexiglas surface was interposed on the inlet section of a channel arbitrarily chosen (channel 16 in 26th plate) to obstruct the flow passage.

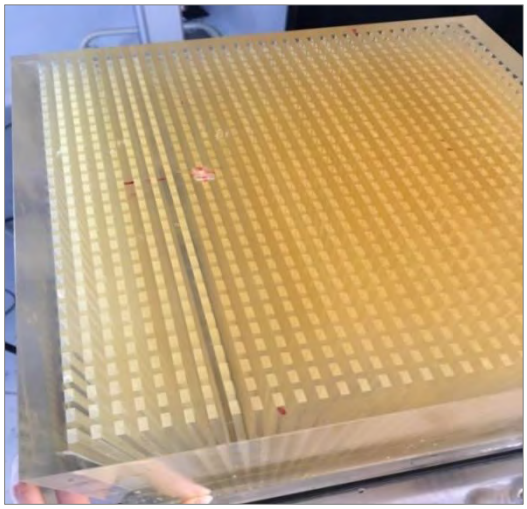

Fig.3. 68 - Channel obstruction in DANAH bundle

The resulting mean velocity field downstream the plugged channel and its neighbors is illustrated in Fig.3.69. It can be observed there are not any traces of turbulent jet out coming from channel 16 which means that a higher jet spacing between channels 15-17 occurs ($\frac{s}{d_h} = 3$) .

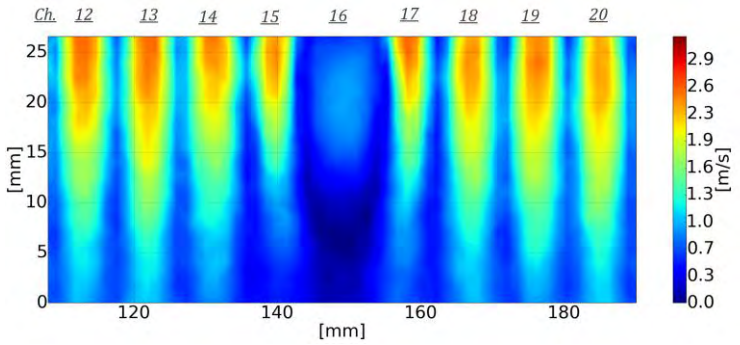

Fig.3. 69 - PIV velocity field downstream the plugged channel

The increased distance leads to a more important entrainment in the mixed region of 15-17 jets, with respect to their outward facing region; the 15 and 17 jets lean towards a lower subatmospheric pressure [66] (parallel jet $s/d_h = 3$). The 15 and 17 jets deflect toward to each other.

For a comparative analysis with the case of equal jet spacing, y-velocity profiles at different positions from the exit channel are drawn in Fig.3.70. Negative values in the shear layer between jets 15-17 appear demonstrating the presence of the *converging region*. The exact location of the merging point between jet 15 and 17 ($v_y = 0$) can also be identified (line y=14).

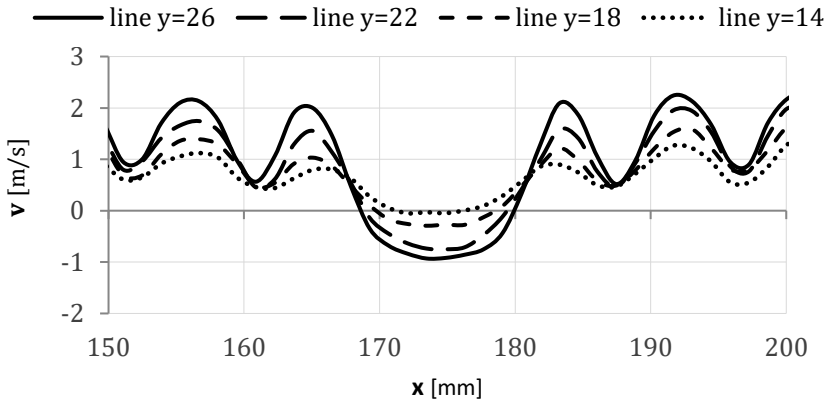

Fig.3. 70 - Y velocity profile downstream the plugged channel

Obviously, also the neighboring jets in z-direction (plate direction) are influenced by the lower pressure regions induced by the plugged channel. Fig.3.71 shows the mean velocity field at O-*Plane 25* and O-*Plane 27* respectively. The flow development of 16th jet in x-y direction suggests a clear tendency of the central jets oh both plates to move towards the low-pressure region.

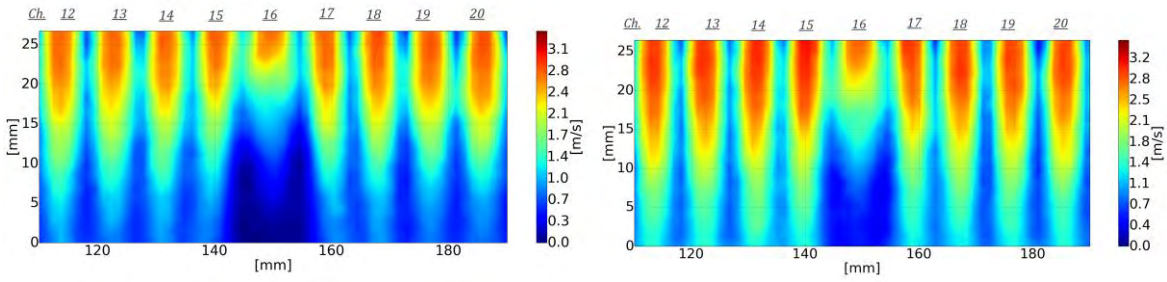

Fig.3. 71 – PIV velocity field at O-Plane 25 (left) and 27 (right) nearby the obstructed channel

3.2.10. Conclusion

An experimental mockup has been conceived and implemented in the CEA thermo-hydraulics loop to study the flow distribution between channels of the SGHE module. It allows acquiring PIV measurements at the inlet header to characterize the flow pattern of the confined jet flow and PIV measurements at the outlet header to estimate the resulting different reparation of flow between channels. The uncertainty analysis shows the accuracy level of each measurement.
In conclusion, bibliographic studies and a detailed analysis of confluent parallel jets at the outlet of the bundle suggests the right strategy to get information about flow distribution.

The preliminary analysis of PIV experimental measurements on DANAH clearly shows the ambitions of the experimental program and the difficulties encountered. For time constraints, one of the initially scheduled DANAH configurations has been then excluded from the analysis, i.e. GD_ (1) _150_NC.
As regards the PIV data at the outlet headers, due to the extreme technicality involved in these measurements and due to time constraints only half of the bundle channel have been investigated (18 – 35).
The available PIV data still provide a trustful experimental database which allows to meet our initial objectives, i.e. the validation of numerical model and the distribution performance comparison between tested DANAH configurations.

Chapter 4

Numerical Study of Flow Pattern in Pre-Distribution Channels

In Section 3.1 of Chapter 3, the experimental strategy conceived for the validation of the fluid flow distribution in SGHE sodium pre-distribution channels has been presented together with a preliminary analysis of flow measurements. In addition, the bibliographic study in Section 2.3, allowed identifying the characteristic fluid flow phenomena occurring in channel bifurcations and which will have a guidance role in the definition of the numerical CFD approach.

First of all, three different turbulence models which could potentially be used to study the flow in bifurcating channels are presented. A first comparison between numerical calculations and EASY-B experimental database aids in retaining one numerical model to be validated against experimental data and to be used to analyze the flow distribution in sodium pre-distribution channels. The bifurcating channel flow is then studied in details to provide an overview of the potential performance in term of flow distribution that can be obtained.
Finally, the validated numerical model is used to perform a parametric study aiming to identify the optimal design for SGHE sodium pre-distribution channels.

The entire CFD analysis is carried out using the ANSYS Fluent® 16.1 in the Windows workstation with 120 GB RAM.

4.1. CFD Numerical approach for the SGHE flow analysis

4.1.1. Turbulence numerical models

Despite most of the research works in Section 2.3.2 used a RANS[13] ε-based turbulence model to study the flow in channel bifurcations, the aim of our investigations and the computational domain dimensions suggest the application of a model providing a more

[13] Remember that the RANS models use the Reynolds decomposition of the velocity field i.e. the velocity U is decomposed as U= $\overline{U}$ + u', with $\overline{U}$ being the average velocity and u′ being the fluctuating velocity

accurate description of near-wall interactions. In the available solver (ANSYS Fluent ®), we would be led to choose between two-equation k-ω-models (Wilcox [72]) and a more sophisticated Reynolds stress transport model [72], i.e. the standard k-ω-model [72], the Shear Stress Transport (SST) model [73] and Wilcox's Stress Omega model [72]. Concerning the two-equation models, the SST model results very interesting due to its potential improvements with regard to the standard k-ω-model. In fact, one of the most known negative features of the standard k-ω-model is its dependence on the freestream values, which might deteriorate the solution for some cases. In this sense, the standard k-ε model is much more stable than the k-ω-model, providing very robust results, no matter the freestream values. On the other hand, the standard k-ω-model is supposed to perform better in the boundary layer region, (even for adverse pressure gradient flows), not needing any specific near-wall treatment. Based on these macroscopic considerations, the SST model blends a standard k-ε model [76] in the fluid bulk with a standard k-ω-model in the boundary layer, using only the positive features of the two original models. Moreover, it can take into account the Bradshaw's relation in duct boundary layer and provides a pseudo-realizability condition by limiting the turbulence kinetic energy production. As conclusion, the SST model is chosen to perform the comparative analysis between models and the experimental data.
The ability of the Stress Omega RSM Model is also investigated in the comparative process. Thanks to its capability of transporting Reynolds stresses, it is supposed to provide the best overall results. However, the poor numerical stability and the very expensive computational cost affecting the RSM solutions lead us toward a new modelling approach provided by Anisotropic SST model [75] [76]. This approach is based on a nonlinear formulation of the Reynolds stress tensors which allows to take into account anisotropic effects. This results in a very good numerical behavior (the added terms are essentially velocity gradients, which do not increase the computational time so much) and in a potentially better fluid flow description. Obviously, there is still the basic lack of the turbulence history, since the turbulence still responds instantaneously to velocity variations. The Anisotropic SST model, validated in one of my previous work [75] on a valuable database for turbulence model validation (NASA and ERCOFTAC), is described in Section 4.1.1.3.

The aim of this section is to compare the three approaches, trying to evaluate their performance on bifurcation channel flow simulations. The best candidate to study the system of channel bifurcation in ASTRID SGHE is then selected.

4.1.1.1. The k- ω SST model

The Shear Stress Transport (SST) model has been proposed by Menter [73]. Transport equations of the turbulent variables the turbulence kinetic energy k and the specific dissipation rate (ω) for an incompressible flow are:

$$\frac{\partial}{\partial t}(\rho k) + \frac{\partial}{\partial x_j}(\rho k u_j) = \frac{\partial}{\partial x_j}\left[\left(\mu + \frac{\mu_t}{\sigma_k}\right)\frac{\partial k}{\partial x_j}\right] + \widetilde{G_k} - \rho\beta^* k\omega \tag{20}$$

$$\frac{\partial}{\partial t}(\rho \omega) + \frac{\partial}{\partial x_j}(\rho \omega u_j) = \frac{\partial}{\partial x_j}\left[\left(\mu + \frac{\mu_t}{\sigma_\omega}\right)\frac{\partial \omega}{\partial x_j}\right] + G_\omega - \rho\beta\omega^2 + D_\omega \tag{21}$$

The turbulent Prandtl numbers for k and ω are expressed in the following way:

$$\sigma_k = \frac{1}{\frac{F_1}{\sigma_{k,1}} + \frac{(1-F_1)}{\sigma_{k,2}}} \tag{22}$$

$$\sigma_\omega = \frac{1}{\frac{F_1}{\sigma_{\omega,1}} + \frac{(1-F_1)}{\sigma_{\omega,2}}} \tag{23}$$

The function F_1 is computed as:

$$F_1 = \tanh(\phi_1^4) \tag{24}$$

$$\phi_1 = min\left[max\left(\frac{\sqrt{k}}{0.09\omega y}, \frac{500\mu}{\rho y^2 \omega}\right), \frac{4\rho k}{\sigma_{\omega,2} D_\omega^+ y^2}\right] \tag{25}$$

$$D_\omega^+ = max\left[2\rho\frac{1}{\sigma_{\omega,2}}\frac{1}{\omega}\frac{\partial k}{\partial x_j}\frac{\partial \omega}{\partial x_j}, 10^{-10}\right] \tag{26}$$

The turbulence kinetic energy production term in the SST models has a limiter defined as:

$$\widetilde{G_k} = min(G_k, 10\rho\beta^* k\omega) \tag{27}$$

where $G_k = \rho\overline{u_\iota u_J}\frac{\partial U_i}{\partial U_j}$

The specific dissipation rate production is given by:

$$G_\omega = \frac{\rho\alpha}{\mu_t}\widetilde{G_k}, \qquad \alpha = F_1\alpha_{\infty,1} + (1-F_1)\alpha_{\infty,2} \tag{28}$$

$$\alpha_{\infty,1} = \frac{\beta_{i,1}}{\beta^*} - \frac{\kappa^2}{\sigma_{\omega,1}\sqrt{\beta^*}} \tag{29}$$

$$\alpha_{\infty,2} = \frac{\beta_{i,2}}{\beta^*} - \frac{\kappa^2}{\sigma_{\omega,2}\sqrt{\beta^*}} \tag{30}$$

The coefficient β is expressed by:

$$\beta = F_1\beta_{i,1} + (1 - F_1)\beta_{i,2} \tag{31}$$

The Cross-Diffusion term D_ω is expressed as follows:

$$\beta = F_1\beta_{i,1} + (1 - F_1)\beta_{i,2} \tag{32}$$

$$D_\omega = 2(1 - F_1)\rho\frac{1}{\sigma_{\omega,2}}\frac{1}{\omega}\frac{\partial k}{\partial x_j}\frac{\partial \omega}{\partial x_j} \tag{33}$$

Finally, the model is closed by the definition of the eddy viscosity:

$$\beta\mu_t = \frac{\rho k}{\omega}\frac{1}{max\left[1, \frac{S^* F_2}{a_1\omega}\right]} \tag{34}$$

$$F_2 = \tanh(\phi_2^2), (15)\ \phi_2 = max\left(\frac{2\sqrt{k}}{0.09\omega y}, \frac{500\mu}{\rho y^2\omega}\right) \tag{35}$$

S* is the modulus of the strain rate tensor, i.e.:

$$S^* = \left(\frac{1}{2}S_{ij}S_{ij}\right)^{1/2} \tag{36}$$

where $S_{ij} = \left(\frac{\partial U_i}{\partial x_j} + \frac{\partial U_j}{\partial x_i}\right)$.

Both the F_1 function and the F_2 function blend the high-Re (k-ε based) and the boundary layer (k-ω based) formulation of the model.

Finally, model constants are:
$\sigma_{k,1} = 1.176, \sigma_{k,2} = 1.0, \sigma_{\omega,1} = 2.0, \sigma_{\omega,2} = 1.168,\ \beta^* = 0.09, a_1 = 0.31,\ \ \beta_{i,1} = 0.075, \beta_{i,2} = 0.0828$.

4.1.1.2. The Stress Omega Reynolds Stress Model

The Reynolds stress model (RSM) closes the Reynolds-averaged Navier-Stokes equations by solving transport equations for the Reynolds stresses, together with an equation for the dissipation rate [77]. This means that seven additional transport equations must be solved

in 3D flows. The Stress Omega model [72], it is based on Reynolds stress transport equations (36) and on the ω transport equation (21) without the term D_ω.

$$\frac{\delta}{\delta t}\left(\rho\overline{u'_\iota u'_\jmath}\right) + \frac{\delta}{\delta x_k}\left(\rho x_k \overline{u'_\iota u'_\jmath}\right) = \frac{\delta}{\delta x_k}\left[\left(\mu + \frac{\mu_t}{\sigma_t}\right)\frac{\delta}{\delta x_k}\left(\overline{u'_\iota u'_\jmath}\right)\right] - \rho\left(\overline{u'_\iota u'_k}\frac{\delta u_j}{\delta x_k} + \overline{u'_\jmath u'_k}\frac{\delta u_i}{\delta x_k}\right) + \emptyset_{ij} + \varepsilon_{ij} \quad (37)$$

where $\varepsilon_{ij} = \frac{2}{3}\delta_{ij}\rho\beta^* k\omega$

In particular the different pressure-strain formulation is modelled as the sum of the slow pressure-strain $\phi_{ij,1}$ and a rapid pressure-strain term $\phi_{ij,2}$:

$$\emptyset_{ij} = \emptyset_{ij,1} + \emptyset_{ij,2} \quad (38)$$

where:

$$\emptyset_{ij} = -C_1\rho\beta^*{}_{RSM}\omega\left[\overline{u'_\iota u'_\jmath} - \frac{2}{3}\delta_{ij}k\right] - \hat{\alpha}_0\left[P_{ij} - \frac{1}{3}P_{kk}\delta_{ij}\right] - \hat{\beta}_0\left[D_{ij} - \frac{1}{3}P_{kk}\delta_{ij}\right] - k\hat{\gamma}_0\left[S_{ij} - \frac{1}{3}S_{kk}\delta_{ij}\right] \quad (39)$$

The Buoyancy and System Rotation Productions have always been neglected, since no system rotation has been identified and buoyancy is not supposed to play a major role in the studied cases.

Note that, the modeling of the pressure-strain and dissipation-rate terms is particularly challenging, and often considered to be responsible for compromising the accuracy of RSM predictions [88].

4.1.1.3. The Anisotropic Shear Stress Transport (ASST) Model

Based on the formulation of the SST model a realizable Anisotropic Shear Stress Transport (ASST) model has been proposed by evaluating a nonlinear formulation of the Reynolds stress tensor as follow [75]:

$$\rho\overline{u'_i u'_j} = \frac{2}{3}\rho k - \mu_t S_{ij} + \rho C_1 k\tau^2\left(S_{ik}S_{kj} - \frac{1}{3}\delta_{ij}S_{kl}S_{kl}\right) + \rho C_2 k\tau^2\left(\Omega_{ik}\Omega_{kj} - \frac{1}{3}\delta_{ij}\Omega_{kl}\Omega_{kl}\right) + \rho C_3 k\tau^2\left(\Omega_{ik}S_{kj} + \Omega_{jk}S_{ki}\right) \quad (40)$$

where $S_{ij} = \left(\frac{\partial U_i}{\partial x_j} + \frac{\partial U_j}{\partial x_i}\right)$, $\Omega_{ij} = \left(\frac{\partial U_i}{\partial x_j} - \frac{\partial U_j}{\partial x_i}\right)$

The closure coefficients C_1, C_2 and C_3 are evaluated as follows:

$$C_1 = \frac{C_{NL1}}{(C_{NL4} + C_{NL5} \cdot S^3)} \tag{41}$$

$$C_2 = \frac{C_{NL2}}{(C_{NL4} + C_{NL5} \cdot S^3)} \tag{42}$$

$$C_3 = \frac{C_{NL3}}{(C_{NL4} + C_{NL5} \cdot S^3)} \tag{43}$$

Table 4.1 shows the values of the five coefficients to be determined:

ASST MODEL COEFFICIENTS	VALUES
C_{NL1}	0.8
C_{NL2}	11
C_{NL3}	4.5
C_{NL4}	1000
C_{NL5}	1.0

Table 4. 1 - NLEVM closure coefficient in present ASST model

The proposed eddy viscosity formulation taking into account the realizability condition (i.e. strain-dependent eddy viscosity in the high-Re region) and the Bradshaw relation in boundary layers is:

$$\mu_t = \frac{\rho \mathcal{B}}{max\left[\frac{\mathcal{B}\,\omega}{C_\mu k}, F_2 S^*\right]} \tag{44}$$

where:

$$\mathcal{B} = a_1 k + C_1 k S^{*2} + C_2 k S^{*2} + C_3 k S^{*2} \tag{45}$$

$$C_\mu = \frac{7.4}{A_1 + S} \tag{46}$$

The value of the A_1 coefficient is $A_1 = \frac{110}{27} = 4.\overline{074}$. The F_2 function is the same as the SST model.

The model is closed through the k and ω transport equations:

$$\frac{\partial}{\partial t}(\rho k) + \frac{\partial}{\partial x_j}(\rho k u_j) = \frac{\partial}{\partial x_j}\left[\left(\mu + \frac{\mu_t}{\sigma_k}\right)\frac{\partial k}{\partial x_j}\right] + \widetilde{G_k} - \rho\beta^* k\omega \quad (47)$$

$$\frac{\partial}{\partial t}(\rho\omega) + \frac{\partial}{\partial x_j}(\rho\omega u_j) = \frac{\partial}{\partial x_j}\left[\left(\mu + \frac{\mu_t}{\sigma_\omega}\right)\frac{\partial \omega}{\partial x_j}\right] + G_\omega - \rho\beta\omega^2 + D_\omega \quad (48)$$

Finally, to be consistent with the NLEV formulation, the turbulence kinetic energy production term can be expressed in the proper form:

$$G_k = -\rho\overline{u_i u_j}\frac{\partial U_i}{\partial x_j} \quad (49)$$

Finally, the specific dissipation rate is expressed in the original form i.e.:

$$G_\omega = \frac{\rho\alpha}{\mu_t}G_k \quad (50)$$

The other parameters not mentioned so far maintains the same definition as the original SST model formulation. Closure constants are:

$$\sigma_{k,1} = 1.176, \sigma_{k,2} = 1.0, \sigma_{\omega,1} = 2.0, \sigma_{\omega,2} = 1.168,$$

$$\beta^* = 0.09, a_1 = 0.31, \beta_{i,1} = 0.075, \beta_{i,2} = 0.0828$$

4.1.2. Computational model and flow boundary conditions

For an accurate experimental validation of numerical models, the computational domain and the fluid flow boundary conditions have to perfectly correspond to the same geometry used in EASY-B experiments.

The dimensions of test sections investigated in Section 3.1 allow for an explicit computation of bifurcation channel domain.

The CFD modelling approach is here detailed for only the simulation of the first mockup of EASY-B. All computations presented in this section are performed following the same procedure. Geometrical features are reported in APPENDIX III.

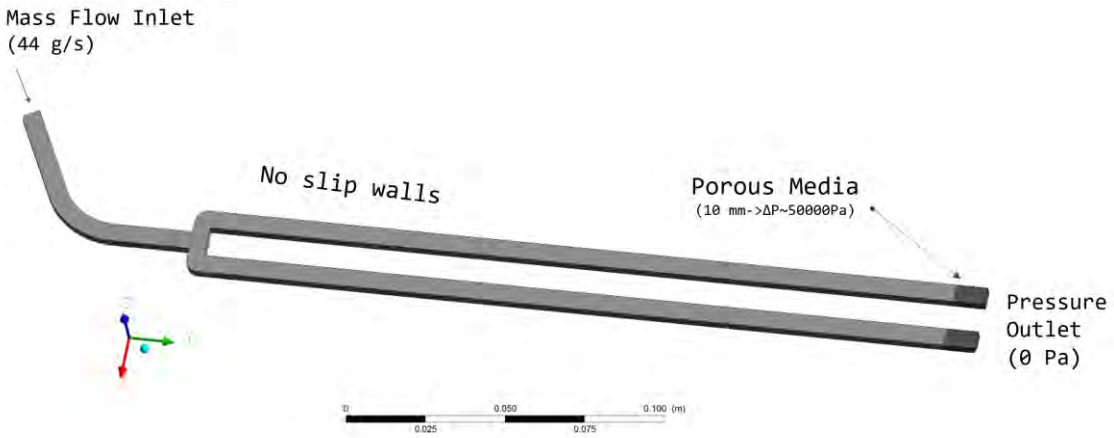

Fig.4. 1 - Computational Model

Inlet pipe

PIV measurements at the inlet pipe of EASY test section demonstrated that a fully developed flow occurs (Section 3.2.7). In CFD simulation, setting the mass flow inlet boundary condition for the incompressible flow corresponds to directly impose a fully developed velocity profile at the inlet. Hence, a shorter length of the inlet pipe of 7,5 d_h is considered for the computational domain (Fig.4.1).

The rightful assumption is further demonstrated by Fig.4.2 where the calculated velocity profile at the inlet is plotted against experimental data. The overlap of the two graphs verifies the uniformity of flow inlet conditions before channel bend.

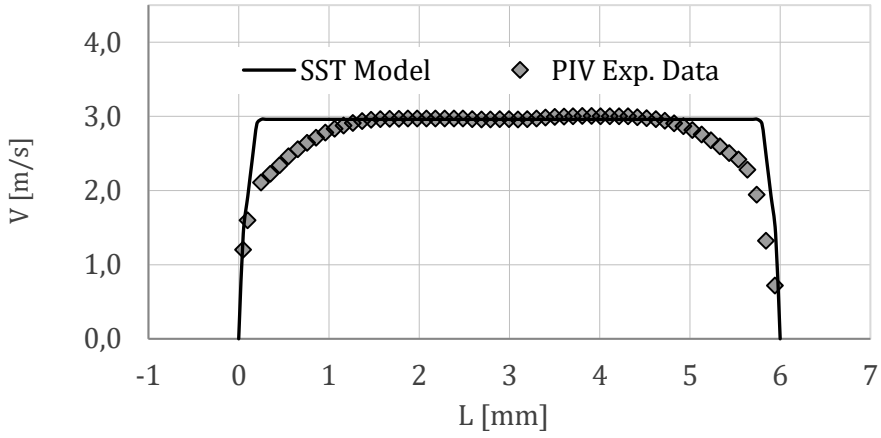

Fig.4. 2 - PIV and CFD inlet velocity profile

To model the additional pressure drops generated by the valve system placed downstream the EASY-B mockup (see Section 3.1.1 for explanation), a porous region is introduced in the computational channel domain (Fig.4.1).
A specific model of the porous source terms allows setting the pressure drop value which is measured by pressure transducers in EASY-B experiments.
For more detailed information about the isotropic porous medium model, see APPENDIX I.

Working fluid
According to EASY-B experiment, the simulated working fluid is water at atmospheric temperature and pressure. Liquid water properties are kept from Fluent database, i.e. density of 998.2 kg/m^3 and a dynamic viscosity of 0.001003 kg/ms.

4.1.3. CFD solver setting

The solver is Pressure-based one and the Coupled pressure-velocity algorithm [78] with pseudo-transient option is used. The coupled scheme, solving the momentum and pressure-based continuity equations together, obtains a robust and efficient single-phase implementation for steady-state flows with superior performance compared to the segregated solution schemes.
Gradients are evaluated through the Green-Gauss Node-Based method. For Pressure, PRESTO scheme [78] is used. For most cases the "standard" scheme is acceptable, but some types of models may benefit from one of the other available schemes even if the computational cost increases. In this case PRESTO is recommended since first of all it improves accuracy and then is highly recommended when porous media are involved.
Second Order Upwind Scheme is used for the spatial discretization of momentum, turbulent kinetic energy and turbulent dissipation rate transport equations.

4.1.4. Grid sensitivity

A grid independence study is conducted to select an economic mesh system as light as possible to maintain a high accuracy of the numerical results. Three structured mesh configurations (hereafter named as Coarse, Medium and Fine) different in the first layer thickness and in the global size of the mesh are studied (Fig.4.3). Due to time constraints the grid convergence study has been performed for only one mockup and one of the

selected turbulent model, i.e. Mockup 1 and k-ω SST model. Geometrical features of the Coarse, Medium and Fine mesh are listed in Table 4.2

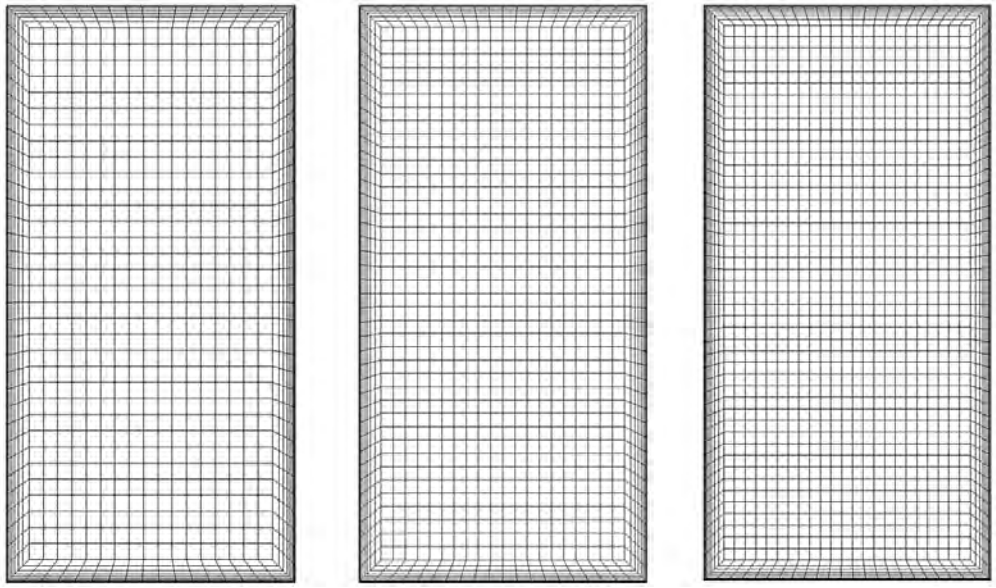

Fig.4. 3 - Coarse, Medium and Fine mesh of channel cross-section

MESH	Cell Size	First layer thickness	Number of cell
Coarse	$1{,}4x10^{-4}$ m	$4x10^{-5}$ m	14 764948
Medium	$1{,}2x10^{-4}$ m	$2x10^{-5}$ m	23 569361
Fine	$1x10^{-4}$ m	$1x10^{-5}$ m	34 602857

Table 4. 2 - Coarse, Medium and Fine mesh features

The inflation option (first layer thickness) has been used to mesh the boundary layer; the total number of layers is 8 with a growth rate of 1.2. As regard to the meshing method, hexahedral elements have been used for the bended inlet pipe and the straight channels before and after bifurcation. Tetrahedral elements have been used for the bifurcation structure. This strategy provides a high mesh quality in term of orthogonal quality and equiangular skewness.

Fig.4.4 shows the mesh detail of transition elements between the hex and tetrahedral grid.

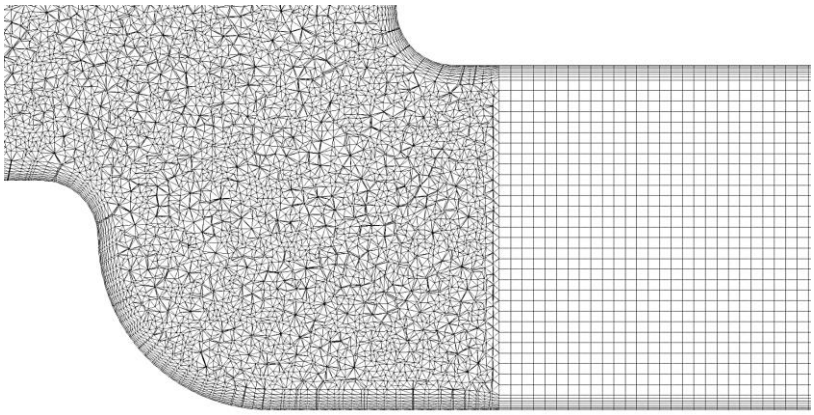

Fig.4. 4 – Mesh detail of bifurcation zone

The dimensionless wall distances, Y+, are evaluated on channel walls before the last bifurcation. Here, the average wall shear stress τ_w is also evaluated in order to establish mesh convergence.

MESH	Y^+ [-]	τ_w [Pa]
Coarse	1.4	16.963
Medium	1.2	17.053
Fine	0.8	17.046

Table 4. 3 - Wall Y+ and average wall shear stress τ_w for the whole channel

As shown in Table 4.3., Coarse, Medium and Fine mesh configurations present sufficiently similar values of τ_w($\Delta\,\tau_{w\ Medium-Fine} = 0.041\%$). Fig.4.5 shows the wall y+ contour for the Medium grid.

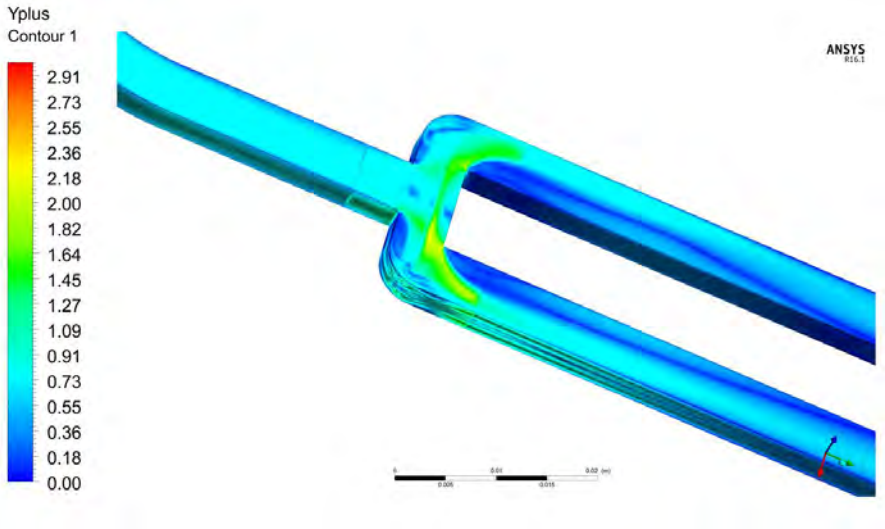

Fig.4. 5 - Wall Y+ contour of bifurcating channel

Moreover, the velocity profile at the centerline of a rectangular cross section at O position (see Fig.4.7) is also drawn for all mesh configurations suggesting a good overlap of the three profiles (Fig.4.6). Based on these trends, we retained Medium Mesh as the reference meshing.

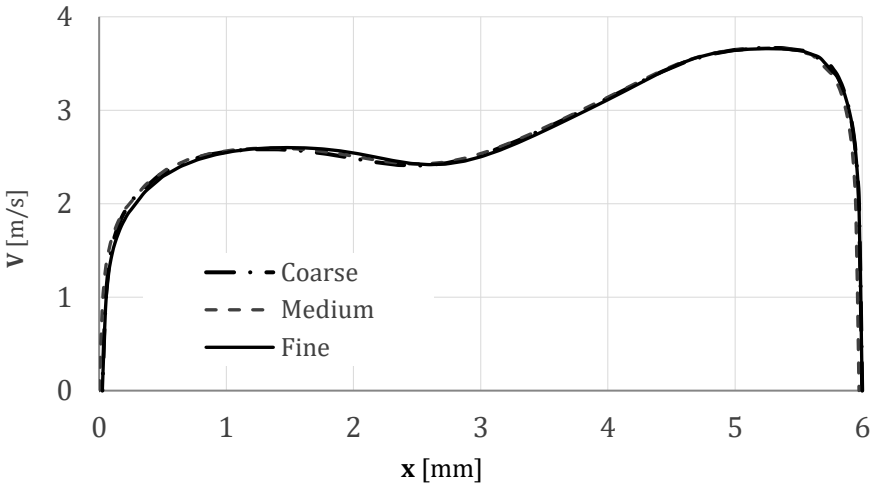

Fig.4. 6 - Mesh Independence Study - Velocity profile at line O

4.1.5. The selection of the CFD numerical model

At this point, once detailed the CFD numerical approach for the analysis of flow in a channel bifurcation, it is possible to compare the numerical results with the experimental data.

It is important to mention immediately that the main purpose of the present paragraph is to evaluate which one of the three turbulence models presented in Section 4.1.1 could give a better prediction of flow phenomena occurring in channel bifurcation.
The vertical velocity profile and u' and v' Reynolds Stresses profiles are plotted on three horizontal lines as illustrated in Fig.4.7. Note that, the selected lines allow testing the performance of numerical models in some critical regions of channel bifurcation where more complex flows occur, i.e. flow development after the inlet bend (line O) and flow separation and reattachment after bifurcation (line C and G).

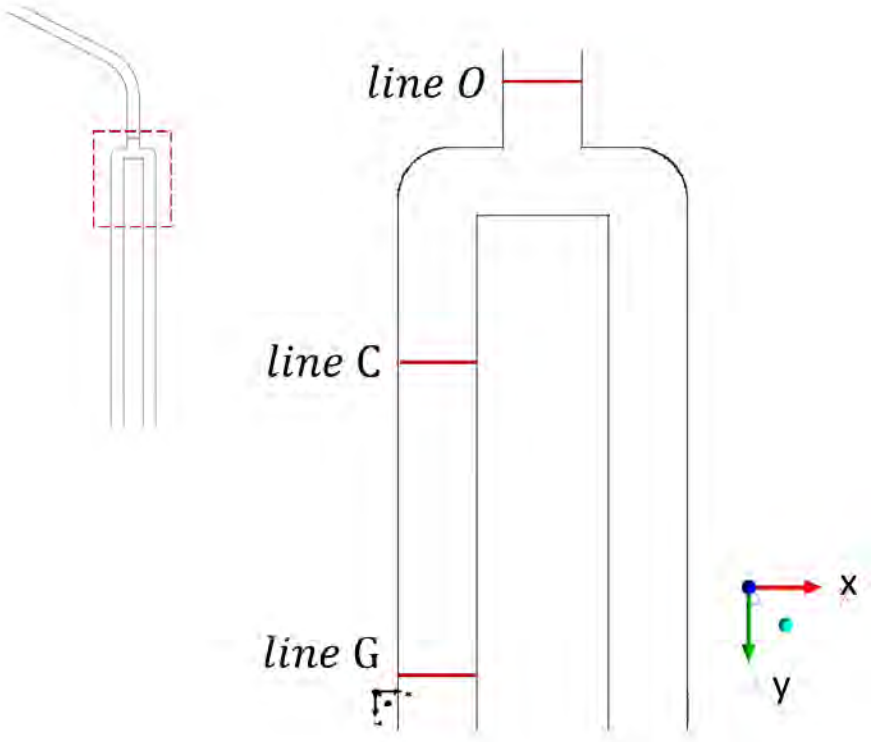

Fig.4. 7 - Selected lines for turbulence model comparison

The vertical velocity v calculated by the k-ω SST, k-ω ASST model and the RSM Stress Omega at *line O, C* and G are plotted in Fig.4.8, 4.9, and 4.10 against the experimental data.

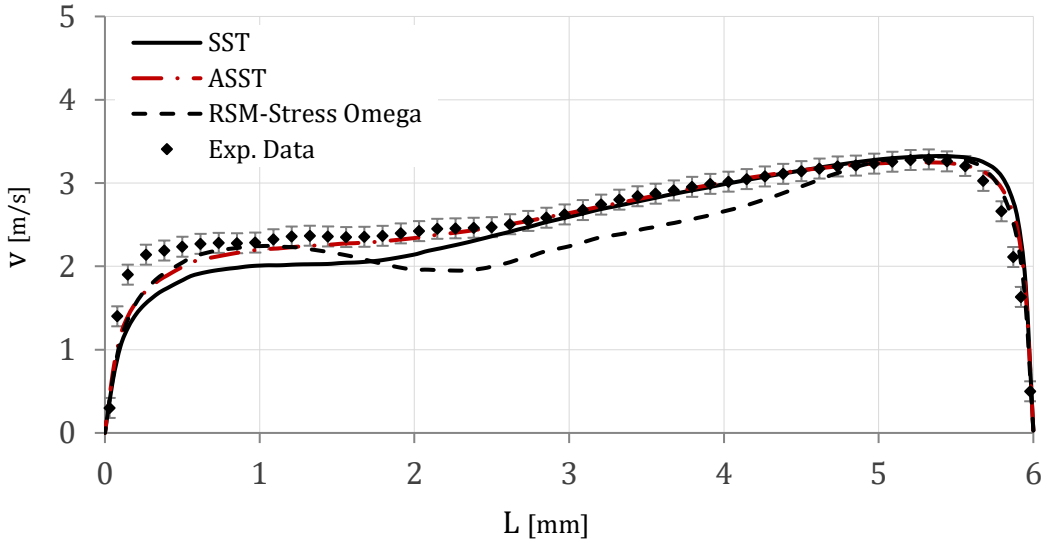

Fig.4. 8 - Experimental vs numerical velocity profile at line O

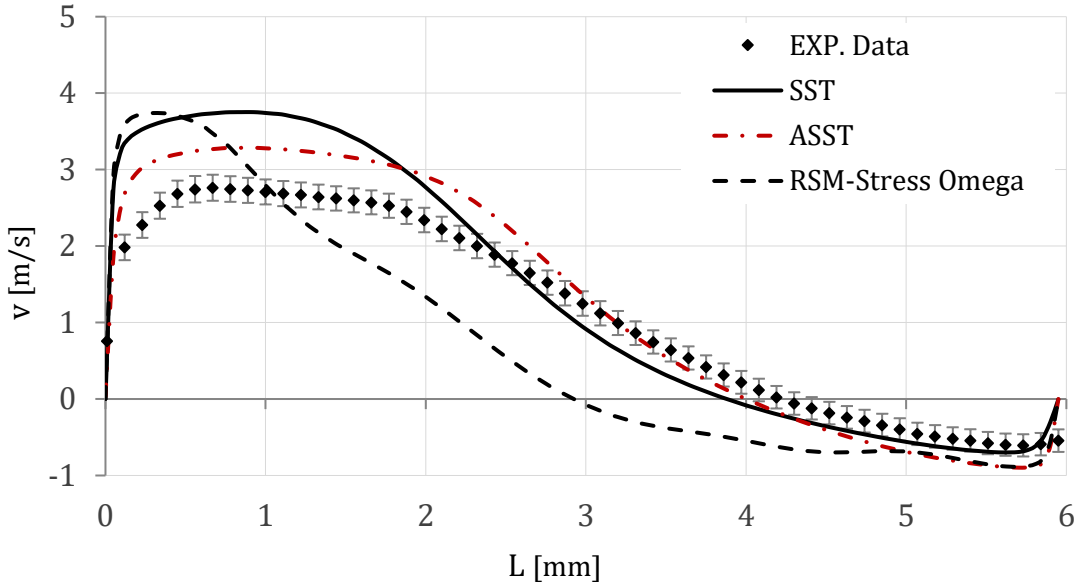

Fig.4. 9 - Experimental vs numerical velocity profile at line C

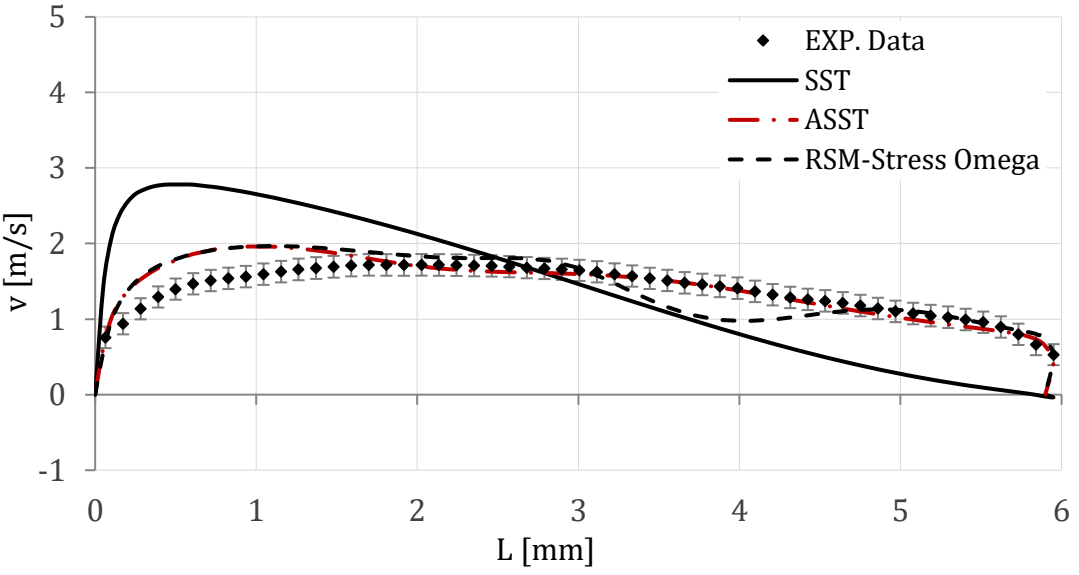

Fig.4. 10 - Experimental vs numerical velocity profile at line G

The comparison between the calculated and measured u' and v' Reynolds Stresses profiles are limited to *line C* and *G*. Results are shown in Fig.4.11-12 and Fig.4.13-14 for u' and v' Reynolds Stress respectively.

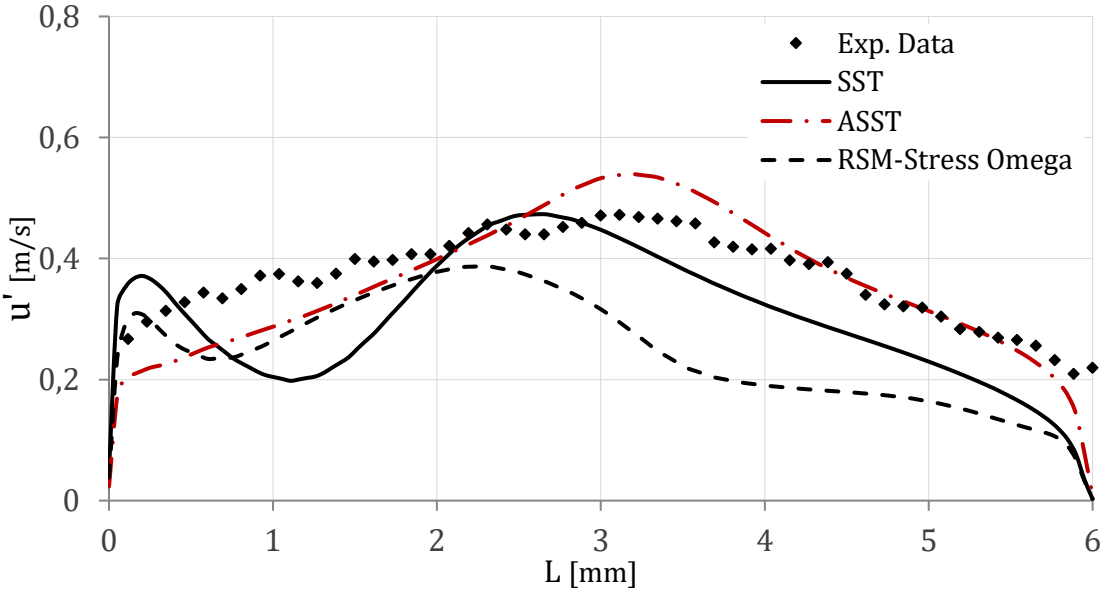

Fig.4. 11 - Experimental vs numerical u′ Reynolds Stress at line C

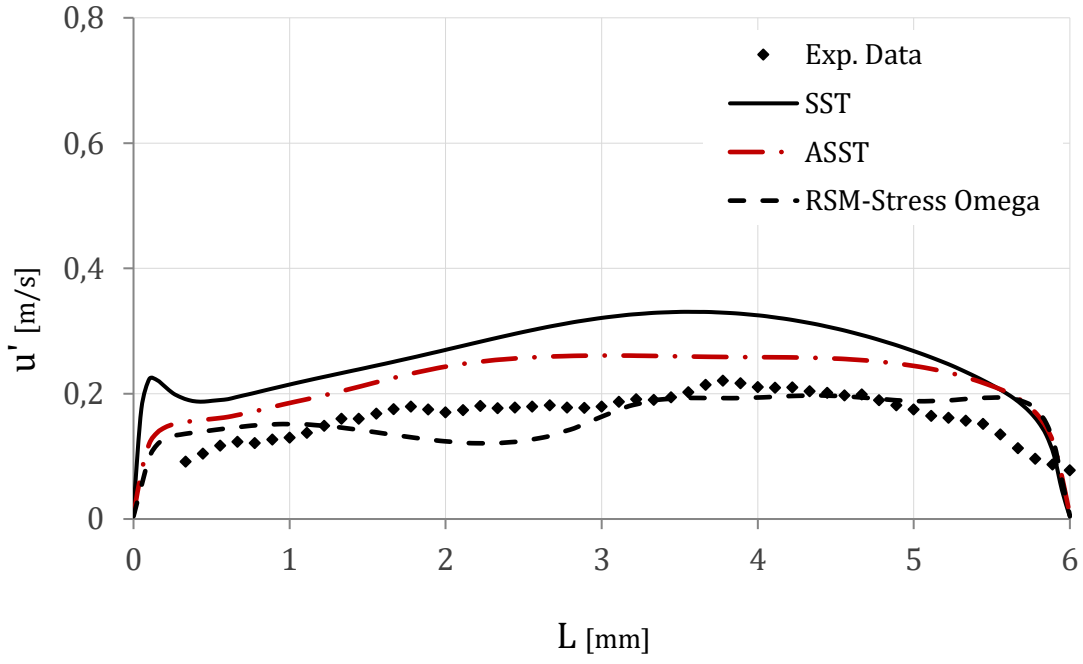

Fig.4. 12 - Experimental vs numerical u′ Reynolds Stress at line G

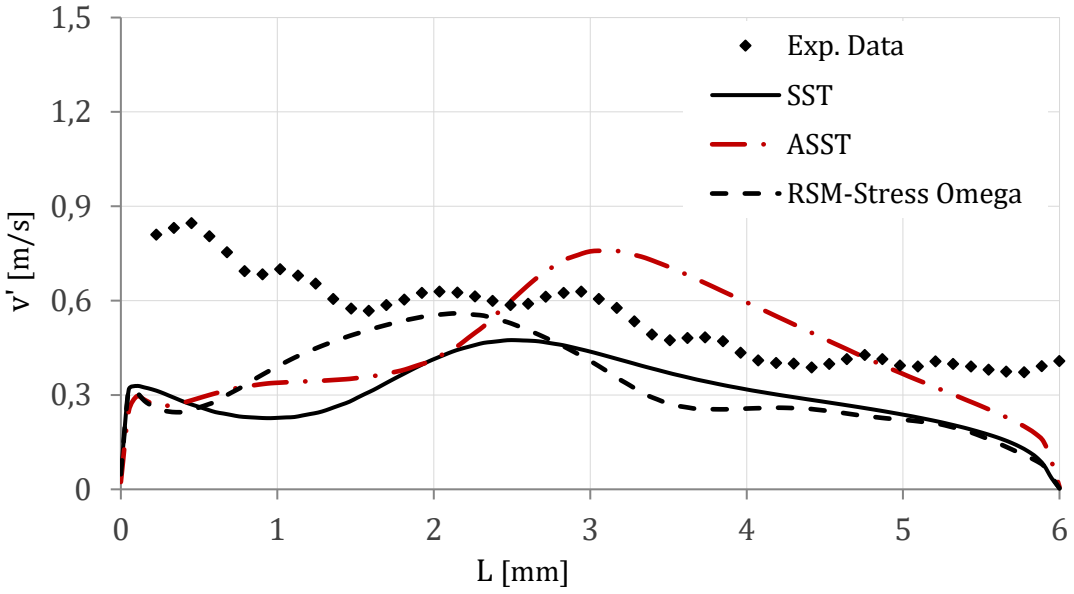

Fig.4. 13 - Experimental vs numerical v′ Reynolds Stress at line C

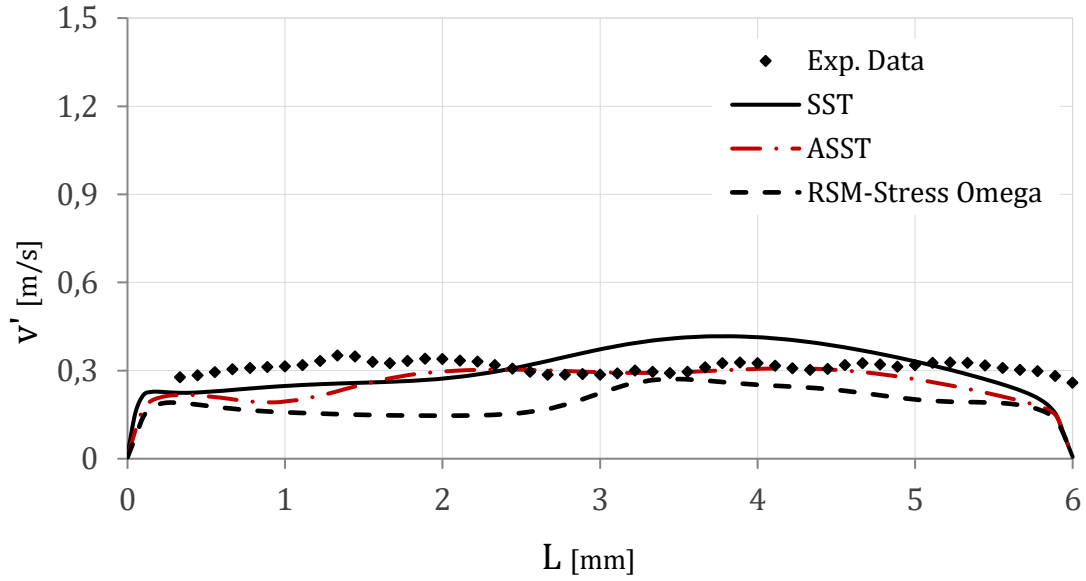

Fig.4. 14 - Experimental vs numerical v′ Reynolds Stress at line G

The comparative analysis of velocity profiles clearly reveals that the anisotropic k-ω ASST model provides the best overall results.

In the first channel before bifurcation, the velocity v on line O seems to be better predicted by the two-equation models, while the RSM-Stress Omega shows some difficulties in the description of flow redevelopment after the inlet bend (Fig.4.8).

At *line C*, more important differences appear between the three turbulence models (Fig.4.9). The SST model overestimates the asymmetry of velocity profile. The reason of model failure has to be searched in the isotropic formulation of turbulent viscosity. In fact, the ASST model, taking into account the anisotropic turbulence and the lateral flow diffusion, better describes the redevelopment of the velocity profile. Again, the RSM-Stress Omega model shows an unexpected behavior.
The results on *line G* make more evident the different model behavior and confirm the conclusions issued from the previous analysis. See that an important asymmetry of the velocity profile is predicted by the isotropic model. The ASST model results are in a perfect agreement with the experimental data.

As regards the velocity fluctuations, the ASST k –ω model gives slightly better results than the two others. In particular, as shown in Fig.4.11 and 4.14, the ASST model is in a better agreement with the experimental data. However, all three models fail in the prediction of the vertical component of Reynolds Stress, v' at line C.

It is interesting to note that, both experiments and computations reveal higher velocity fluctuations on *line C* (u' and v' on Fig.4.11 and 4.13) with respect to those on *line G*. This suggests the presence of instabilities and high perturbed flow in the separation zone after bifurcation [79]. This issue will be analyzed in more detail in Section 4.2.

From the above comparison and considering the unexpected behavior of the Stress Omega-RSM, the ASST model is chosen as reference model for the following analysis. The anisotropic ASST model gives global results that are better than those of the RSM model. Moreover, it keeps a very shorter computational time, resulting to be a very good option for the industrial tools which will be used to design the pre-distribution channels of ASTRID SGHE.

4.2. Model Validation and Flow Analysis

4.2.1. Longitudinal evolution of principal flow

The analysis of the flow through one-stage channel bifurcation is of great significance in the validation of numerical model used to design the pre-distribution channels of ASTRID SGHE module. In fact, as derived from bibliographic studies [80-82], a complex anisotropic flow usually occurs in geometries presenting similar features to T-junction or 90° bend pipe. The correct prediction of flow separation and reattachment phenomena becomes of primary importance.

The anisotropic ASST model and PIV experimental data have been used to investigate the flow through the two bifurcating channels described in Section 3.1, i.e. Mockup 1 and 2. A more detailed analysis aiming to determine the correct position of separation (SP) and reattachment point (RP) will be performed for the first test section.

Flow Analysis: Mockup 1

Fig.4.15 compares the time-averaged flow field measured by PIV and the velocity contour calculated by k-ω ASST model. For sake of clarity, only the most interesting sections of the bifurcating channel have been investigated in Fig.4.15. All velocity data are plotted on the middle plane of channel ($z = 1.5mm$).

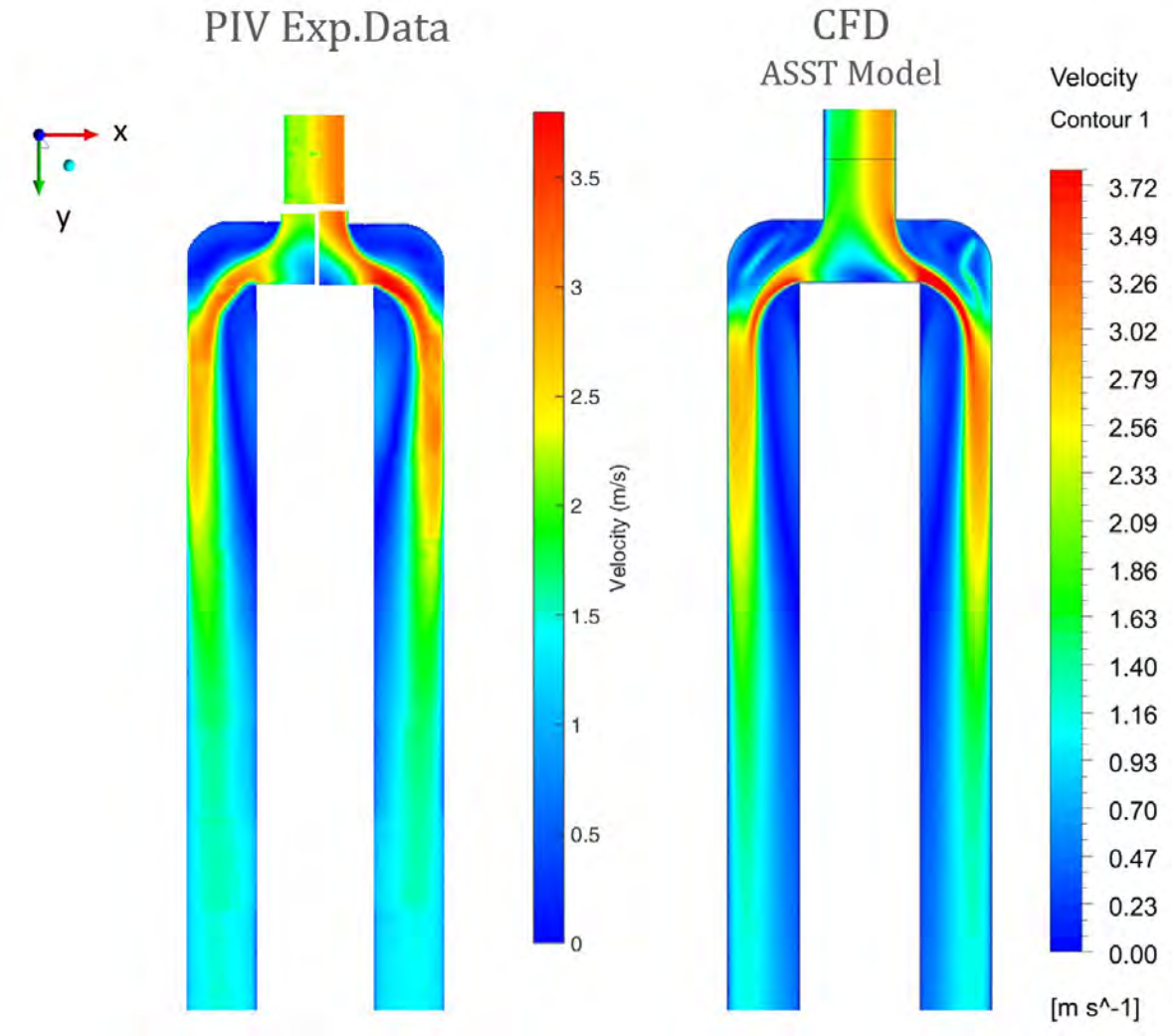

Fig.4. 15 - Velocity field comparison on the middle plane of Mockup 1 (PIV data at the left and k-ω ASST computation at the right)

First of all, a very good agreement between experimental and numerical data can be observed in Fig.4.15.

Referring to velocity contours in Fig.4.15, the longitudinal evolution of the mean velocity is briefly described. After leaving the principal bend channel, the flow impacts on the bifurcation wall. Here, higher pressure region occurs due to the dynamic contribution of the impinging flow (stagnation point). Then, the flow accelerates in both axial directions towards the generated channel bends and the radial pressure gradient developed by the centrifugal force leads to an important flow separation. The flow accelerates towards the outer walls and further downstream redevelops coming back towards the inner walls.

The longitudinal evolution of the mean velocity seems to be correctly described by the numerical model. However, a more rapid flow redevelopment appears in PIV measurements.

In order to provide a more accessible representation of the flow separation region near the inner wall, the y-velocity profiles have been plotted at different positions of the bifurcating channel, for both PIV experimental data and k-ω ASST model results (Fig.4.16). The red dotted lines correspond to the experimental data point whereas the black solid lines to the numerical results.

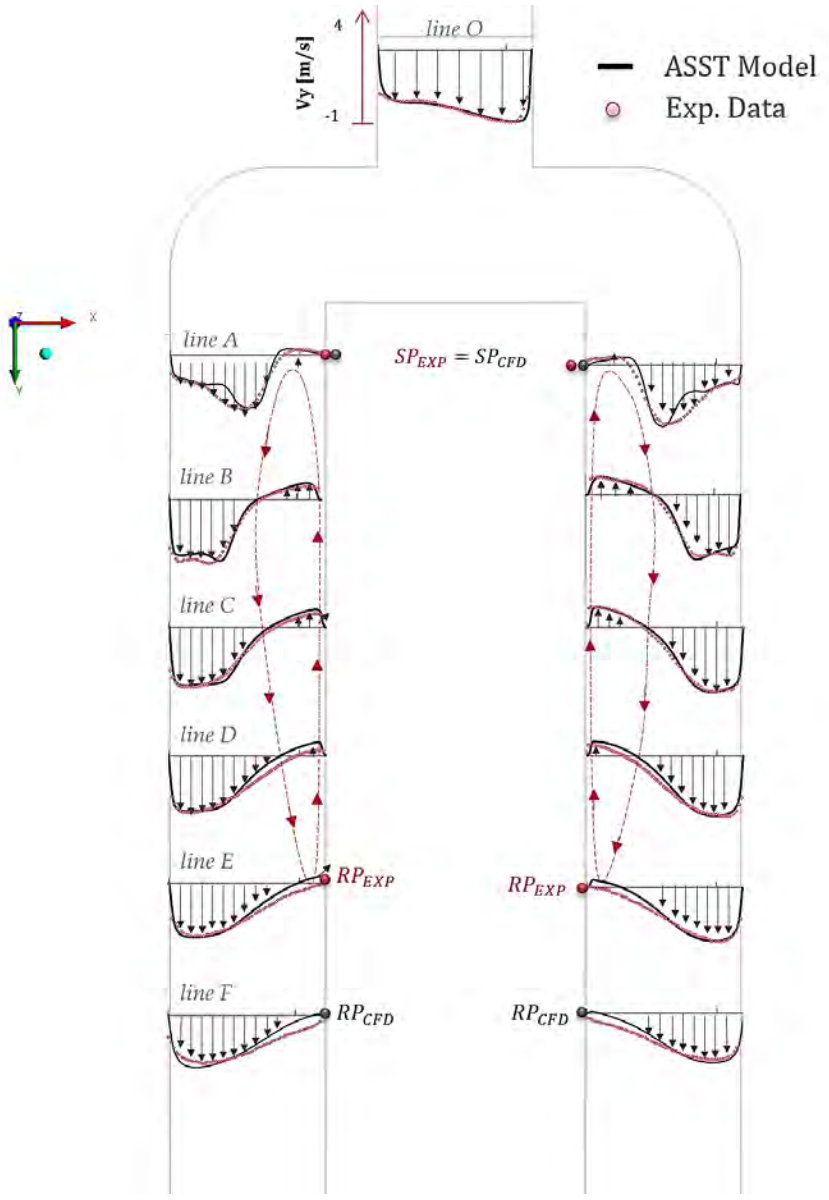

Fig.4. 16 - Longitudinal evolution of flow in Mockup 1 - v velocity profiles

The first quantitative comparison (*line O*) refers to the inlet velocity profile downstream the inlet bend. The perfect overlap of the two lines increases the consistency of the validation process of flow through bifurcations.
At *line A* ($L/d_h = 0.38$[14]), the negative velocity values near the inner walls show the starting point of flow separation ($SP_{PIV} = SP_{CFD}$). The local maximum of the velocity profile manifests the local acceleration of the flow along the bend line (Fig.4.16) whereas the lower values at the outer walls are due to the presence of the low recirculation region at the bifurcation corners (Fig.4.17).

At *line B* and *C* ($L/d_h = 1.63$ and 2.88), the flow skews towards the outer wall and a more asymmetric velocity profile can be noticed. Note that, at line C of the left channel, numerical results seem to slightly overestimate the negative velocity.

Further downstream (*line D-F*), the velocity profiles try to recover their fully developed shape. RP_{PIV} and RP_{CFD} points in Fig.4.16 indicate the position of the reattachment points for both numerical and experimental data. As expected, PIV measurements show a more rapid reattachment of the fluid flow with respect to computations *(line E* at $L/d_h = 5.38$). The reattachment point moves downstream in ASST simulations (*line F* at $L/d_h = 6.23$).

Starting from PIV velocity profiles over the channel length (red dotted profiles), we can try to draw the experimental large vortex occurring in the near wall region. The two red dashed lines in Fig.4.16 display the two clockwise rotating vortices issued by PIV measurements. For a direct comparison with velocity vectors computed by the ASST model, the two-experimental red dashed lines are superposed on Fig.4.17.

[14] In this section, L is counted starting from the bottom wall of bifurcation ($y = 0$)

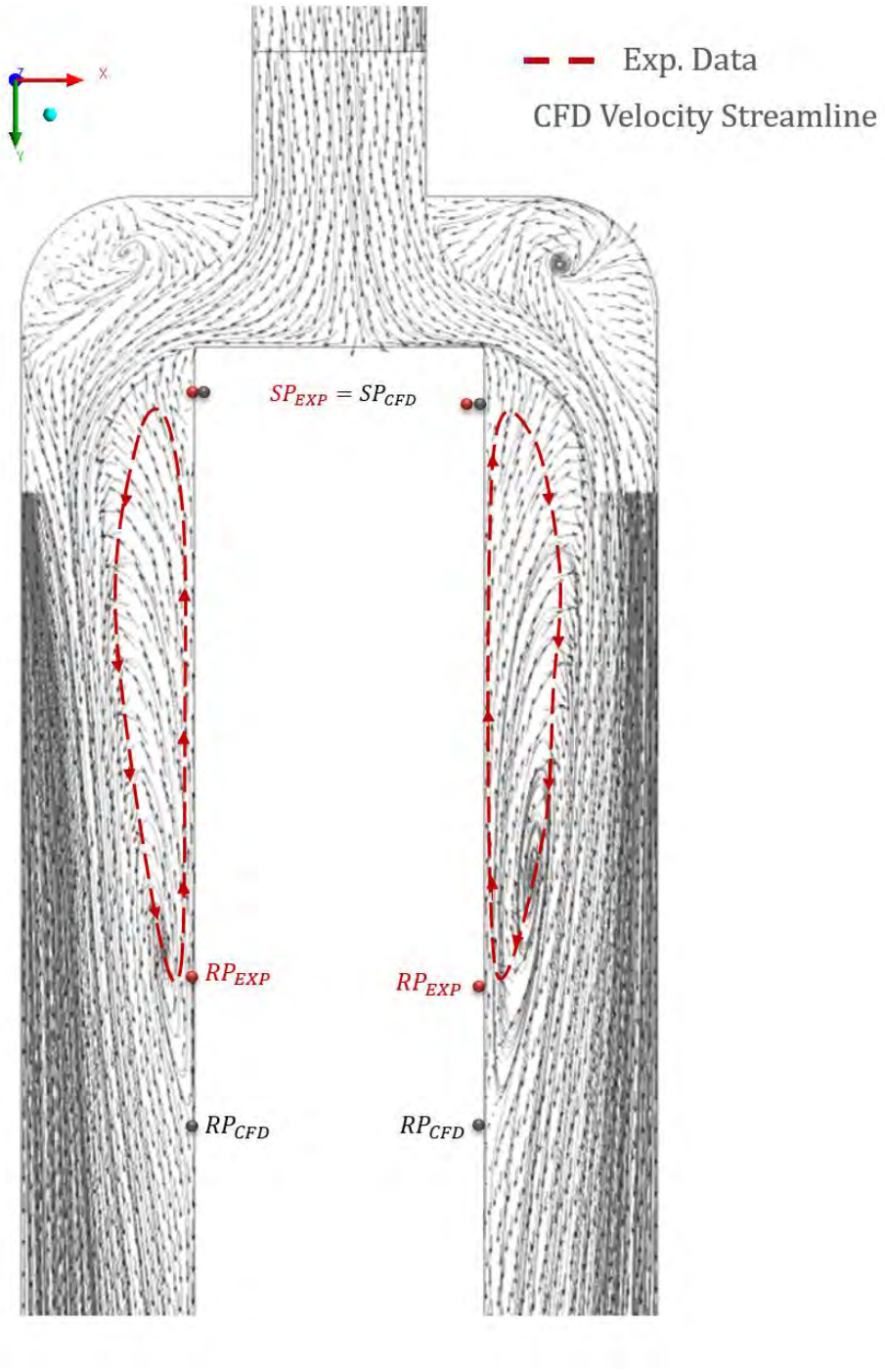

Fig.4. 17 - CFD velocity Streamlines and vectors at the middle plane of Mockup 1

Larger vortices appear in the near wall region and the low recirculation regions at the bifurcation corners can be visualized. Referring to the Fig.4.17, it can be concluded that, despite the anisotropic formulation of turbulent eddy viscosity, the ASST model still fails

in the prediction of the recovery length. However, the turbulence model comparison in Fig.4.9-10 shows the significant improvement yield by the new anisotropic model.

On the other hand, lots of research works on curved ducts justify the model prediction failure in recovery lengths by the complex unsteady flow occurring in the low-velocity region near the inner walls [79-81]. They demonstrated the presence of secondary flows in planes normal to the main flow direction which are characterized by rotating vortices generated by the centrifugal force.
Unfortunately, PIV measurements of the secondary flow are not available for EASY-B experiments. However, the higher velocity fluctuations in Fig.4.11-15 prove the presence of secondary flow (see Section 4.1.5).

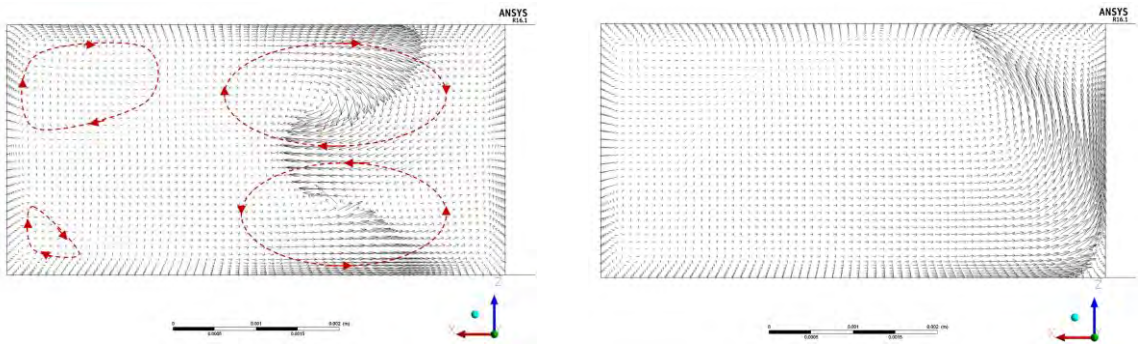

Fig.4. 18 - Velocity vectors on plane normal to the mean flow direction at line B (left) an E (right)

The ASST calculated velocity vectors on x-z planes normal to the main flow direction show the rotating vortices of the secondary flow near bifurcation (Fig.4.18 left), whereas they disappear further downstream after the complete flow redevelopment in generated channels (*line E* of Fig.4.1).

A similar analysis has been performed for the bifurcating channel of Mockup 2. Fig.4.19 shows the mean velocity contours for both PIV experimental data and ASST computation.
Also for the case of channel bifurcations with a curvature fillet at the inner wall, the anisotropic model exhibits great performance.
It can be noticed that, unlike the previous study (Mockup 1), the flow vein remains attached to the inner channel walls and separates slightly further. The pressure gradient in the bend region is too small to move forward against the viscous forces. As a consequence, the low-velocity regions near the inner walls are less disturbed. The curvature fillet alleviates the flow recirculation in this zone providing shorter recovery lengths.

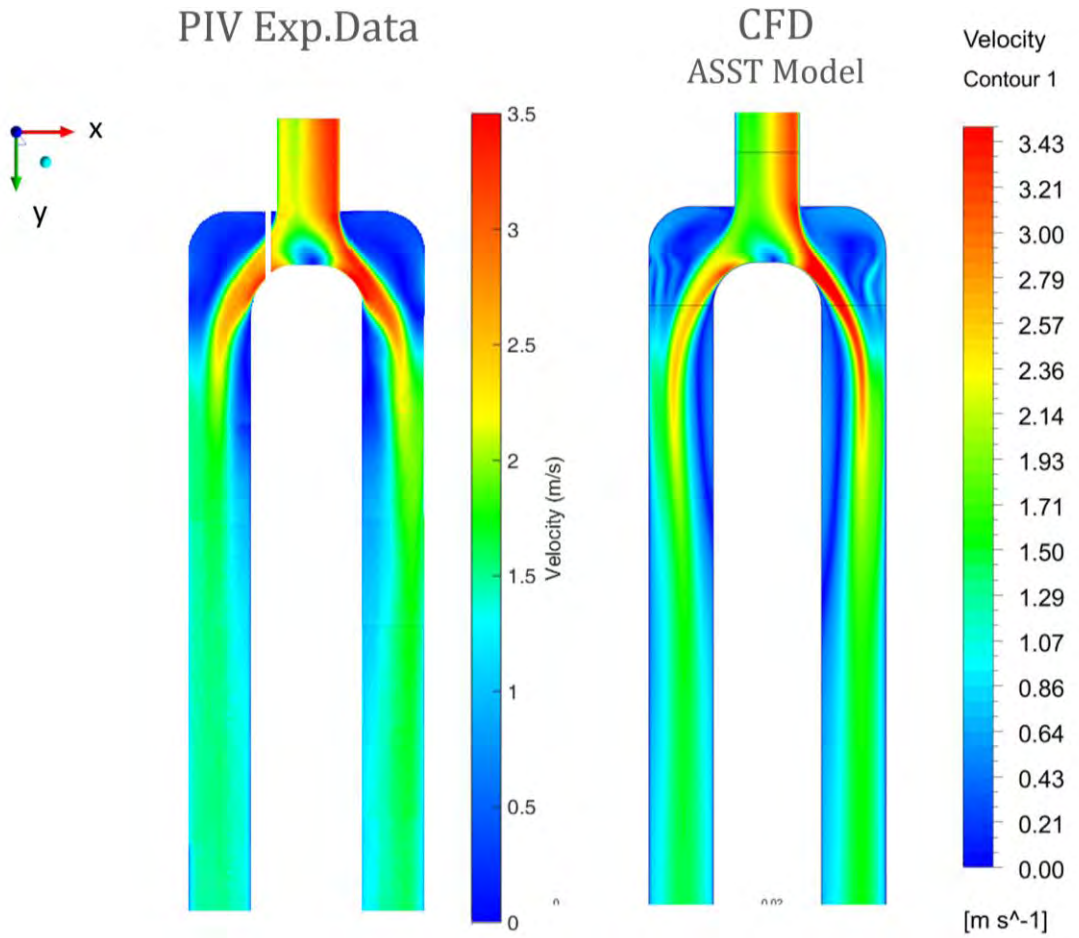

Fig.4. 19 - Velocity field comparison on the middle plane of Mockup 2 (PIV data at the left and k-ω ASST computation at the right)

For a more accurate comparison, aiming to identify the separation and reattachment regions, velocity profiles are plotted on *line A* (at $L/d_h = 0{,}38$), *line B* (at $L/d_h = 1.63$) and *line D* (at $L/d_h = 4.13$) for both generated branches (Fig.4.20-22.).

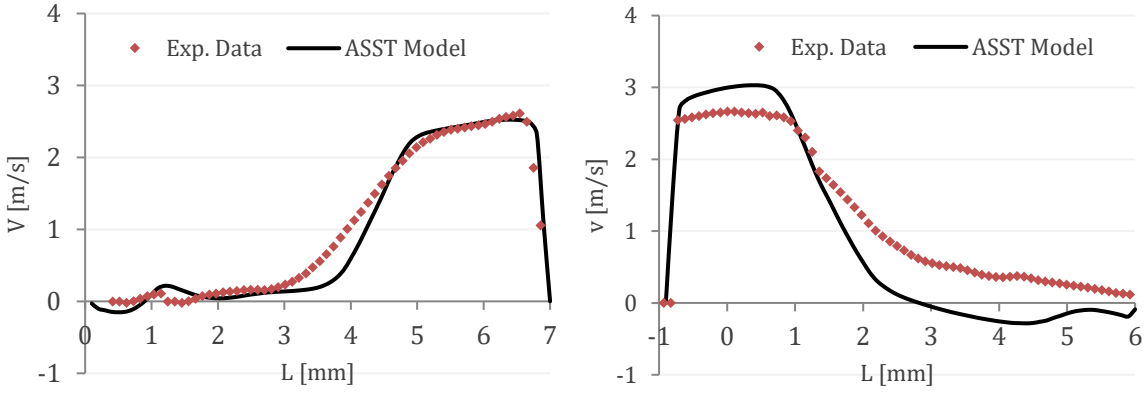

Fig.4. 20 - Velocity profile v at line A on left (left) and right (right) generated branch

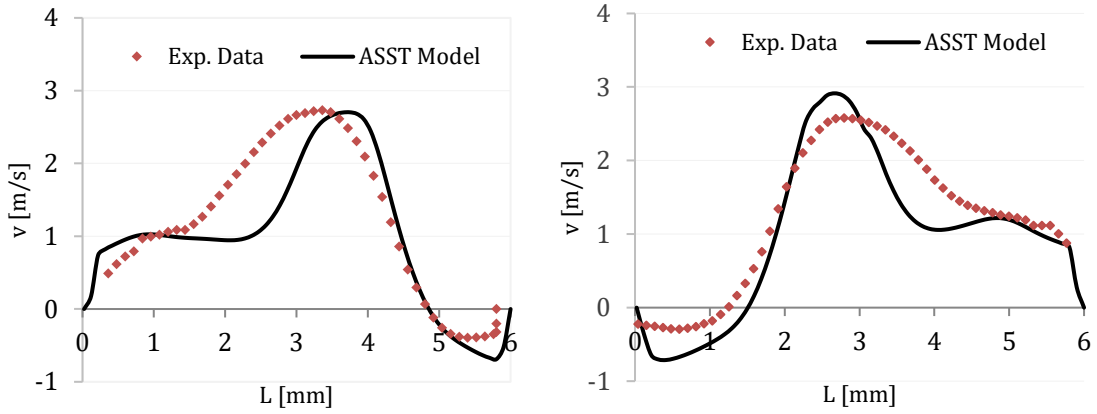

Fig.4. 21 – Velocity profile v at line B on left (left) and right (right) generated branch

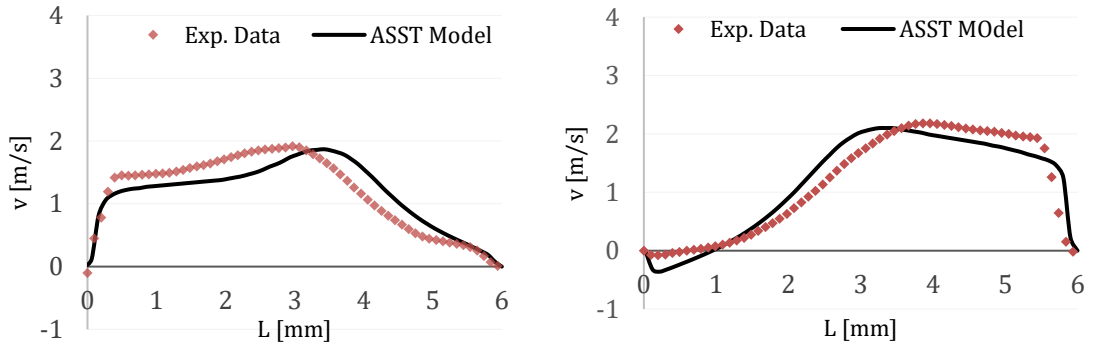

Fig.4. 22 - Velocity profile v at line D on left (left) and right (right) generated branch

Velocity profiles on *line A* clearly show the absence of flow separation at the inner walls. After the impingement on the curvature bifurcation, the flow accelerates remaining attached to the walls. ASST predictions are in good agreement with experimental data even if some discrepancies can be noticed at the outer wall of the right branch. Here, the numerical model seems to describe more important recirculation at the bifurcation corner involving flow separation.

For L/d_h equal to 1.63 (*line B*), the flow separation at the inner walls occurs. Comparing with the velocity profiles at the same lines in Fig.4.16, it can be noticed that the separation point (SP) moves downstream in the present configuration due to the curvature inner radius of bifurcation.

As demonstrated by the local maximum in Fig.4.21, the flow acceleration occurs at the center line of the bend. However, the minor pressure gradient cannot move the flow towards to the outer wall. This allows a more rapid reattachment of the flow vein.

Again, some discrepancies between experimental and numerical prediction can be noticed at the outer sides of velocity profile in Fig.4.21. The ASST model encounters difficulties in the description of the vortex structures growing in bifurcation corners.

Further downstream at *line D* (Fig.4.22), the flow through the left channel completely reattaches the inner wall, while in the right channel it is reached immediately after.

See again that the ASST results are always conservative with respect to the experimental results.

4.2.2. Mass Flow Rate Validation

The analysis of the velocity field in Section 4.2.1 allows for a global validation of the flow field in bifurcating channels. However, to investigate the different repartition of flow between generated channels, mass flow rate measurements in EASY-B experiments need to be compared with the ASST computations.

Table 4.4 and 4.5 summarize the results for the first two mockups studied in this work, i.e. Mockup 1 and Mockup 2. See that, the experimental results are presented together with the uncertainties values. Section 3.2 explained in details the uncertainty quantification method of pressure drops system and the empirical correlation between mass flow and pressure drops.

Mockup 1	$\dot{m}_1$ [g/s]	$\dot{m}_2$ [g/s]
Exp. Data	21.78 ± 2.05	20.67 ± 2.71
ASST Model	22.62	22.33

Table 4. 4 – Experimental vs numerical mass flow rate comparison for both generated channels of Mockup 1

Mockup 2	$\dot{m}_1$ [g/s]	$\dot{m}_2$ [g/s]
Exp. Data	22.77 ± 1.31	23.26 ± 1.89
ASST Model	22.15	22.29

Table 4. 5 – Experimental vs numerical mass flow rate comparison for both generated channels of Mockup 2

The ASST model predictions are in good agreement with the experimental data. The experimental uncertainties range completely contains the calculated values.
It can be noticed that, simulations give a correct estimation of the distribution tendency between generated channels. A different feeding of two generated channels is expected

because of the inlet bended flow. However, very slight differences of mass flow values occur in tested bifurcating channels; thus, the simulations may be questionable in term of convergence and stability. In this sense, result monitors ensure oscillations of mass flow rate lower than 0.01 g/s.

The problem is mostly related to mockup designs used for model validation. They involve very low differences in mass flow between generated branches. Therefore, if we consider the indirect estimation of mass flow, the accuracy of pressure sensors and the hydraulic resistance of two branches, which can never be identical due to the manufacturing tolerance, it could be very difficult to provide a consistent validation of the numerical model.

4.3. Parametric study and Design optimization of the header design

In the first part of the Chapter 4, a basic structure of symmetric flow channel bifurcation allowed to validate the CFD turbulence model proposed to study the sodium distribution in SGHE plate channels.
The selected turbulence model can now be used to finalize the SGHE design process with a decisive and trustworthy optimization of the bifurcation system. An optimal configuration is then proposed for the ASTRID project.

4.3.1. The bifurcation system in SGHE module – Optimization Criteria

The first step of a successful optimization strategy is to point out the principal functions of the flow bifurcations within the entire SGHE distributor system.
An overview of the SGHE module helps achieve this fundamental objective (Fig.4.23).

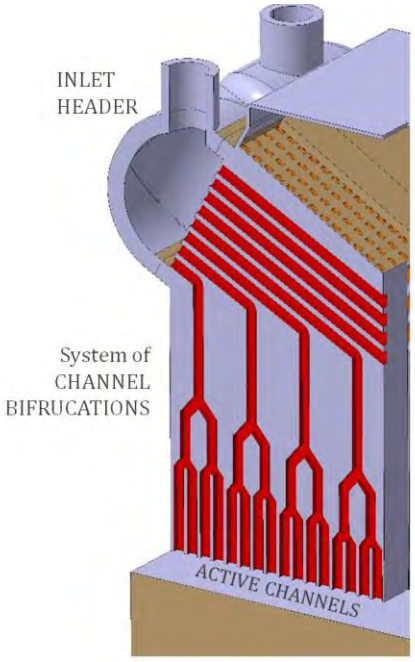

Fig.4. 23 – Detail of SGHE module – Sodium plate

First of all, the bifurcation system has been integrated in sodium pre-distribution channels to reduce the flow maldistribution induced by the poor inlet header design (Section 2.4.1). As already explained in Chapter 2, the increase of pressure drops in the heat core allows for a homogeneous repartition of flow between active channels. Hence, the optimal design of bifurcating channels has to provide the correct amount of pressure drop to minimize σ_{header}. Note that, the upper limit of bundle pressure drop is imposed by the coupling circuit layout of ASTRID reactor, i.e. 50 000 Pa.

Secondly, the bifurcation system design shall not introduce any additional flow maldistribution between its generated active channels. In fact, as demonstrated in Section 4.2.1, the flow phenomena occurring in the bifurcation region could be themselves a new cause of flow maldistribution between generated channels (σ_{b}[15]). Therefore, the optimal bifurcation design has to distribute the flow in downstream branches in such a way to minimize σ_b.

Then, the bifurcation design has to guarantee the same distribution performance whatever the flow conditions at the inlet header. A relationship between σ_{header} and $\sigma_{bifurcation}$ could exist if channel bifurcations show different behavior for different inlet Reynolds numbers. In this case, the additional maldistribution $\sigma_{bifurcation}$ should be combined with the header-induced maldistribution, according to the following statistical relationship:

$$\sigma_{h+b} = \sqrt{\sigma_h^2 + \sigma_b^2 \pm 2\sigma_h\sigma_b\rho(\sigma_h, \sigma_b)} \tag{51}$$

where $\rho(\sigma_h, \sigma_b)$ is the Pearson's coefficient, commonly used to measure the strength of a linear association between two standard deviations.

Therefore, the optimal channel bifurcation design has to show the least sensitivity to Reynolds number ($\rho(\sigma_h, \sigma_b) = 0$).

Finally, the flow bifurcation system shall fulfill the criteria for SGHE module compactness. Hence, the length necessary for pre-distribution channels should be as short as possible in order to leave the maximum amount of space for heat transfer.

In addition, reader has to note that the concept of flow bifurcation system indirectly results in a greater mechanical integrity of the header component. In fact, depending on bifurcation stages, the number of channel facing the inlet header decreases, so that the header volume. The smaller header volume better resists under the external pressure in the vessel (Fig.1.7).

---

[15] The bifurcation-induced maldistribution ($\sigma_{bifurcation}$), will be evaluated using the following factor, based on standard deviation:

$$\sigma_b = \frac{\sqrt{\frac{\sum_i^N (\dot{m}_i - \bar{\dot{m}})^2}{n}}}{\bar{\dot{m}}} x100$$

where m_i is the average mass flowrate in a channel; $\bar{m}$ the average mass flowrate of the whole channels; N is the number of channels in the last stage of bifurcations which is fours in the case of two-stage bifurcations.

The optimization criteria, used to select the most performant design of channel bifurcation, are listed below:

- Bundle pressure drop required to minimize σ_{header}
- Reduction of bifurcation-induced maldistribution ($\sigma_{bifurcation} \rightarrow 0$)
- Independence from Reynolds number
- Compactness of SGHE module

The optimal design will be the result of an overall evaluation and compromise between the above-mentioned criteria.

4.3.2. The bifurcation system – Parametric Study

The bibliographic study in Section 2.3 allowed us identifying the key geometric parameters that would take part to the optimization process of channel bifurcations. Fig.4.24 shows a basic bifurcation structure together with the variable parameters having major influence on flow distribution.

However, due to ASTRID project requirements, some of them cannot be modified. For instance, the hydraulic diameter of channels after and before the bifurcation and the distance between channels at the last stage (W) are imposed by thermal-hydraulic requirements and the observance of safety warnings (see Section 2.4.1 for explanation).

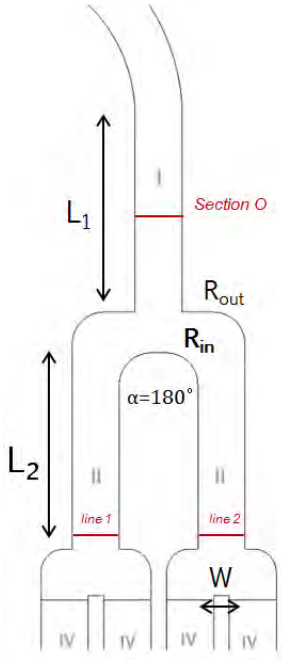

Fig.4. 24 - Bifurcation structure

In addition, based on Liu et al. analysis of different bifurcation angles α, a tee-shape bifurcation structure with $\alpha = 180°$ is chosen for SGHE pre-distribution channel design (more precise control during manufacturing) [42].
Two stages of tee-shape bifurcations are also considered the optimal compromise solution between the mechanical integrity of inlet header (4-fold reduction of channel number facing the header) and the complex manufacturing process.
As conclusion, referring to Fig.4.24, two geometrical factors are identified for the optimization study of pre-distribution channels [91], i.e.:

- R_{in} : Inner curvature radius of bifurcation structure;
- L_1 and L_2: Channel length before (L_1) and after the first bifurcation (L_2).

Their effects on σ_b and bundle pressure drop ΔP are investigated under different inlet flow conditions (Reynolds number).
To name each type of channel configuration studies below, the following nomenclature is used:

$$Rx\_yy - zz$$

where the first group denotes the structure of inner bifurcation fillet; the second and the third group the length of channels upstream and downstream the first bifurcation.

As regard to the numerical model, ANSYS Fluent SST k-ω model has been used for all computations. Although it has been demonstrated that it performs less well than the anisotropic ASST, its direct availability in the Fluent Solver and its rapid convergence to the solution justify this preference.
The working fluid is sodium at the temperature of 437°C ($\rho = 847.2\ kg/s, \mu = 0.000261\ Pa\ s$). Reader is reminded that the final goal is to propose the optimal pre-distribution channel design to be integrated in ASTRID SGHE module.
Fig.4.25 illustrates the computational domain and boundary conditions.

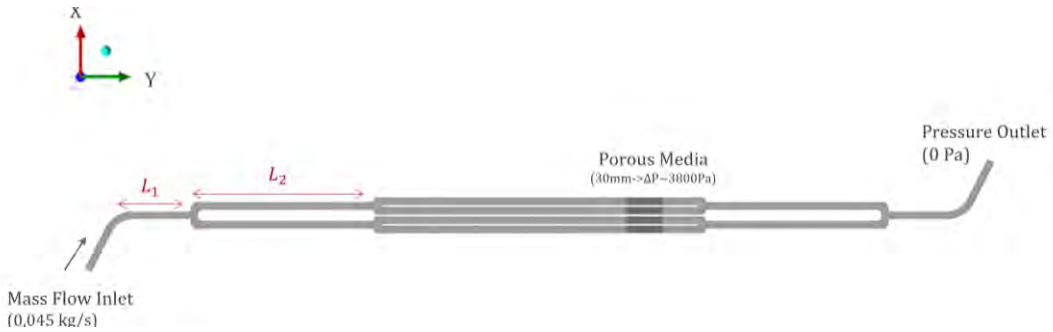

Fig.4. 25 - Computational domain and boundary conditions

4.3.2.1. Influence of the bifurcation structure

Two different configurations of the bifurcation structure are considered in the present section. While the channel lengths remain unchanged ($L_1 = L_2 = 25mm$), two values of the inner curvature radius R_{in} have been tested, i.e.:

- $R_{in} = 0\ mm$ (R0_25-25)
- $R_{in} = 4\ mm$ (R4_25-25)

To better understand their effect on flow maldistribution, a particular attention is paid to the velocity profile on lines 1 and 2 in Fig.4.26. In fact, as already mentioned, the development of the velocity profile upstream the last stage of bifurcation is the main responsible of flow distribution uniformity.

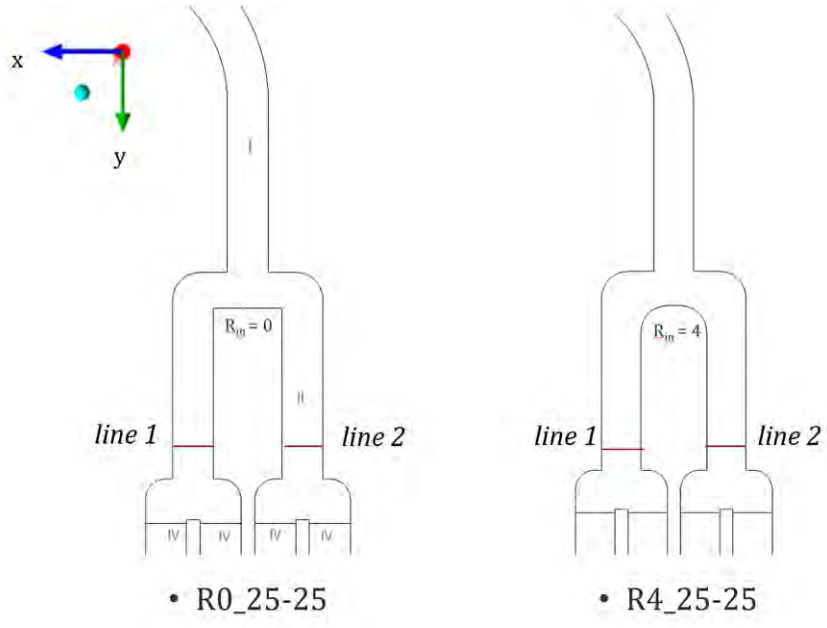

Fig.4. 26 – Structures of flow channel bifurcation – R0 and R4 bifurcation

Fig.4.27 shows the velocity $v_y/\overline{v_0}$ on line 1 and 2 respectively. Note that, v_y represents the local velocity in the main direction of fluid flow and $\overline{v_0}$ is the average inlet velocity.

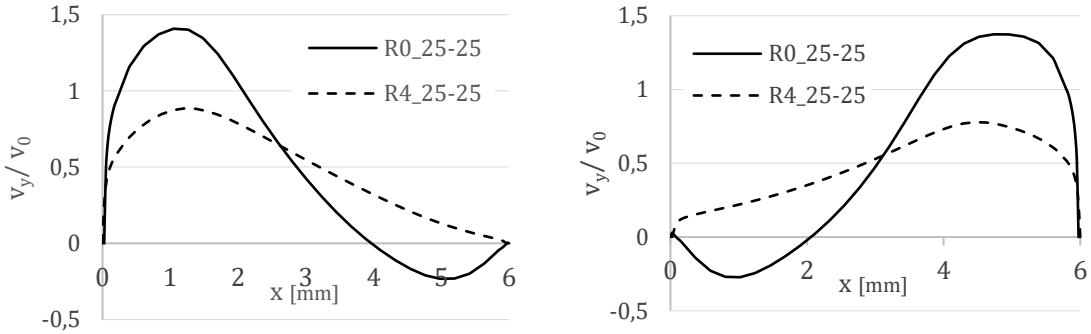

Fig.4. 27 - Velocity profiles at line 1 (continue curve) and line 2 (dashed curve)

The bifurcation structure with $R_{in} = 0\ mm$ shows a more important asymmetry of velocity profile with positive velocity peak shifted towards the outer walls and negative ones towards the inner ones. Differently for $R_{in} = 4\ mm$, for which a more uniform velocity profile occurs. The curvature fillet alleviates the recirculation flow and negative velocity values quickly vanish.

Looking at the velocity profile on the investigated lines it is possible to foresee that in the first configuration more fluid will be convey to the external channels at the last stage ($R_{in} = 0\ mm$). The velocity streamlines in Fig.4.28 helps to understand the described behavior.

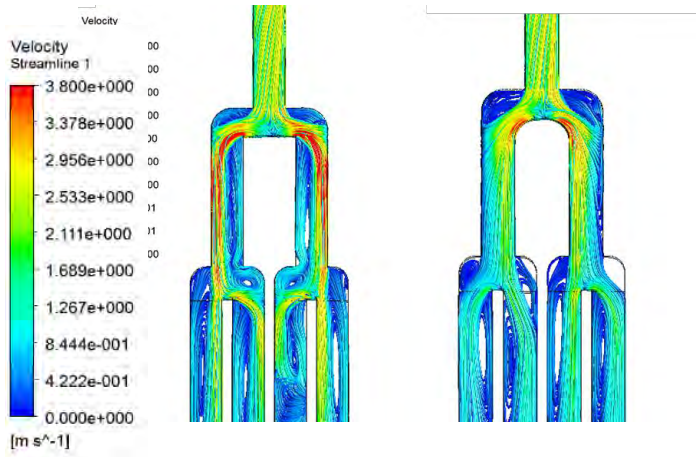

Fig.4. 28 - Velocity streamlines of flow at channel bifurcation for case R0_25-25 and R4_25-25

Channel configuration	σ[%]	ΔP [Pa]
R0_25-25	15.83	45703
R4_25-25	6.25	38600

Table 4. 6 – Maldistribution factor and pressure drops

The maldistribution factors are reported in Table 4.6 together with the pressure drop values at the inlet of bifurcating channel. The higher performance of the bifurcation structure with the curvature inner radius ($R4$) is now unquestioned.

First of all, the $R4$ structure requires a shorter channel length for the flow to reach symmetric velocity profile; this is in total agreement with the compactness criterion. In addition, its lower pressure losses facilitate their integration in the bundle of the SGHE module whose pressure drops are limited to 50 000 Pa.

4.3.2.2. Effect of inlet Reynolds number

In previous tested channel configurations, we always considered an inlet flow rate of 0.044 kg/s (Re 38 000), which is the proper value in case of perfect distribution in SGHE bundle. However, as demonstrated in several occasions, the ASTRID header design could not allow a uniform repartition of flow among all pre-distribution channels.

In order to ensure the distribution performance of bifurcating channels whatever the inlet flow conditions, it is important to study the sensitivity of their design to different Reynolds numbers.

The hydraulic behavior of R0_25-25 and R4_25-25 channel design is investigated for different inlet Reynolds numbers, i.e.

- $Re = 4\,000$
- $Re = 10\,000$
- $Re = 20\,000$
- $Re = 40\,000$
- $Re = 60\,000$

The selected range of inlet Reynolds is issued from preliminary calculations of header-induced maldistribution in Section 2.4.1.

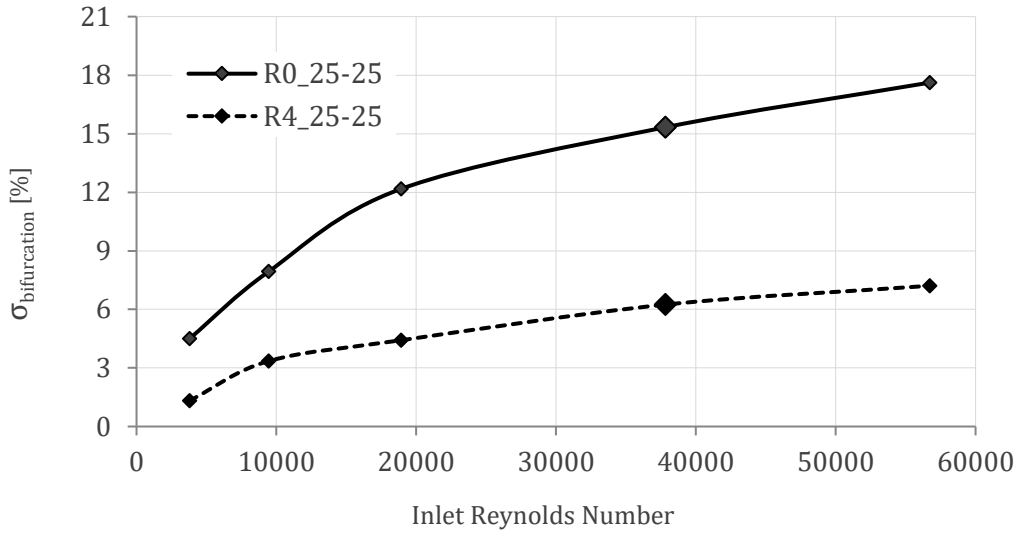

Fig.4. 29 - Flow maldistribution σ_b for different Reynolds numbers

Fig.4.29 shows that the higher the inlet Reynolds number, the worse is the flow distribution uniformity. This is due to the magnitude of flow separation and vorticity inside the bifurcation zone that progressively increases with the Reynolds number.

Moreover, the slope of R0_25-25 curve in Fig.4.30 makes evident its more important sensitivity to Reynolds number with respect to the R4_25-25 design. This means that the R4 design could aid the independence between σ_{header} and $\sigma_{bifurcation}$. The separate analysis between the header and channel bifurcations performance adopted in this work is then justified.

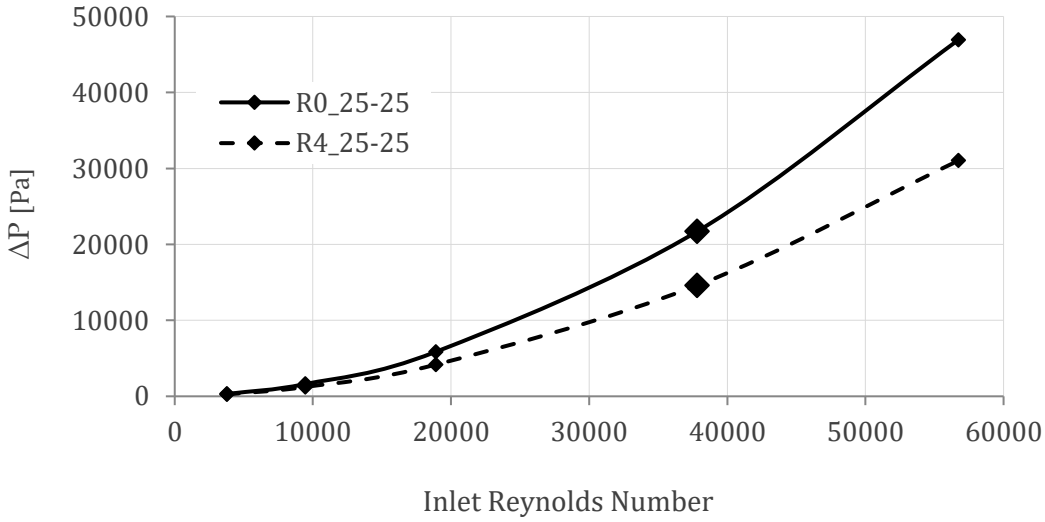

Fig.4. 30 - Pressure drops for different Reynolds numbers

Therefore, lower pressure losses and lower dependence on Reynolds number lead our choice towards R4 channel configurations.

4.3.2.3. Effect of channel length after the first bifurcation

Once identified the structure of pre-distribution channel bifurcation, the influence of channel length L_1 and L_2 is analyzed.

This section aims at determining the ratio $l = \mathrm{L}/d_h$ that gives at channels before and after the first bifurcation a sufficiently long distance to uniform flow distribution with the minimum amount of space and pressure drops.

The flow maldistribution factor and the pressure losses are plotted as function of $\frac{\mathrm{L}}{d_h}$ in Fig.4.31 and Fig.4.32 respectively.

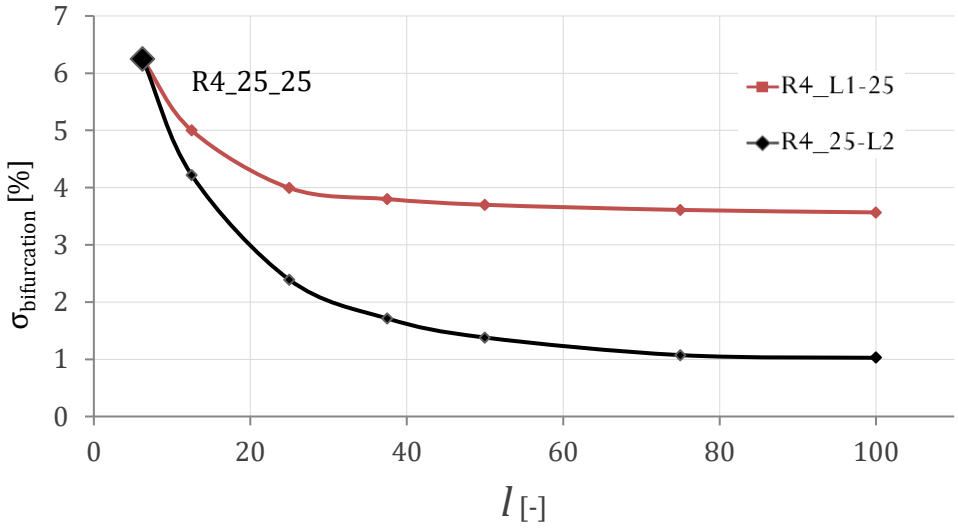

Fig.4. 31 - Flow maldistribution σ_b for different length L1 and L2

Note that the comparative analysis has been performed by varying first the length of channel L_1 (red line) while the L_2 remains fixed at 25mm and then, inversely for the channel L_2 (black line).

Fig.4.31 shows how the flow maldistribution factor decreases with the channel length until it reaches a constant value, i.e. 60 for normalized length $l_1$and 80 for l_2. However, it should be noticed that the increase of channel length L_2 is more advantegeous than L_1. In fact, acting on channel length L_2, it is possible to obtain a maldistribution improvement of 50% higher.

Referring to Fig.4.32, for both studied cases, the pressure drop increases linearly with channel length. However, being equally directly proportional to the square of velocity, a higher slope characterized the pre-distribution channel with longer L_1. As conclusion, the R4 distributor with larger channel length L_2 is to be preferred.

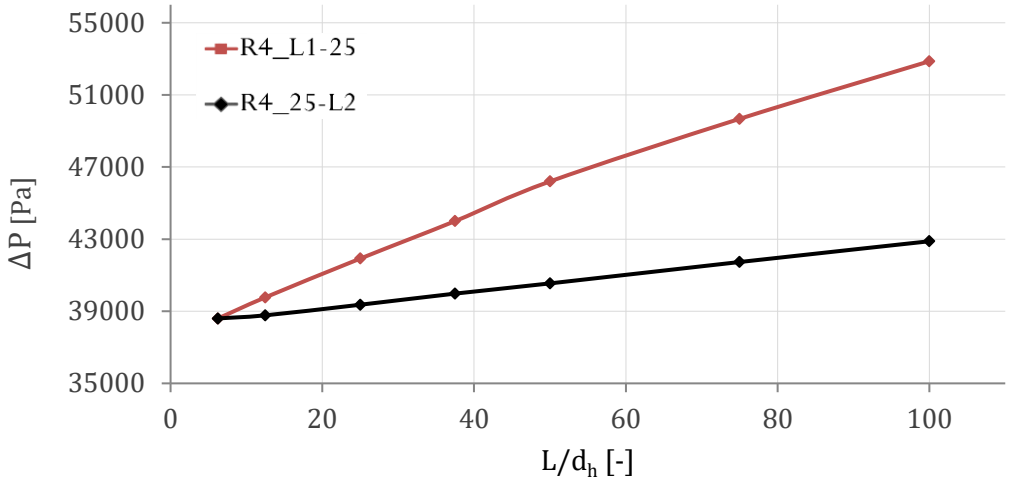

Fig.4. 32 - Pressure drops for different length L_1 and L_2

4.3.3. Distribution performance comparison and conclusion

In Fig.4.33 all the previous parametric studies are summarized. The influence on the bifurcation-induced maldistribution is graphically displayed by different bar height.

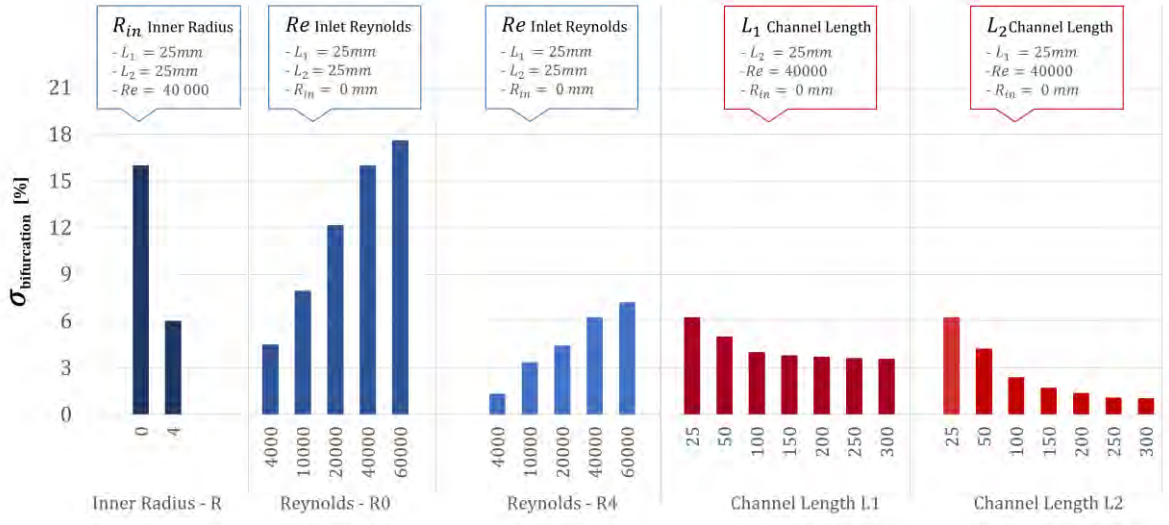

Fig.4. 33- Two-level bifurcating channel parametric study

The first three groups represent the parametric study on the structure of the inner fillet of bifurcation. The first group of blue bars compares the flow distribution associated to the two-different inner radius, i.e. $R_{in} = 0mm$ and $R_{in} = 4mm$. The second and third group analyze the sensitivity of each of them to the inlet Reynolds number.
From this analysis, it clearly emerges that the bifurcation structure with a curvature inner fillet leads to a minor perturbation of flow in the pre-distribution channel. This means a more uniform distribution between generated channels for the same plate length. In addition, the lower pressure drops and the least sensitivity from Reynolds number make this design the one which better fulfils the optimization criteria.

The two-last groups in Fig.4.33 concern the optimization of channel lengths in a pre-distribution channel with $R_{in} = 4mm$. The effect of channel length before and after the first bifurcation has been study separately, i.e. red bars for L_1 and orange bars for L_2.

Marked benefits in term of flow distribution can be noticed from the increase of L_2. In addition, the lower pressure drop permits an easy integration in the bundle of the SGHE. However, it should not to be neglected that, a slightly increase of L_1 can definitively reduce the flow maldistribution due to the inlet bend. A deterioration in term of pressure losses is of course expected.

As conclusion, the final pre-distribution channel design resulting from this optimization process implies two-stage bifurcations with a $R_{in} = 4mm$ and an increase of both lengths L_1 and L_2 according to the proportions indicated in Table 4.7.

Rx_L_1-L_2	**$\sigma_{bifrucation}$ [%]**	**ΔP [Pa]**
R4_50-150	0.62	51 000

Table 4. 7 - Proposed design for two-levels symmetric bifurcating channel

The proposed design allows achieving the required objective in term of flow maldistribution within the limit in pressure drop imposed for the integration of the module in the circuit (i.e. ~50 000 Pa). However, it should be noticed that the total length of the pre-distribution channel could be too large with respect to the plate compactness criterion.
Anyway, the maldistribution factor lower than the unit ($\sigma_b = 0{,}62\%$) means that the bifurcation system does not affect the performance of the module.
The global maldistribution factor of ASTRID SGHE module (Eq.51) can then be reduced as follow:

$$\sigma_{h+b} = \sqrt{\sigma_h^2 + \sigma_b^2 \pm 2\sigma_h\sigma_b\rho(\sigma_h, \sigma_b)} \cong \sigma_{header} \quad (51.1)$$

From this point onwards, the distribution performance of the SGHE module will be evaluated taking into account only the header-induced maldistribution.

4.4. A new design for ASTRID SGHE bifurcating channels

Previous analysis in Section 4.3 shows that even if the flow maldistribution σ_b induced by two-stage bifurcating channels could be improved thanks to varying geometric features, none of the studied configurations perfectly fulfills the selection criteria mentioned in Section 4.3.1. For instance, the optimal bifurcating channel R4_50-150 still involves high pressure drop and a large plate length.

On the other hand, the better understanding of the effects of several geometric factors and flow conditions on maldistribution allow us to propose a new solution to homogenize flow distribution in pre-distribution channel bundle of ASTRID heat exchanger.
For example, a further improvement of distribution channels is shown on the right of Fig.4.34. The basic two-level bifurcating channel design is also illustrated for comparison on the left.

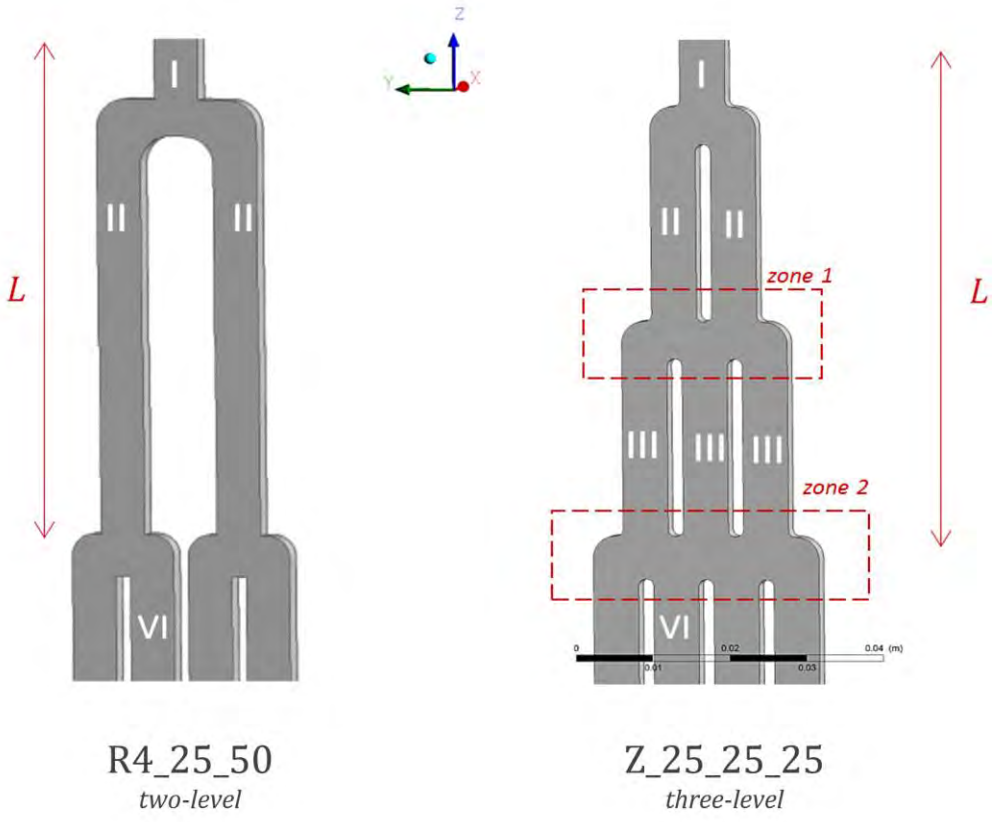

Fig.4. 34 - Two-level (left) and three-level (right) bifurcating channel

Here, the introduction of a supplementary bifurcation level (III) and the lateral connections between channels at the bifurcation zones (*zone1* and *zone2*), which are

surrounded by red dotted lines in Fig.4.34, lead to a significant reduction of maldistribution factor [37].

An evidence of the best performance of the new proposed design is provided by Table 4.8, where three different pre-distribution channels are compared. Note that, the total length L from the principal channel to the generated ones is kept fixed ($L_1 + L_2 = l_1 + l_2 + l_3$= 75mm).

Rx_L_1_L_2_L_3	$\sigma_{bifrucation}$ [%]	ΔP [Pa]
R0_25_50_-	8.23	49 790
R4_25_50_-	4.22	43 550
Z_25-25-25	2.83	43 330

Table 4. 8 – Flow distribution performance and dressure drops

It can be noticed that, the bifurcation singularities in the improved channel are less important than that of two-level bifurcated flow channel. This induces lower pressure losses and a less disturbed flow that progressively reaches final channels (IV).

In addition, transverse zone in second and third level of bifurcations allows for a redistribution of flow wherever important adverse pressure gradient exists. The effect in communication zones is to ''delocalize'' the velocity and pressure so that a condition of homogeneous flow field is generated.

Fig.4.35 shows the velocity vectors occurring in the communication zone "*zone 2*" of the new channel design.

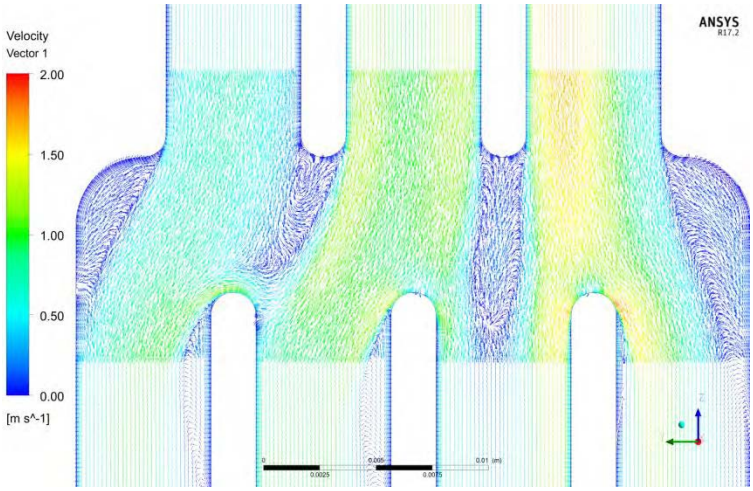

Fig.4. 35 - Velocity vectors at "zone 2" of Mockup 3

For the time being, PIV measurements have been performed on the three-level bifurcating channels, i.e. Mockup 3 in Chapter 3.
In fact, as for the two previous conceptual designs, the validation of the numerical model is the first step of the design process.
The measured velocity field on the middle plane of pre-distribution channel is compared with numerical results of the ASST model (Fig.4.35).

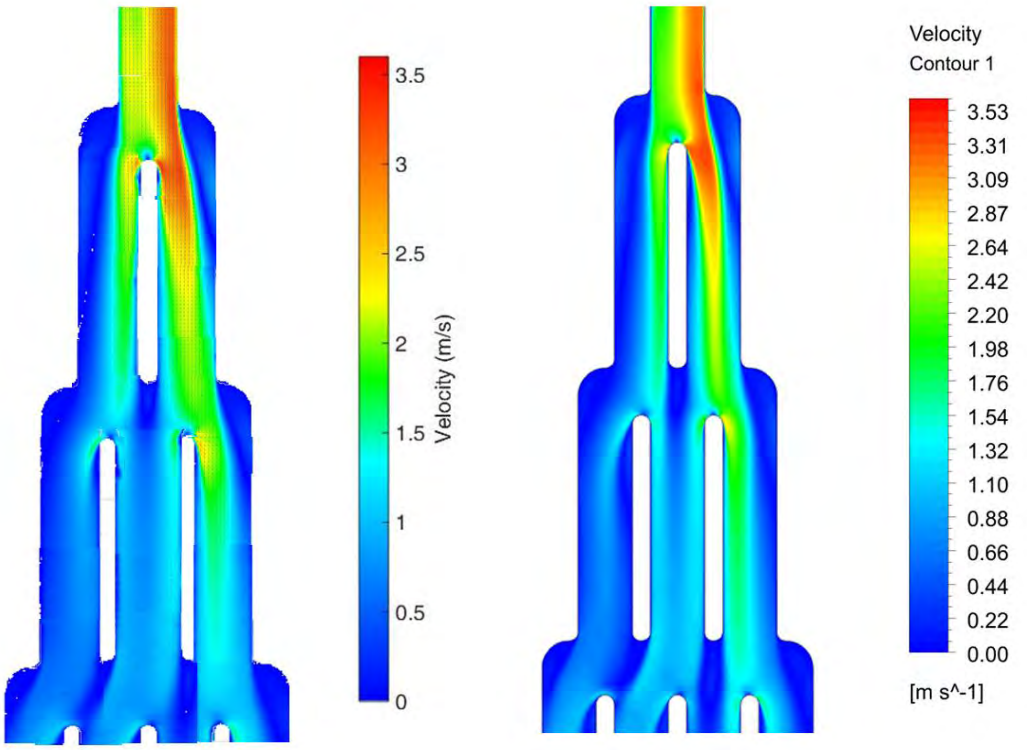

Fig.4. 36 - Velocity field comparison on the middle plane of Mockup 3 (PIV data at the left and k-ω ASST computation at the right)

The preliminary analysis in Fig.4.36 gives the necessary confidence to pursue the investigation of this new concept of pre-distribution channels for the ASTRID sodium distribution system in the SGHE module.

4.5. Conclusions

In the present chapter a detailed analysis of flow in bifurcating channels has been done to identify the physical phenomena ongoing in the sodium pre-distribution channels and the resulting flow distribution.

The longitudinal evolution of flow has been analyzed with PIV experimental data and ASST numerical results.

The numerical prediction was extensively validated against experimental data and reasonable agreement between prediction and measurement has been obtained. It is shown that the developed numerical code is capable of capturing all major features of the flow. However, the ASST numerical model overestimates the reattachment length so that the channel length required to reach a more uniform velocity profile. Numerical results are then conservative with respect to the experimental data; ASST model can be safely used to design ASTRID sodium pre-distribution channels.

An optimal design of sodium pre-distribution channel with two-level of bifurcation has been proposed. It provides the required pressure drop to reduce the maldistribution due to the inlet header while allowing an easy integration in the tertiary circuit. Its bifurcation structure ensures an equal repartition of flow between generated channels simplifying the design study on the entire SGHE module. In fact, from here, the flow maldistribution issue will deal only with header design whereas the bifurcation system will be reduced and represented by additional pressure losses in the channel bundle.

The weak point of this proposed solution (two-level bifurcation) is the resulting length of sodium plate which could be in contrast with the compactness criterion of ASTRID SGHE. If this is the case, a new improved configuration has been proposed in the last section of the chapter. Its conceptual design is the best overall compromise between the uniform flow distribution and the pressure drops. However, the optimization in term of channel length has still to be done (see perspectives in Section 6.2.2).

Chapter 5

Numerical Study of Flow Pattern in Compact Heat Exchanger

In the second part of Chapter 3 (Section 3.2), the experimental strategy conceived for the validation of the fluid flow evolution in the inlet header and the consequent flow distribution in the ASTRID SGHE bundle has been presented together with the preliminary analysis of flow measurements. This allows identifying the characteristic fluid flow phenomena occurring in the test section and which will have a guidance role in the definition of the numerical CFD approach.

First of all, two different turbulence models which could potentially be used to study the flow in SGHE module are selected and discussed in details. Then, the computational domain, the porous medium model and the boundary conditions for fluid flow are described.
A first comparison between the numerical calculations and the DANAH experimental database allows retaining one numerical model to be validated against experimental data. The selected model is then used to characterize the three-dimensional jet flow at the inlet header and to study its correlation with the repartition of flow between channels. In the final part, the physical and geometrical parameters which could have an influence on flow distribution in the SGHE module are investigate. The most performant design for the SGHE module is proposed.

The entire CFD analysis is carried out using the ANSYS Fluent® 16.1 in the Windows workstation with 120 GB RAM.

5.1. CFD Numerical approach for the SGHE flow analysis

5.1.1. Turbulence numerical models

Bibliographic studies in Section 2.4.2 showed that a high-Reynolds ε-based number approach may actually provide correct information about the evolution of large vortices growing at inlet distributor like the SGHE header.
Hence, the choice of the numerical model is between a two-equation k- ε model (i.e. that of [78]) and a more sophisticated Reynolds stress transport model (i.e. [86]), varying in the Reynolds Stresses modelling.

For the two-equation models, three turbulence models are available in the ANSYS Fluent ® solver, i.e. the Standard [83], the RNG [84] and the Realizable k-ε [85]. Nevertheless, due to the potential improvements of the k –ε Realizable model with regard to the standard k-ε and the RNG model. In fact, the different formulation of the turbulent viscosity and a new transport equation for the dissipation rate is expected to provide superior performance for complex flows like jet impingement, separating flows and swirling flows.
In addition, for the present case study, the Realizable k-ε preserves the advantage of the relatively low computational cost and the typical robustness of a standard k- ε model.

For the Reynolds stress transport model based on a ε-transport equation, the possible choice is between the Linear Pressure Strain-RSM model and the Quadratic Pressure Strain-RSM model [86-87]. However, due to the time constraints and a poor numerical stability of the Quadratic Pressure Strain-RSM model, this latter has been excluded from the model comparison.
The Linear Pressure Strain-RSM model by Gibson and Launder [86-87] used for the present analysis is still computationally expensive (50–60% more CPU time; 15–20% more memory over k–ε model) and converges slowly with respect to the Realizable k –ε model.

As conclusion, the final choice is to use the Realizable k –ε model and the Linear Pressure Strain-RSM model to numerically investigate the flow field in the DANAH mockup configuration. The subsequent comparison with the experimental data will provide the most performant turbulence model to be used for the entire flow analysis. The numerical formulation of the selected models will be detailed below.

5.1.1.1. The Realizable k- ε model

The Realizable model by Shih [85] is the most recently developed of the three k –ε variations and features two main differences from the standard k –ε model. It uses a new equation for the turbulent viscosity and the dissipation rate transport equation has been derived from the equation for the transport of the mean-square vorticity fluctuation. The form of the eddy viscosity (turbulent) equations is based on the realizability constraints. This is not satisfied by either the standard or the RNG k –ε models which makes the realizable model more precise than both models aiming at predicting flows such as separated flows and flows with complex secondary flow features.
In terms of the improved changes by Shih, the transport equations become:

$$\frac{\partial}{\partial t}(\rho k) + \frac{\partial}{\partial x_j}(\rho k u_j) = \frac{\partial}{\partial x_j}\left[\left(\mu + \frac{\mu_t}{\sigma_k}\right)\frac{\partial k}{\partial x_j}\right] + G_k + -\rho\varepsilon \tag{52}$$

$$\frac{\partial}{\partial t}(\rho\varepsilon) + \frac{\partial}{\partial x_j}(\rho\varepsilon u_j) = \frac{\partial}{\partial x_j}\left[\left(\mu + \frac{\mu_t}{\sigma_\varepsilon}\right)\frac{\partial \varepsilon}{\partial x_j}\right] + \rho C_1 S\varepsilon - \rho C_2 \frac{\varepsilon^2}{k + \sqrt{v\varepsilon}} \tag{53}$$

where $C_1 = \max\left[0{,}43, \frac{\eta}{\eta+5}\right]$ and $\eta = S\frac{k}{\varepsilon}$.

In these equations, G_k represents the generation of turbulent kinetic energy that arises due to mean velocity gradients. This term is defined as:

$$G_k = -\rho\overline{u_i u_j}\frac{\partial u_i}{\partial u} \tag{54}$$

σ_k and σ_ε are the turbulent Prandtl numbers for the turbulent kinetic energy and its dissipation. They connect the diffusivity of k and ε to the eddy viscosity.

Similar to the other variations of the k –ε models [83-84], the turbulent viscosity is determined by the formula given below. However, it produces different results since C_μ is not constant:

$$\mu_t = \rho\, C_\mu \frac{k^2}{\varepsilon} \tag{55}$$

where C_μ is computed from:

$$C_{\mu} = \frac{1}{A_0 + A_s \frac{kU^*}{\varepsilon}} \tag{56}$$

where:

$$U^* = \sqrt{S_{ij}S_{ij} + \tilde{\Omega}_{ij}\tilde{\Omega}_{ij}} \qquad \text{and} \quad \tilde{\Omega}_{ij} = \overline{\Omega_{ij}} - \varepsilon_{ijk}\omega_k - 2\varepsilon_{ijk}\,\omega_k \tag{57}$$

In the above equation, $\overline{\Omega_{ij}}$ is the mean rate of rotation tensor viewed in a rotating reference frame with angular velocityω_k. The constants A_0 and A_S are defined as:

$$A_0 = 4.04,\ A_S = \sqrt{6}\cos\emptyset$$

where:

$$\emptyset = \frac{1}{3}cos^{-1}\left(\sqrt{6}\,\frac{S_{ij}S_{jk}S_{ki}}{\tilde{S}^3}\right), \qquad \tilde{S} = \sqrt{S_{ij}S_{ij}}\,, \qquad S_{ij} = \frac{1}{2}\left(\frac{\partial u_j}{\partial x_i} + \frac{\partial u_i}{\partial x_j}\right) \tag{58}$$

It has been shown that C_{μ} is a function of the mean strain and rotational rates, the angular velocity of the rotating system, and the turbulent kinetic energy and its dissipation rate. The standard value of C_{μ} = 0.09 is found to be the solution of equation 2.32 for an inertial sub layer in the equilibrium boundary layer.

The constants C_2 , σ_k and σ_{ε} have been determined by Shih [85] and are defined as follows:

$$C_2 = 1.9,\ \sigma_k = 1.0,\ \sigma_{\varepsilon} = 1.2$$

5.1.1.2. The Linear Pressure Strain – Reynolds Stress Model

The Reynolds stress model (RSM) closes the Reynolds-averaged Navier-Stokes equations by solving transport equations for the Reynolds stresses, together with an equation for the dissipation rate. This means that seven additional transport equations must be solved in 3D flows.

The exact transport equation for the six independent Reynolds stresses in RSM can be written as in equation (36).

The dissipation tensor is defined as:

$$\varepsilon_{ij} = \frac{2}{3}\delta_{ij}\rho\varepsilon \tag{59}$$

The dissipation rate (i.e. ε) is defined by the same equations (with ($\sigma_{\varepsilon} = 0$)) as in Standard $k-\varepsilon$ Model [83].

In RSM-LPS Model of Gibson and Launder [[86-87]], the pressure strain term is decomposed into three components:

$$\begin{aligned}\Phi_{ij} = \Phi_{ij,1} + \Phi_{ij,\ 2} + \Phi_{ij,w} \\ = -\frac{C_1\rho\varepsilon}{k}\left(\overline{u_i'u_k'} - \frac{2}{3}\delta_{ij}k\right) \\ - C_2\left(\left(P_{ij} - C_{ij}\right) - \frac{2}{3}\delta_{ij}\left(\frac{P_{kk}}{2} - \frac{C_{kk}}{2}\right)\right) \\ + C_1{}'\frac{\varepsilon}{k}\left(\overline{u_k'u_m'}n_kn_m\delta_{ij} - \frac{3}{2}\overline{u_i'u_k'}n_in_k - \frac{3}{2}\overline{u_i'u_k'}n_in_k\right)\frac{C_l k^{\frac{3}{2}}}{\varepsilon d} \\ + C_2{}'\left(\Phi_{km2}n_kn_m\delta_{ij} - \frac{3}{2}\Phi_{ik2}n_in_k - \frac{3}{2}\Phi_{jk2}n_in_k\right)\frac{C_l k^{\frac{3}{2}}}{\varepsilon d}\end{aligned} \quad (60)$$

In high-Reynolds model, the wall-reflection term $\Phi_{ij,w}$ is considered in the pressure-strain formulation.

5.1.2. Computational model and flow boundary conditions

For an accurate experimental validation of numerical models, the computational domain and the fluid flow boundary conditions have to perfectly correspond to that used in DANAH experiments.

However, performing simulations with the explicit geometry of DANAH test section would take a very long computational time and it would be even impossible because of the limitation in mesh count of the available workstation (RAM requirements). Consequently, a series of physical and numerical assumptions have been considered for the computational model as shown in Fig.5.1.

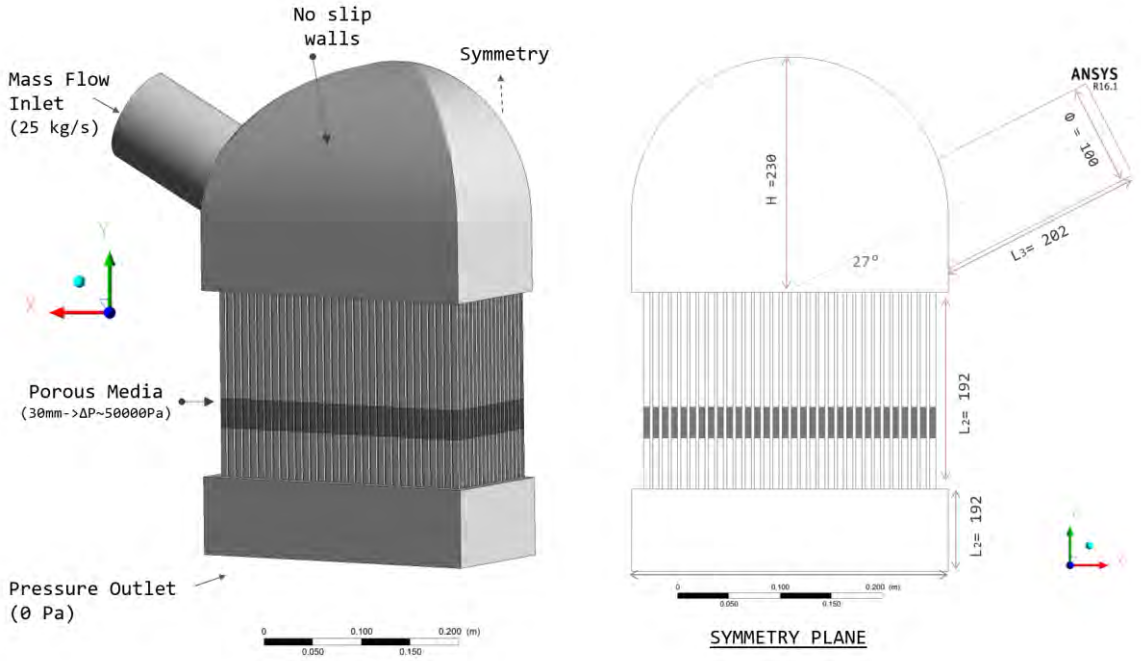

Fig.5. 1 - Computation Model

Flow Symmetry Assumption

The first physical assumption, based on test section design project, is the flow symmetry with respect to the central x-y admission plane (Symmetry Plane in Fig.5.1). Only half of the model is considered in the whole numerical simulation. This allows halving the number of mesh elements.

In Section 3.2.8, it was demonstrated that the flow symmetry at the inlet header of DANAH experiments is not perfect. Due to manufacturing tolerance, a perfect symmetry of the mockup could never be ensured. However, considering the measured differences of flow field between symmetry planes, the flow symmetry assumption in computations is then tolerable.

Porous Region

With the same objective of channel section restrictions in DANAH channels, a porous region is introduced in the computational channel domain. The 2m channel length and the bifurcation system of the real geometry of the SGHE bundle can be modeled as smaller and more regular channel geometries of equivalent pressure losses.

In this sense, 30 mm of the channel computational domain has been defined as porous zone (Fig.5.1). A specific model of the porous source terms allows setting the desired pressure drop value (50000 Pa for DANAH experiment) in a very short channel length.
Nevertheless, as it can be noticed in Fig.5.1, some channel fluid zones are preserved before and after the above-mentioned porous region. In fact, it was demonstrated that the coupling between the fluid and the porous region might be hard to manage; the porous media could distort the physics of the flow depending on the specific boundary conditions.
The explicit channels downstream the porous zone are of primary importance in order to ensure a real velocity profile of the outcoming jets to be compared with the experimental database at the outlet header.
The explicit channels upstream guarantee a fully developed velocity profile at the entrance of the porous medium (see Fig.5.1). In this way, the pressure drop in the various configurations will not depend on the jet impingement into the bundle cross section.

For more detailed information about the isotropic porous medium model, see APPENDIX I.

Outlet header

In Section 3.2.9, it was also demonstrated that the outlet pipe of the experimental test section has no influence on the flow distribution. This means that, for the actual purpose of experimental validation, the computational domain of the outlet header could be reduced to a regular box of smaller geometry (Fig.5.1). A gauge pressure equal to 0 Pa pressure outlet boundary condition is used.

As further validation, two preliminary CFD simulations including the whole geometry of the outlet header and the reduced one have been done. For a reduction of more than 25% in term of mesh elements, the maldistribution factor varies less than 1%. No differences have been detected in the inlet header velocity field.

Inlet pipe

PIV measurements at the inlet pipe of DANAH test section demonstrated that a fully developed flow occurs before the admission in the header (see Section 3.2.7). In CFD simulations, setting the mass flow inlet boundary condition for the incompressible flow corresponds to directly impose a fully developed velocity profile at the inlet. Hence, a shorter length of the inlet pipe of $2d_h$ is then considered in the computational domain (Fig.5.1).

According to the main goal of validating the numerical model, what is ought to be checked is that the same inlet boundary conditions results in both numerical and experimental analysis. The calculated velocity profile in the admission at 70 mm from the header wall is plotted against experimental data in Fig.5.2. The agreement between both is perfect.

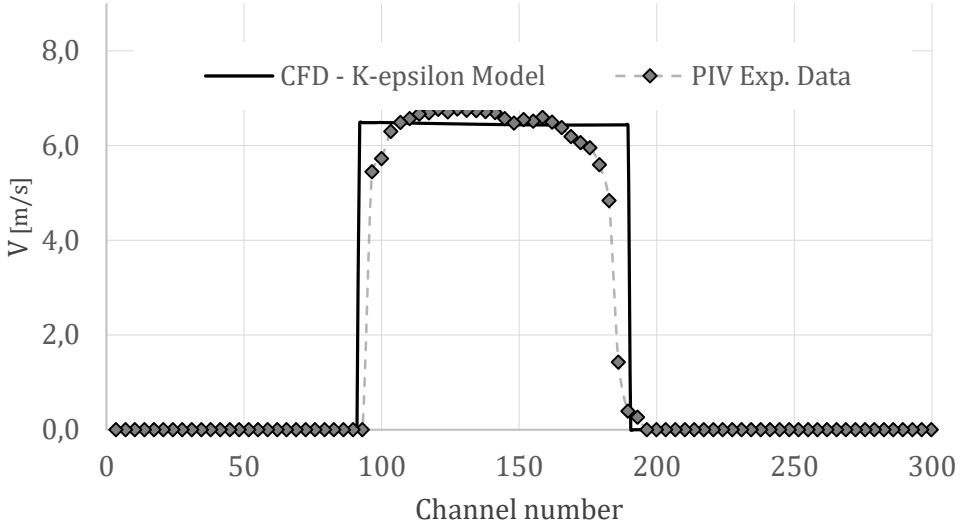

Fig.5. 2 – PIV and CFD inlet velocity profile

Working fluid

According to DANAH experiment, the working fluid is water at ambient temperature and atmospheric pressure. Liquid water properties are kept from the Fluent database, i.e. density of 998.2 kg/m^3 and a dynamic viscosity of 0.001003 kg/ms.

5.1.3. CFD solver setting

The solution settings used to investigate the present flow case study are in line with those of simulation of pre-distribution channels.

The solver is Pressure-based one and the Coupled pressure-velocity algorithm with pseudo-transient option is used.

Gradients are evaluated through the Least-Squared method. For Pressure, PRESTO scheme is used.

Second Order Upwind Scheme is used for the spatial discretization of momentum, turbulent kinetic energy and turbulent dissipation rate transport equations.

Note that, the RSM calculation was started from the converged solution of Realizable k- ε model with pressure discretized with a second order method and momentum, k, ε, Reynolds stresses with first order upwind scheme. Once a first converged solution was obtained, pressure discretization was shifted to PRESTO then k, ε, Reynolds stresses discretization to second order and until the final solution was reached.

5.1.4. Grid sensitivity

A grid independence study is conducted in order to ensure a low sensitivity of the numerical simulations to the computational grid.

Due to time constraints, the grid convergence study has been performed for only one of the selected turbulent model, i.e. Realizable k-ε. In order to assess its robust applicability, three different meshes varying in cell size and in first boundary layer thickness have been tested and illustrated in Fig.5.4. The domain in the red dotted box (Fig.5.3) shows to the mesh view in Fig.5.4. Geometrical features of the Coarse, Medium and Fine mesh are listed in Table 5.1.

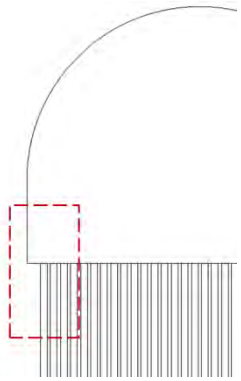

Fig.5. 3 - Mesh view

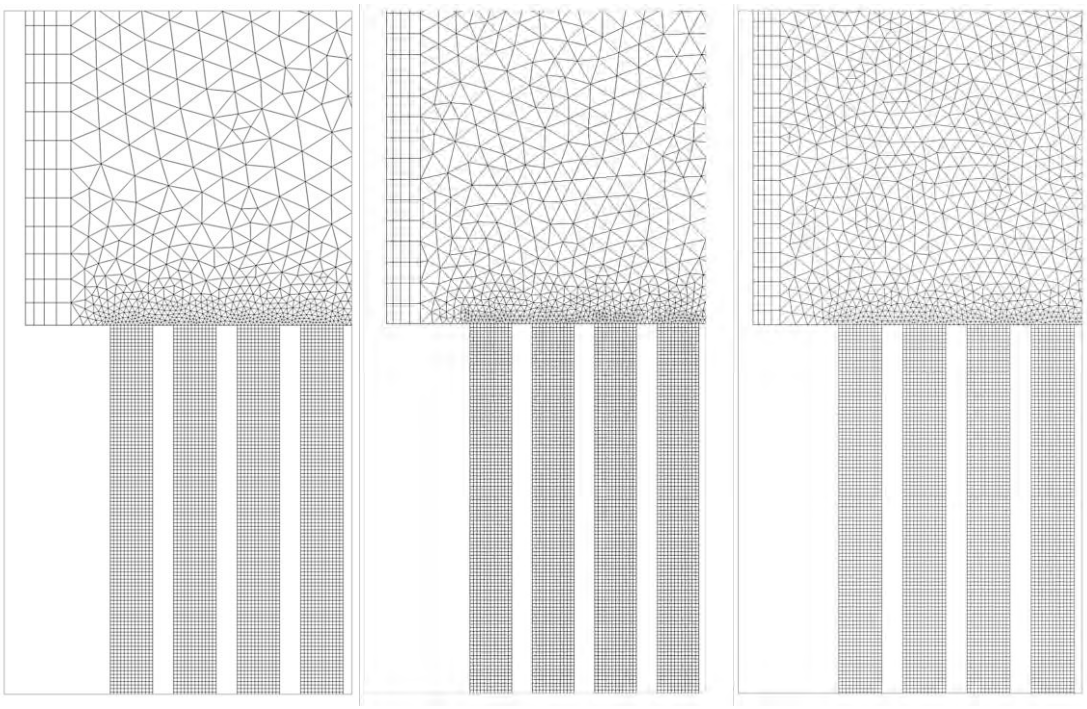

Fig.5. 4 –Coarse, Medium and Fine Mesh at the inlet header

MESH	Cell Size	First layer thickness	Number of cell
Coarse	$4x10^{-3}$ m	$1.2x10^{-3}$ m	32 316 473
Medium	$3x10^{-3}$ m	$9x10^{-4}$ m	34 618 488
Fine	$2x10^{-3}$ m	$7x10^{-4}$ m	37 969 080

Table 5. 1- Coarse, Medium and Fine mesh features

The size of the cell elements in the channel bundle is kept constant and equal to $7 * 10^{-4}m$ for the convergence study. The inflation option (first layer thickness) has been used to mesh the boundary layer; the total number of layers is 4 with a growth rate of 1.2. As regard to the meshing method, hexahedral elements have been used for the tube bundle and for the inlet pipe, whereas tetrahedral ones for the inlet and outlet header. This strategy provides a high mesh quality in term of orthogonal quality and equiangular skewness.

Furthermore, being interesting in parallel jets flow field at the outlet of the bundle channel, an additional adaptive mesh refinement has been successively applied to the limited region of interest as shown in Fig.5.5. The increased number of mesh elements allows for a more accurate comparison between the solution and experimental data.

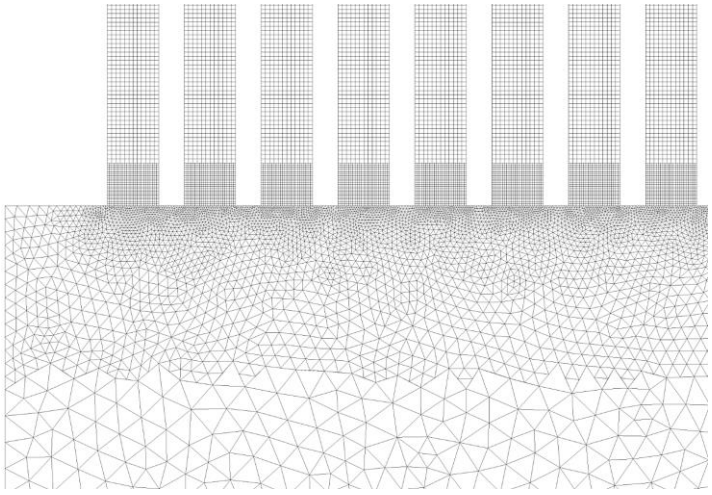

Fig.5. 5 - Mesh detail at the outlet header

Grid sensitivity results for the velocity magnitude profile and the flow distribution parameter σ are shown in Fig.5.6 and Table 5.2.
Here, the normalized velocity profile V/V_{inlet} is plotted at *line 1* of the symmetry plane (Fig.5.8) for the three successively refined meshes together with the experimental results

(*I-Plane 3* of the BD_2_75_NC test section). Fig.5.6 shows a good overlap of the three profiles with slight differences with respect to the coarse mesh.

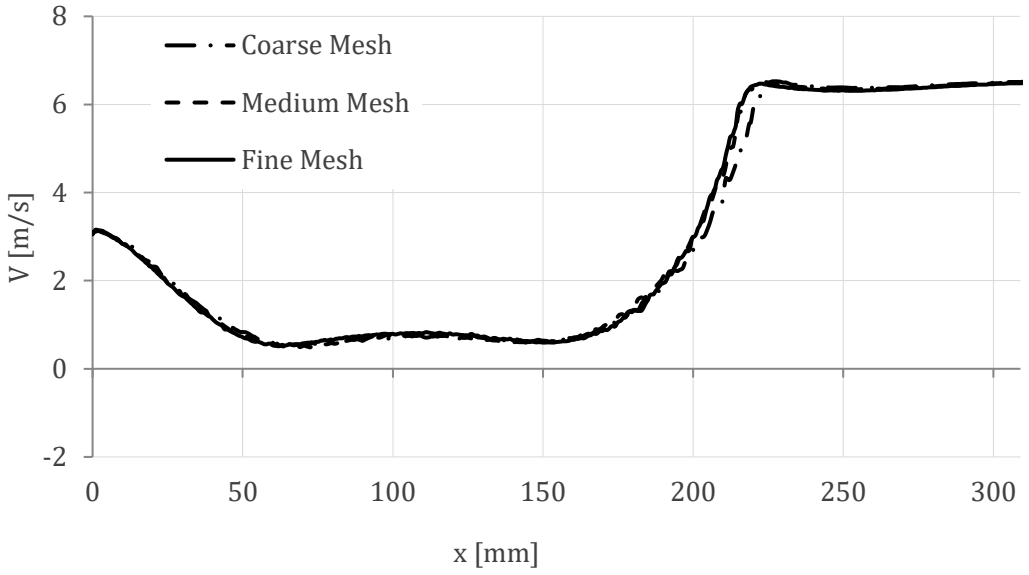

Fig.5. 6 - Mesh Independence Study - Velocity profile at line 1

In addition, the "maldistribution" factor σ based on standard deviation presents a very similar value for the studied cases (Table 5.2).

MESH	Coarse	Medium	Fine
Maldistribution Factor	2.88 %	2.85%	2.82 %

Table 5. 2 – Maldistribution factor - Coarse, Medium and Fine mesh

Based on these trends, the medium grid can be retained as the reference meshing for future calculations. In fact, being the best compromise between the accuracy of solution and the computational cost, it presents appropriate values of Wall y+. The boundaries of the header domain are treated with wall functions, so first cells with y+ higher than 30 are required, which it is not the case for the coarse grid. Fig.5.7 shows the Wall y+ contours for the medium grid.

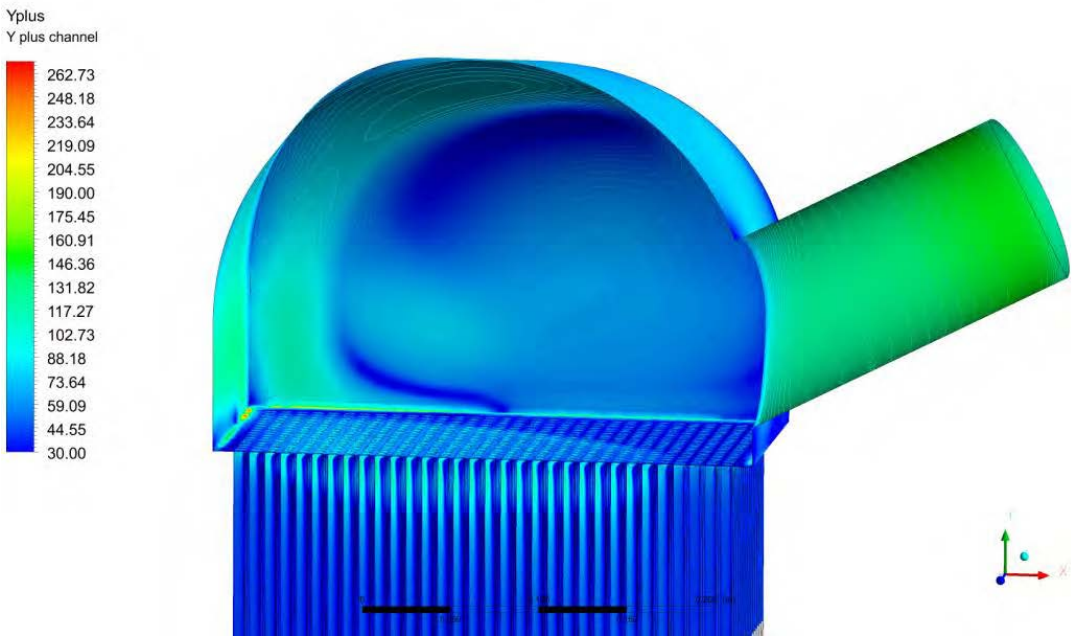

Fig.5. 7 - Wall Y+ contour at the inlet header

5.1.5. The selection of the CFD numerical model

At this stage, once detailed the CFD numerical approach for the analysis of flow in a general design of SGHE module, it is possible to compare the numerical results with the experimental data.

It is important to mention immediately that the main purpose of the present paragraph is to evaluate which one of the two turbulence models presented in Section 5.1.1 gives a better prediction of the flow phenomena occurring in the SGHE module geometry.
The comparative analysis is then limited to the inlet header where more complex flows occur. Here, the impinging jet involves several flow mechanisms, such as entrainment, impingement, separation and high streamline curvature which could be a crucial test for the turbulence modeling.

The mean velocity profile V and the $u'u'$ and $v'v'$ Reynolds Stresses profiles are plotted on some horizontal lines of the symmetry plane (I- Plane 3) (Fig.5.8).

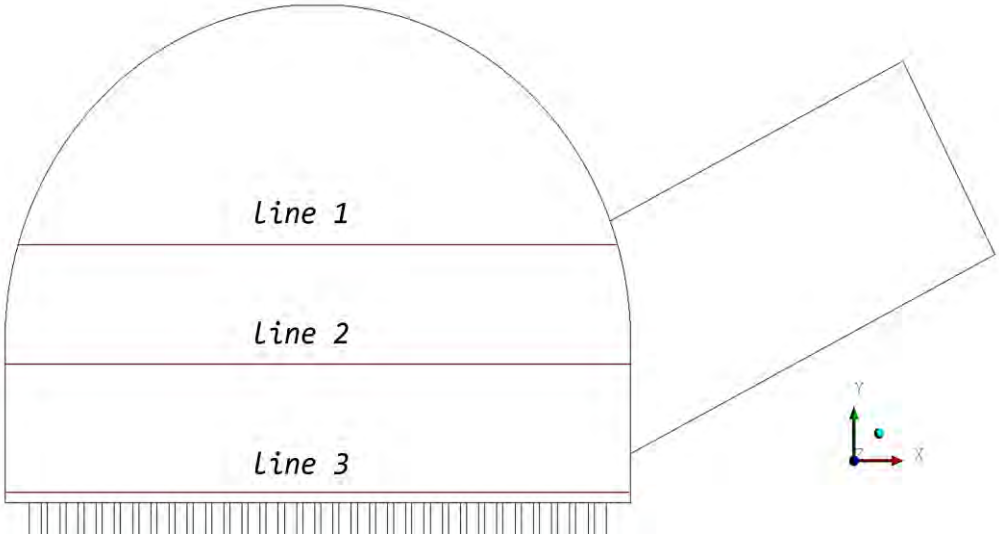

Fig.5. 8 - Selected lines for turbulence model comparison

Mean velocity *V* calculated by the k-ε Realizable model and the Reynolds Stress model (LPS) at *line 1, 2* and *3* are illustrated in Figs.5.9, 5.10 and 5.11 versus the experimental data.

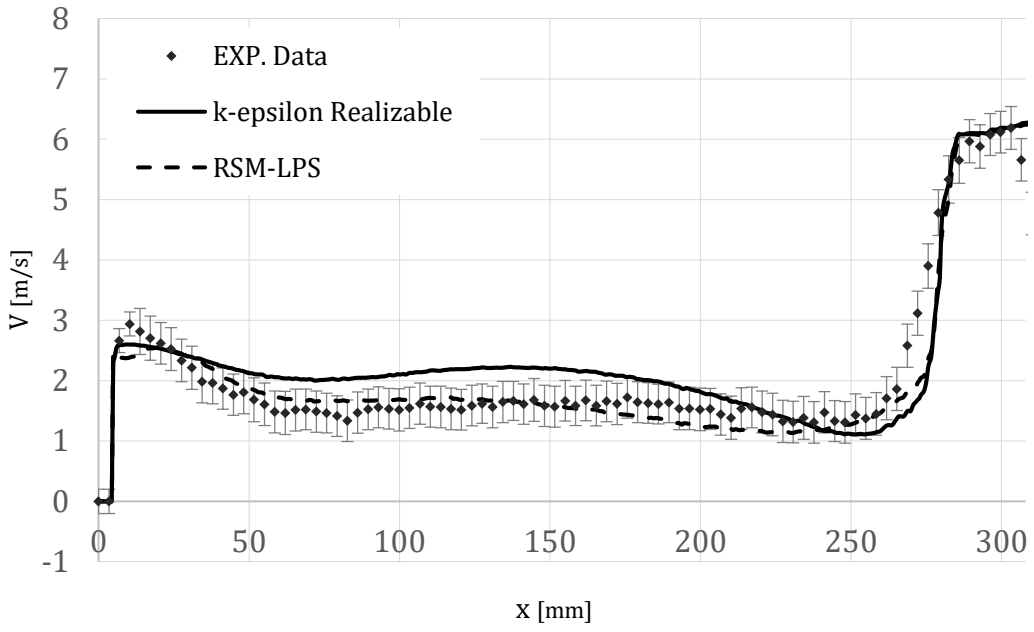

Fig.5. 9 - Experimental vs numerical mean velocity profile at line 1

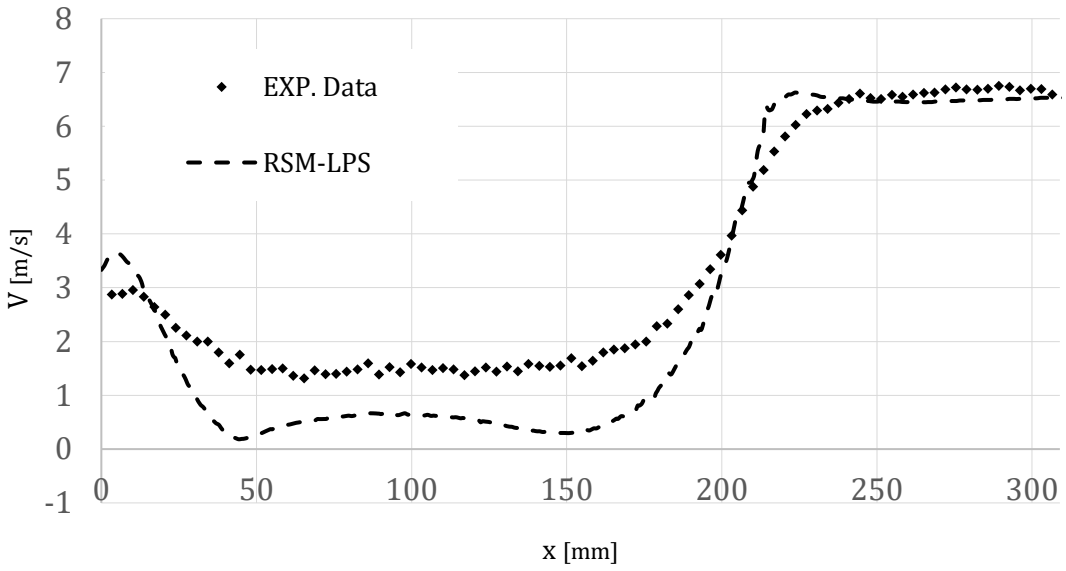

Fig.5. 10 - Experimental vs numerical mean velocity profile at line 2

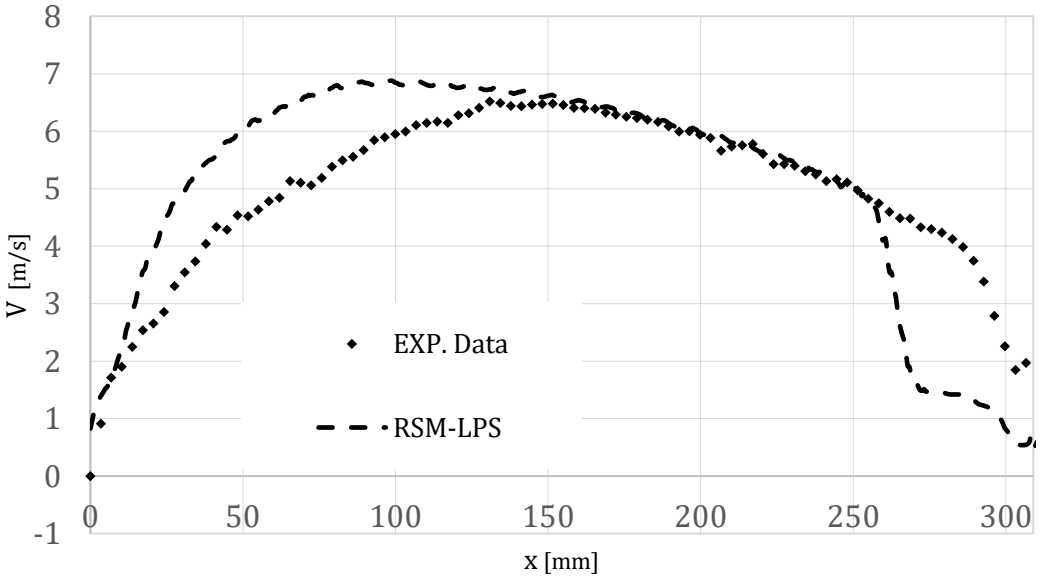

Fig.5. 11 - Experimental vs numerical mean velocity profile at line 3

The comparison between the calculated and measured $u'u'$ and $v'v'$ Reynolds Stresses profiles are limited to the central line, i.e. *line 2*. Results are shown in Fig.5.12 and Fig.5.13 for $u'u'$ and $v'v'$ Reynolds Stresses respectively.

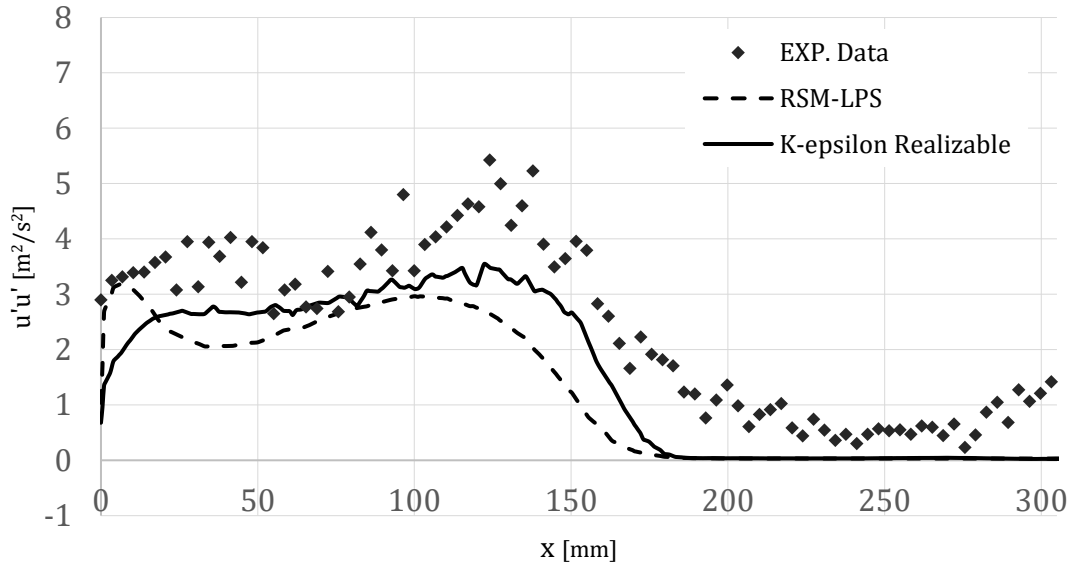

Fig.5. 12 - Experimental vs numerical u'u' Reynolds Stress at line 2

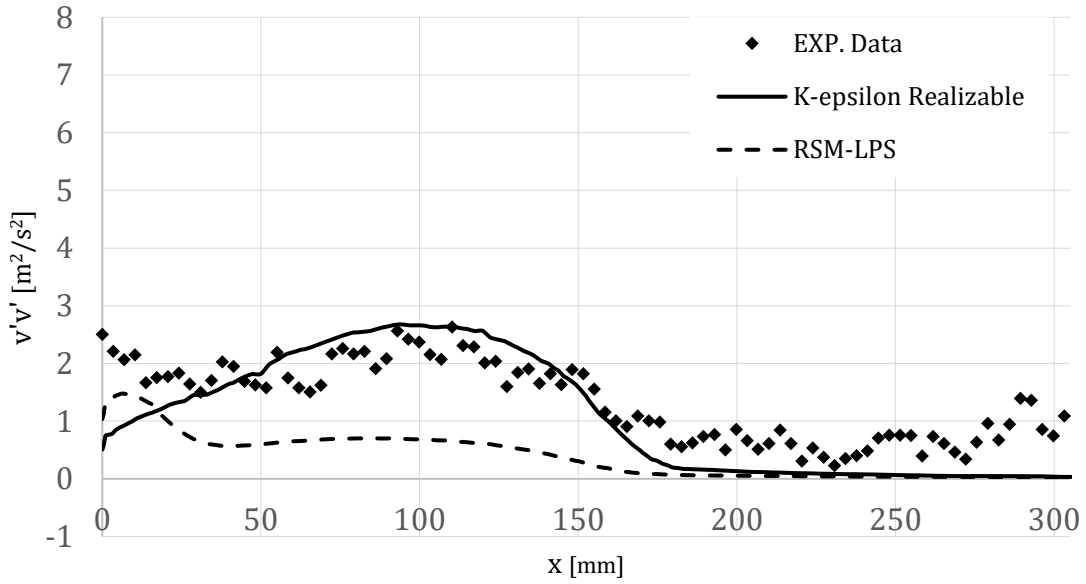

Fig.5. 13 - Experimental vs numerical v'v' Reynolds Stress at line 2

The comparative analysis reveals that, even though the RSM-LPS model provides fairly good results (particularly very good at the line 1 on Fig.5.9), the Realizable k-ε model leads to best overall results.

The mean velocity on all investigated lines at the inlet header (Fig.5.9) is very well predicted by both turbulence models. At the bottom part of the inlet header (line 2 and 3 in Fig.5.10-11), the k –ε Realizable model seems to provide slightly better results except for the zone near the right corner where both models fail in the description of the low velocity region. Nevertheless, as already mentioned, very close to the walls, PIV measurements are less trustworthy (Section 3.2.6).
As regards the velocity fluctuations, the k –ε Realizable model gives better predictions than the RSM-LPS model (Fig.5.12-13). In particular, as shown in Fig.5.12, the k –ε Realizable model captures far better the Reynolds stress $v'v'$. It is really surprising, since the RSM-LPS model is expected to better capture complex flows taking into account the anisotropic turbulence.

From the above comparison and considering the low computational cost of the two-equation turbulence models, the k –ε Realizable model is chosen as reference model for the following analysis [92].

5.2. Model Validation and Flow Analysis

5.2.1. Inlet header Flow

The analysis of jet flow impingement and recirculation at the inlet header volume is of primary importance because directly responsible for the repartition of sodium flow between the parallel channels of the SGHE bundle.

To investigate the inlet header flow, PIV and k –ε Realizable numerical data will be presented.
Fig.5.14, Fig.5.15 and Fig.5.16 compare PIV measurements and k–ε Realizable computations on five different x-y planes whose position is detailed in Section 3.2.3, i.e. I-*Plane 1*, *2*, *3*, *4* and *5*.

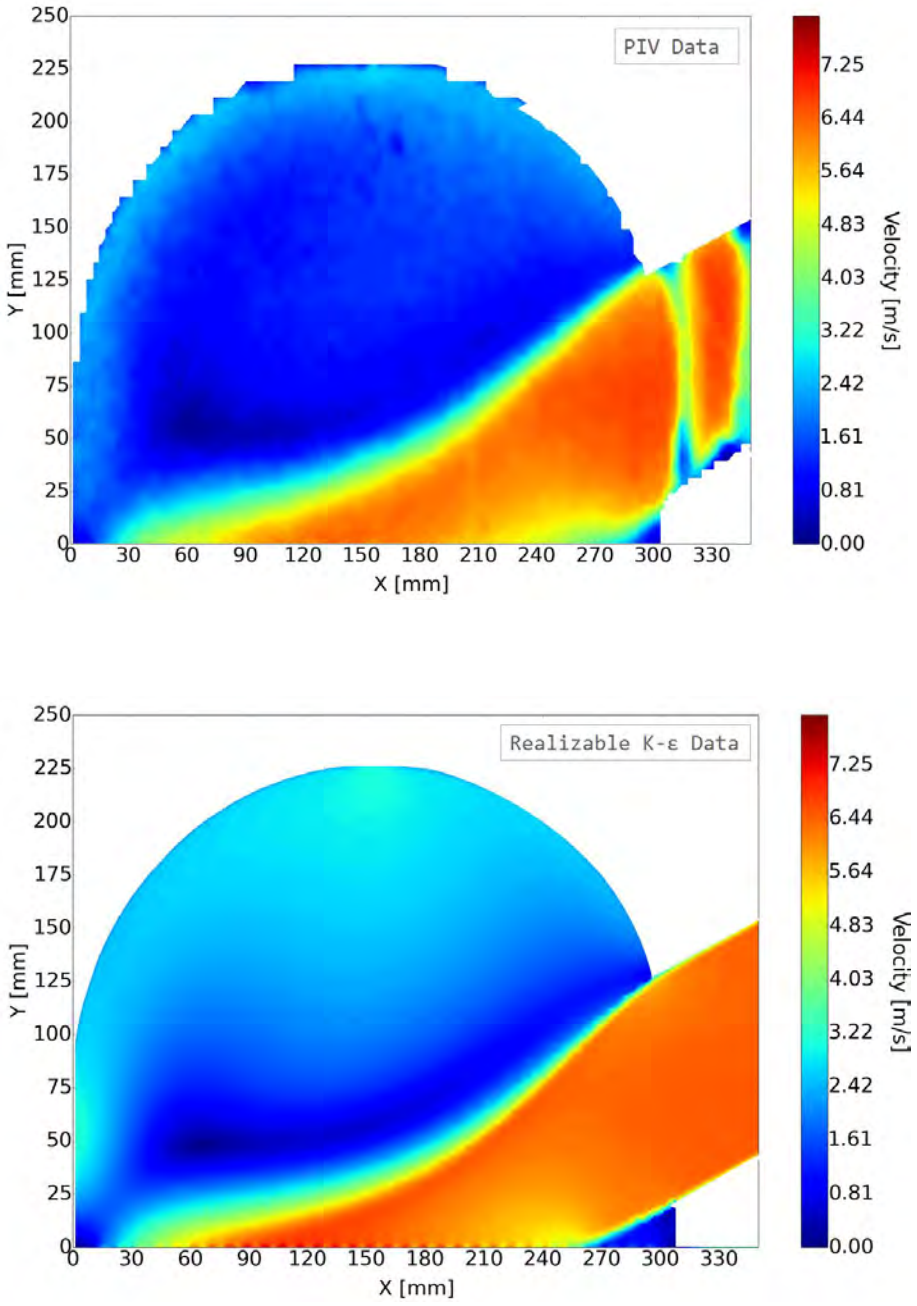

Fig.5. 14 - Velocity fields on Plane 3 (PIV data on top and Realizable K-ε computation on the bottom)

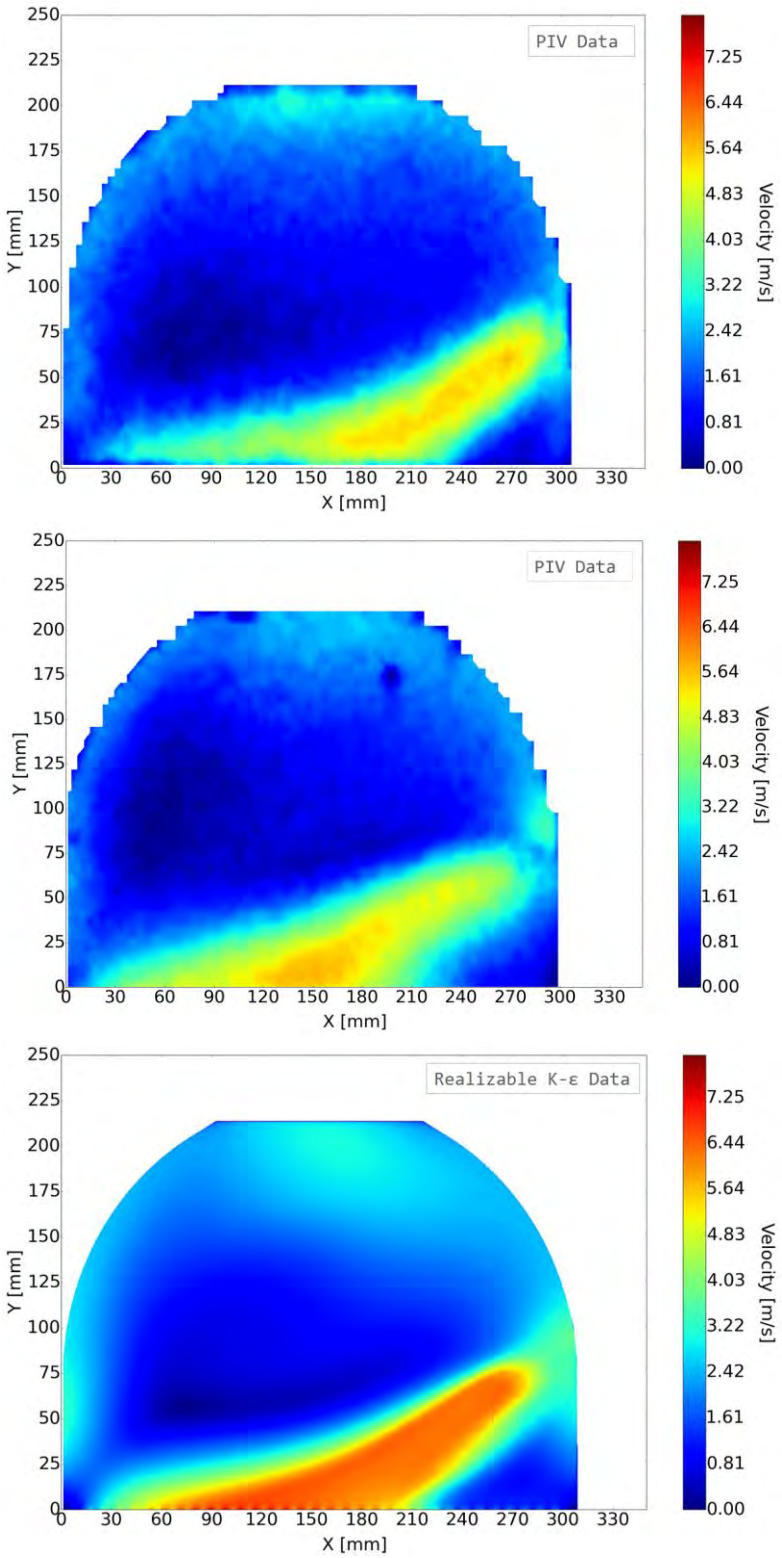

Fig.5. 15 - Velocity fields on I-Plane 2 and I- Plane 4 I (PIV data on top and Realizable K-ε computation on the bottom)

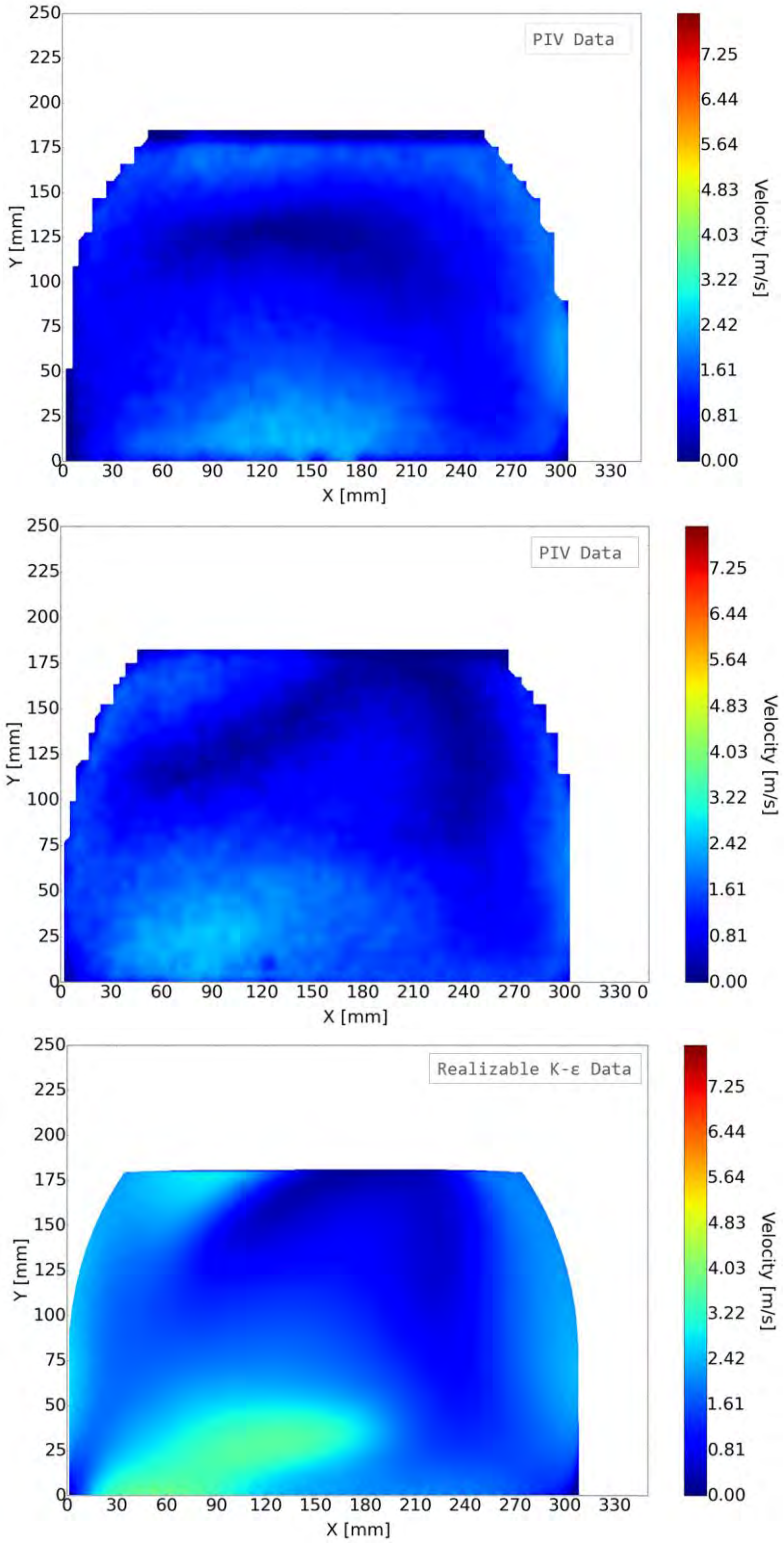

Fig.5. 16 - Velocity fields on I-Plane 1 and I- Plane 5 I (PIV data on top and Realizable K-ε computation on the bottom)

A first qualitative comparison confirms that the Realizable k-ε model provides confident results describing the physical behavior of the jet flow on all three planes at the inlet header.

Both numerical and experimental measurements at the symmetry plane of the header (I-Plane 3 in Fig.5.14) reveal the presence of the three typical flow regions characterizing the impingement of a confined jet [89], i.e. free jet region, impingement region and recirculation region (Fig.5.15). A schematic draw of the physical evolution of the confined three-dimensional jet flow on the central plane is illustrated in Fig.5.17.

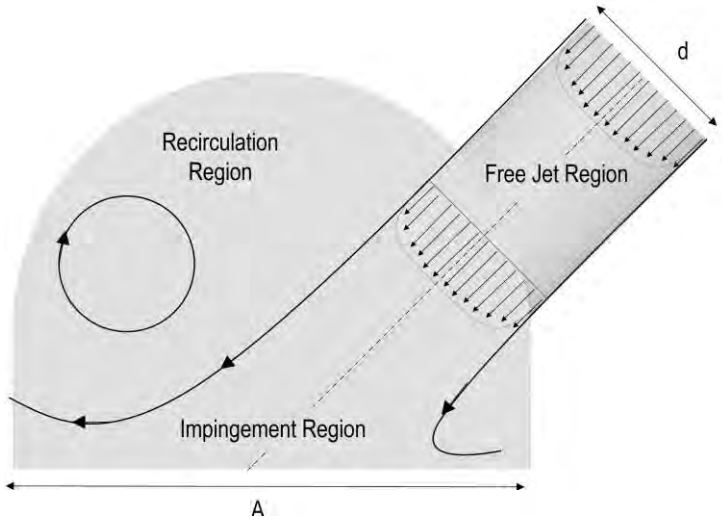

Fig.5. 17 – Physical evolution of a confined jet flow

The *free jet region* is established as fluid exits the admission tube in the confined header (Fig.5.17). Here the jet core, characterized by a relatively uniform velocity, is surrounded by a free shear layer where the jet entrains the water fluid and slowly expands. As the jet approaches the bottom channel bundle at the impingement region, the flow decelerates in the vertical direction (pressure increase) and accelerates in the horizontal direction near the stagnation point. The flow acceleration in the horizontal direction forms a wall jet tracing the header boundaries. As shown in Fig.5.17, a recirculation region occurs at the center.

The flow, driven by both the impinging jet and the wall jet, originates stable vortex structures. The main vortex, rotating in clockwise direction, causes the flow to move from the wall back towards the impinging jet. A slightly deflection of the inlet jet can be noticed in Fig.5.14.

The predictions of the numerical model result in a perfect agreement with the experimental PIV data. The only differences could be noticed at the outer wall and at the

top of the header where a more important flow recirculation seems to appear according to computations.

Slightly further from the admission tube, at *Plane 2-I* and *4-I*, it is still possible to recognize the main flow of the turbulent jet (Fig.5.15). As expected, after leaving the inlet pipe, the three-dimensional jet laterally diffuses in the wider volume of the header driven by the high-pressure gradient.
As shown in Fig.5.15, the numerical model well captures the physical behavior of the three-dimensional jet flow, even though it seems to over-estimate the stream wise jet velocity. In particular, the analysis of the two velocity components reveals an over prediction of the horizontal velocity v_x.
Due to the complex recirculating flow occurring in the volume of the header, it is very difficult to understand the origin of these discrepancies between numerical and experimental results. The calculated velocity vectors in Fig.5.18 show the evolution of the three-dimensional jet in the header volume.

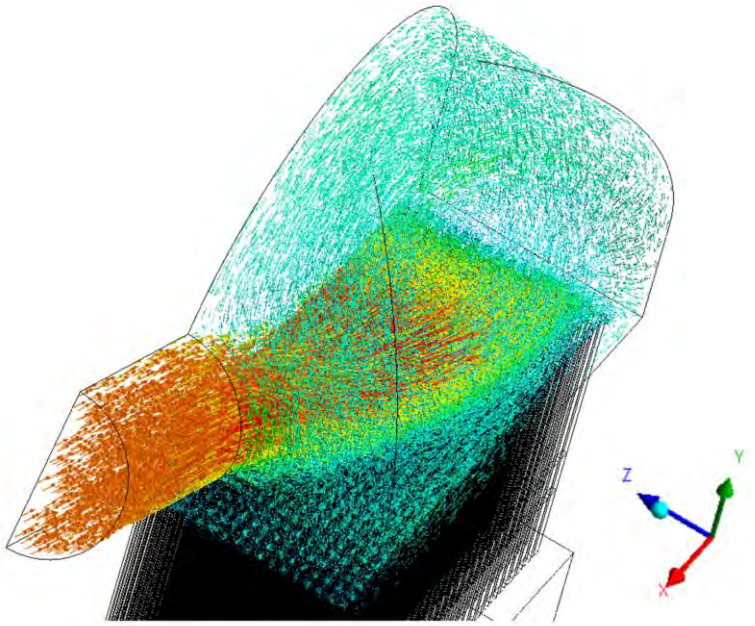

Fig.5. 18 – CFD velocity vectors: Jet flow evolution at the inlet header

In literature, research studies on three-dimensional wall jets usually describe an anisotropic growth of the three-dimensional jet which makes the jet evolution challenging to predict by means of an isotropic eddy viscosity model. Namgyal et al. [90]

demonstrated that the diffusion of a three-dimensional jet in z and y direction is influenced by secondary flows that develop in the jet due to the presence of the wall. However, the DANAH experimental setup prevents the analysis of the secondary flow and the verification of this hypothesis.

Furthest from the admission, at *Plane 1-5I* (Fig.5.16), the fluid kinetic energy of the jet is consumed by the vortex growing in the header. This results in the decrease of fluid velocity. Again, the numerical model over-predicts the fluid velocity.

The analysis of other tested DANAH configurations reveals the same discrepancies between numerical and experimental results on symmetric planes further from the admission.

5.2.2. Outlet header Flow

As it has been already mentioned, the final objective of the overall analysis is to evaluate the flow distribution between the parallel channels of the ASTRID heat exchanger.
In previous section, it has been demonstrated that, the flow analysis in the inlet header will not be sufficient to reach this goal.
In fact, if we look at the calculated mean velocity vectors in Fig.5.19, for both inlet and outlet header, it can be noticed that to estimate the flow distribution between channels starting from the inlet, we should be able to isolate the vertical velocity at the early entry of the channels. However, due to the scattered light, the PIV measurement system cannot guarantee the reliability of the velocity vectors close to the bundle surface where the jet impingement occurs. Differently at the outlet header, after leaving the channel bundle, the confluent jets display a well-established regular flow which allows a more direct access to the velocity distribution information between channels (see Section 3.2.9 for explanation).

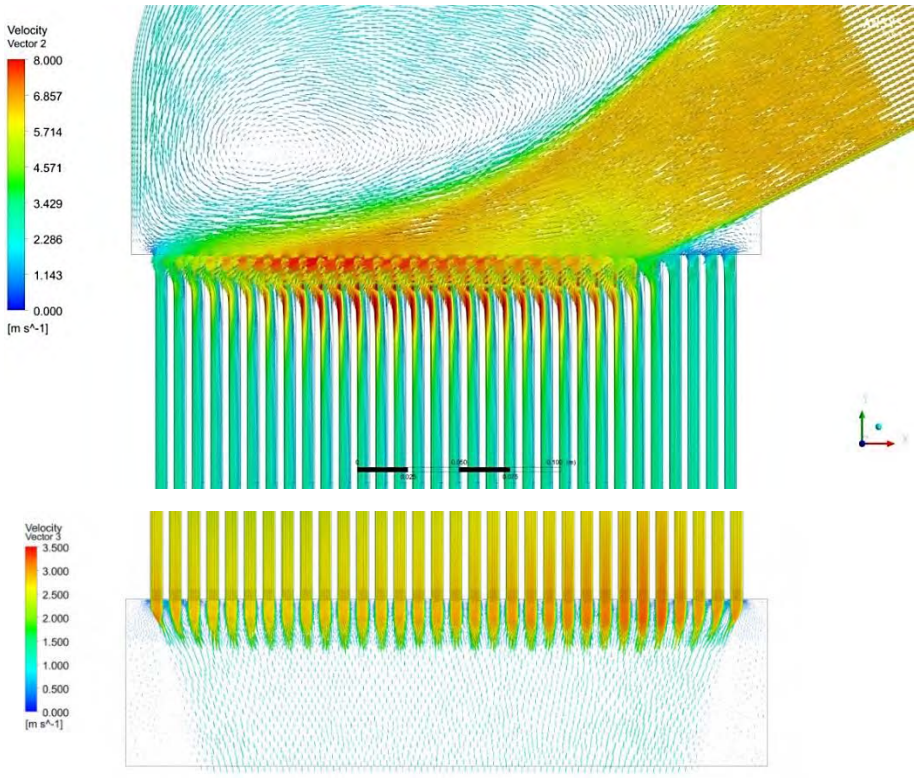

Fig.5. 19 - Velocity vectors at the inlet and outlet header

To investigate the flow distribution between the channels, PIV measurements at the outlet of each plate of the bundle (35 plates) have been done as described in Section 3.2.3. Fig.5.20 compares PIV measurements and k –ε Realizable computation on one of the 35 x-y planes which is placed near the center of the bundle (Fig.3.42), i.e. O-*Plane 20*.

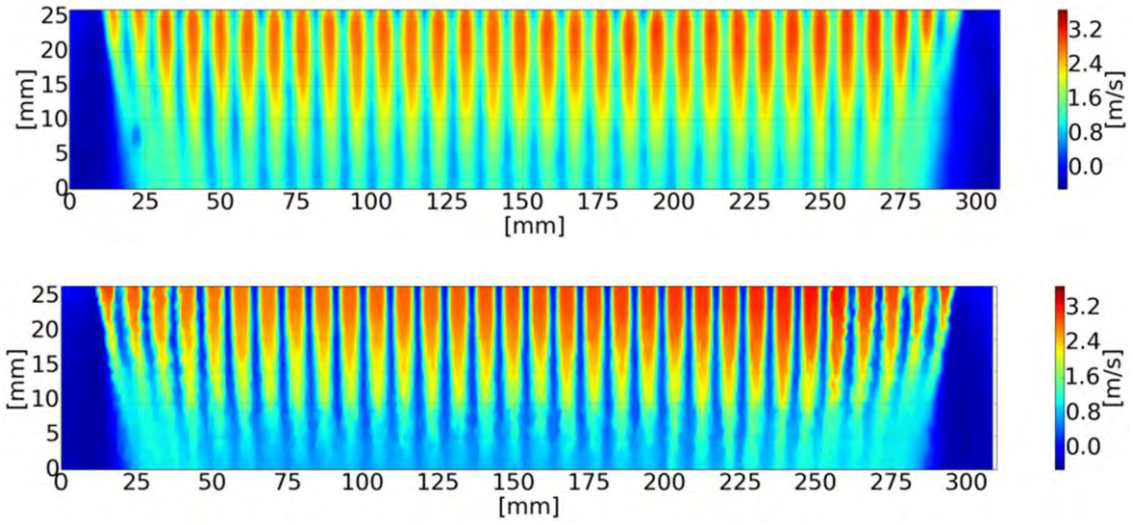

Fig.5. 20 - Velocity field on O Plane 20 (PIV data on top and Realizable K-ε computation on the bottom)

See that, the k –ε Realizable model provides a good prediction of the typical flow phenomena characterizing the evolution of multiple closely spaced jets, i.e. their interactions and the deflection of peripheral jets due to their confined arrangement.
However, slight differences can be noticed in the entrainment regions between parallel jets, where a more important velocity is measured by PIV. The k –ε Realizable model seems to underestimate the later diffusion of the equally spaced jets.

Looking more accurately at the two velocity fields plotted in Fig.5.20, it is also possible to detect the same tendency of flow distribution. A more important velocity characterizes the jets at the right side of the channel array. These channels are placed in correspondence of the impingement point where the inlet jet has a more important vertical component.

The validation of the flow maldistribution factor

It is important to note that the velocity fields in Fig.5.20 give only a preliminary and qualitative validation of the numerical model. A post-processing method has been then conceived and detailed in Section 3.2.9.4 in order to derive a measurement representative of the flow distribution between channels. Obviously, the same procedure will be applied on CFD data in order to perform a consistent comparison.

An example of the adopted procedure is illustrated in Fig.5.21 for both PIV and CFD results at the *O-Plane 20*. It consists on deriving the velocity y-velocity profile with respect to x, at a specific distance from the channel outlet (y= 21 mm). Setting the condition for a maximum, the 32 velocity peak values can be easily obtained. The amount of variation of the extrapolated peak values (standard deviation) allows quantifying the flow maldistribution on the plate (Plate maldistribution parameter σ_P). Reader has to note that only 28 peaks values have been considered for the analysis. As already explained in Section 3.2.9.4, the two external values in each linear array are affected by the jet deflection phenomena and so they are not representative of the real velocity in the channel.

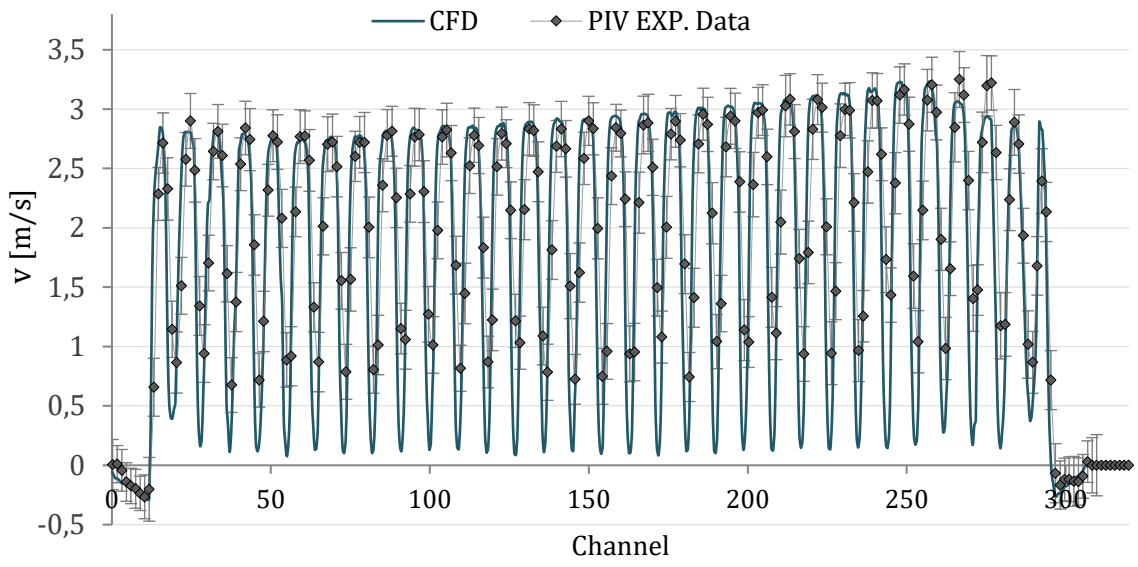

Fig.5. 21 - PIV and CFD velocity profiles at y=21mm on Plane 20 O

For the specific case of Plate 20, the maldistribution factor computed by the k –ε Realizable model is $\sigma_{P\,20-CFD} = 4.7\,\%$, whereas PIV measurements give $\sigma_{P\,20-PIV} = 3.1\,\%$ From the comparison between the two extrapolated values, the turbulence model seems to predict a more important flow maldistribution. Note that, error bars are plotted together with the experimental data points in Fig.5.21. They further validate the prediction of the numerical model.

Applying the same methodology for each plate, it is now possible to rebuild the 3D velocity distribution profile for the entire bundle. Fig.5.22 and Fig.5.23 show the 3D surface chart measured by PIV and calculated by CFD respectively. Here, each extrapolated velocity peaks are plotted over the channel number (x) and the plate number (y).

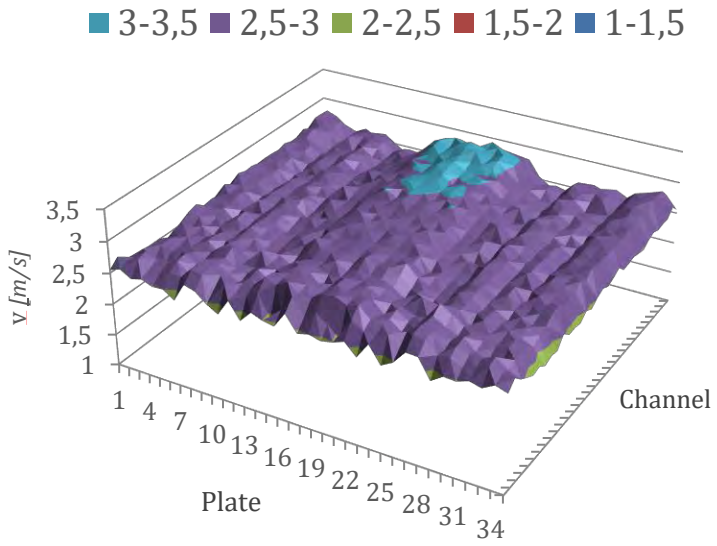

Fig.5. 22 -PIV Velocity profile distribution on the entire bundle

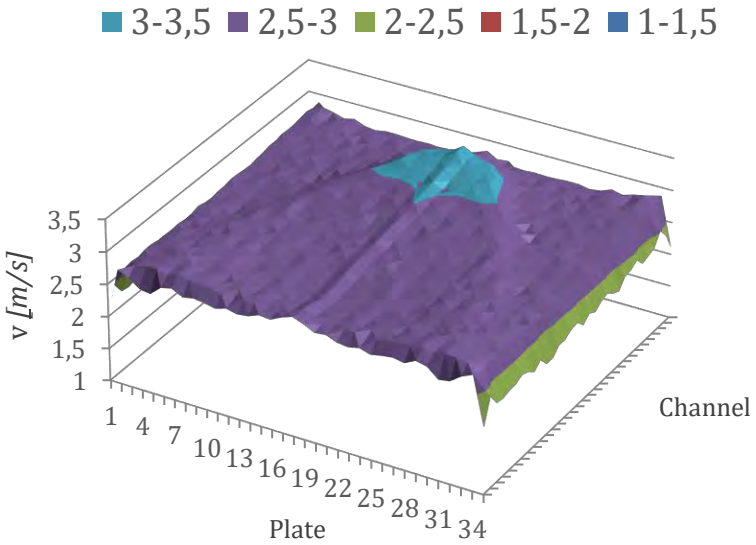

Fig.5. 23 - CFD Velocity profile distribution on the entire bundle

Looking to the two figures, it can be concluded that the k –ε Realizable model is able to predict the flow repartition between parallel channels induced by the jet flow at the normal header of compact heat exchangers. The overfeeding of channels in Fig.5.23-24 reflects the impingement zone at the inlet header where the jet impacts vertically into the bundle.

For a more detailed analysis, a global maldistribution factor σ, which is calculated as standard deviation of the whole velocity peak values, is assigned to the two 3D velocity distributions in Fig.5.22 and Fig.5.23, i.e. $\sigma_{PIV} = 4.4\%$ and $\sigma_{CFD} = 3.3\%$. The dispersion values may appear not in agreement with the previous conclusions on a single plate (O-Plane 20) announcing an overestimation of flow maldistribution by CFD simulations. However, if one looks at the PIV wavy surface in Fig.5.22, the misunderstanding is clear. The higher global maldistribution factor measured by PIV takes into account errors related to the laser plane positioning at the outlet of each plate. The ridges on the 3D profile correspond to the plates in which the laser plane has been correctly positioned by the operator at the very center of the channel outlet. Differently for other planes where the laser sheet is slightly shifted from the center; in this case the confluent jet velocity appears lower. As conclusion, the global maldistribution factor calculated simultaneously for each plate of the bundle inevitably increases.

A further evidence of this deduction is provided by the separated analysis of the maldistribution factors for each plate of the bundle. The graph in Fig.5.24 compares the plate flow maldistribution parameter for both PIV and numerical simulation.

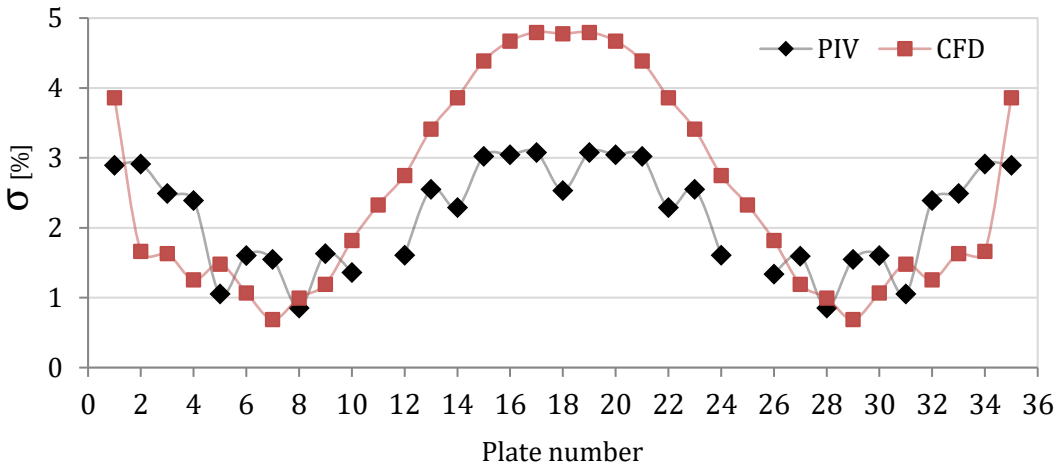

Fig.5. 24 - CFD and PIV Plate Maldistribution Factors

It can be noticed that the experimental flow maldistribution factor never exceeds the value of 3%, whereas the global maldistribution factor on the entire bundle is estimated at 4,4% (Fig.5.22). Excluding some errors due to the measurement procedure itself, the comparison between plate flow maldistribution factors allows to conclude about the performance of the numerical model.

5.3. Parametric study and Design optimization of the header design

In the first part of the Chapter 5, a preliminary design of the SGHE module allows to validate the CFD numerical approach and the turbulence model proposed to study the flow distribution.
The selected turbulence model can now be used to finalize the SGHE design process with a decisive and trustworthy optimization of the header design. An optimal configuration is then proposed at the end of this section.

As already explained in Chapter 2, this proposed solution has to meet all primary and secondary functions of the SGHE (see the *Project requirements* in Section 2.4.2). However, it is important to mention immediately that the optimization criteria considered in the present design process are focused only on one of the primary function, i.e. the uniformity of flow distribution between the channels.
All considerations related to the mechanical integrity of the component (secondary functions) contribute indirectly as guidelines for the selection of the optimal design.

5.3.1. Overview of the SGHE and optimization parameters

As already explained in Section 2.4.1, due to the ASTRID project requirements, some geometrical parameters of the SGHE design cannot be modified and are then excluded from the optimization process. For instance, all parameters associated to the exchanging zone and the diameter of the admission pipe are imposed for the achievement of thermal-mechanical performance (23.4 MW_{th}) and the observance of safety warnings.

Looking at the conceptual design of the entire SGHE module in Fig.5.25, it is now possible to identify and to characterize the physical and geometric parameters which could effectively improve the flow distribution between the channels. Fig.5.25 (right) zooms on the inlet header, which is the key component involved in this optimization process.

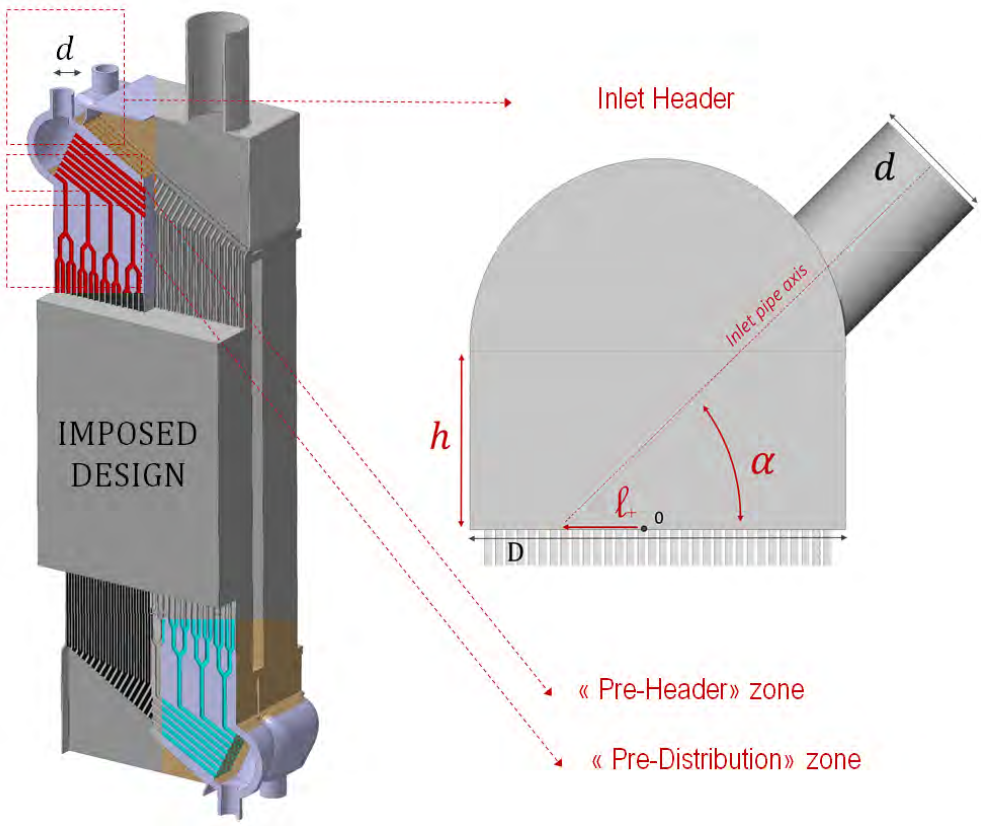

Fig.5. 25 - SGHE Layout (left) and optimization parameters at the inlet header (right)

First of all, as already seen in Section 4.3, the pressure drop in sodium side can be regulated by acting on the bifurcation design of pre-distribution channels in the "*Pre-distribution*" zone. In this sense, it is interesting to study the influence of bundle pressure drop on header-induced maldistribution, i.e.:

- Pressure drop in the channel bundle.

Concerning the inlet header, three geometrical parameters have been identified and illustrated in Fig.5.25, i.e.:

- Height of the inlet header, h.
- Inlet pipe impingement point, l.
- Inlet pipe angle, α.

Finally, the improvement due to the introduction of lateral communications in "Pre-header" zone is studied, i.e.:

- System of lateral channel communications (C).

Note that the design of the channel communications tested in this section is the result of a specific optimization study which is detailed in APPENDIX II.

As already mentioned, the main optimization criterion used in this study is the relative standard deviation between mass flows of the entire channel bundle (*Flow maldistribution factor*, σ). In addition, in order to detect the eventual presence of important local temperature gradients in the channel bundle, the maximum local difference of mass flow between two adjacent channels (*Local maldistribution factor*, $\nabla\dot{m}_{\max}$) is also calculated for each studied configuration.

5.3.2. Influence of pressure drop ΔP

According to the Lalot criterion, the increase of pressure drop in the sodium bundle leads to a higher Lalot distribution factor, η, which means a more uniform flow distribution between the channels.

$$\eta = \frac{\left(\frac{1}{2}\rho v_0^2 + \overline{\Delta P}\right)}{\overline{\Delta P}} \tag{6}$$

To quantify the influence of pressure drops on flow maldistribution (σ), six calculations are made on the same geometry distribution ($\alpha = 90°, h = 75mm, l = 0mm, NC$[16]) varying only the pressure drops along the bundle, i.e.:

- $\Delta P = 10\,000\ Pa$
- $\Delta P = 30\,000\ Pa$
- $\Delta P = 50\,000\ Pa$
- $\Delta P = 70\,000\ Pa$
- $\Delta P = 90\,000\ Pa$
- $\Delta P = 110\,000\ Pa$

Fig.5.26 shows the flow maldistribution factor σ as a function of the bundle pressure drop.

[16] No connections between channels

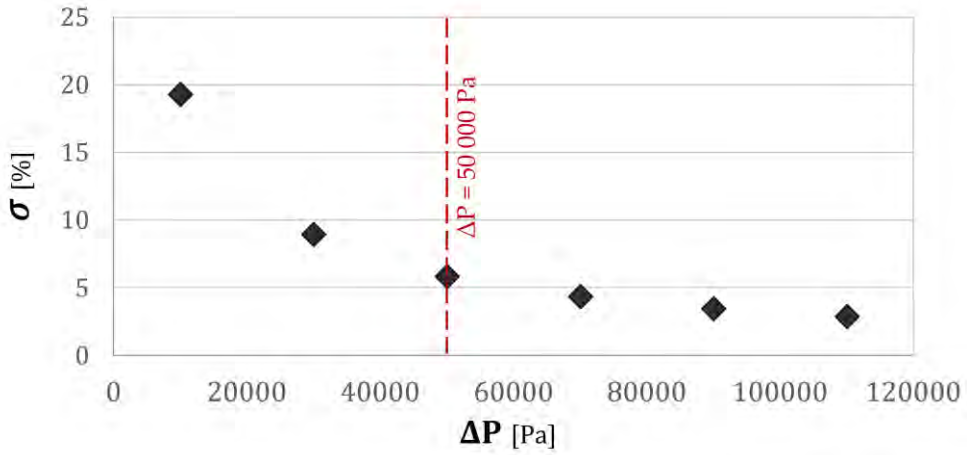

Fig.5. 26 - Flow maldistribution factor for different pressure drop ΔP

As expected, the flow maldistribution decreases with the increase of pressure drop. However, for pressure drop values higher than 50 000 the improvement in term of flow uniformity between channels is not so significant. The curve reaches an asymptote after $\Delta P = 70\,000$ Pa.

The pressure drop of 50 000 Pa is then considered as the best compromise between a uniform flow distribution and an easy integration of the SGHE in the tertiary circuit of ASTRID (limited pressure drops). This value is kept fixed for the remaining calculations in the optimization process.

5.3.3. Influence of h

Different configurations of the inlet header are considered in the present section. While the header shape and the position of the inlet pipe remain unchanged, four different values of the dimension *h* have been tested, i.e.:

- *h*= 0 mm
- *h*= 75 mm
- *h*= 150 mm
- *h*= 250 mm

This parametric study resumes the Green experimental campaign of DANAH (see Section 3.2.3).

It is important to point out immediately that, acting only on the header height (h in Fig5.25), the parameter l, related to the jet impingement position, subsequently changes. In fact, if h increases while the position of the inlet pipe is kept fixed, the distance between the axis of the inlet pipe and the center of the channel bundle changes. All conclusions derived from this study should be carefully interpreted, having in mind that h and l are correlated.

In Fig.5.27 and Fig.5.28 the 3D distribution of mass flow with the associated standard deviation and local gradient of mass flow are presented for the four investigated cases.
For a better understanding of the 3D flow distribution map, the velocity magnitude contours at the symmetry section of the inlet header are illustrated for each studied configuration.

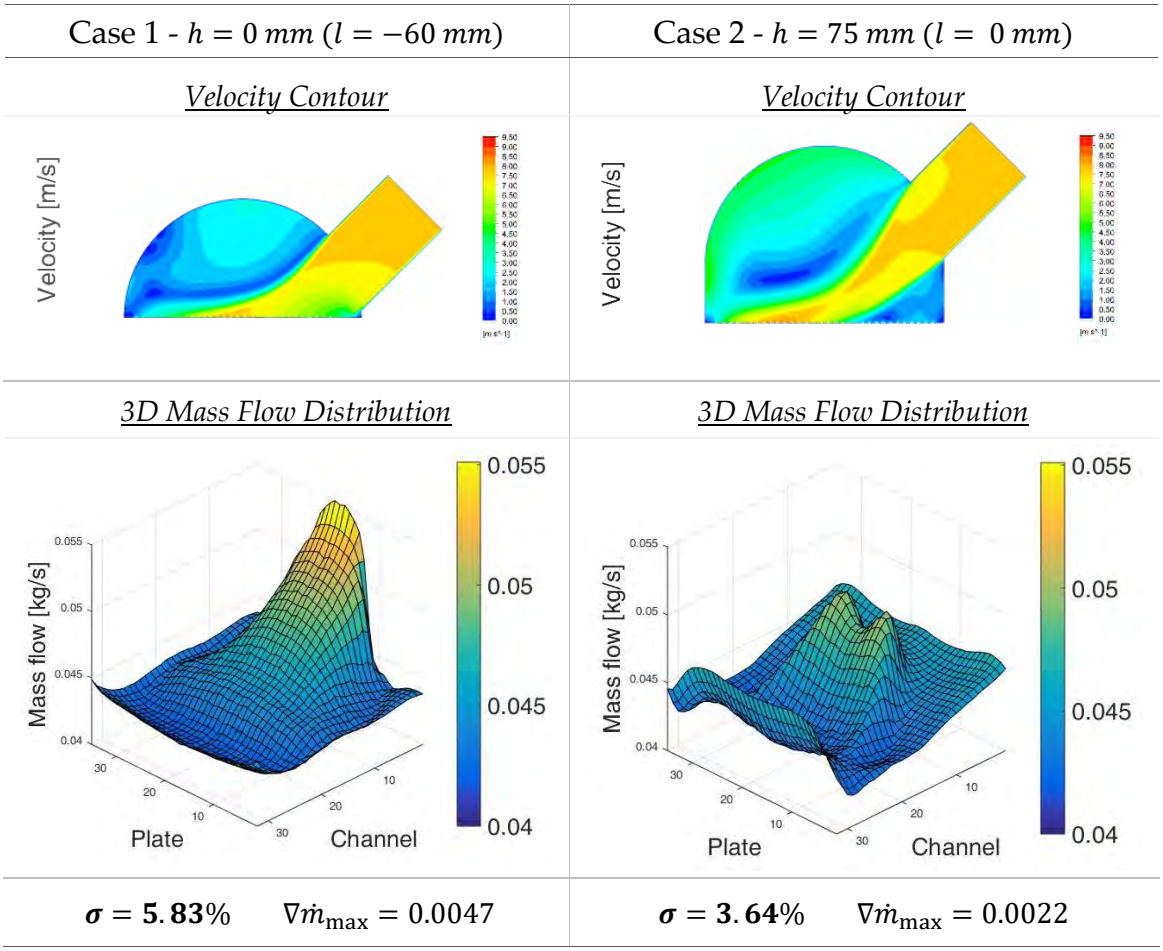

Fig.5. 27 -3D Mass Flow Distribution and velocity contour for different inlet header heights (h= 0 mm and h= 75 mm)

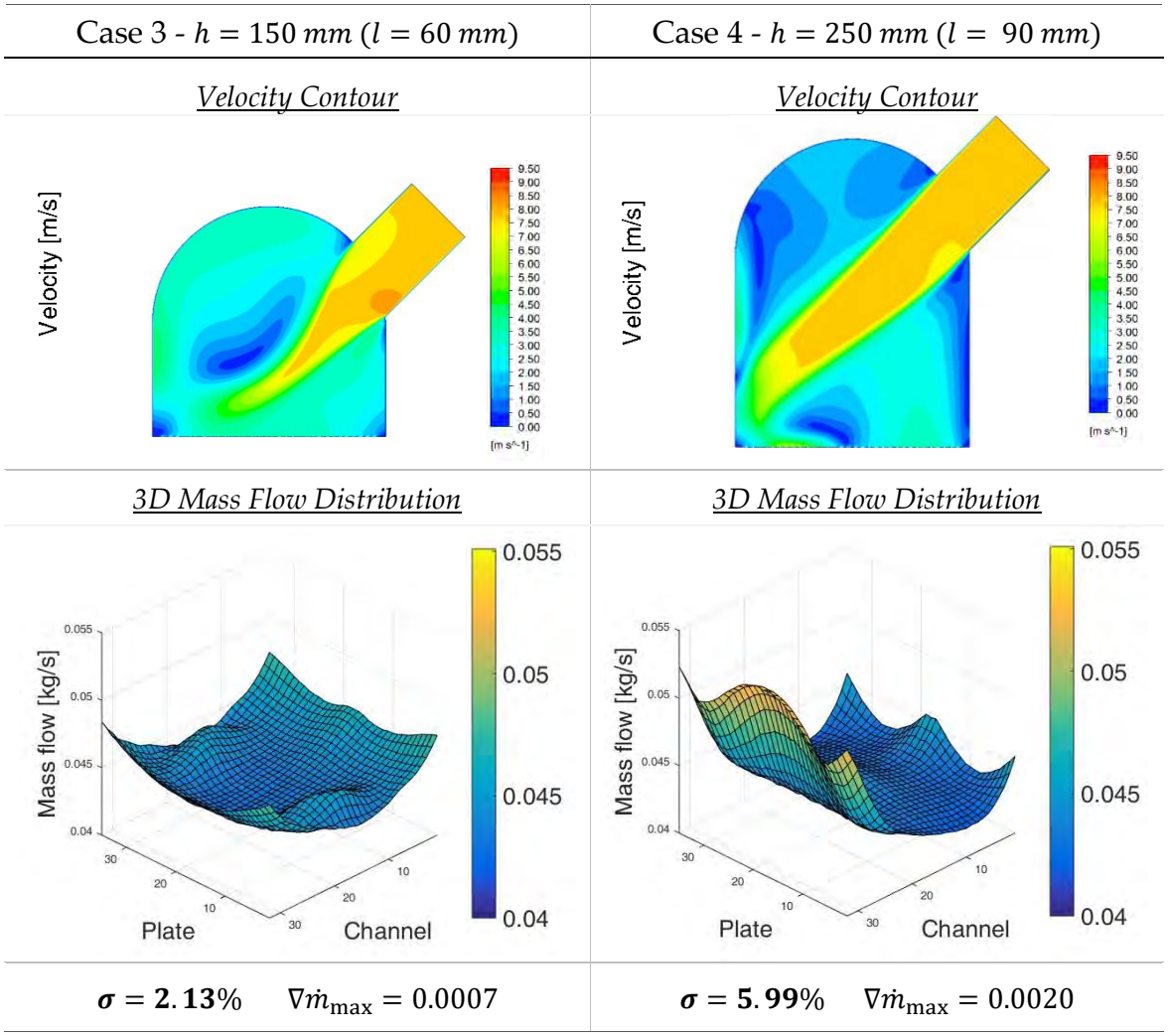

Fig.5. 28 - 3D Mass Flow Distribution and velocity contour for different inlet header heights (h= 150 mm and h= 250 mm)

As expected, the flow maldistribution decreases with the increase of the header volume. In fact, looking at the three first simulations, a more uniform distribution occurs as the header height increases. However, for higher value of *h*, the distribution of mass flow gets worse.

The 2D velocity contours in Fig.5.27 and 5.28 help to explain the surprising distribution trend. First of all, it can be noticed that with the increase of *h*, the inlet jet has more and more space to slow down and to create a recirculation in the header. If *h*=0mm, the channels on the right are more feed since the inlet jet impacts them directly avoiding flow recirculation. When *h*=75mm and *h*=150 mm, the impact of the jet moves towards the left part, as well as the overfeeding channels. Note that, in these cases the flow jet evolution

allows for a more homogenous repartition of flow. After the impact on the bundle, the jet is broken into two parts; one enters directly the channels and the other one recirculates in the header and feeds other channels afterwards.

When h=250mm, the inlet jet does not impact on the bundle but on the bottom part of the header wall. In this configuration, the jet flow is deflected directly in the left part of the channels bundle which is now more fed. This phenomenon avoids the suitable flow recirculation leading to a wrong mass flow distribution.

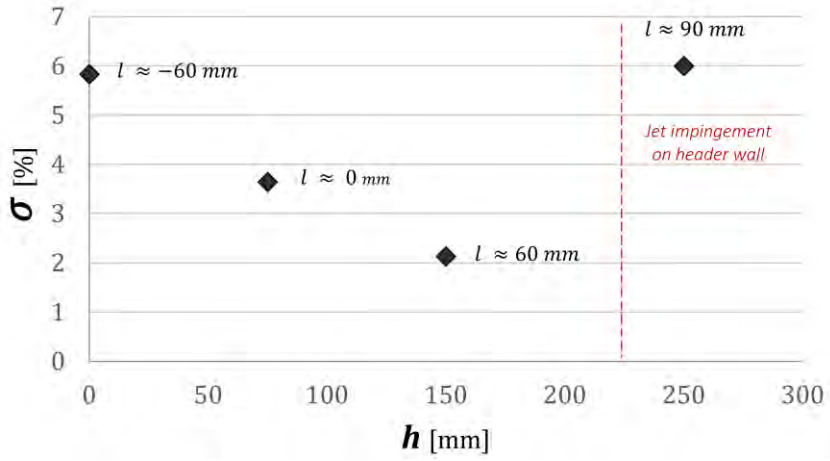

Fig.5. 29 - Flow maldistribution factor for header height *h*

Fig.5.29 summarizes the impact of the admission angle on flow maldistribution.

One of the most important conclusions of this parametric study is about the key role of the jet flow recirculation. In fact, due to the important difference between the jet flow dimension and the large cross-section of the bundle, a direct feeding of channel should be avoided; slowing down the flow jet in the header volume and leaving it recirculates is indeed the suitable way to achieve the uniform flow distribution.

5.3.4.Influence of l

On the basis of the previous study, it is not possible to distinguish which parameter between h and l has a major influence on mass flow distribution. In this section, this aspect is clarified keeping h fixed and changing l. This study is done to understand the influence of shifting only the inlet pipe position (l).

Three simulations have been considered, i.e.:

- $l = -60\ mm$

- $l = 0\ mm$
- $l = 60\ mm$

Note that, l = -60 mm and l = 60 mm represent respectively the two limit cases where the inlet jet impingement is on the extreme left and right of the channel bundle without having jet impingement on the bottom part of the header wall. It would be no sense in enlarging the investigation range in our optimization process. All the others parameters are kept fixed: h=75mm, $\alpha = 45°$, $\Delta P = 50\ 000\ Pa$ and any connections between channels (NC).

In Fig.5.30, the 3D surface of mass flow distribution and local gradient of mass flow are presented.

Case - l= - 60 mm	*Case - l= 0 mm*	*Case – l = 60 mm*
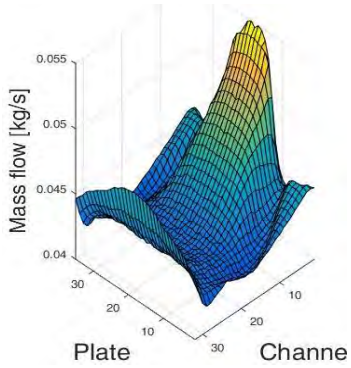	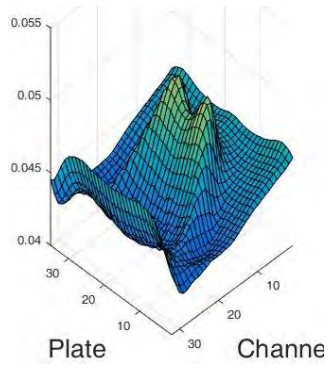	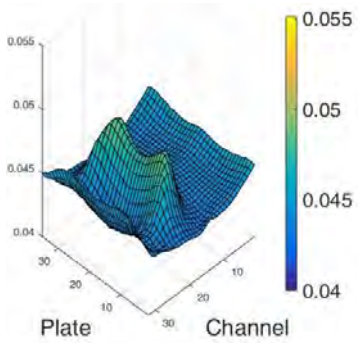
$\boldsymbol{\sigma = 5.79\%}$ $\nabla \dot{m}_{\max} = 0.0037$	$\boldsymbol{\sigma = 3.64\%}$ $\nabla \dot{m}_{\max} = 0.0022$	$\boldsymbol{\sigma = 2.45\%}$ $\nabla \dot{m}_{\max} = 0.0015$

Fig.5. 30 - 3D Mass Flow Distribution and for different jet impingement position

The results clearly show that shifting to the left the inlet pipe position allows for better flow distribution. This is essentially due to the inlet jet which has more space to slow down before the impact on the channel bundle.
The same trend has been anticipated in the previous parametric study.

5.3.5. Influence of h, *l* being constant

Once established the influence of jet flow impingement position, l, it is important to give some conclusions about the real impact of the header height h on flow distribution. For this purpose, only two different configurations, varying in h and keeping l fixed, have been considered, i.e.:

- *h*=75 mm and *l*=60 mm
- *h*=150mm and *l*=60 mm

Case - h= 75 mm - l=60mm	*Case - h= 150 mm - l=60mm*
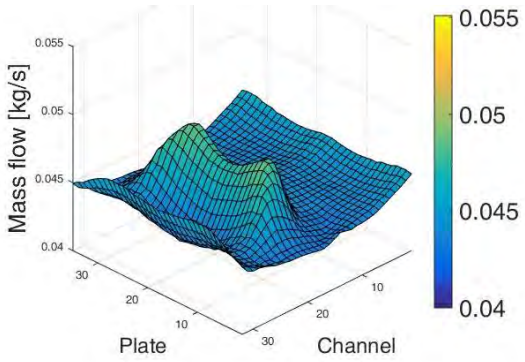	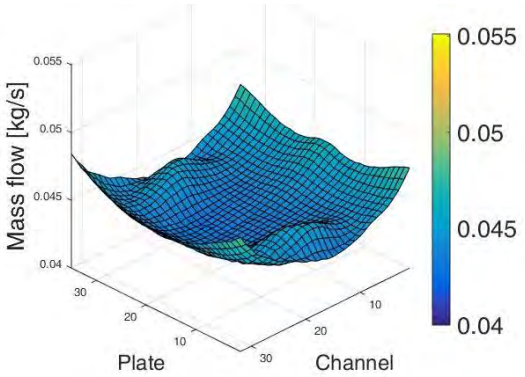
$\boldsymbol{\sigma = 2.45\%}$ $\nabla \dot{m}_{\max} = 0.0015$	$\boldsymbol{\sigma = 2.13\%}$ $\nabla \dot{m}_{\max} = 0.0007$

Fig.5. 31 - 3D Mass Flow Distribution and for different header height h

Slight differences can be noticed between both cases (Fig.5.31); doubling the value of h up to 150 mm, σ is only decreasing of 0.3 %. This latter result is important because it implies that the increment of volume has not an important influence on the flow distribution.

In addition, the small improvement does not justify the arise of problems related to the compactness and to the mechanical integrity of a component characterized by a higher header volume.
As conclusion, a header volume as small as possible will be considered for the optimal design.

5.3.6.Influence of α

The last variable parameter of the inlet header is the admission angle of the inlet pipe, α (Fig.5.25). Five different inclinations of the inlet pipe axis have been considered to study its impact on flow distribution, i.e.:

- $\alpha = 0°$
- $\alpha = 30°$
- $\alpha = 45°$
- $\alpha = 60°$
- $\alpha = 90°$

The fixed parameters are: h=75 mm, l=0 mm, $\Delta P = 50\,000$ NC.
Note that, the horizontal admission angle ($\alpha = 0°$) is here investigated for sake of completeness; the resulting SGHE layout could never be adopted for the ASTRID project.

Fig.5.32 shows the 3D surface charts of mass flow distribution with the relative standard deviation and the maximum local gradient of mass flow for the five studied configurations.

Case - $\alpha = 90°$	*Case* - $\alpha = 60°$	*Case* - $\alpha = 45°$
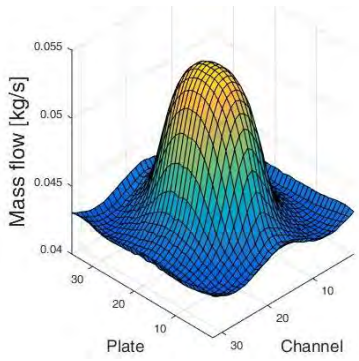	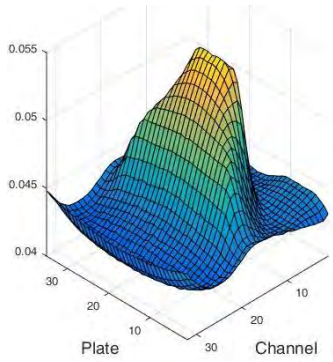	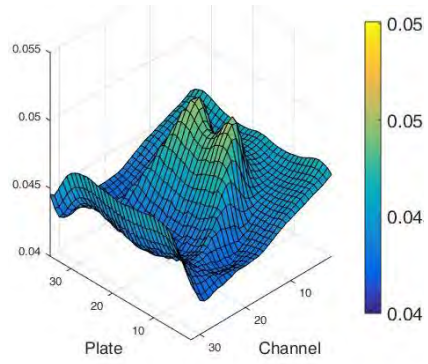
$\boldsymbol{\sigma = 7.62\%}$ $\nabla \dot{m}_{\max} = 0.0037$	$\boldsymbol{\sigma = 6.30\%}$ $\nabla \dot{m}_{\max} = 0.0038$	$\boldsymbol{\sigma = 2.45\%}$ $\nabla \dot{m}_{\max} = 0.0015$

Case - $\alpha = 30°$	*Case* - $\alpha = 0°$
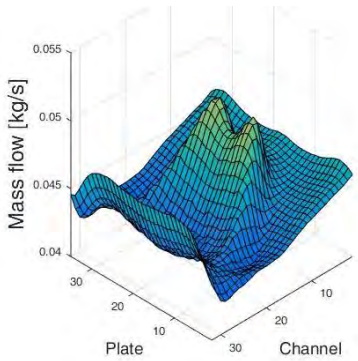	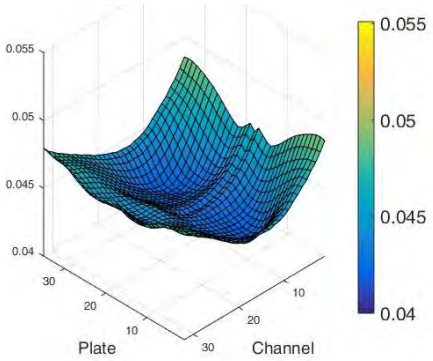
$\boldsymbol{\sigma = 4.02\%}$ $\nabla \dot{m}_{\max} = 0.0022$	$\boldsymbol{\sigma = 3.47\%}$ $\nabla \dot{m}_{\max} = 0.0009$

Fig.5. 32 - 3D Mass Flow Distribution for different admission angles

The trend of the maldistribution factor σ as a function of the admission angle is then plotted on the graph in Fig.5.33. The flow maldistribution improves as the admission angle decreases.

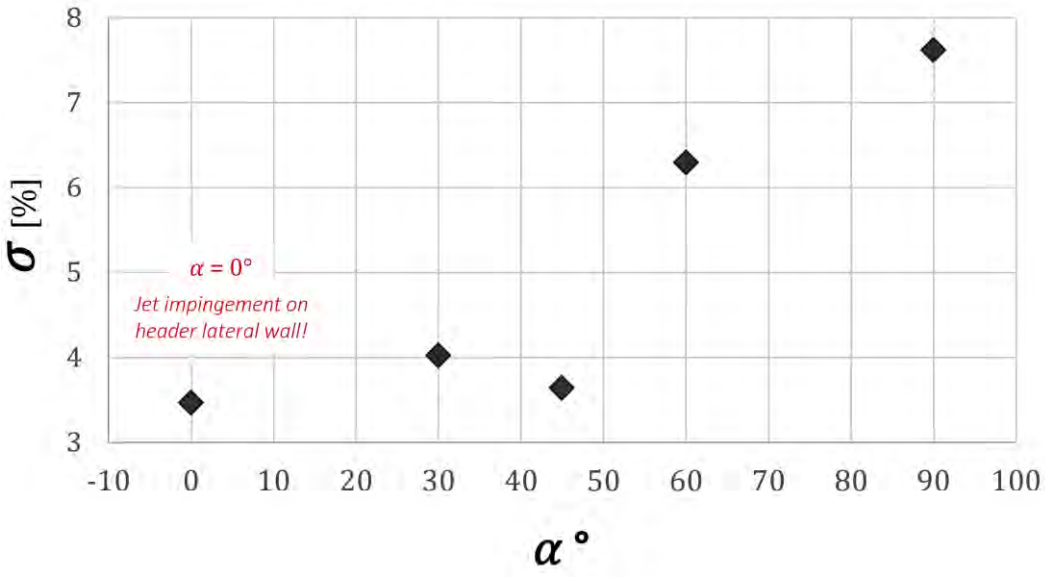

Fig.5. 33 - Flow maldistribution factor for different admission angles α

Referring to Fig.5.33, starting from 90° and decreasing α, the flow maldistribution factor decreases until 45°, which is a local minimum, then it gets worse. After a local maximum at α around 30°, σ starts to decrease again.

Specifically, in header configurations with α=90°and α=60°, the bad flow distribution is due to the vertical impingement of jet flow at the center of the channel bundle. The jet flow impingement avoids the correct flow recirculation leading to a more uniform repartition of mass flow.
Impingement conditions leading to a favorable splitting of the jet and flow recirculation actually occur for $\alpha = 45°$.

A further decrease of the admission angle ($\alpha = 30°$), results in a deterioration of flow distribution. In fact, in this case the inclination angle directs the jet towards the left bottom corner of the inlet header. As result, the jet cannot accelerate in the horizontal direction avoiding the required flow recirculation for a flow redistribution. Similar conditions occur for the header configuration with h=250 mm in Section 5.3.3.

Finally, header with the admission angle of $\alpha = 0°$ seems to provide the best flow distribution. This is essentially due to new flow recirculation conditions occurring in the volume which are illustrated by velocity streamlines in Fig.5.34. After the horizontal impingement on the lateral header wall, the jet splits in two equal parts and recirculates in the volume before feeding the channels of the bundle.

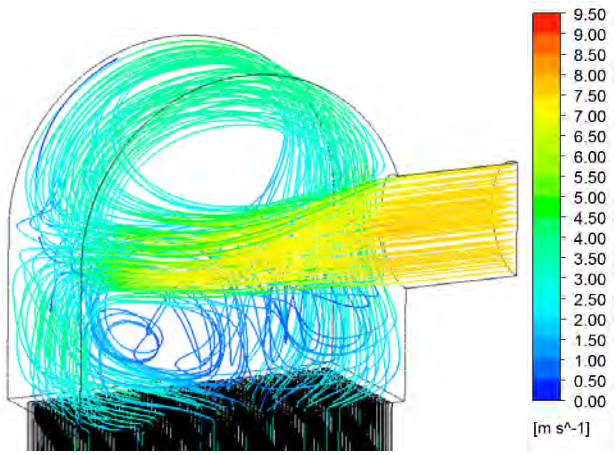

Fig.5. 34 - Velocity streamlines at the inlet header for $\alpha = 0°$

In conclusion, $\alpha = 45°$ and $\alpha = 0°$ seems to be the two best candidates for the admission pipe angle. However, for the time being, the SGHE layout and the arrangement with the pressurized vessel exclude headers with horizontal admission angle ($\alpha = 0°$) from suitable solutions for the optimal configuration.

5.3.7. Influence of adding connection: pre-bundle

The purpose of this study is now to evaluate the impact of the channel connections on flow distribution. The performance of the system of channel communications, optimized in APPENDIX II, has been tested for the first header configuration studied in Section 5.3 ($h = 0mm,\ l = -60mm0,\ \alpha = 45°$).

In Fig.5.35 the 3D surface of mass distribution with σ and the maximum local mass flow gradient are presented[17].

[17] Meshing all channel communications implies an increment of 25000000 grid elements. The coupled method for p-v coupling can't be used anymore because of RAM requirement. A SIMPLE algorithm must be used. To evaluate the differences induced by using a different method, a calculation with SIMPLE has been made with α=90° to compare the solution with the one with coupled in paragraph [4.3.3] and not big differences are found (as an example there is only 0.3% of difference between the two σ).

Case – NO Channel Communications	*Case –Channel Communications*
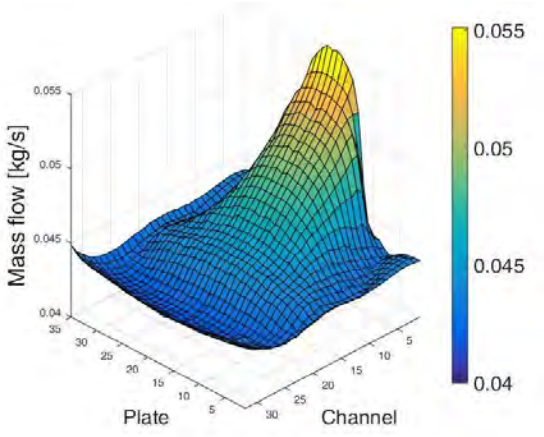	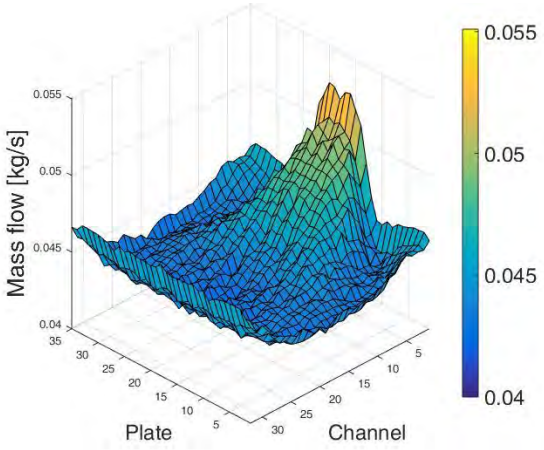
$\boldsymbol{\sigma = 5.83\%}$ $\nabla \dot{m}_{\max} = 0.0047$	$\boldsymbol{\sigma = 3.74\%}$ $\nabla \dot{m}_{\max} = 0.0023$

Fig.5. 35 -3D Mass Flow Distribution without and with channel communications

The results show an improvement of 2% on the maldistribution factor σ with respect to the case with no connections ("NC"). The maximum local gradient is also halved.

Note that, the effectiveness of the channel communications is strictly dependent from the flow conditions occurring at the entrance of the bundle. A greater improvement was noticed for different inlet flow conditions varying in the intensity of flow maldistribution and the position of mass flow peak values (see APPENDIX II for explanation).

5.3.8. Distribution performance comparison and proposed solution for ASTRID SGHE

Fig.5.36 summarizes all the previous parametric studies on flow distribution. The histograms plotted on the graph are a graphical representation of the distribution performance of each investigated configuration. The bars are assembled in five different groups, each of one corresponds to a specific parametric study. The variable parameter is reported on the graph together with the other ones which are kept constant.

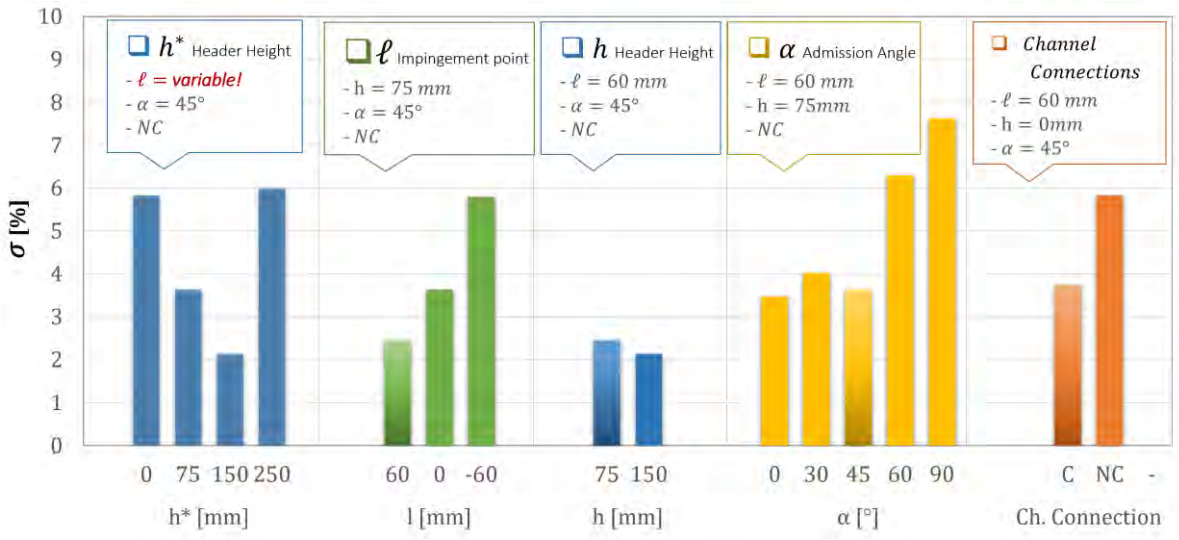

Fig.5. 36 – Flow distribution performance – Optimization study

The first group of blue columns represents the parametric study on the header height h. As already explained, in this study the geometries are modified only by increasing the length h ($\alpha = 45°$), so the position of the inlet jet impingement on the channels (length l) changes consequently. This is the reason why the second group of blue columns is added (h). This additional study allows concluding about the influence of header height h while the length l is kept fixed.

The green columns represent the study on the jet impingement position. The three conceivable lengths have been tested for the header of height 75mm.

The influence of the admission angle α is illustrated by the yellow columns, whereas the performance of the channel communications by the orange ones.

The overall analysis helps to identify the key solution to the flow maldistribution problem, i.e. the jet flow recirculation.

It is now clear that the direct feeding of channels should be avoided. However, the arrangement of SGHE module in the pressure vessel forces the inlet jet to impact on the bundle channels ($\alpha \neq 0°$). Hence, the admission angle and the length l have to provide an appropriate jet impingement on the bundle.

First of all, the angle has to be enough inclined to accelerate the jet flow along the horizontal direction after the impact on the bundle ($\alpha = 30° \div 45°$). Then, the presence of the lateral header wall obliges the flow to recirculate forming a jet tracing the header boundaries.

Secondly, concerning the length l, the impingement point has to be located on the left ($l > 0\ mm$) as much as possible without having jet impingement on the wall ($l < 60mm$).

Concerning the header volume, it seems not to have a significant impact on the flow distribution. So, the most compact solution will be selected in order to ensure the mechanical integrity of the component (small header).

Finally, despite its relative improvement in term of σ, the introduction of channel communications helps to the homogenization of flow distribution between the channels.

Table 5.3. lists the main geometrical features of the optimal solution identified for the ASTRD SGHE module.

	h	l	α	Connections
SGHE '17	*[mm]*	*[mm]*	*[°]*	*[-]*
	75	60	45	C

Table 5. 3 – Optimal SGHE Design ('17)

5.4. Conclusions

In the present chapter the analysis of flow in the integral design of the SGHE module has been done to identify the physical phenomena ongoing in the header volume and the consequent flow distribution between channels of the bundle.
The confined three-dimensional jet flow evolution and the flow distribution in the bundle have been analyzed at the inlet header with PIV experimental data and Realizable k-ε results. It was demonstrated that the adopted computational approach allows to correctly quantify the flow maldistribution induced by the inlet distributor in the SGHE module.

Once validated the numerical model, a design optimization has been performed taking into account the key parameters which have a significative influence on the flow jet behavior. The best performance design of the inlet header and the admission pipe are proposed in the last section.
This design provides a very uniform distribution while maintaining a small header volume which better resists to the external pressure constraints.
The sodium piping system connection requires an inclined angle for the header admission tube (compact pressure vessel in Fig.1.7). The optimal angle ($\alpha = 45°$) issued from the optimization study provides a beneficial jet impingement on the bundle in term of flow recirculation.

In addition, the optimal pressure drop of the channel bundle interferes with the jet flow providing a high resistance to the jet impingement. The jet is forced to recirculate in the header volume allowing for a better distribution.
The flow distribution resulting from the header design is then further improved by a system of channel communications installed in the first part of the bundle. The communication system, which is a sort of perforated grid integrated in the bundle, provides a redistribution of flow and pressure field between pre-distribution channels.

Referring to the very low maldistribution factor provided by this optimal design of the SGHE module, it can be concluded that the final goal to reduce flow maldistribution as much as possible has been achieved. With respect to the original design of the SGHE, the maldistribution factors decreased from 25 to 2%.
However, this promising result does not allow to conclude about the mechanical integrity of the bundle. In fact, a thermal analysis is required to evaluate the thermal stresses resulting from the mass flow distribution between channels (see Section 6.2.1).

Chapter 6

Conclusions and Perspectives

6.1. Conclusions

In the framework of CEA R&D program to develop an industrial prototype of Sodium cooled Fast Reactor, the present thesis contributed to validate the use of compact heat exchanger technology for the Brayton Gas-power conversion system in the tertiary loop of ASTRID reactor.

The design of the sodium distribution system in the HE module has been the object of the present work. The component was affected by a real problem of flow maldistribution between parallel channels degrading thermal and mechanical performance of the SGHE module.
Therefore, the present thesis started studying the flow "maldistribution" in compact heat exchanger in order to understand the main causes and to figure out potential design solutions to the problem. The bibliographic study attributed the origin of the "maldistribution" issue to the imbalance between the low pressure drop bundle and the high velocity at the inlet distributor.

To overcome this problem, the design of the sodium distribution system illustrated in Fig.6.1 has been proposed.
A system of bifurcations has been introduced in pre-distribution channels to increase pressure losses while the header design tries to guide the jet flow evolution for a more uniform distribution. Lateral communications between pre-distribution channels have been recommended to further homogenize the distribution before flowing in the active part of the bundle.

The sodium distribution system has to be studied numerically and experimentally to demonstrate its hydraulic performance and the fulfillment of ASTRID project requirements.

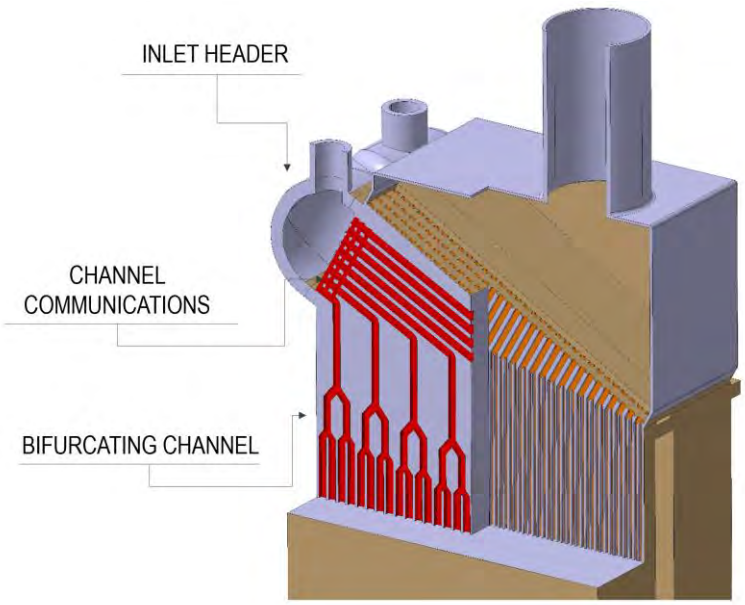

Fig.6. 1 – Proposed design solution SGHE (2017)

Different flow phenomena at different scales actually contribute to the performance of the proposed design in Fig.6.1. Therefore, the thesis strategy required a previous separated investigation of bifurcating pre-distribution channels followed by the global flow "maldistribution" analysis in the integral module.

As regard to the bifurcation system, the basic idea was to design a short bifurcating channel able to increase pressure drop without introducing any additional maldistribution. In this sense, it has been demonstrated that a proper flow separation at bifurcation is the key success factor.

Therefore, to provide a reliable turbulence model to correctly describe the flow separation in bifurcating channel, an experimental database has been collected. The Particle Image Velocimetry (PIV) campaign and mass flow measurements at generated branches allowed us acquiring the hydraulic database for model validation. The ASST model was proved to be a very good option for the final characterization of ASTRID bifurcating system giving great results in a very short computational time.

Once designed the bifurcation system, the global flow maldistribution has been studied experimentally and numerically. The attention has been focused on the influence of the inlet header design on flow repartition between channels. The thesis strategy has proposed to represent the bifurcation system by means of additional pressure drop in the regular bundle simplifying the analysis of the global flow maldistribution.

The complex evolution of the three-dimensional jet flow, since it drives the performance of HE has required a detailed analysis. The ability of numerical models to correctly describe the jet flow and the resulting flow distribution between channels needed to be verified.

No actual test case has been found in literature to be fully applicable to the present study, so a modular experimental test section, DANAH, has been conceived. The Particle Image Velocimetry (PIV) campaign and the elaborate post-processing of velocity data validated the numerical model proving, at the same time, the efficiency of the additional pressure drops in the bundle. The Realizable k-ε model has been retained as reference model to perform the optimization of the inlet header.

As conclusion, the large experimental and numerical program carried out during this PhD work provided a reliable numerical approach to study the flow maldistribution problem in the SGHE module. Thanks to the second test section on the integral sodium distribution system, a direct experimental evidence of the performance of proposed design solutions have been conferred as solid base in support to the qualification program of the Sodium-Gas energy conversion system.

6.2. Perspectives

The work done in this thesis deals with all hydraulic issues related to the sodium maldistribution problem in SGHE. It provides innovative design options, which have been validated by large experimental campaigns, and leads to a valuable improvement in term of flow distribution. Optimization studies on some distribution components still remain.

It can be concluded that the present PhD provided important results to complete the first step for the assessment of the sodium distribution system which has to limit the thermomechanical loading of the component.

6.2.1. Thermo-mechanical analysis of proposed SGHE design

As already explained, the SGHE design proposed in the present thesis is the result of an optimization process based on the hydraulic performances in term of sodium distribution. Theoretically, this is only the first step of the entire design process which includes a thermal analysis of the sodium temperature field and the quantification of thermal and pressure stresses in the bundle. These latter need to be evaluated according to the RCC-

MRx code to verify the acceptance criteria. Fig.6.2 illustrates a schematic diagram of the design process.

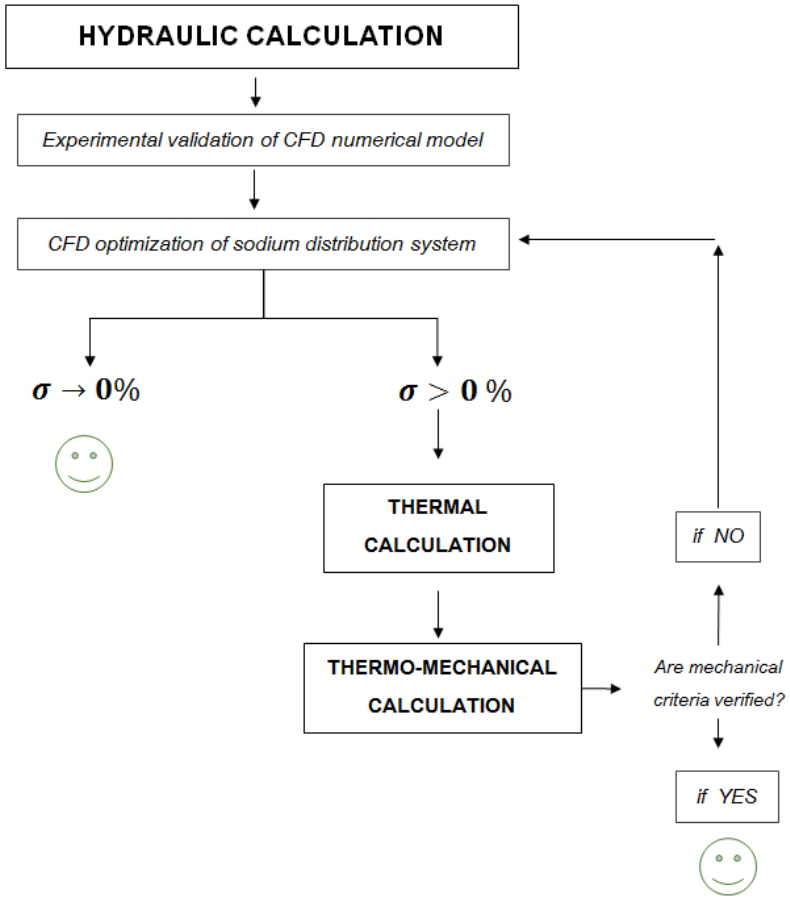

Fig.6. 2 - Design process SGHE

However, this process would require lots of assumptions and a very long time to asses a proper thermo-mechanical analysis of ASTRID SGHE module.
On the other hand, thermomechanical margins are small if one takes into account all damages evaluation process. For this reason, the maldistribution has to be as lower as possible, σ approaching 0% is the main goal.

Anyway, to give an estimation of the global performance of proposed solutions, the ε-NTU method has been applied to calculate the resulting sodium temperature field. The maximum temperature difference between two sodium channels has been then compared with that one occurring in the 2014 design of SGHE module.

Note that, in this phase of the project, the ε- NTU method is a valid substitute of CFD thermal calculations since it is conservative in term of temperature maldistribution. In fact, one of the most important assumptions of this method is that the heat exchange between two adjacent sodium channels is neglected. In case of maldistribution of mass flow (different temperature between sodium channels), this would lead to a consistent error in the evaluation of the outlet temperature. If the exchange between adjacent channels is considered, the maldistribution of temperatures should decrease.

The ε-NTU method has been applied to one of the distribution case studied during this thesis work, i.e. $\alpha = 90°$, h=75 mm, l=0mm, Channel Connections, $\Delta P = 50\,000\,Pa$. Note that this is not the optimal configuration identified in Section 5.3.8.

The 3-D surfaces of the normalized sodium mass flow in the channels and the normalized sodium temperature at the channel outlets are presented in Fig 6.3 (both curves are normalized with the respective mean value).

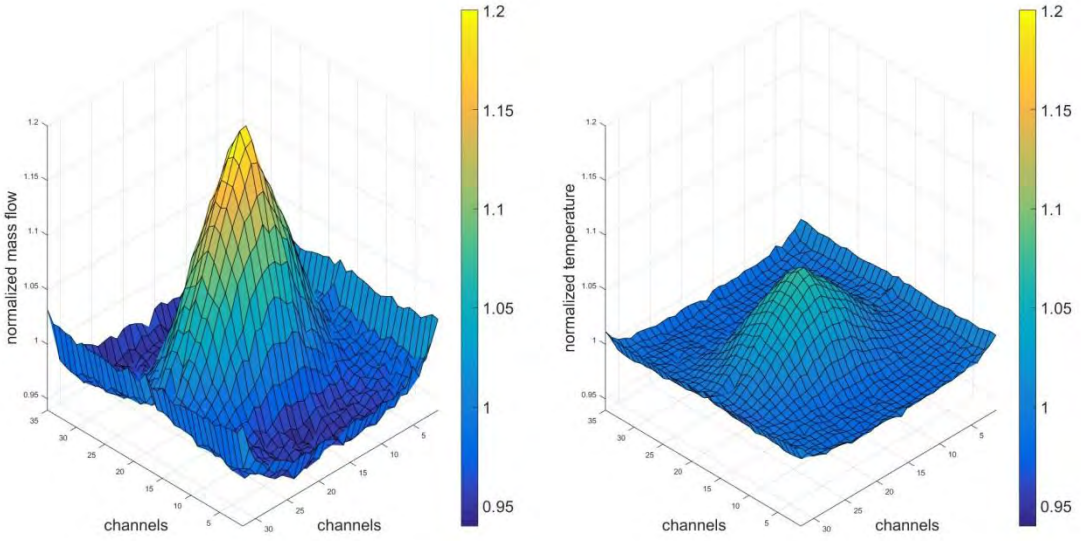

$\sigma = 4.81\%$ $\sigma = 1.82\%$

Fig.6. 3 - Mass flow and ε-NTU temperature distribution

First of all, it is possible to notice that, the maldistribution of temperature results lower than the maldistribution of mass flow in relative terms, which is good from the mechanical point of view. Secondly, as obvious, the shapes of the 3D surfaces are the same.

The mean outlet temperature calculated is 347°C, instead the minimum and maximum values are respectively 340°C and 371°C. The total ΔT on the outlet channels surface is about 30°C.

Table 6.1 compares the sodium temperature fields occurring in the starting 2014' design of SGHE module and the improved one. See that, the maximum temperature difference is reduced by 75%. A further mechanical calculation is necessary to verify the equivalent thermal stresses of 2017 SGHE design.

SGHE	Velocity inlet	Pressure Drop	Lalot criterion	Maldistribution factor	Mass Flow Rate		Temperature		
	m/s	Pa	-	%	kg/s		°C		
'14	10	6 000	2.77	25	min	max	min	max	mean
					0.008	0.239	314	437	348
'17	10	60 000	1.29	4.81	0.011	0,013	340	371	347

Table 6. 1 - Distribution performance of 2014 design of SGHE module

6.2.2. Optimization of communication zone in bifurcating channels

In the last section of Chapter 4, a new performant design of bifurcating channels has been proposed. The basic idea was to introduce communication zones before branching channels taking advantage of pressure gradients to homogenize the velocity field such as channel communications in the "Pre-Header" component (see APPENDIX II).

The comparative analysis in Table 4.8 showed the efficiency of the communication zones, however due to the PhD scheduled deadlines, any optimization study has been performed on these linking structures. Increased dimensions of communication zones at each stage of bifurcation could reduce the channel length necessary to minimize bifurcation-induced maldistribution.

6.2.3. Experimental validation of channel communications

DANAH facility developed at the CEA and described in Chapter 3, has been deeply utilized during this work. It has been initially scheduled to test the pre-header component in two different configurations of DANAH, i.e. one characterized by a very bad initial flow distribution and the other corresponding to the best suited configuration for ASTRID.

However, DANAH facility has remained out of work for a long time due to several technical reasons and it was decided to delete the first test of Pre-header from the experimental program.

Unfortunately, no exploitable results for CFD model validation could be obtained from the second test. In fact, the effectiveness of the channel communications is strictly dependent from the flow conditions occurring at the entrance of the bundle, which were already quite good in the DANAH configuration chosen for the "Pre-header" test. Here, the lower pressure gradient between channels and the uncertainty of PIV measurements avoid any consistent conclusion about the performance of the "Pre-Header".

It is then recommended to test the efficiency of channel connections on DANAH configurations characterized by important flow maldistribution.

As regards to the numerical approach used to study the system of channel connections, a k-ε Realizable model with enhanced wall treatment for the ε-equation has been chosen as reference model. The choice of this model is the result of a comparative study, on a single sodium plate, which involves two other models, i.e. the k-ω SST and the k- ε Realizable model with standard wall functions. The Realizable k-ε model with enhanced wall treatment has proved to be as accurate as the k - ω SST model, but the computational effort required is definitely lower.
Nevertheless, the available work station does not allow meshing the whole channel bundle of SGHE module. Therefore, the optimization of channel communications has been performed on a reduced geometry of a square bundle channel composed by 10 plates of 10 channels (see APPENDIX II). This provides some important conclusions about the key geometric parameters influencing the flow distribution, however the optimization on the real geometry of SGHE bundle has not yet been done.
In this sense, the modelling of an anisotropic porous medium which allows for the pressure and velocity field induced by a specific design of channel communication could be a reliable solution to the numerical study of channel connections in the SGHE.

6.2.4. Improvement of the numerical approach

The numerical model used to study the evolution of the three-dimensional jet flow in the inlet header is the Realizable k-ε model. It showed very good predictions at the central impingement plane whereas, further from this, some discrepancies with experimental data can be noticed. The reason of model failure was initially searched in the isotropic

formulation of eddy diffusivity in modeling the Reynolds stress tensor, which prevents them from accounting for the inequality of the normal stresses.

The Reynolds Stress Model-LPS was then tested instead, because it offers a greater potential for predicting the anisotropic phenomena. However, any improvement has been noticed. This is probably due to the higher order correlations need to be modeled with some drastic assumptions of unknown validity, where even the principles and basic techniques for their modeling have not been established yet, at least in the near wall region [88].

For this reason, the same practice of modeling the anisotropy in the flow which has been used for the pre-distribution channels (ASST model) is recommended for the k-ε model. The Modified SZL model of Baglietto et. al. [88] which couples the linear k-ε model with a 2^{nd} order non-linear Reynolds stress formulation could be tested for the present application.

Moreover, the modeling approach of the present work has been that of RANS turbulence models. However, other finer models could be used to investigate innovative channel flow characteristics that RANS models hardly show, i.e. SAS or LES.

APPENDIX I

Porous medium model

Section 4.1.2 and Section 5.1.2 demonstrated the need of porous medium modelling to reduce the mesh element count and computational time in simulations. Being not interested in the explicit analysis of flow pattern in the active bundle (Chapter 4) and in the bifurcation system (Chapter 5), porous media have been used to represent their equivalent pressure drop in more regular geometries. The porous medium region has been introduced in each channel of the bundle in order to preserve the channel discretization while reducing their length. Pressure drops from singularities (header/channel section restriction) and the post-processing of the channel-by-channel flow are then possible.

As regard to the mathematical model considered to set the pressure loss as a function of the calculated velocity field, source terms have been added to the equations of the momentum [78]. This source term, $S = \frac{\Delta P}{L_{PM}} \left[\frac{Pa}{m}\right]$ contributes to pressure gradient in CFD porous region creating pressure drop proportional to the calculated velocity field.

ANSYS Fluent proposes different laws to modelized homogeneous porous medium [78]. A power law model has been selected for the present PhD work, i.e.:

$$S = -C_0|v|^{C_1} \tag{61}$$

where $|v|$ is the mean velocity at the mesh center.
Now, we need to determine the expression of two parameters, C_0 and C_1.

If we consider the case of the pre-distribution channel in Chapter 4, porous media has to provide the equivalent pressure drop of 2-meter channel bundle ($L_{ch-bundle}$).
The pressure drops of a turbulent channel flow be expressed by Darcy formula, i.e.:

$$\Delta p_{ch} = \frac{1}{2} * f_{Da} \frac{L_{ch}}{D_h} \rho v^2 \tag{62}$$

where f_{Da} is the friction factor, L_{ch} the channel length, D_h hydraulic diameter and ρ the fluid density.
The friction factor and the Reynolds number can be expressed as follow:

$$f_{Da} = 0{,}3164 * Re^{-0{,}25} \tag{63}$$

$$Re = \frac{\rho v D_h}{\mu} \tag{64}$$

By replacing Eq.63-64 in Eq.62:

$$\Delta P = \frac{1}{2} * \left(0.3164 * \rho^{0.75} * D_{hydr}^{-1.25} * \mu^{0.25} * Lch\right) * v^{1.75} \tag{65}$$

Looking at Equation (), it could be possible to recognize the value parameters C_0 and C_1. However, as already mentioned, in the meshed computational domain declared as porous region (L_{PM}), Fluent solves the friction losses to which adds the pressure losses related to the source term. This means that to be rigorous, the value of Lch in Equation has to be equal to:

$$Lch = L_{ch-bundle} - L_{PM} \tag{66}$$

As conclusion, the parameters C_0 and C_1 in equation () are defined as follow:

$$C_0 = \frac{\frac{1}{2} * \left(0.3164 * \rho^{0.75} * D_{hydr}^{-1.25} * \mu^{0.25} * (L_{ch-bundle} - L_{PM})\right)}{L_{PM}} \tag{67}$$

$$C_1 = 1.75 \tag{68}$$

The porous media model described above has been validated in [46]. CFD results of flow distribution in the SGHE explicit geometry of half sodium plate are compared with results where sodium plate is modeled as porous media. Xavier et al. showed that flow distribution with the porous medium model is reproduced within ± 3% for 94% of flow rate values [46].

.

APPENDIX II

Optimization of channel connections – *"Pre-Header"*

The present appendix summarizes the optimization study performed on the system of lateral communications in the "Pre-Header" zone. The influence on flow distribution of different geometrical parameters and different boundary conditions are presented below.

The computational domain considered for the entire optimization study is shown in Fig.II.1. A square bundle channel composed by 10 plates of 10 channels has been considered as a good compromise between CFD computational effort and the analogy with the real geometry of 32x35 SGHE bundle channel.
A porous media region is introduced to represent the pressure losses of the bifurcation system and the entire length channel in the active bundle, i.e.: 50 000 Pa.

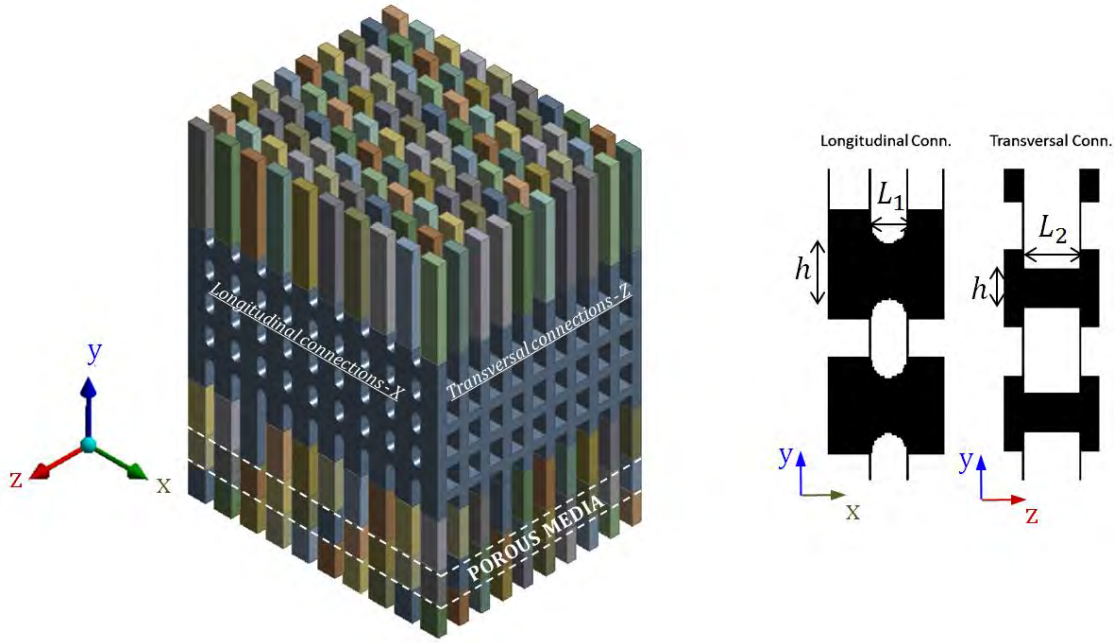

Fig.II. 1 - Computational domain

Geometrical features are listed in Table II.1.

	h	L_1	L_2	N° Stage
Channel	0.112	0.006	0.003	-
Longitudinal connection	0.004	0.006	0.003	4
Transversal connection	0.003	0.006	0.0045	4

Table II. 1 - Geometrical features

The simulating working fluid is water at atmospheric temperature and pressure. Liquid water properties are kept from Fluent database, i.e. density of 998.2 kg/m^3 and a dynamic viscosity of 0.001003 kg/ms.

Optimization parameters

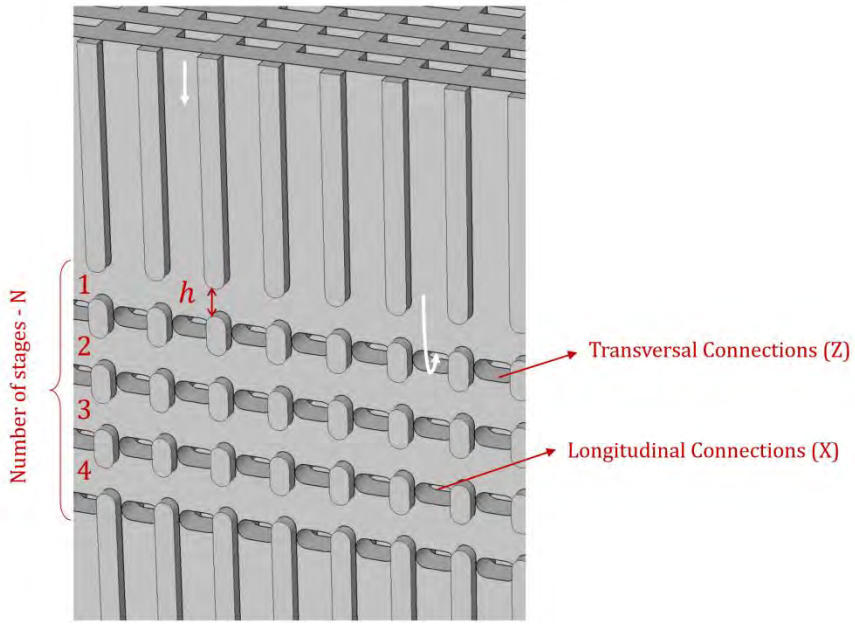

Fig.II. 2 - Optimization parameters

Fig.II.2 shows a zoom on the pre-header zone and channel connections. Geometrical parameters in red are optimized. They are changed once at a time to get a reliable evaluation of the influence of each parameter.

1. Presence of longitudinal connections (X)
2. Presence of transversal connections (Z)
3. Connection height (h)
4. Number of longitudinal connections stages (N_s)
5. Presence of obstacles (O)

In addition to the above mentioned geometrical parameters, the efficiency of the communication system is tested for different inlet mass flow distribution values and different mass flow inlet profiles.

II.1. Channel connections

In order to evaluate the efficiency of longitudinal and transversal connections three different configurations with same boundary conditions have been tested. Geometries used in parametric are showed in Fig.II.3, i.e.:

- Pre-header bundle without longitudinal connections ("*C-Z*")
- Pre-header bundle without transversal connections ("*C-X*")
- Pre-header bundle with both longitudinal and transversal connections ("*C-XZ*").

"Pre-Header" configuration		
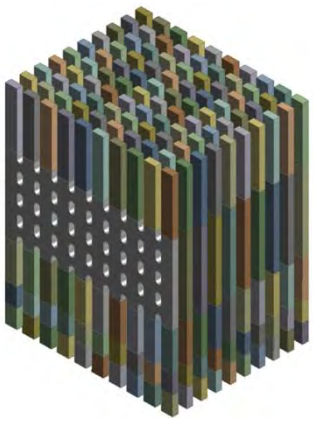	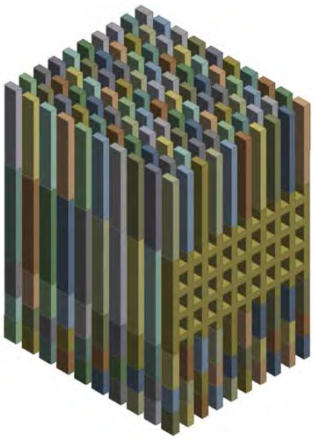	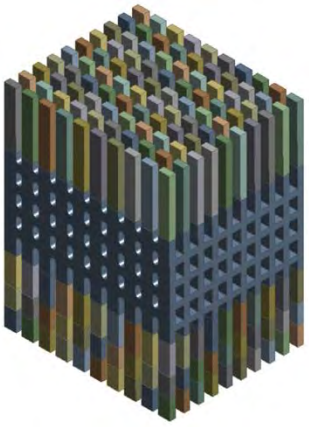
Pre-Header "C-X"	**Pre-Header "C-Z"**	**Pre-Header "C-XZ"**

Fig.II. 3 - Parametric Study: Influence of lateral communications

The mass flow profile set as inlet boundary condition is plotted in Fig.II.4.

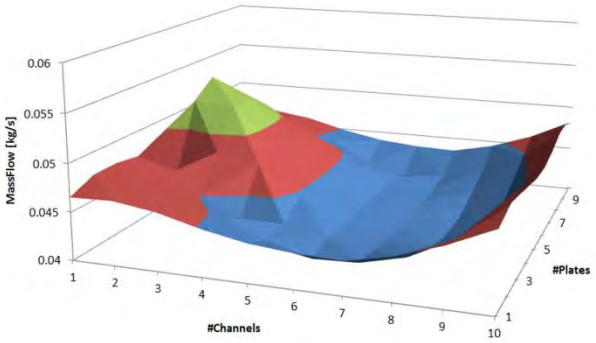

Fig.II. 4 - Mass flow inlet profile

The associated inlet flow maldistribution factor is reported in Table II.2 together with the resulting flow distribution at the outlet.

	Pre-Header "C-X"	Pre-Header "C-Z"	Pre-Header "C-XZ"
σ_{Inlet} [%]	6.7134	6.7134	6.7134
σ_{Outlet} [%]	1.4028	5.5937	0.7584
P_{Inlet} $[Pa]$	60 700	62 200	63 300

Table II. 2 - Inlet/Outlet flow maldistribution factor and Pressure Inlet

It can be concluded that the presence of longitudinal connections clearly improves flow distribution while the transversal connections seem to no affect the blending of mass flow in different channels. This is essentially due to the geometrical differences between X and Z connections (Table II.1). This leads to different directional efficiency.

In fact, mechanical calculations made on gas-side components of the heat exchanger and sodium-gas plate arrangement imposed some limitations on design criteria. One of the geometrical features imposed by previous thermo-mechanical design is the minimum distance between plates: it was fixed to 0.0045 m. The distance between channels was already set as well: it was conceived to be 0.003 m.

II.2. Longitudinal connection height, h

How connection dimensions and in particular its height affects the mass flow blending have been studied comparing the following different configurations with same boundary conditions. The reference geometry (C-XZ) with a connection height of 0.004 m has been compared to one with a connection height of 0.002m (C_h_X0.002), 0.006m (C_h_X0.006) and 0.008m (C_h_X0.008) (Fig.II.5).

Longitudinal connection heigth

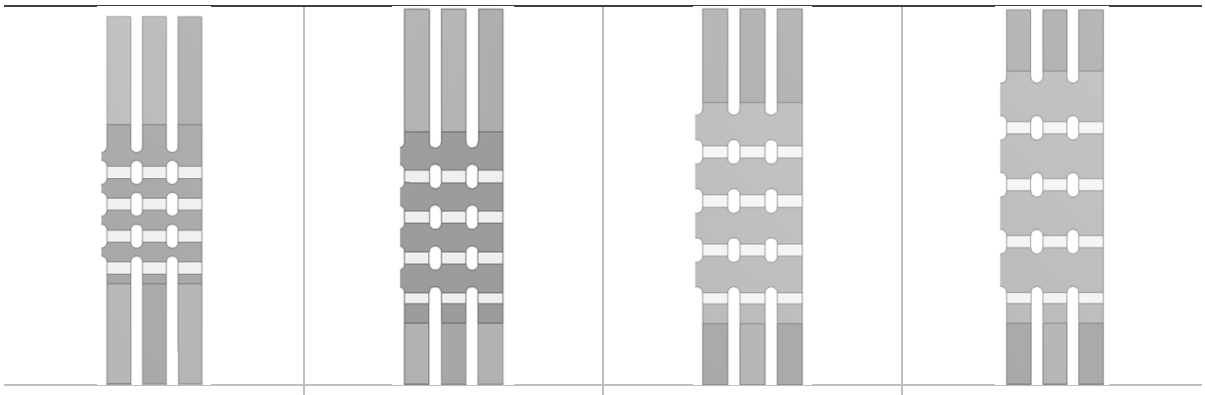

"C_h_X0.002"** **"C-h_X0.004"** **"C-h_X0.006"** **"C-h_X0.008"

Fig.II. 5 - Parametric Study: Longitudinal Connection height

The mass flow profile set as inlet boundary condition is plotted in Fig.II.6 (Gaussian profile).

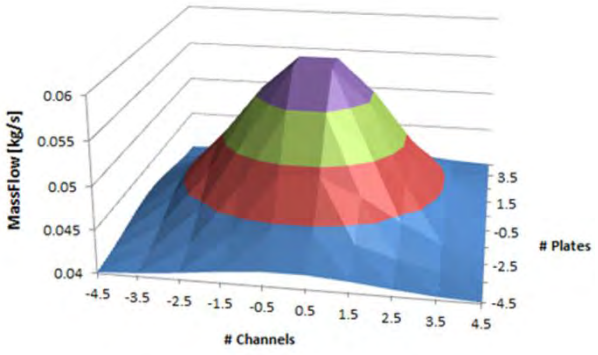

Fig.II. 6 - Mass flow Gaussian inlet profile

The associated inlet flow maldistribution factor is reported in Table II.3 together with the resulting flow distribution at the outlet.

	"C-XZ_X0.002"	**"C-XZ_X0.004"**	**"C-XZ_X0.006"**	**"C-XZ_X0.006"**
σ_{Inlet} [%]	11.38	11.38	11.38	11.38
σ_{Outlet} [%]	0.99	1.00	0.94	0.89
P_{Inlet} $[Pa]$	61 000	61 000	61 100	61 100

Table II. 3 - Inlet/Outlet flow maldistribution factor and Pressure Inlet

As predictable, consequently of the increment in connections height, the global outlet maldistribution decreases. However, the improvement is quite negligible if we consider the accuracy range of CFD. The same can be said for the inlet pressure values.

As conclusion, the longitudinal connection height is excluded from key parameters affecting the efficiency of the communication system.

II1. Influence of number of stages in longitudinal connections

The number of stages of longitudinal connections is another variable that has been deepened studied during channel grid design optimization. Its influence on pre-header performances has been analyzed in the present section.

The geometrical configurations taken into account for this analysis are the reference geometry that has 4 stages of connections, a 5-stage geometry and a 3-stages geometry. In Fig.II.7 geometries are showed.

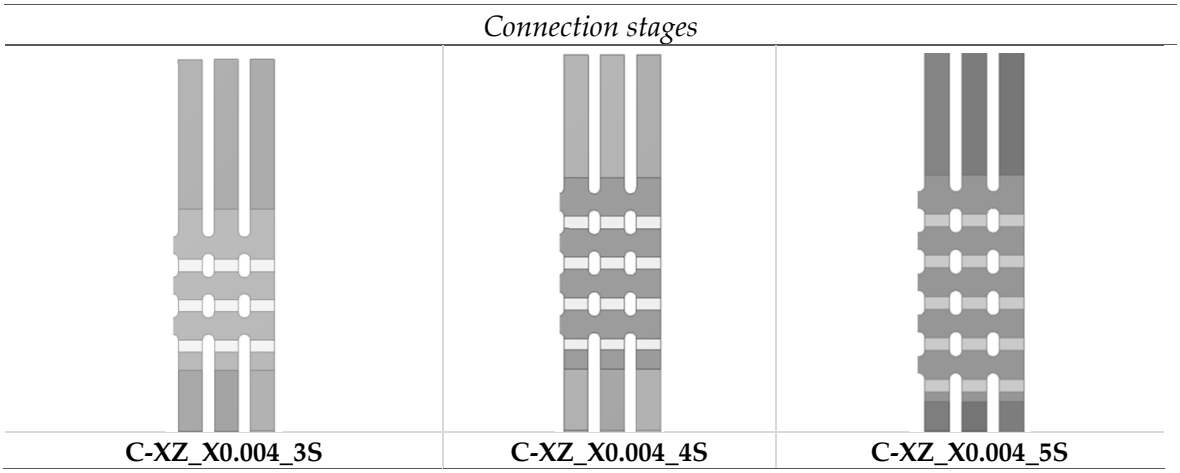

Fig.II. 7 - Parametric Study: Number of lateral connections stage

The mass flow profile set as inlet boundary condition is the same considered in Section II.2. The associated inlet flow maldistribution factor is reported in Table II.4 together with the resulting flow distribution at the outlet.

	C-XZ_X0.004_3S	**C-XZ_X0.004_4S**	**C-XZ_X0.004_5S**
σ_{Inlet} [%]	11.38	11.38	11.38
σ_{Outlet} [%]	1.13	1.00	0.95
P_{Inlet} $[Pa]$	60 000	61 000	61 900

Table II. 4 - Inlet/Outlet flow maldistribution factor and Pressure Inlet

From data in Table II.4, it seems that greater the number connection stages is, better is the mass flow blending. Nevertheless, it seems that benefits from increasing the number of connections stages become less visible with the number of stage increment.
By the way, it is important to evaluate if the increment of stages is truly worthy for the SGHE module: this evaluation should take into account both manufacturing and module compactness considerations. For instance, the increase in stage number requires a more important connection zone length with respect to the increase of connection height (compactness criterion).

As conclusion, a four-stage connection system with larger connections height has been considered has optimal design for the SGHE, i.e. $C-XZ\_X$ 0.008_$4S$. The same connection geometry has been considered in Section 5.3., where its performance has been evaluated in the integral design of the 32X35 SGHE bundle.

II.3. Influence of longitudinal obstacles

Section II.1-3 proved the advantages of fostering the physical blending thanks to modelling the longitudinal connection's shape. Starting from this consideration, the position of longitudinal connections was shifted in order to enhance the blending effect. In the new configuration (*C-XZ-O*) the flow is facing obstacles due to the new position of connections[18]. In previous geometries these obstacles were between two different channels. Fig.II.8 clarifies connections set-up in the different configurations (red circles).

Presence of obstacles	
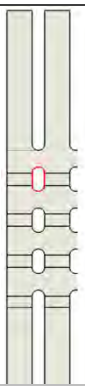	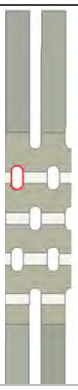
C-XZ	**C-XZ_O**

Fig.II. 8- A new design of lateral communications

The mass flow profile set as inlet boundary condition is the same considered in Section II.2. The associated inlet flow maldistribution factor is reported in Table II.5 together with the resulting flow distribution at the outlet.

	"C-XZ"	**"C-XZ_O"**
σ_{Inlet} [%]	11.38	11.38
σ_{Outlet} [%]	1.00	0.76
P_{Inlet} [Pa]	61 000	71 100

Table II. 5 - Inlet/Outlet flow maldistribution factor and Pressure Inlet

This result enforces the previous consideration on mass flows blending: higher is the grade of blending, lower is the value of outlet σ. In Pre-Header configuration "*C-XZ_O*" fluid flow is forced to change direction because of the presence of obstacles; in this configuration x and z components of velocity are higher, consequently the efficiency of

[18] In geometry 18 marginal channels have been split in half in order to estimate the efficiency of longitudinal obstacles without considering wall effects (those are negligible for the real configuration of the 32*35 channel grid). In order to gain a more trustworthy simulation, marginal channels are split in half. Consequently, mass flows are halved so the velocity profiles for both geometries are identical.

longitudinal connections grows. However, this design solution provokes too high pressure at the inlet due to the presence of obstacles. Reader is remembered that to provide an easy-integration in the ECS circuit, an upper limit of sodium bundle pressure drop exists, i.e. 0.5 bar[19]. This limit value could be exceeded if justified by a real improvement on flow maldistribution.

II.4. Inlet mass flow maldistribution intensity

The analysis of geometrical parameters influence on pre-header performances is of paramount importance during the optimization design stage: previous simulations deepened the knowledge of fluid flow behavior throughout the channel grid and help to define the best configuration for the definitive pre-header.
How boundary conditions affect channel grids performances will disclose if the pre-header's efficiency isn't strongly dependent from external conditions. If so, this component could be adaptable to other heat exchanger.

In order to easily test the pre-header under different external conditions, 5 mass flow profiles have been defined. They correspond to Gaussian distributions varying in peak intensity. Those profiles have been tested on the reference geometry ("C-XZ"). The associated inlet flow maldistribution factor is reported in Table II.5 together with the resulting flow distribution at the outlet.

	#Mass Flow 2	**#Mass Flow 1**	**#Mass Flow 3**	**#Mass Flow 4**	**#Mass Flow 5**
σ_{Inlet} [%]	13.90	16.46	11.38	9.47	6.70
σ_{Outlet} [%]	1.23	1.46	1.00	0.80	0.52
Decrement factor	91%	91%	91%	91%	92%

Table II. 6 - Inlet/Outlet flow maldistribution factor and maldistribution decrement factor

II.5. Mass flow inlet peak position

The analysis of how inlet peak position affects pre-header performances was carried out with the same method shown for previous simulations: 3 mass flow inlet profiles with different peak positions have been defined. In this case global maldistribution was equal to 9.98 for all the profiles. The shape of mass flow inlet profiles is illustrated in Fig.II.9.

[19] The upper limit of pressure drop for the entire SGHE is imposed to 1,5 bars.

Mass flow inlet – Peak position

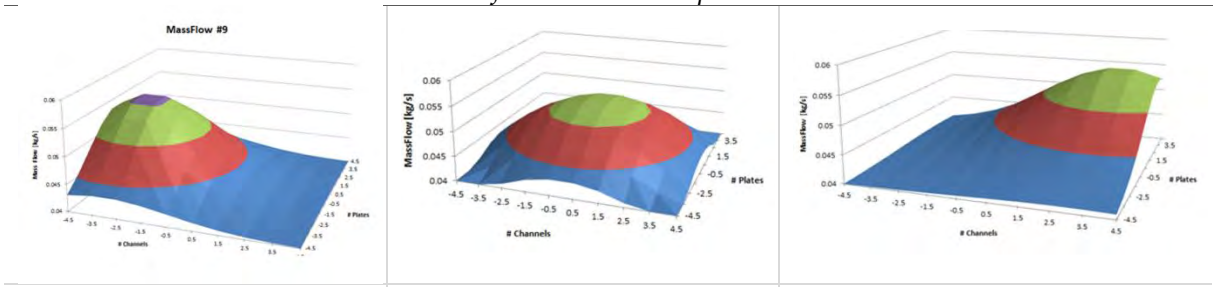

C-XZ_Left	C-XZ_Center	C-XZ_Right

Fig.II. 9 – Mass flow inlet peak positions

This parametrical study has been done on the reference geometry ("*C-XZ*").
Table II.7 shows the mass flow distribution improvement as function of the peak position.

	C-XZ_Left	C-XZ_Center	C-XZ_Right
σ_{Inlet} [%]	9.98	9.98	9.98
σ_{Outlet} [%]	1.44	0.798	2.08

Table II. 7 - Inlet/Outlet flow maldistribution factor

The analysis of outlet maldistribution unquestionably discloses the best position to get higher mass flow blending. When the peak is in central position, all connections, both longitudinal and transversal, take part actively in the blending. As soon as the peak is shifted in a peripheral zone of the bundle, the efficiency falls down. Note that, connection systems perform less well when the inlet peak is shifted on the right.

As conclusion, the inlet peak position has a more important impact on the efficiency of the connection system with respect to the peak intensity. This means that the introduction of channel connections in the SGHE module is suggested for admission tube angles close to 90° (Section 5.3.6).

APPENDIX III

III.1. EASY-B: Mockup 1

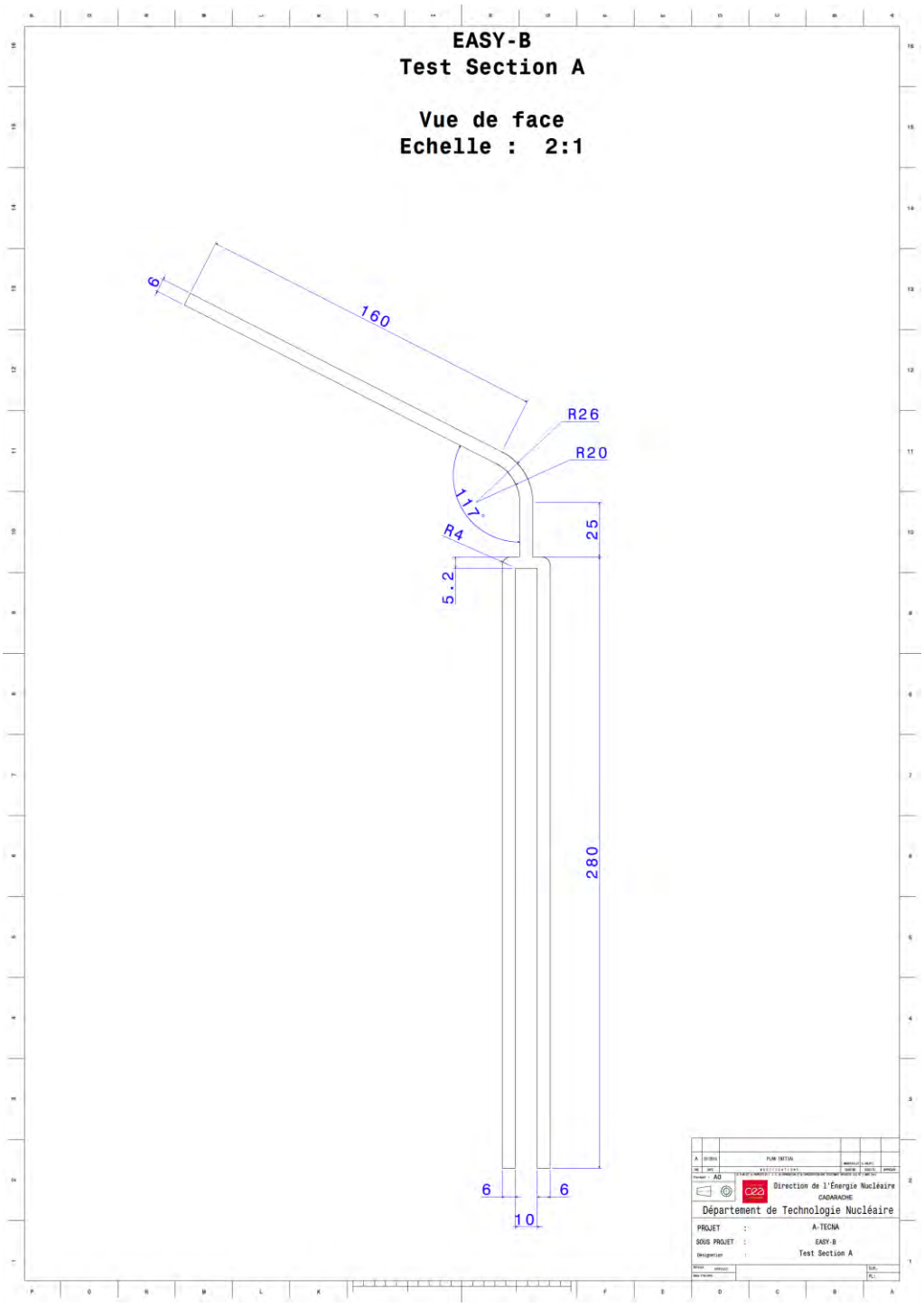

III.2. EASY-B: Mockup 2

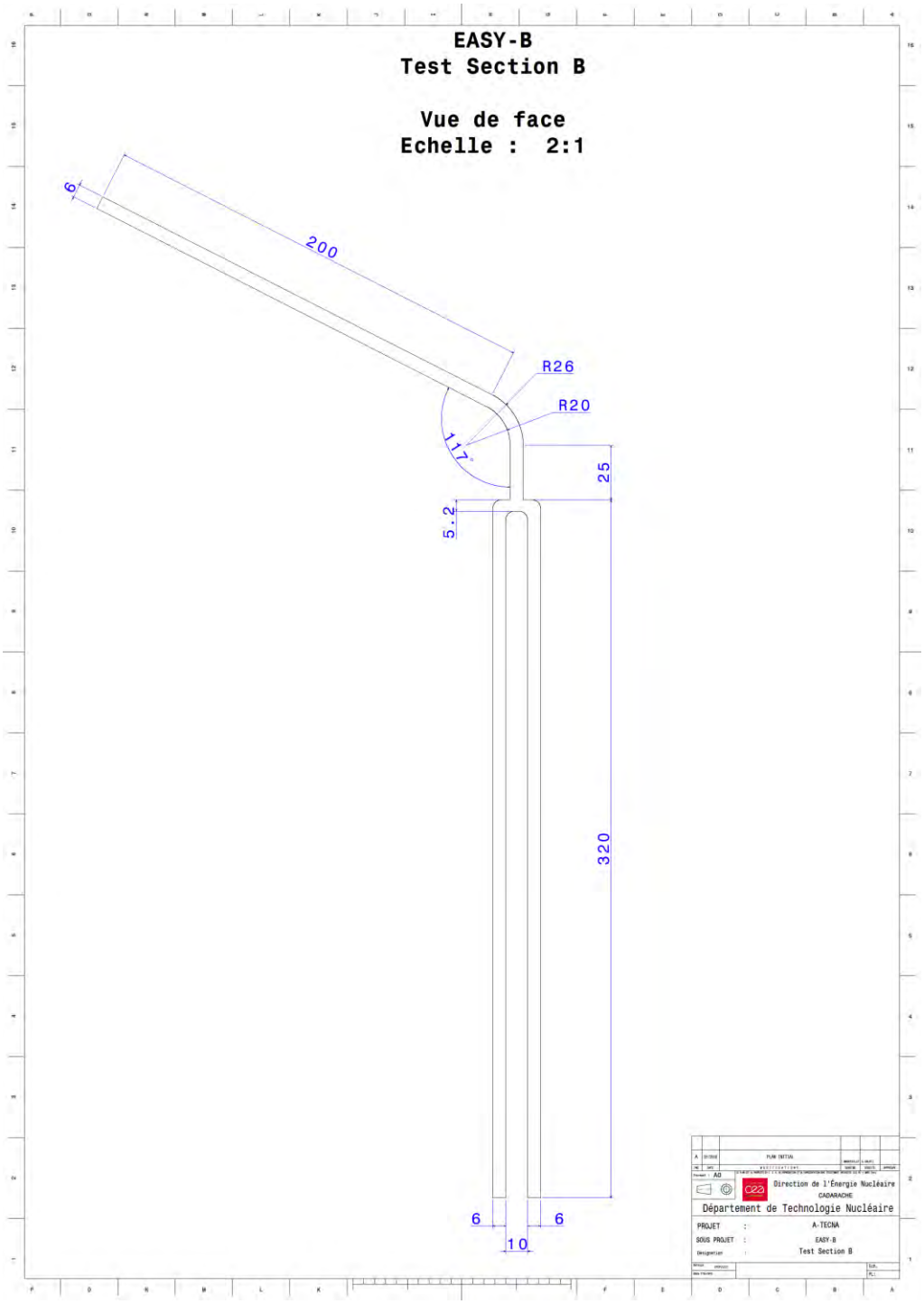

III.3. EASY-B: Mockup 3

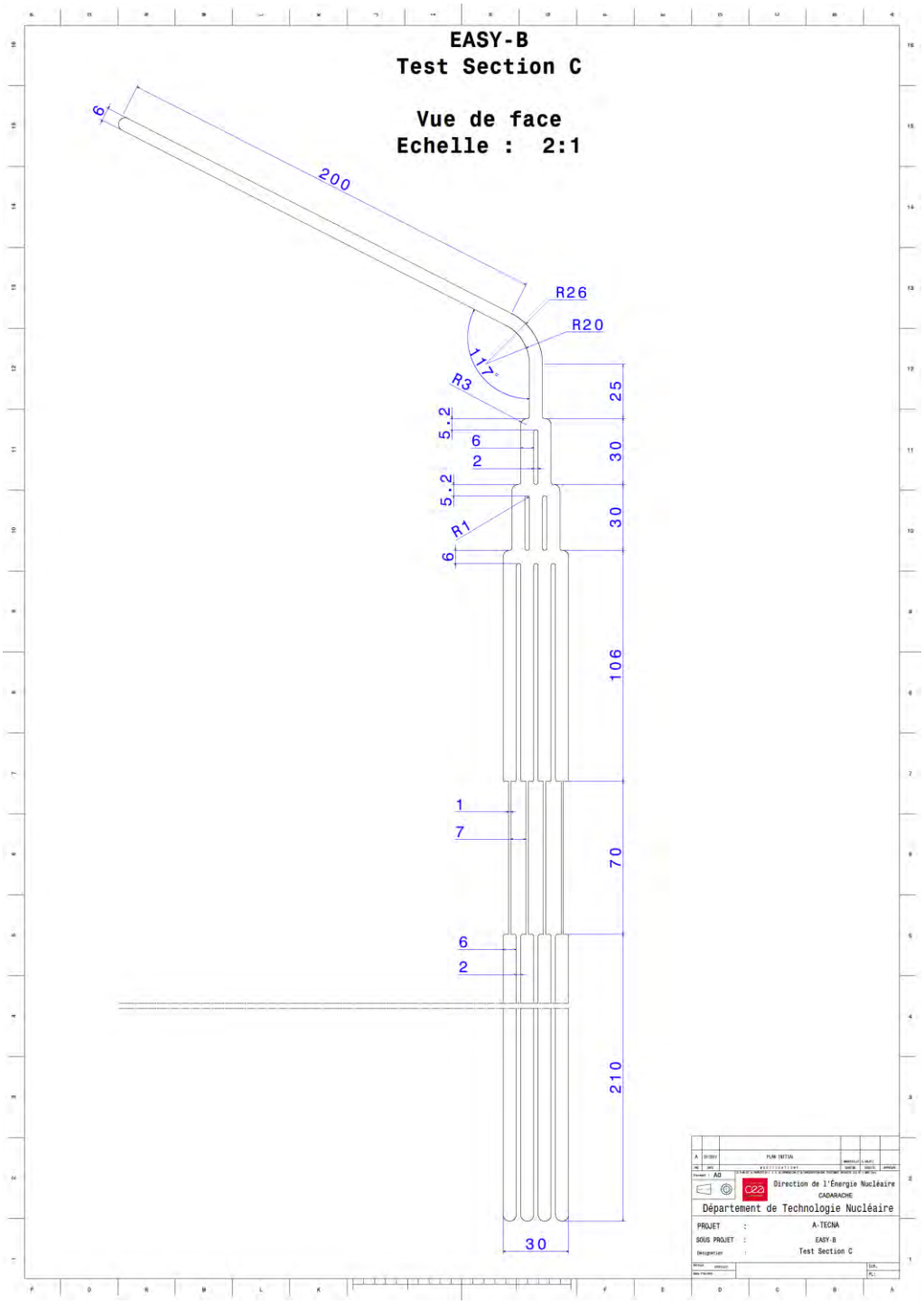

III.4. DANAH: Inlet header (1)

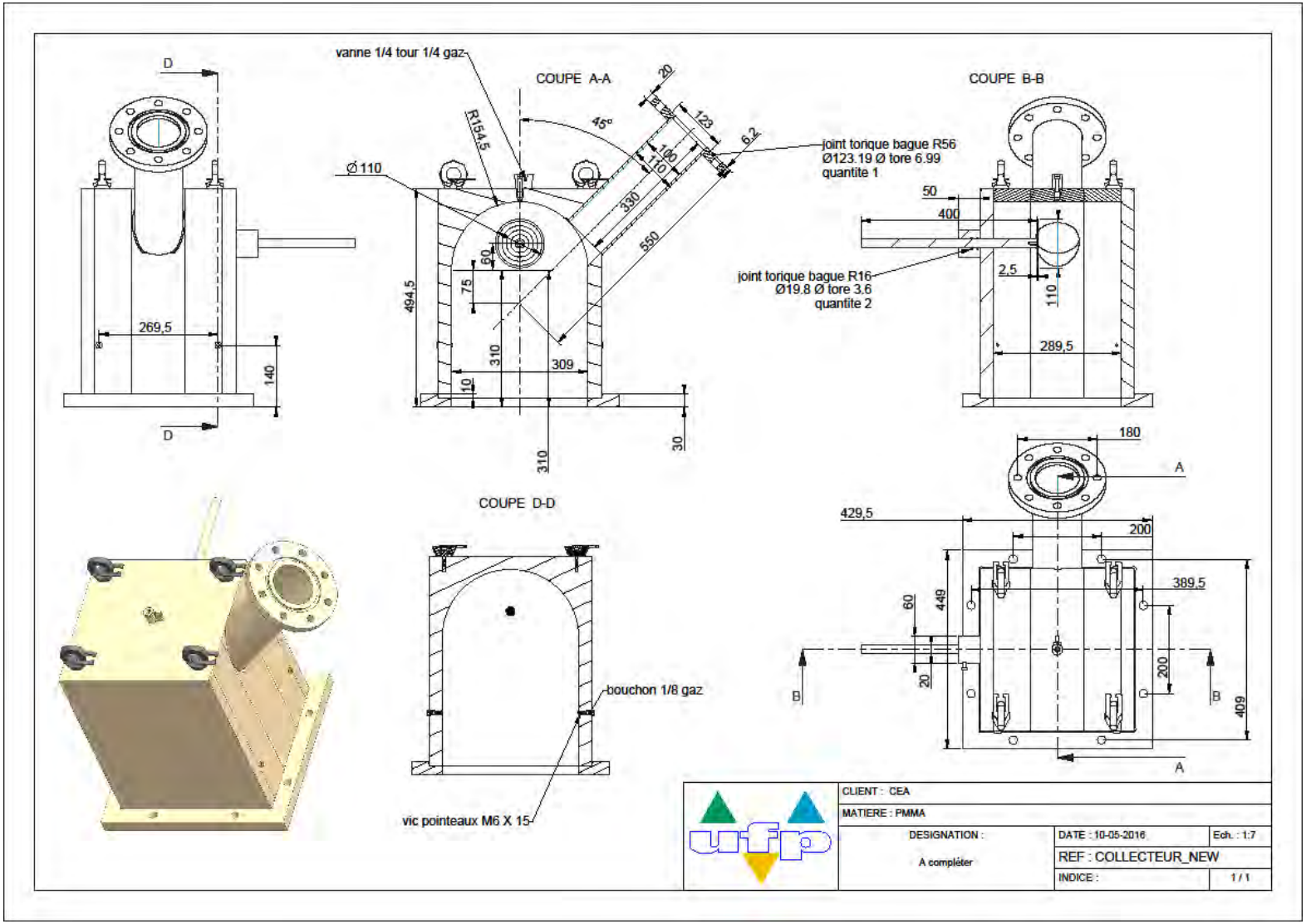

III.5. DANAH: Inlet header (2)

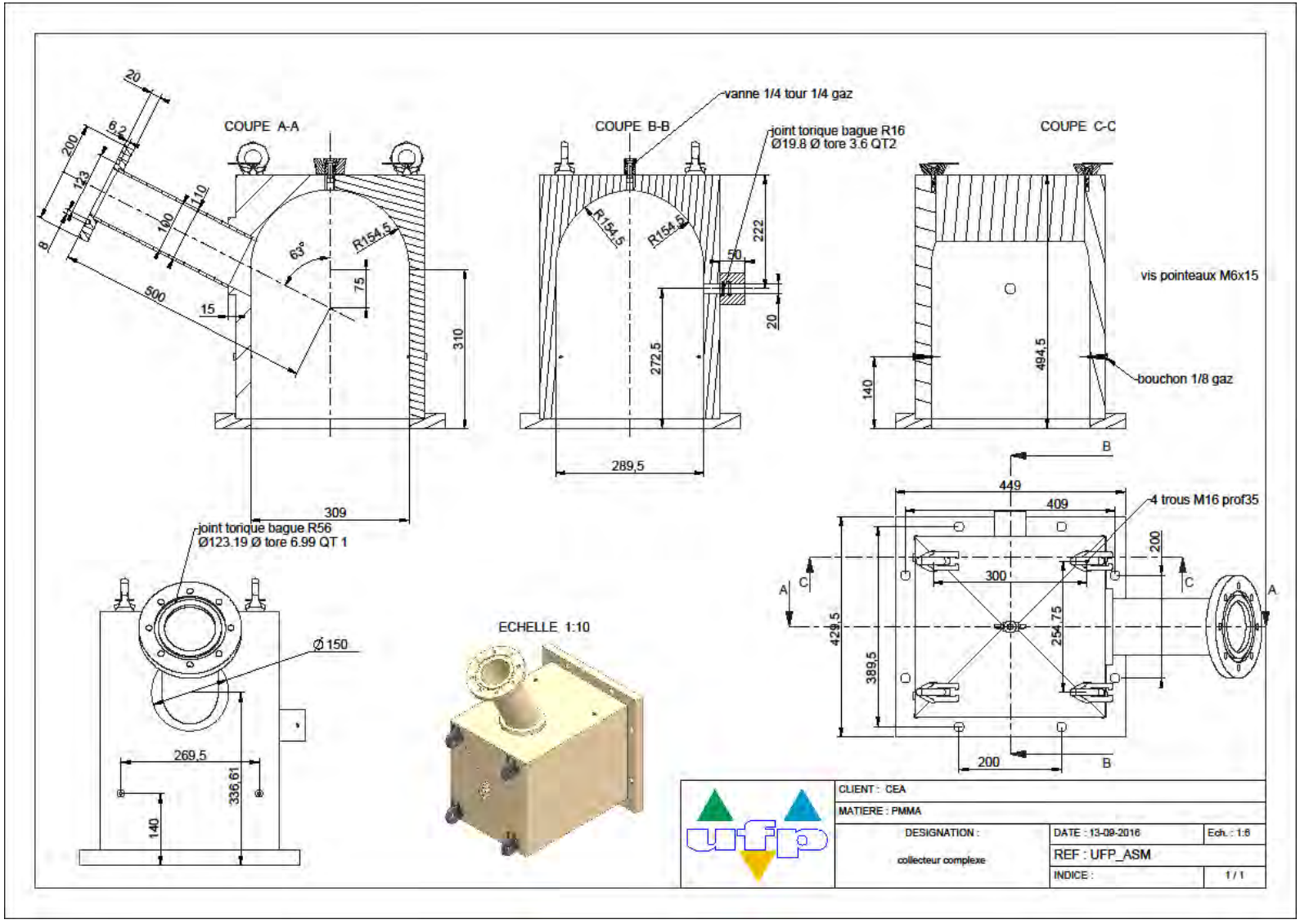

III.6. DANAH: Outlet header

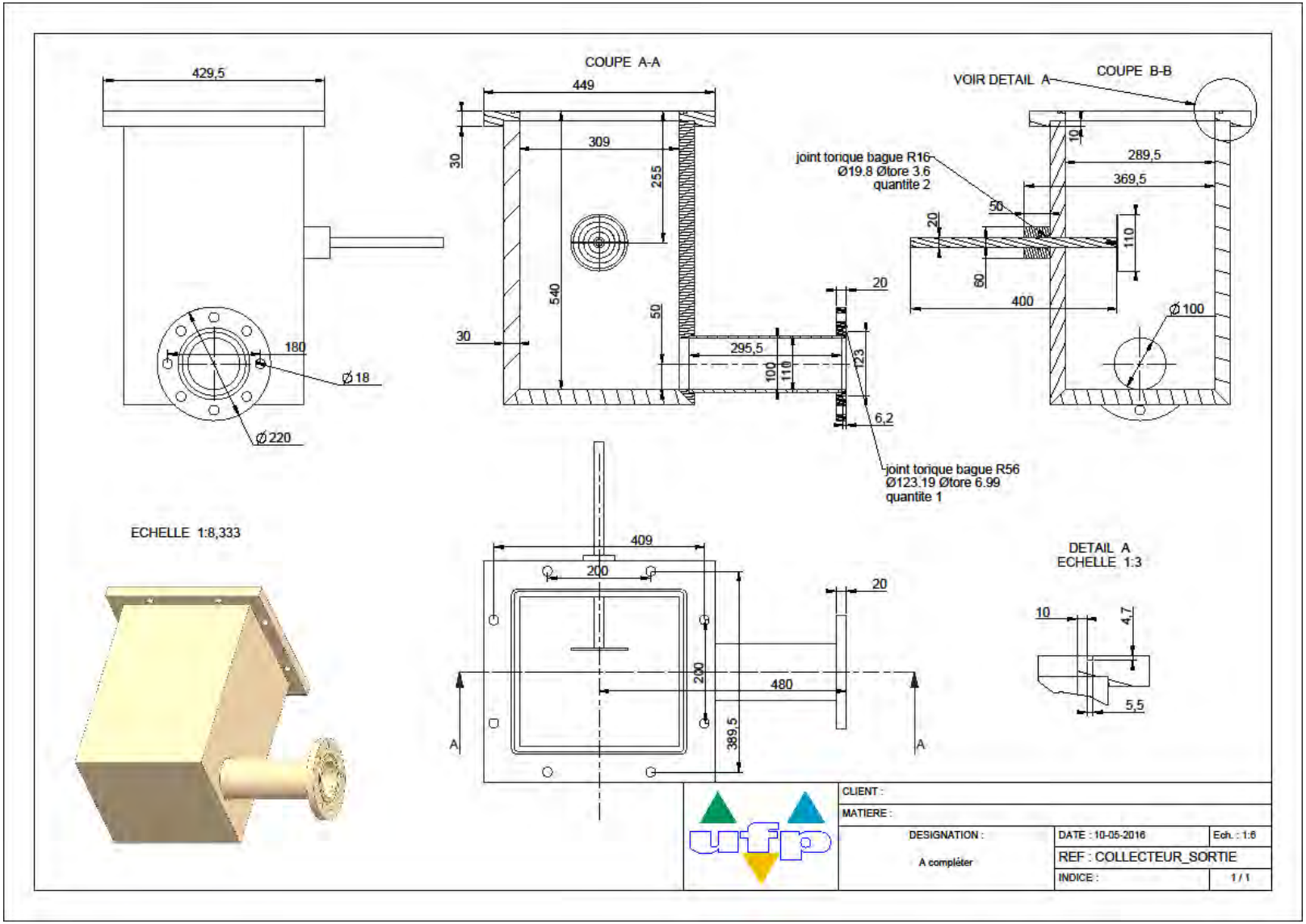

DANAH: Bundle channel

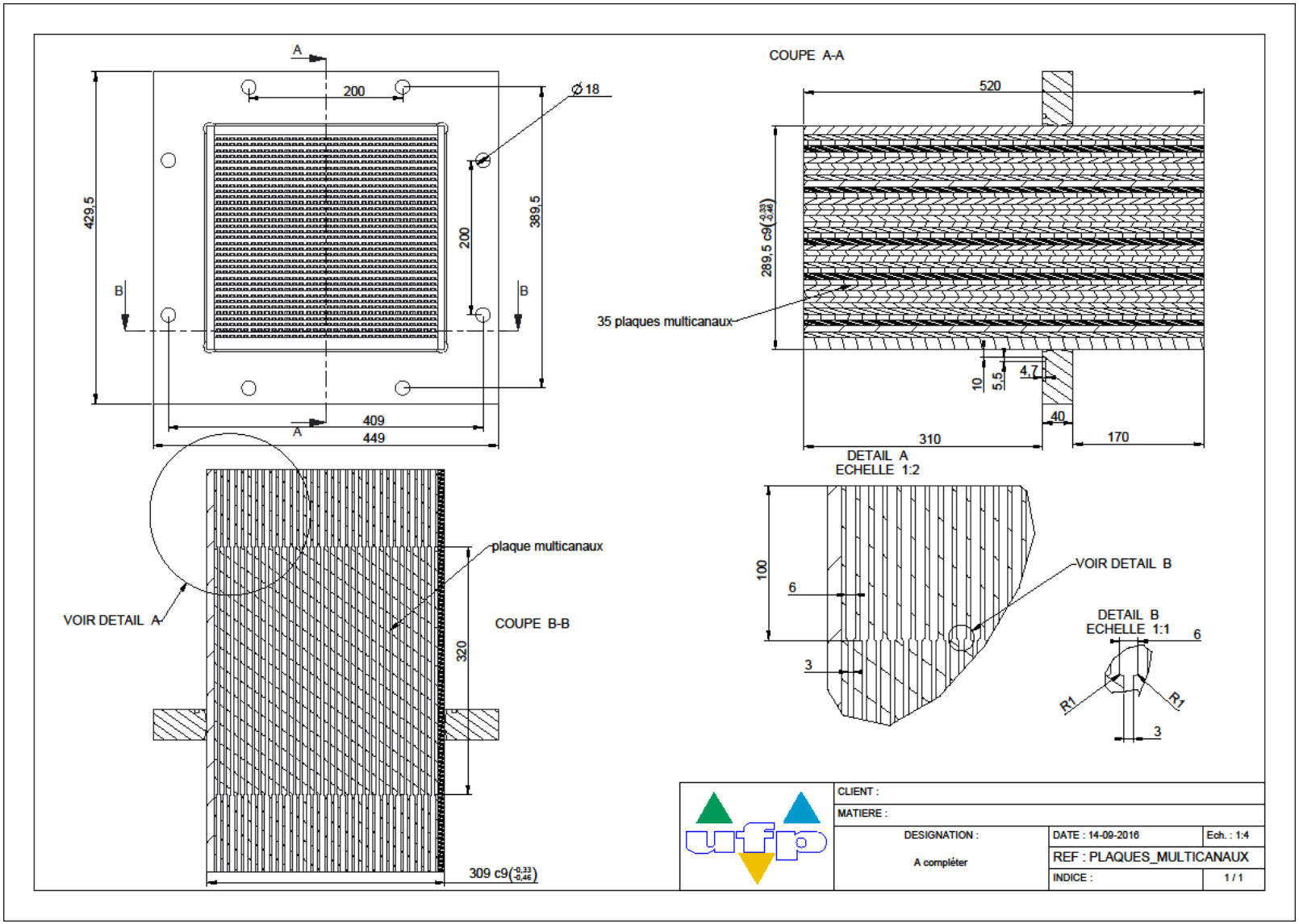

III.7. DANAH: Bundle channel wedge

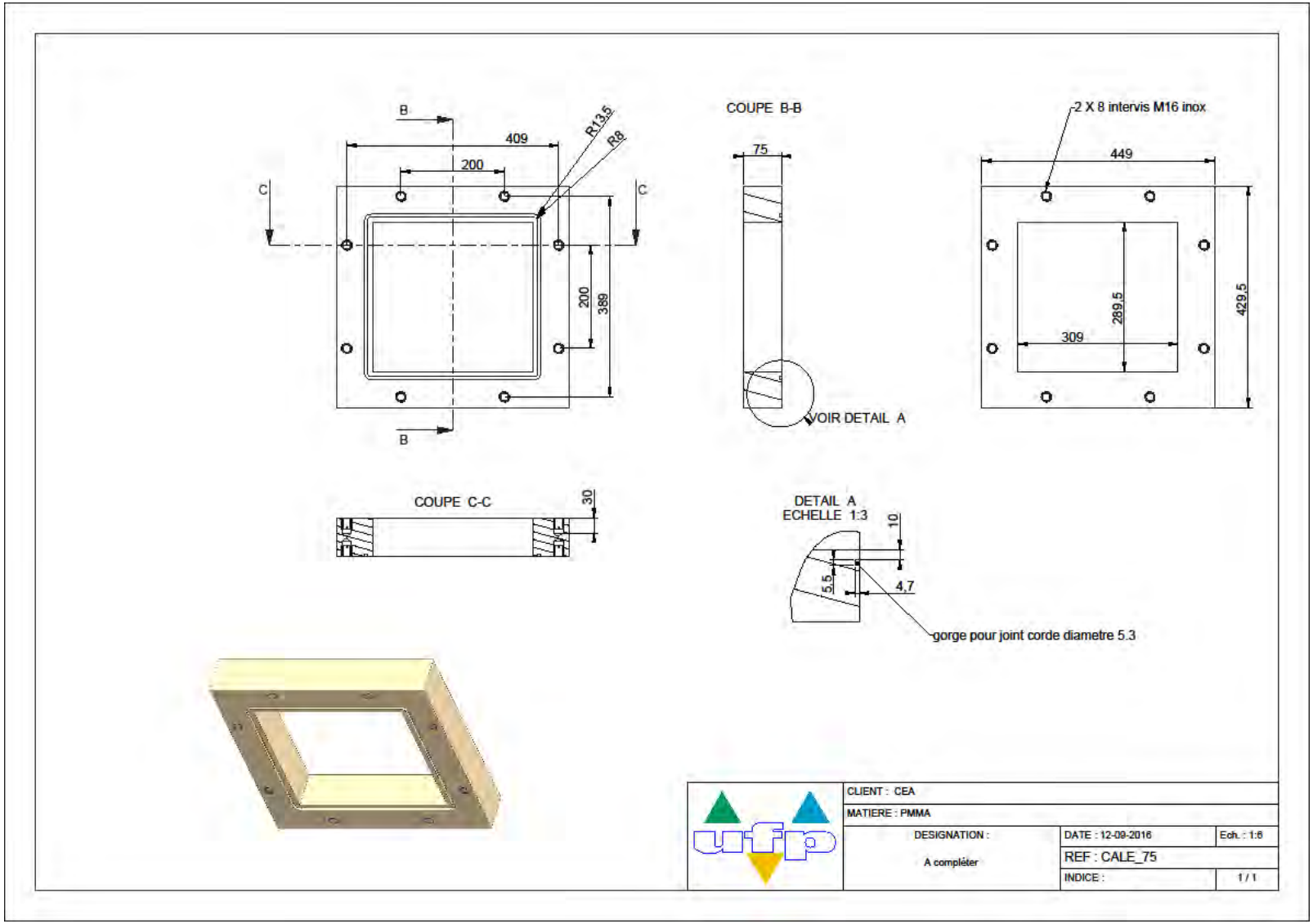

Bibliography

[1] IAEA. *http://www.world-nuclear.org*. s.d.

[2] Matthew Fuhrmann. "How Atoms for Peace Programs Cause Nuclear Insecurity" *Atomic Assistance*

[3] Energiforsk - Swedish Energy Research Centre. "Fourth Generation Nuclear Power"

[4] GIF Portal. *https://www.gen-4.org*

[5] Mycle Schneider "Fast Breeder Reactors in France" *Science and Global Security, 17:36–53, 2009*

[6] F. Varaine "ASTRID -Progress Report and Prospect" *CIAE – CEA Meeting on Fast Reactor Cooperation -3rd ASTRID-CFR 600 Meeting*

[7] P. Le Coz, J.F. Sauvage and J.P. Serpantie "Sodium-cooled Fast Reactors: the ASTRID plant project" *Proceedings of ICAPP 2011 – Nice, France, May 2-5, 2011, paper 11249, pp.419-425*

[8] M. Saez et al. "The use of gas based energy conversion cycles for sodium fast reactors" *Proceedings of ICAPP'08, Anaheim, USA, June 8-12, 2008, paper 8037, pp.565-573*

[9] L. Cachon et al. "Status of the Sodium Gas Heat Exchanger (SGHE) development for the Nitrogen Power Conversion System planes for the ASTRID SFR prototype" *Proceeding of ICAPP'15, Nice (France), Mai 03-06, Paper 15362.*

[10] Vitillo et al. "Experimental and numerical activities in support of the design of ASTRID Sodium-Gas Heat Exchanger" *Proceeding of NURETH'16, Chicago (USA), Aug 30- Sept 04, Paper 16321(2015).*

[11] J.M., Kitto J.B and Robinson "Effect of Maldistribution of Flow and heat Transfer Equimenet Performance" *Heat Transfer Engineering, n.d.: Vol.10.*

[12] R.K.Shah and D.P.Sekulic. "Fundamentals of Heat Exchanger Design" *n.d.*

[13] A. Acrivos, B.D. Babcock and R.L. Pigford "Flow distribution in Manifolds." *Chemical Engineering Science, 1959.*

[14] RA, Bajura. "A model for flow distribution in manifolds" *Chemical Engineering Science, 1959: 93: 7-12.*

[15] Bajura and Jones « Flow distribution manifolds fast reactors », *Journal of Fluids Engineering, 1976Engineering Science, 1959: 654-665.*

[16] M.K. Bassiouny and H.Martin "Flow distribution and pressure drop in plate heat exchangerI; U-type arrangement" *Chemical Engineering Science*, 1984: 39, 693-700.

[17] Bassiony MK and Martin H "Flow distribution and pressure drop in plate heat exchangerI. Part 2. Z-type arrangement" *Chemical Engineering Science, 1984: 39: 7001-704.*

[18] A.B.Datta and A.K.Majumdar "Flow distribution in parallel and reverse manifolds" *International Journal Of Heat and Fluid Flow 98 (1980): 253-626.*

[19] Junye Wang "Theory of flow distribution in manifolds." *Chemical Engineering Journal" Volume 168, Issue 3, 15 April 2011, Pages 1331-1345.*

[20] J.Y.Wang "Pressure drop and flow distribution in parallel-channel configurations of fuel cell stacks: U-type arrangement" *Hydrogen Energy, 2008: 33:6339-6350.*

[21] J.Y.Wang. "Pressure drop and flow distribution in parallel-channel configurations of fuel cell stacks: Z-type arrangement" *Hydrogen Energy, 2010: 5498-5509*.

[22] C. Wang, K.Yang, J. Tsai and I. Chen "Characteristic of flow distribution in compact parallel flow heat exchanger, part II: Modified inlet header" *Applied Thermal Engineering, 2011: 31: 3225-3242.*

[23] C. Wang, K.Yang, J. Tsai and I. Chen "Characteristics of flow distribution in compact parallel flow heat exchanger, part I: Typical inlet header" *Applied Thermal Engineering, 2011: 31:3226-3234.*

[24] Huang C. and Wang C "The design of uniform tube flow rates for Z-type compcat parallel flow heat exchangers" *International Journal of Heat and Mass Transfer, 2013: 57: 608-622.*

[25] Fu H., Watkins A.P. and Yianneskis "The effects of flow split ratio and flow rate in manifolds." *International Journal for numerical methods in fluid*, 1994: 18: 871-886.

[26] B.D. Launder, D.B. Splalding "The Numerical Computation of Turbulent Flow." *Computer Methods in Applied Mechanics and Engineering, 1984: 3.*

[27] Lalot S., Florent P., Lang SK. "Flow maldistribution in heat exchangers." *Applied Thermal Engineering, 1999: 19: 847-63.*

[28] Jiao A, Zhang R, Jeong S. "Experimental investogation of header on flow maldistribution in plate-fin heat exchanger" *Applied Thermal engineering, 2003: 23:1235-1246.*

[29] Wen J, Li Y, Zhou A and Zhang K. "An expeirmental and numerical investigation of flow patterns in the entrance of plate-fin heat exchanger" *Heat and Mass Transfer, 2006: 49: 1667-167.*

[30] Wen J, Li Y, Zhhou A, Zhang K and Wang J "PIV experimental investigation of entrance configuration on flow maldistribution in plate-fin heat exchanger" *Cryogenics , 2006: 46: 37-48*.

[31] Wen J, Li Y and Yansong M. "PIV Investigation of flow pattern in entrance configuration of Plate-fin heat exhanger." *Journal of Chemical Engineering, 2006: 15:15-23*.

[32] Wen J, Li Y, Zhou A and KZhang K. "An experimental and numerical investigation of flow patterns in the entrance of plate-fin heat exchanger" *Heat and Mass Transfer, 2006: 49: 1667-1678.*

[33] Z. Zhang and Yan Zhong Li. "CFD simulation on inlet configuration of plate-fin heat exchanger." *Cryogenic, 2003: 43.*

[34] Appasaheb Raula, B. N. Bhasme and Dr. R.S. Mauryac "A numerical investigation of

fluid flow maldistribution in inlet header configuration of plate fin heat exchanger" *Energy Procedia 90 (2016) 267 – 275.*

[35] Wen J, Li Y. "Study of flow distribution and its improvement on the header of plate-fin heat exchanger" *Cryogenics, 2004: 44: 823-83*

[36] Ramos-Alvarado B, Li P, Liu and Hernandez-Guerrero A "CFD study of liquid-cooled heat sinks with microchannel flow field configurations for electronics, fuel cells, and concentrated solar cells" *Applied Thermal Engineering, 2011: 31: 2494-2507*.

[37] Almeida MP, Andrade JS, Buldyrev SV, Cavalcante FSA, Stanley HE, Suki B. "Fluid flow through ramified structures." *The American Physical Review, 1999: 60.*

[38] A, Bejan "Constructal theory network of conducting paths for cooling a heat generating volume." *International Journal of Heat and Mass Transfer, 1997: 40: 799-816.*

[39] Bejan and S. Lorete "Constructal theory of generation of configuration in nature and engineering" *Applied Physics Reviews 2006 (1), 5 (2006).*

[40] A. Bejan "Advanced Engineering Thermodynamics" *2nd ed. (Wiley, New York, 1997).*

[41] Liu H., Li P., Lew J and Juarez-Robles "Experimental study of the flow distribution uniformity in flow distributors having novel flow channel bifurcation structures" *Experimental Thermal and Fluid Science, 2012: 37: 142-153.*

[42] Liu H. and Li P. "Even distribution/dividing of single-phase fluids by symmetric bifurcation of flow channels." *International Journal of Heat and Fluid Flow, 2013: 40: 165-179.*

[43] Liu H., Li P and Wang K. "The flow downstream of a bifurcation of a flow channel for uniform flow distribution via cascade flow channel bifurcations." *Applied Thermal Engineering, 2015: 81: 114-127.*

[44] Schlichting H. "Boundary Layer Theory" F*ourth ed. McGraw-Hill, New York, 1960*.

[45] Zhang C, Lian Y, Hsu C, Teng J, Liu S, Chang Y and Greif R. "Investigations of thermal and flow behavior of bifurcations and bends in fractal-like microchannel networks: Secondary flowand recirculation flow." *International Journal of Heat and Mass Transfer, 2015: 85: 723-731.*

[46] Jeanningros, Xavier. "*ASTRID* - ECSG : Thermohydraulique des collecteurs Na ». *Note Technique, CEA/DEN/CAD/DTN/STCP/LCIT/NT/2015-050-INDICE A, 2016*.

[47] Christophe Garnier « ASTRID - Etude des collecteurs sodium de l'ECSG et dimensionnement selon le RCC-MRx"*Note Technique, CEA/DEN/CAD/DTN/STCP/LCIT/NT/2015-049-INDICE A, 2015.*

[48] Christoophe Garnier. *Personnal Communication*.

[49] CEA Nuclear Energy Division. « Sodium-cooled Nuclear Reactors » *CEA Saclay et Groupe Moniteur (Éditions du Moniteur), Paris, 2016.*

[50] D. Guenadou, I. Tkatshenko and P. Aubert "Plateau Facility in Support to Astrid and the SFR Program: An Overview of the First Mock-Up of the Astrid Upper Plenum, MICAS", *Proceedings of the16th International Topical Meeting on Nuclear Reactor Thermal Hydraulics (NURTEH16), Chicago, Illinois, August 30-September 4, 2015*

[51] *https://www.piv.de*

[52] Huang, H., Dabiri, D., & Gharib, M "On errors of digital particle image velocimetry" *Measurement Science and Technology, 1997, 8(12), 1427*.

[53] Adrian, R. J. & Yao, C. S. "Pulsed laser technique application to liquid and gaseous flow and the scattering power of seed materials" *Applied Optics, 24(1), 44.52, (1985)*.

[54] Westerweel, J "Efficient detection of spurious vectors in particle image velocimetry data" *Exp. in Fluids, (1994) 16, 236-247*.

[55] "PIV Uncertainty". *La Vision Manual*.

[56] K T Christensen and F Scarano. "Uncertainty quantification in particle image velocimetry ". *Meas. Sci. Technol. 26 070201 (2015).*

[57] Andrea Sciacchitano and Bernhard Wieneke "PIV uncertainty propagation" *Measurement Science and Technology, Volume 27, Number 8. 29 June 2016.*

[58] Brown, Glenn. "The Darcy–Weisbach Equation". *Oklahoma State University–Stillwater.*

[59] C.F Dietrich "Uncertainty, Calibration and Probability: The Statistics of Scientific and Industrial Measurement" *Chapter 8, Routledge, 12 July 2017.*

[60] Charonko J.J. and Vlachos P.P. "Estimation of uncertainty bounds for individual particle image velocimetry measurements from cross-correlation peak ratio" *Meas. Sci. Technol. 24 065301. 2013.*

[61] Sciacchitano A., Neal D. R., Smith B. L., Warner S. O., Vlachos P.P., Wieneke B. and Scarano F. "Collaborative framework for PIV uncertainty quantification: comparative assessment of methods" *Meas. Sci. Technol. 26 074004 2015.*

[62] Insight 4G Manual. "Global Image Acquisition, Analysis and Display Software". *Version 11.1.*

[63] ANSYS Fluent 16.1. *Theory Guide*.

[64] Miozzi M., Lalli F. and Romano G.P. "Experimental investigation of a free-surface turbulent jet with Coanda effect", *15th Int Symp on Applications of Laser Techniques to Fluid Mechanics, Lisbon, 2010*.

[65] Blevins R.D. "Applied Fluid Dynamics Handbook", *Van Nostrand Reinhold Co., New York, 1984.*

[66] Tanaka E. "The interference of two-dimensional parallel jets (1st report, experiments on dual jet)" *Bull JSME Vol.13, pp.272-280, 1970.*

[67] Bunderson E. N. and Smith B. L., "Passive mixing control of plane parallel jets, Experiments in Fluids" *Vol.39, pp.66-74, 2005.*

[68] Lai J.C.S. and Nasr A., "Two parallel plane jets: comparison of the performance of three turbulence models" *Proc Instn Mech Engrs, Vol.212, Part G.*

[69] Tanaka E. "The interference of two-dimensional parallel jets (2nd report, experiments on dual jet)." *Bull JSME Vol.13, pp.272-280, 1974.*

[70] Tanaka E. "The interference of two-dimensional parallel jets (3rd report, the region near the nozzle in triple jets)" *Bull JSME, Vol. 18, No. 124, 1975.*

[71] Samuele Viario "Experimental and numerical analysis of confined parallel jets" *Politecnico di Milano, 2011.*

[72] D.C.Wilcox "Turbulence Modeling for CFD", *DCW Industries, 1998.*

[73] F.R.Menter, M.Kuntz and R.Langtry "Ten years of industrial experience with the SST Turbulence model" *Turbulence, Heat and Mass Transfer 4, Begell House, Inc., 2003.*

[74] B.E.Launder and D.B.Spalding "Lectures in Mathematical Models of Turbulence", *Academic Press, 1972.*

[75] F.Vitillo, C.Galati, L.Cachon and P.Milan "An anisotropic shear stress transport (ASST) model formulation" *Computers & Mathematics with Applications Volume 70, Issue 9, November 2015, Pages 2238-2251.*

[76] Chiara Galati "Numerical and Experimental Study for ASTRID Sodium-Gas Heat Exchanger Design Application" *Dipartimento di Ingegneria Astronautica, Elettrica ed Energetica, Università di Roma.*

[77] M. M. Gibson and B. E. Launder "Ground Effects on Pressure Fluctuations in the Atmospheric Boundary Layer" *J. Fluid Mech., 86:491-511, 1978.*

[78] ANSYS Fluent 16.1. *Manual*.

[79] Prasun Dutta, Sumit Kumar Saha, Nityananda Nandi and Nairit Pal. "Numerical study on flow separation in 90° pipe bend under high Reynolds number by k-ε modelling". *Engineering Science and Technology, an International Journal 19 (2016) 904–910.*

[80] NEA/CSNI/R. "T-Junction Benchmark exercise" Report of the OECD/NEA-Vattenfall. 2011.

[81] A. Kalpakli and R. Örlü "Turbulent pipe flow downstream a 90° pipe bend with and without superimposed swirl". *International Journal of Heat and Fluid Flow 41 (2013) 103–111.*

[82] R. Rohrig, S. Jakirlic and C. Tropea "Comparative computational study of turbulent flow in a 90° pipe elbow" *International Journal of Heat and Fluid Flow 55 (2015) 120–131.*

[83] B. E. Launder and D. B. Spalding "Lectures in mathematical models of turbulence". *Academic Press, 1972, London, England.*

[84] V. Yakhot and S. A. Orszag. "Renormalization group analysis of turbulence: I. Basic theory". *Journal of Scientific Computing, 1986, Vol. 1, No. 1, pp. 1-51.*

[85] T.-H. Shih, W. W. Liou, A. Shabbir, Z. Yang, and J. Zhu. "A new k-ε eddy-viscosity model for high Reynolds number turbulent flows". *Model development and validation, Computers & Fluids, 1995, Vol. 24, No. 3, pp. 227-238.*

[86] M. M. Gibson and B. E. Launder. "Ground effects on pressure fluctuations in the atmospheric boundary layer". *J Fluid Mech., 1978, Vol. 86, pp. 491-511.*

[87] B. E. Launder "Second-moment closure: Present... and Future?" *Inter. J. Heat Fluid Flow, 1989, Vol. 10, No. 4, pp. 282-300.*

[88] E. Baglietto, H. Ninokata and T. Misawa, "CFD and DNS methodologies

development for fuel bundle simulations", *Nuclear Engineering and Design, Vol. 236, pp.1503-1510, 2006.*

[89] L. Cachon, C. Galati, X. Jeanningros and A. Molla « Module d'échangeur de chaleur a plaques dont les canaux intègrent en entrée une zone de répartition uniforme de d ébit et une zone de bifurcations de fluide » *PATENT FR16 57543, 3 August 2016.*

[90] Xavier Jeanningros. *Personnal Communication*.

[91] C. Galati, X. Jeanningros, L. Cachon, L. Prat and C. Gourdon "Preliminary Analysis of Flow Maldistribution in ASTRID Sodium-Gas Hear Exchanger", *Proceeding of ICAPP'16, San Francisco (USA), Avril 17-21, Paper 16321.*

[92] C. Galati, L. Cachon, L. Prat and C. Gourdon "Experimental and numerical validation of flow maldistribution in compact Heat exchanger", *Proceeding of NURETH'17, Xian (China), September 03-08, Paper 21083.*